The University of Nottingham

UNITED KINGDOM · CHINA · MALAYSIA

MULTI-SCALE MODELLING AND MATERIAL CHARACTERISATION OF TEXTILE COMPOSITES FOR AEROSPACE APPLICATIONS

by

Qing Pan

Thesis submitted to the University of Nottingham

for the degree of Doctor of Philosophy

July 2016

ACKNOWLEDGEMENTS

First of all, I would like to express my gratitude to my supervisor, Prof. Shuguang Li, for encouraging me to undertake a PhD in the first place, and for providing a continuing support, guidance and advice throughout my PhD course. His constant willingness to generously share his vast expertise has greatly helped me to find solutions to the emerging issues and achieve a considerable progress in the last three years.

I would also like to thank my co-supervisors Prof. Andrew Long and Dr. Elena Sitnikova. Their advices and guidance have made profound difference to my project. Especially for Dr. Elena Sitnikova who made direct contribution to my published paper and PhD thesis.

Acknowledgements are due to AVIC Commercial Aircraft Engine Co. Ltd. (ACAE), who made this project possible by kindly providing comprehensive support both financially and technically.

I would like to thank all the people from the Composites Group, who helped me in the course of my project. In particular, I would like to thank other members of the project team, Tianhong Yu, Weiyi Kong and Xiantao Zhao, for the helpful discussions that we had. I must also extend my sincere gratitude to Dr. Shoufeng Hu from ACAE, whose knowledgeable and constructive feedback provided constant source of wisdom and an indispensable contribution to my research.

Last but not least, I would like to recognise the incredible support I received from my family in the last few years. I wish to express my deepest gratitude to my wife, Xing Zhu, for all her sacrifices, understanding and support. I’m very thankful to my grandparents and to my parents, whose support and encouragement have empowered my aspiration. My acknowledgement also goes to my daughters for allowing me to concentrate on my PhD study.

Abstract

Textile composites offer an excellent alternative to metallic alloys in the aerospace engineering due to their high specific stiffness and strength, superb fatigue strength, excellent corrosion resistance and dimensional stability. In order to successfully apply these materials to engineering problems, a methodology to characterise and predict the constitutive response of these materials is essential. The lack of the modelling tools for modern textile composites that would facilitate systematic analysis and characterisation of these materials hinders the wide adoption of such material systems in engineering applications. This defines the focus of the project as represented in this thesis.

A multi-scale modelling methodology has been established for the material characterisation and representing the constitutive response of the material at a macroscale. For material characterisation at micro- and mesoscales, an automated material characterisation toolbox, UnitCells©, has been employed and substantially developed in both the scope and complexity through this project. When applying this toolbox, the user selects the required type of a textile or unidirectional reinforcements and provides a parametric input, based on which a finite element model of a unit cell for the composites is generated automatically. The effective properties that can be predicted using this toolbox include stiffness, thermal expansion coefficient, thermal and electric conductivities, static strength and dynamic strength (associated with deformation localisation as the limit of the applicability of unit cells but a conservative estimate of the material strength). There are seven types of microscale models and eleven types of mesoscale models available in the toolbox at present.

To represent a constitutive relationship for textile composites at a macroscale, the artificial neural network (ANN) algorithm has been adapted and developed into a useful modelling tool, referred to as the ANN system. A criterion defining an ultimate failure of the material has been proposed. The outcome has made it possible for a user defined material subroutine to be established which can be employed in the analysis of structures made of such textile composites by providing the effective constitutive behaviour of them in a most efficient manner. As a validation, ANN system was used to predict the critical velocities of three types of layer-to-layer interlock 3D woven composite panel subject to ballistic loading. The predicted results matched well with the testing results. Furthermore, as an illustration of potential capability, the ANN system has been used to simulate impact of a textile composite fan blade containment casing in an idealised fan blade off scenario.

Through the project, the capability of predicting the impact behaviour of textile composites has been established. This involves unit cell modelling at micro-/mesoscales for material characterisation, strength prediction with due consideration of strain rate sensitivity of the constituent materials, and ANN system to deliver the characterised constitutive relationship in terms of a user defined material subroutine for practical applications at macroscale, such as structural impact analysis.

Contents

List of Figures

List of Tables

Abbreviations and Notations

Abbreviations

2D	Two-dimensional
3D	Three-dimensional
ANN	Artificial neural network
DDSDDE	Jacobian matrix in UMAT subroutine
FAA	Federal Aviation Administration
FBO	Fan blade-out event
FCC	Face centred cubic packing unit cell
FE	Finite element
FEM	Finite element method
GF1	First type of E-glass fibre reinforced layer-to-layer interlock composites
GF2	Second type of E-glass fibre reinforced layer-to-layer interlock composites
PCA	Principal component analysis
RTM	Resin transfer moulding
RVE	Representative volume element
SCP	Simple cubic packing unit cell
T300 CF	T300 carbon fibre reinforced layer-to-layer interlock composites
UC	Unit cell
UD	Unidirectional fibre-reinforced composites

Notations

C	The strain rate scaling constant
E	Young’s modulus
G	Shear modulus

m	Damage evolution parameter
S	Strength
S_c	Compressive strength
S_t	Tensile strength
S_{Xc}	Compressive strength along *X* direction
S_{Xt}	Tensile strength along *X* direction
S_{xy}	Shear strength in *XY* plane
S_{xz}	Shear strength in *XZ* plane
S_{Yc}	Compressive strength along *Y* direction
S_{Yt}	Tensile strength along *Y* direction
S_{yz}	Shear strength in *YZ* plane
S_{Zc}	Compressive strength along *Z* direction
S_{Zt}	Tensile strength along *Z* direction
u, v, w	Displacements
x, y, z	Coordinates
α	Coefficient of thermal expansion
γ	Shear strain component
ε	Normal directional strain component
$\dot{\varepsilon}$	Strain rate
ν	Poisson’s ratio
ρ	Density
σ	Normal directional stress component
τ	Shear stress component

Chapter 1 Introduction

1.1 Background and Motivation

The trend in the use of composites in aircraft engines is on the increase. As the bypass ratio of commercial aircraft engines increases to achieve higher fuel efficiency, the fan section of the engine becomes larger and heavier. The Federal Aviation Administration (FAA) aircraft engine certification requires that engines should be capable of containing failed fan blades at their full operation speed [1]. This is to prevent the fragments of failed fan blades getting into the other parts of the aircraft, causing further damage and hazards.

A detached fan blade is required to be contained by the engine component called fan blade containment casing. It is a ring around the fan as shown in the sketch of an engine in Figure 1.1 [2]. During normal operation, the containment casing provides the outer flow path for air passing through the fan and also serves as a structure for attachment of the inlet and other components. Its most important function, however, is to contain a detached fan blade in a fan blade-out or fan blade off (FBO) event [3]. The fragments of the released fan blade, if allowed to penetrate the wall of the containment casing, would damage fluid lines, control cables, oil tanks and airframes, which may seriously compromise the safety of the airplane and passengers on board. Therefore, FAA in the United States and European Aviation Safety Agency (EASA) in Europe require that fan blade containment casings of all commercial aero engines should have the capability to contain the released high energy fragments in an FBO event [1, 4]. Since the fan blade containment casing is the heaviest component of the engine, yet not subjected to temperatures, it has been a key area of development among all major commercial aircraft engine manufacturers to employ composites to reduce the weight of the casing without compromising the safety requirements [5].

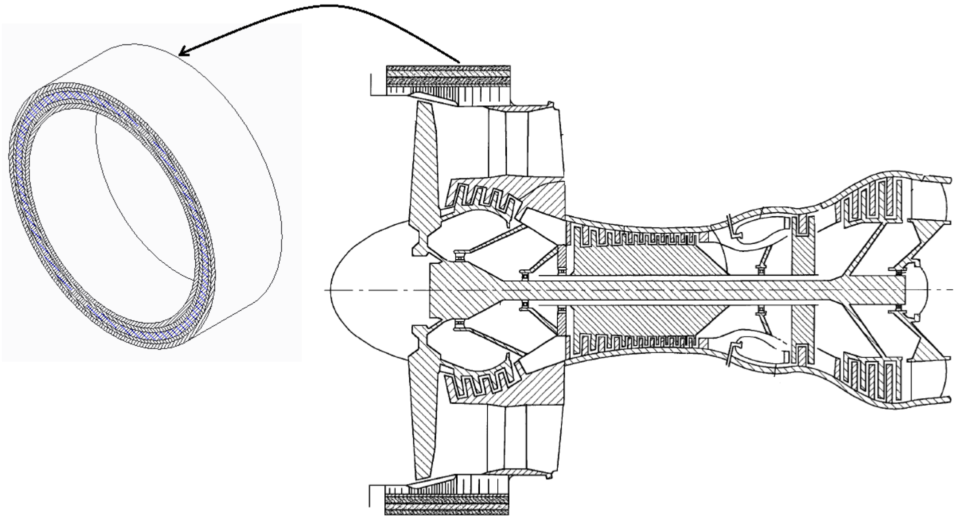

Figure 1.1 Illustration of fan blade containment casing of aero engine [2]

Traditionally, fan blade containment casings were designed to ensure that the metallic casing wall is sufficiently thick to resist penetration of the blade. This approach is called a ‘hard wall’ design [5]. Some possibilities such as fatigue fracture, bird ingestion or other foreign object damage, may lead to the blade release in rare events [6, 7]. Since the fan blade may release with a velocity higher than 400m/s [8], the impact resistance of containment casing is required to be very high. The containment casings are usually made of metals, such as titanium alloy [9]. Carney et al. [8] suggested axially convex curved geometry containment. This casing was made of titanium and stainless steel (Ti-6Al-4V and SS-304L). The design idea about this is to use the plastic deformation in the casing to dissipate some kinetic energy before the full weight collision of blade.

However, during normal engine operation, most of the material required for blade containment casing is a parasitic weight that reduces the engine thrust/weight ratio and increases fuel consumption. Therefore, when designing a containment casing of the modern engine, the material, geometry and wall thickness have to be carefully selected to reduce the weight of the ring while offering sufficient perforation resistance.

An alternative approach, a ‘soft wall’ design, that used a fabric wrap on the outside of a metallic liner to provide blade containment, was investigated in the late 1970s and early 1980s [10]. This design of the casing involves applying a fabric wrap as an outer layer of the casing and this can be a lower weight option for some engines. For a ‘soft wall’ design, fragments of failed blades penetrate some designated soft layers, while the kinetic energy is absorbed before finally being arrested by the outer layers of the casing. The major disadvantage of this design was the requirement that a sufficient space had to be allocated to allow for the deformation of the casing to absorb energy. This led to an increase of the overall cross-sectional area of the engine, which could in turn undermine the performance of the engine.

The selection of a ‘hard wall’ or ‘soft wall’ design for a specific engine depends on the relative weight of the two approaches in addition to other system-level design issues and overall costs.

Composite materials offer an excellent alternative to the conventional alloys employed for making containment casings, due to their outstanding physical, mechanical and thermal properties, which include high specific stiffness and strength, good fatigue strength, excellent corrosion resistance and dimensional stability [5]. Because of the nature of composite materials, integrated containment casings can make full use of the advantages of composite. However, the mechanical performance of the composites is strongly related to the type of the fibrous reinforcements and their placement architecture in the composite.

Furthermore, because of the anisotropic properties and complex failure mechanisms, the material characterisation of the composites is challenging, which in turn makes design of the composite containment casings more complicated than that of the metallic ones. On the other hand, because of the complex structure of composite material, the layout, architecture and volume fraction of reinforcement can be altered to optimize material performance under the required stress states.

The most commonly used type of composites is the composite laminates and two-dimensional (2D) weave laminates. However, laminated composites have very low impact resistance in the through-thickness direction because of the low strength of the interface between the layers [11]. This restricts the use of laminated composites for constructing fan blade containment casings, since the most significant loading of a fan blade containment casing is transverse impact in an FBO event.

Because of the weak impact resistance of interfaces, laminated UD and layered woven composites are not ideal candidates for fan blade containment casings. The delamination issue can be avoided by using 3D textile composites, which have three dimensional reinforcements, including the through-thickness direction [12]. Unlike conventional laminated composites, which are usually only reinforced in the plane of the laminate, 3D textile composites do not have planar interfaces. From the published literature, there are many types of 3D textile composites, such as 2D tri-axial braided, 3D woven [13] and 3D braided patterns [14, 15, 16, 17, 18].

With complicated yarn architectures, material characterisation of 3D textile composites becomes a lot more challenging than that of laminates. A number of methods for predicting the effective stiffnesses of 3D textile composites have been proposed in the literature [15, 16, 17, 18]. However, these methods either do not deliver a good accuracy of predictions, or are too complicated to achieve high level of automation. Furthermore, no modelling methodology is available to date for predicting the strengths of 3D textile composites. Lack of a systematic methodology for 3D textile composite material design, analysis and optimisation prevents its effective implementation in engineering design.

1.2 Aim and Objectives

The aim of this research is to develop a systematic methodology for analysis of composites based on various types of 2D and 3D textile reinforcements, so that the performances of them can be designed and optimised. The outcome will serve as a set of effective design tools, which can be readily applied for design of textile composite components in aerospace engineering, in particular, in the development of composite fan blade containment casings for civil aeroengines.

The following objectives are set to ensure that the aim is achieved.

(1) To develop a comprehensive toolbox for micro- and mesoscale unit cell (UC) modelling, with the mesoscopic unit cells addressing textile composites specifically.

(2) To develop a methodology to predict the effective strength of textile composites, taking account of strain rate effect on stiffness and strength.

(3) To develop a methodology to represent the constitutive behaviour of a 3D textile composite as a homogenized material which can be employed in macro scale modelling, e.g. the impact to the fan casing in an FBO event, with the failure of the homogenised material predicted under the general stress states.

(4) To characterise textile composites using the unit cell (UC) models under static, dynamic and thermal stress states, with systematic verifications to facilitate each of the multiscale homogenisation techniques developed.

(5) To demonstrate the capability of the developed models in material selection and geometric parameters optimisation.

(6) To implement various models including the damage model, developed in a separate project parallel to the present one through appropriate interfaces to commercial FEM codes, Abaqus and LS-DYNA, in terms of user defined material subroutines with comprehensive verifications before experimental validation.

(7) To apply the predicted material properties of textile composites to impact simulation and validate the predictions by comparing them with the experimental results.

1.3 Methodology

The main work of this thesis is to develop systematic theoretical and computational models useful for the design and analysis of polymer textile composite fan blade containment casing. To ensure the models are predictive, accurate and robust, the investigations were carried out at three scales: micro-, meso- and macroscales. Theoretical models were developed at each level for practical stress states, including static, dynamic and thermal loading. A comprehensive verification programme was carried out for each model. Appropriate experimental validation techniques were established to support the theoretical developments.

1.3.1 Microscale modelling

The assembly of fibre and matrix forms a basic building block for a fibre reinforced composites. It can represent a lamina in a conventional laminate, or a yarn in a textile composite, as a unidirectional (UD) composite. Unit cell models developed at a microscale level has been applied to determine the effective properties of UD composites. Material responses under static, dynamic and thermal stress states were considered and elastic properties (moduli, Poisson’s ratios, etc.), dynamic properties (rate sensitivity constants, etc.), thermal expansion, thermal conductivity and strengths were determined so that the UD composite materials could be fully characterised. Periodic boundary conditions were employed to derive the suitable boundary conditions for various types of unit cell models. The effective material properties determined through the microscale material characterisation serve as the input for mesoscale UC modelling.

1.3.2 Mesoscale modelling

For applications to 3D textile composites, after the fibre-matrix assembly has been homogenised using the microscale models, there is still a high level of heterogeneity due to the structural arrangement of fibres or yarns in the composites. This is one of the main advantages of the textile composites, as the yarns can be placed in a way that ensures an optimal performance of the material under prescribed stress states. Unit cell modelling was applied again at a mesoscale to determine the effective properties of the 3D textile composite material under static, dynamic and thermal stress states.

The main challenge in mesoscale modelling is to appropriately represent the complicated architecture of the yarns. This is particularly important for accurate predictions of the effective properties. Since the process of generating UC models is time-consuming, parametric studies would require a substantial modelling effort, when a set of models with the same textile architecture but different geometric parameters need to be generated. To facilitate such analysis, an automatic material characterisation toolbox UnitCells© has been employed and substantially developed in both the scope and complexity through this project. The predicted results of 3D textile composites as the outcomes from the mesoscale models offered an effective way of constructing a material mode for macroscale structural simulations.

Within this length scale modelling, in order to systematically cover a sufficiently wide range of parameter variations, a piece of software was developed which could also be used for material selection as a key part of design procedure. The models developed should be able to predict the performances of the composites from limited parameters, such as the textile architecture and the material properties of the constituents. Success of this development would minimise the need of material testing, hence reduce the associated costs, and substantially reduce the design cycle period.

1.3.3 Macroscale modelling

With UnitCells© toolbox, effective stiffness and strengths of the homogenised textile composites can be calculated properly. However, for the impact simulation of a composite component, a suitable failure criterion for homogenised textile composites under multi directional stress state is needed.

Available failure criteria are all meant to be applicable to UD composites only. It has been demonstrated in the present project how misleading it would be if any of them was blindly applied to a non-UD composite. In absence of phenomenological failure criterion directly applicable to homogenised textile composites, an advanced interpolation algorithm, artificial neural network (ANN), was adapted and developed into a useful modelling tool, referred to as the ANN system. An ANN system includes training case, ANN structure, outcome database and user material subroutine. An ANN system was used to represent the material behaviour of the textile composites at macroscale, which was considered to be a monolithic material. As a part of the ANN system, an element deletion criterion was proposed to predict the final failure of this fictitious monolithic material. UnitCells© was used to generate the training case for the ANN system.

1.3.4 Verification and validation

Each of the models developed in this project underwent verifications and validations. Some verification cases could be simple numerical tests to ensure that the model works properly. For such simple cases, the correctness of the solutions could be judged based on common sense. They offer ‘sanity checks’ on the model before it is applied for any more meaningful cases as applications. Such simple test cases were introduced and carried out as comprehensively as possible. After passing systematic sanity checks, the predictions were compared with the published experimental data and/or published numerical predictions.

The research presented focused primarily on theoretical development and implementation of textile composite multiscale modelling methodology. Being a part of a larger project on the simulation methodology for impact damage in composite components of aero-engines, it had natural overlaps with the work done by different researchers in the same team. Specifically, in terms of validation, experimental data from coupon tests and impact tests on textile composites were employed to validate the predicted results in the present project came from the other parts of the larger project. Throughout the thesis, every such instance is clearly specified in the text by an appropriate description and referencing.

1.3.5 Parametric studies

The theoretical models, once developed and validated, were employed in systematic parametric studies. A parametric study was carried out mainly in two areas, textile architecture selection and geometric parameters optimization for specified textile architecture.

For the textile architecture selection, several types of 3D woven and 3D braided composites were studied and their effective properties were estimated.

The layer-to-layer interlock 3D woven composite material was selected as an example to illustrate the process of geometric parameters optimization. A parametric study was carried out based on three well-defined parameters and an optimal combination was obtained. The textile composite with the optimal parameters is expected to provide favourable mechanical properties for containment casing, especially for impact resistance.

1.4 Thesis Layout

This thesis is comprised of nine chapters. Following this introduction the chapter by chapter thesis layout is as follows.

Chapter 2 is devoted to a literature review which has been split into three main areas. A brief review on relevant experimental work and the methods for modelling of fan blade containment casing are presented. Then, the methods of micro- and mesoscale material properties characterization are summarised. Finally, strain rate sensitivity study methods are reviewed. Overviews of specific technologies are presented in the related chapters. For instance, the formulation of periodic boundary conditions is introduced in Chapter 3. The review of failure criteria is presented in Chapter 4. An overview of artificial neural network (ANN) is given as a part of Chapter 6.

The details of the automatic composites characterization toolbox UnitCells© are described in Chapter 3. The background theory employed when developing the UnitCells© is presented. This covers method of generating the fabric architecture, imposition of the periodic boundary conditions, periodic mesh generating method and effective stiffness extraction. Some examples of UnitCells© application for predicting the effective properties of textile composites are demonstrated.

The method of predicting the effective strengths of the composite is systematically formulated in Chapter 4. The adopted failure criteria and damage evolution law were introduced and coded into a user material subroutine for implementation with Abaqus. Using UnitCells©, effective strengths of several types of 3D woven and 3D braided composites were predicted.

In Chapter 5, the methodology of characterising strain rate sensitivity of 3D textile composites from microscale to mesoscale is described. A T300 carbon fibre layer-to-layer interlock 3D woven composite was used to illustrate the process of strain rate sensitivity characterisation.

The theory and application of ANN system at multiple length scales are presented in Chapter 6. On microscale, ANN for UD composites was introduced. On mesoscale, ANN for 3D braided composite was employed as an example of application. On macro scale, ANN for laminate was studied as an illustration of the capability of ANN in representing failure and damage of complicated composite materials.

The unit cell modelling and ANN system are validated in Chapter 7. The unit cell modelling method and UnitCells© toolbox was validated by comparing the predictions with the published results and testing data. To assess the accuracy of ANN system, critical velocities of three types of textile composites were predicted using ANN and compared with the experimental results. To illustrate the capability of ANN system, impact of IM7 carbon fibre reinforced layer-to-layer interlock 3D woven composite containment ring was simulated by using a homogenised finite element (FE) model.

A parametric study is presented in Chapter 8. As an illustration, an optimal geometric parameters combination for layer-to-layer interlock 3D woven composites was determined to obtain the best impact resistance.

Finally, the outcomes of the research conducted in this project are summarised as concluded in Chapter 9. Potential research directions for the future work based on the findings of this project are also proposed in that chapter.

Chapter 2 Literature Review

2.1 Introduction

This chapter presents and reviews the up-to-date developments in the field of textile composite research which are relevant to the subject investigated here.

The aim of this research is to offer and develop systematic methodology for design, analysis and optimisation of composites. These methodologies are intended for applications in engineering, such as the design of aerospace components, in particular, the fan blade containment casing for civil aero-engines. Therefore, an overview of fan blade containment casing is presented which focuses on the experimental testing and finite element (FE) modelling methods.

The challenge of FE modelling of composite components is the material behaviour representation. The techniques for multiscale modelling from micro- to meso- and macroscale material properties characterization are reviewed in detail. Effective stiffness prediction is relatively easy, as there are reasonably established methods. As for strength prediction of textile composites, there is genuine lack of an efficient method.

Finally, in order to take into account the strain rate effects on material properties under high velocity impact, the study of strain rate sensitivity was reviewed.

2.2 Test and Numerical Simulation of Fan Blade Containment Casings

3D textile composites have superior impact resistance to conventional laminated composites due to the absence of uninterrupted planar interlaminar interfaces which are prone to rapid delamination propagation undermining the impact strengths. However, evaluation of the performance of 3D textile composites is much more difficult due to the complicated yarns architecture. The main challenge of the design of a composite fan blade containment casing is to estimate the impact resistance of the containment casing at macro scale both experimentally and numerically. The first task is to determine the impact velocity and impact direction of released blade of the fan in a fan blade off (FBO) event before the impact velocity and impact direction can be reproduced in laboratory.

As reported in the open literature, the fan blade containment casing tests, such as energy absorption tests, ballistic tests and penetration tests, are regarded as an essential assessment of aero-engine safety [5]. Such tests are costly, as they require special testing facilities and instrumentation. Only limited data can be found in open publications.

Xuan and Wu [19] presented the results of a series of fan blade containment casing tests. A double edged notched blade was released at a certain rotating speed and subsequently impacted the inner wall of the containment ring. These tests were conducted over a range of blade lengths (113–123 mm) and releasing speeds (6800–15 000 rpm) using the high-speed rotor spin testing facility. The containment ring and blade in this paper are both made of steel, the test results were not expected to be directly useful for composite containment casing test. However, some useful ideas can be extracted from this test. The main innovation was calculation of the releasing speed and the initial kinetic energy of the blade, which are two key parameters that need to be considered when designing the testing blade. The root of the blade had a notched cross-section. The tensile stress was produced by the centrifugal force. The stress over the cross-section increased with the rotating speed. When the stress exceeded the ultimate tensile strength of the material, the failure occurred, and the blade was released with a certain kinetic energy. The blade release speed and the initial kinetic energy were calculated by relating those properties to the ultimate tensile strength of the notched blade.

Naik et al. [20] proposed another typical methodology for fan blade out containment test. The details of the experiments to characterize the behaviour of Kevlar, Zylon 500D and Zylon 1500D fabrics were presented. The special experiment was the ballistic impact tests for comparison between the energy absorbing characteristics of the three kinds of fabric specimens. Two different projectiles were fired from the gas gun on to a Kevlar fabric that was wrapped around a large 12 inch wide steel ring. In each test the positions of two or more points on the projectile were recorded as functions of time by using high speed digital video cameras. The impact velocity and residual velocity were determined by fitting a straight line to the position and time points. Then the energy absorbed can be calculated using these velocities.

Since the mechanical tests at the component level are costly and time-consuming, at the preliminary design stage of the engine, the ballistic impact tests on flat panel are sometimes used. Zhang et al. [9] introduced a set of ballistic impact tests using an air gun shooting at flat panel. The shooting velocity of air gun ranged from 50 m/s to 500 m/s, usually classified as moderate velocity. However, the target specimens are made of titanium alloy TC4, which may be very different from the test of textile composite materials. Nevertheless, these tests can offer some valuable information about the details of ballistic impact tests.

Smith [21] presented a study on a 2D tri-axial braided composite material. In this paper, the results of impact testing of composite panels indicated that composite materials made with a tri-axial braided architecture could have improved impact resistance as compared with conventional laminated composites, and improved crack propagation resistance as compared to aluminium. The 2D tri-axial braided textile was wound to construct the containment casing. This design can reduce the weight effectively, but it also has its disadvantages. Since the 2D tri-axial braided composite has quasi-isotropic properties, this design did not make full use of the advantages of composite material. The main shortcoming of this design is that the structure as a rolled up 2D braided composite still has interface between layers, and these interfaces would be prone to delamination.

Roberts et al. [22] from NASA have carried out a set of flat panel ballistic impact tests. They used a 2D tri-axial braided composite panel impacted by hard projectiles and soft projectiles, respectively. They found that using a hard projectile would be helpful for measuring the resistance of the material to local penetration at the contact points, such as that between the blade and case. On the other hand, a soft projectile impact to composite panels was employed in order to induce a high strain energy density into the composite material before penetration of the panel. This can be useful for investigating the rate sensitivity properties of composites at a high strain rates.

In addition to the experimental testing, based on the experimental data, some of the researchers proposed empirical equations to estimate the impact properties of the material. Among these empirical equations, the best known is V_{50} equation, which is an empirical equation used to estimate ballistic impacts on aircraft structure and skins from engine debris for the first time. V_{50} is defined as the velocity at which there is a 50% possibility of penetration. The equation is based on numerous tests, considering the debris mass, geometry, impact orientation and other influencing factors [23]. This equation can be used to determine a range of critical variations when devising ballistic impact experiments. This can somewhat reduce the demand on the trial and error process.

As mentioned above, tests of fan blade containment casing are very costly and time-consuming. On the other hand, with increasing computational power and improving dynamic nonlinear finite element methods, a number of 3D simulations on the blade containment design have been conducted.

For numerical simulation, the velocity and orientation of released blade can be simulated in software in a straightforward manner, by kinematic analysis. The definition of the constitutive behaviour of the composites is however an issue, especially for the textile composites, for which there are no readily available models in the commercial software packages. Furthermore, developing such a model is a great challenge, because of the complicated yarn architecture and complicated mechanism of failure between and within the yarns.

The yarn architecture within the textile composites cannot be explicitly modelled in the containment casing model, since the model will be too complicated to generate mesh and conduct analysis. Instead, a homogenized macroscale model can be used. Constitutive behaviour of the homogenized model has to be presented under the general stress states.

Xuan and Wu [19] carried out numerical modelling to simulate the blade impact on the containment ring. The simulation was conducted by using nonlinear dynamical analysis software, MSC.Dytran. The Cowper–Symonds relationship was used for the consideration of strain-rate effects for both the blade and the containment ring. The most important conclusion of this paper is that large plastic deformation area and/or penetration and perforation failure may appear in the second impacted region on the containment ring when the releasing speed of the blade is high. Following the first impact to the containment ring, the blade bends into a “U” shape. However, the simulations [19] were carried out for a steel containment casing, hence for composite containment casing the material behaviour will be different.

Stahleckera et al. [24] developed a constitutive model of a 2D woven dry fabric, implemented it as a user-defined subroutine in LS-DYNA and validated the model. It was used to simulate the ballistic impact to the fabric representing the FBO event. The model incorporated the rate sensitivity of the material constitutive relationship. There was an increase in the peak stress and failure strain with an increased strain rate. There is a lack of rational considerations in that model, as the stress–strain relationships were assumed to be decoupled, and every stress component was a function of only one strain component. Although the coupling components of the stiffness matrix were very small, they still should not be ignored without justification.

Based on the literature overview conducted, no reasonable constitutive model could be identified that could be applied directly to represent the material behaviour of 3D textile composites at macroscale, which hinders the development of numerical simulation of 3D textile composite containment casing. Therefore, methodology for material characterization of 3D textile composites has to be established to bridge this gap.

2.3 Material Characterization

In order to simulate and evaluate the impact resistance of composites, the effective properties of the material need to be determined first. The effective properties of the composites are related to the properties of it constituents, the matrix and the reinforcement, and the internal micro/meso- structure of the composite.

Generally, three major approaches are commonly applied to obtain the effective properties of composites: (a) experimental testing (b) analytical methods and (c) finite element methods [25, 26].

In experimental investigations, the composite specimens are tested under different types of loading, such as tensile loading, compressive loading and shear loading [20, 27, 28]. The effective elastic properties and strength are obtained from the experimental stress-strain curves. These properties provide the basis for development of the constitutive model.

Due to the variability as a characteristic of composites, it is necessary to test several specimens experimentally before an average or a meaningful median is taken as the representative measure. Therefore, this method is relatively costly and time-consuming. Furthermore, for textile composites, experimental methods may not always be an available choice at the first stage of textile architecture design, because there are infinite numbers of combinations of geometry parameters for textile composites. It’s not efficient and economic to optimise the performance through experiments.

Analytically, the effective properties of UD composites can be evaluated using the rule of mixtures [29, 30]. Within the rule of mixtures, the longitudinal stiffness is predicted based on the assumption of uniform strain, while the transverse stiffness is predicted based on the uniform stress assumption, which means rule of mixtures give upper bound for longitudinal stiffness and lower bound for transverse stiffness [31].

More sophisticated estimates of effective elastic properties are also available, for example, Hashin and Rosen's concentric cylinders model [32], and similar micromechanics based approaches [33, 34, 35, 36, 37]. However, their extension to 3D textile composites may still be a significant challenge. Textile composites, such as 3D braided composites [15], have complicated microstructures depending greatly on the manufacturing processes, such as pitch length, braiding angle and volume fraction. These make analytical predictions of the effective properties of 3D textile composites a challenge.

For example, Pan [38] developed a theoretical approach to predict the properties of woven fabric, which was based on a number of assumptions, for example, the interactions between yarns were ignored and the variations of the structural and geometrical parameters were assumed as negligible. With these assumptions, the material represented by this model would be significantly different from the original material, thus it is not expected to produce accurate predicted results. Furthermore, this approach would not predict the strength without the experimental results.

Sun and Qiao [39] developed a fibre-inclination model to predict the elastic properties and strength of five-axial 3D braided composite materials. The 4-step (or 4-axial) braided composite model was regarded as an analogy to a laminate. The yarns of the unit cell in the same direction were treated as a lamina with the matrix around the yarn. Each lamina was assumed to be transversely isotropic under the local coordinate system, and their effective properties can be obtained by using the rule of mixtures. The generalized stiffness matrix of each lamina was calculated and transformed to global coordinate system. The average stiffness matrix was calculated and inverted to obtain the average compliance matrix. The engineering elastic constants were calculated from the average compliance matrix.

Shokrieh and Mazloomi [40] proposed a new analytical model to predict the stiffness of 3D four-axial braided composites. They used a so-called Multi-Unit Cell Model of 3D four-axial braided composites, which is comprised of three kinds of unit cells, namely interior, surface and corner. Each of the unit cells had unique mechanical properties and was considered as a unidirectional composite. Mechanical properties of the UD composites were obtained from rule of mixtures. With the properties of UD composites, the stiffness matrix of UD composites was defined, and the total stiffness matrix of the 3D braided composites was finally obtained using a volume-averaging method.

The two methods introduced above used the results from rule of mixtures as the input. The rule of mixtures is known to be inaccurate except for the Young's modulus in the fibre direction. These methods were based on some kind of average of stiffness matrix which usually had a certain assumption regarding the strain distribution and hence tends to produce an upper bound of the effective properties.

Aboudi [31] introduced a micromechanical analysis method for two phase composite materials called the method of cells. It based on the periodic structure of the reinforcement. The analysis was conducted on the representative element, which was defined as a repetitive block. Displacement and traction continuity conditions at the interface and equilibrium conditions were applied to the representative element to calculate the average stress and strain. The representative element was divided into several subcells, each of the subcells occupied by a single constituent material. For example, the representative element of UD composites was divided into four subcells, one of them is a square region of fibre, and the others are square region of matrix. This method was extended to a composite material with a more complicated structure of reinforcement, such as 3D multi-phase composites [41, 42]. This method can produce more accurate predictions than the rule of mixtures, and can be used to predict the effective properties of UD composites, laminate composites and particle reinforced composites. However, this method was not extended to predict the effective properties of 3D textile composites.

From the literature, it can be seen that the analytical methods of predicting the material properties of the 3D composites are commonly based on various assumptions, typically a uniform distribution of strain or stress field, but often avoiding stating so explicitly, and generally disregard the geometric structures in the 3D composites. Therefore, stiffness predictions using these methods have low accuracy. Besides, the analyses seemed too complicated to carry out automatically. Furthermore, no theoretical method has been successfully applied to the prediction of the strength of textile composites accurately.

On the other hand, the finite element method (FEM) has been known for its versatility and widely used for predicting the effective properties of composite materials, in particular, modern textile composites [43, 44]. The architecture of yarns and fibres can be modelled explicitly and represented properly by applying appropriate software, e.g. TexGen [45]. Analyses are often based on micromechanics of composites, where properties of the constituents and the architecture of the composite are assumed to be known. Thus, a representative volume element (RVE) or a unit cell (UC) model can be constructed depending on the geometry and stress state of the composite. The properties of the composite are then obtained through an analysis of the RVE or unit cells (UC) model by numerical methods. The overall properties of composites can be predicted quite accurately by a finite element (FE) model, as long as the properties of the constituents (reinforcement and matrix) are properly represented in the model. Moreover, if the models have been parameterised properly, it is convenient to carry out parametric studies afterwards using the FE model.

For the purpose of homogenisation, terminologies of representative volume elements (RVE) and unit cells (UC) are often adopted by users, sometimes in an interchangeable manner but occasionally there could be a little signs of confusion. An RVE can be defined as the smallest volume of the material which remains representative of the bulk/effective properties of the material [26, 46, 47]. What is implied by ‘smallest volume’ is that, if the volume is enlarged to incorporate a larger volume of the material, the effective properties evaluated through the RVE employed will remain constant but any further reduction will result in noticeable fluctuations in the evaluated effective properties as a result of false boundary conditions employed, indicating that the volume is no longer representative. When RVEs are used in this way, there is clearly an issue of convergence for which the user has to satisfy him/herself before a specific size is adopted, which may require a significant effort. For that reason, RVEs should be resorted to only if there is a lack of regularity in the microstructure of the material. It is the authors’ perception that a unit cell is best used to describe a basic unit out of a regular microstructure, which repeats itself according to certain symmetry transformations to reproduce the entire microstructure. Apparently, a unit cell is always an RVE but not vice versa, because a unit cell is required to be periodic while a RVE does not have to be periodic, provided that it remains representative. Unlike RVEs for irregular microstructures where boundary conditions cannot be prescribed precisely, boundary conditions can be obtained precisely for unit cells, provided that the boundary conditions are formulated and imposed correctly according to the geometric symmetries present in the microstructure. A larger sized model consisting of a number of unit cells should produce identical results to those from a single unit cell, i.e. there is not the same issue of convergence as in RVEs as described above.

The properties of the composites are then obtained through an analysis of the RVE or UC model by numerical methods. The overall properties of composites can be predicted quite accurately by an FE model, as long as the properties of the constituents (reinforcement and matrix) are properly represented in the model. Moreover, if the models have been parameterised properly, it is convenient to carry out parametric studies employing FE modelling.

For instance, a unit cell model of 3D braided composite is shown in Figure 2.1 (b). With properties of the constituents (fibre and matrix) appropriately defined, the overall properties of composites can be predicted with reasonable accuracy by a FE model.

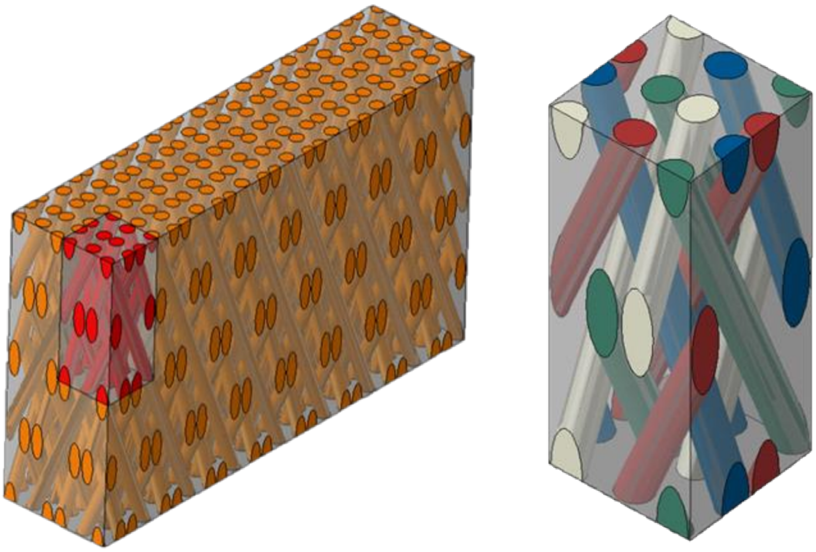

Figure 2.1 (a) 3D braided composite architecture (b) Unit cell of 3D braided composites

The accuracy of overall effective material property predictions obtained from FEM relies on how well the FE model represents the real material. Therefore, it is sometimes necessary to model the detailed architecture of the composite materials.

On a microscale level, yarns within 3D textile composite can be regarded as unidirectional fibre-reinforced composites (UD). Typical idealised packing schemes of UD composites are of the hexagonal and square arrangements [48]. Both of these have a relatively simple geometry, and can be devised relatively easily.

The mesoscale models of composite materials, especially those of 3D woven and 3D braided composites, can have very complicated yarn architectures if a detailed representation of the real composite structure is required. The yarn cross sections in textile preforms are not perfectly regular and they usually vary along the length of the yarns due to the interactions between the adjacent yarns [49]. The path of the yarns may also have some degree of irregularity [50]. The yarns may get further disturbed during the forming and curing process; this makes it a very challenging task to represent all the geometric details of mesoscale models. A number of idealisations have to be introduced as approximations in order to make theoretical modelling possible while preserving the main features of the textile architectures.

Bigaud and Hamelin [51] introduced a simplified model. In their model, the unit cell was discretized into a number of cubic elements, and material properties were determined at each integration point. These kinds of models are easy to create, but they are unable to capture the local stresses at the interfaces between yarns and matrix. Thus, the accuracy and applicability of this kind of model was limited, for example it cannot be used to predict strength.

Chen et al. [15] proposed a microstructure for a 3D braided preform. In their model, the preform was divided into three different ranges: interior, surface and corner. Yarns in the interior range were regarded as of a constant cylindrical cross section with straight path. This type of straight yarn model reflects better details than the discretized model described above, which may obtain more accurate effective properties. However, for real composite materials, the cross sections of yarns are not constant due to the interaction between adjacent yarns [49] and yarn are not straight.

Fang et al. [16] proposed a simplified idealisation for 4-axial braided composites that the yarns within all representative volume cells take an octagonal cross section and they all have surface contact to the neighbouring yarns. The octagonal cross sections were then divided into seven ranges and each range was assigned with a local coordinate system.

Jiang et al. [52] suggested a more detailed model for 3D braided composite by defining the paths of yarns as curves governed by mathematical functions. This model might be able to produce more accurate results, but creating curved yarns is not always straightforward.

The approximate models above are applicable to the analysis to obtain effective properties to some extent. However, none of the above models is able to represent the varying yarn cross sections, which is a very important feature of textile composites.

With the realistic geometry, appropriate boundary conditions have to be applied to unit cell model to obtain reasonable effective properties. Since the idealised textile architecture has periodic geometry, the so called periodic boundary conditions can be adopted [53]. Generally, boundary conditions include displacement boundary conditions and traction boundary conditions, but for FE analyses, traction boundary conditions should not be imposed [54]. Therefore, only periodic displacement boundary conditions were imposed to unit cells.

A key step in the application of unit cells is to impose periodic boundary conditions to the unit cells concerned. Successful imposition of such boundary conditions requires the coordinates of nodes as well as the tessellations on any pair of opposite faces to be precisely related. Due to the complicated yarn architectures of textile composites, it is often difficult to ensure identical tessellations on corresponding faces of the unit cell before periodic boundary conditions can be imposed [48, 54, 43].

From the discussion above, it is easy to conclude that representing the yarn architecture properly and generating periodic mesh are the main challenges for creating unit cell model of textile composites. Therefore, systematic methods need to be developed to create realistic geometry and generate periodic mesh for textile composites with complicated yarn architectures.

2.4 Strain Rate Sensitivity Study

In order to investigate the dynamic properties of composite materials under high velocity impact, strain rate effects must be taken into account. The rate dependent behaviour of composites, which are generally strain rate sensitive materials, has been investigated in a number of studies. However, despite there being numerous publications, there is still a lack of clarity as to how the rate dependent composite behaviour should be represented, as different studies report different results.

Roberts et al. [55] have given some details about the experiments for testing the properties of tri-axial braided composite material, especially for the impact properties. In order to obtain a high strain energy density in composites before failure, a soft projectile was used. With this kind of test, the impact resistant of composites can be evaluated properly without local failure.

Nia and Sadeghi [56] conducted an experimental study on compressive mechanical behaviour of bare and foam-filled honeycomb structures in the through-thickness direction at low strain rate tests using Instron 8503. Results showed that the mean crushing strength of these structures was highly dependent on the strain rate, as the strain rate increased from 5.25 s^{-1} to 10.5 s^{-1}, an increase in the mean crushing strength of up to 40% was observed in some specimens. Strain rate has less effect on mean crushing strength of foam-filled honeycomb structures than that of bare honeycomb structures. The test results also indicated that the strain rate does not change the densification strain, but could affect the deformation and increase the number of folds of honeycomb wall, and consequently dissipated more energy.

The Split Hopkinson pressure bar (SHPB) [57] is a well-known characterization tool for the mechanical response of materials loaded at high strain rates. A general set up of a SHPB system is schematically shown in Figure 2.2. Generally, this SHPB system was used to characterise the compressive properties of materials. In addition to this compression version, there are other versions with loading mechanisms for tension, torsion and their combinations [57, 58].

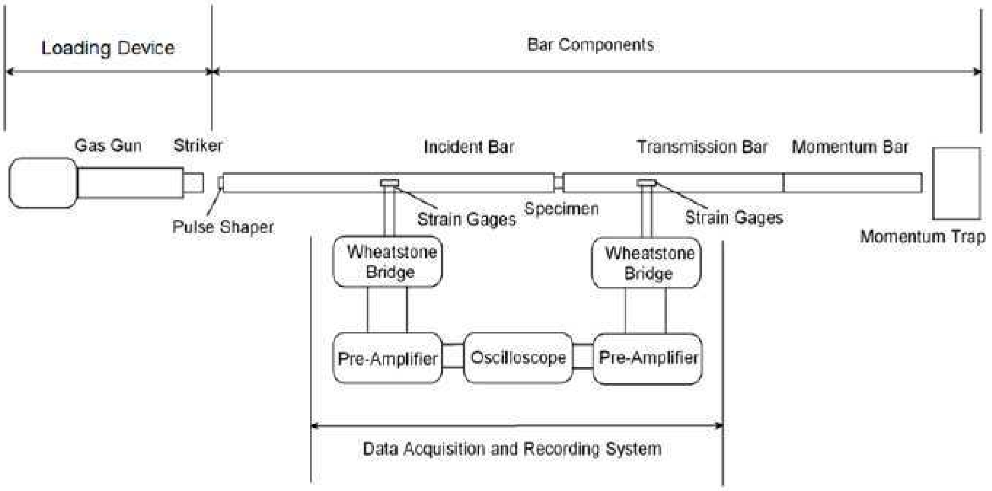

Figure 2.2 A general SHPB system [57]

Foroutan et al. [59] presented the test results of rate-dependent in-plane damage behaviour of woven CF composites using a tensile version of Hopkinson bar setup, and compared the results with static test results. Fabric composites with three different fibre architectures (plain weave, 2x2 twill weaves and 8-harness satin weaves) and two different materials (carbon/epoxy and carbon/BMI) were tested. They confirmed that the shear behaviour of woven composites is more rate-dependent than their tensile counterpart.

Mahmood and Majid [60] studied the in-plane shear behaviour of unidirectional glass fibre-reinforced polymeric composite under quasi-static and intermediate strain rate stress states. Their experimental results showed that the shear properties were sensitive to strain rate. Under dynamic loading, with increasing strain rate, the shear failure strength increased while the shear modulus decreased. They concluded that strain rate effects on these properties could be approximated adequately by an exponential growth function of the strain rate.

Hou et al. [61], studied the high strain rate tension properties of 3-D angle-interlock woven carbon fabric (3DAWF) both experimentally and numerically (using finite elements). It was found that the tensile behaviour of the 3DAWF was rate sensitive, namely, both the failure stress and failure strain increased with the strain rate. Through the FE analysis, a geometrical model was established for microstructure to describe the failure mechanisms of the 3DAWF under high strain rate tension.

López-Puente and Li [62] presented a numerical analysis of the influence of strain rate on the response of carbon/epoxy woven composites. Unit cell models at two different length scales have been developed in order to simulate the behaviour of such composites. An anisotropic plasticity with different hardening rules under different stress states was proposed for the carbon fibre yarns. Results show reasonable variations of the composite strengths under dynamic loads. An important aspect of the paper was their observation of effective strain rate sensitivity due to the undulations in the woven reinforcement, as neither the reinforcement phase nor the matrix had been assigned any rate dependent properties.

Hufenbach et al. [63, 64], presented a rheological model to identify the strain rate deformation and failure behaviour of textile reinforced polypropylene. According to the rheological model, polypropylene matrix can be modelled using a Burgers model [65] and glass fibre can be modelled using a Zenerk model [63]. A Burgers model is a viscoelastic material model which consists of a Maxwell model [66] and a Kelvin–Voigt model [67] in series. A Zenerk model is a model combining a purely elastic spring and a Kelvin–Voigt model in series. The Maxwell model is a purely viscous damper and a purely elastic spring connected in series, while the Kelvin–Voigt model is a purely viscous damper and a purely elastic spring combined in parallel.

Furthermore, two rheological models for polypropylene matrix and glass fibre were combined in series or parallel in order to represent UD plies. Based on the rheological models, a strain rate function was implemented to account for strain rate dependent elastic and strength properties.

Mohotti et al. [68] proposed a strain rate dependent constitutive material model to predict the high strain rate behaviour of polyurea. Their model was based on the well-known nine parameter Mooney–Rivlin material model. A rate dependent term was introduced into the original Mooney–Rivlin model and was validated using high strain material data for polyurea.

Daniel et al. [69 , 70] proposed a strain rate dependent failure criteria for unidirectional carbon/epoxy material under multi-axial loading. From the tests, they found both modulus and strength were strain rate sensitive. They proposed a failure mode based criteria which can be used to predict the failure of composite material at static, intermediate strain rate and high strain rate.

Cowper and Symonds [71] proposed an empirical model (known as the Cowper-Symonds model) to describe the strain rate hardening of metals. This model has been widely used, in particular, it has been implemented in LS-DYNA. However, this model was originally proposed for metal and cannot be extended to composites in a straightforward manner.

Yen [72] proposed a two parameters scaled model. In their model, the stiffness and strength are scaled by a ratio which is related to current strain rate. A reference strain rate has to be defined in this model, strain rates smaller than this value were treated as static. Therefore, the strain rate of static test was selected as reference strain rate.

From the above review, it is easy to see that strain rate sensitivity of composites is a complicated matter and it is therefore difficult to say which model is the best. For a specific material, experiments are required to determine the suitability of the model employed. The accuracies of different models can be judged by comparing the simulation results and the experimental results.

2.5 Summary

Some important aspects of the present research, namely, the test and simulation of fan blade containment casings, material characterization and strain rate sensitivity study, have been reviewed in this chapter.

The overviews of other specific technologies employed in this research are presented in the appropriate chapters. In particular, the formulation of periodic boundary conditions is introduced within Chapter 3. The review of failure criteria will be presented in Chapter 4. The theoretical background and details of implementation of ANN will be given as a part of Chapter 6.

Chapter 3 Unit Cell Modelling for Textile Composites

3.1 Introduction

With their complex mesoscopic architectures, textile composites have reinforcement along three directions, including the through-thickness direction. Unlike in conventional laminated composites, there are no planar interfaces, hence no delamination failure mode in textile composites, and this substantially improves the impact resistance of textile composites in comparison with that of the laminated composites. However, because of the complicated reinforcement architecture, the material characterisation of textile composites can be extremely challenging, and there are no readily available software/modelling tools that can be utilised for this purpose.

According to the literature survey in Chapter 2 on material characterization, the most promising approach for characterising the textile composites is based on the unit cell modelling, when the material represented by its basic repeating cell. Accurate material representation requires accurate mesostructured geometry representation and imposition of the appropriate boundary conditions. The analysis of this kind has been previously developed by Li and Wongsto [43, 47], and it was applied to characterisation of the composites of the unidirectional fibrous reinforcement and particulate reinforcement. The imposition of periodic boundary conditions proves to be demanding if dealt with individually but it is a process which can be automated. To achieve this, a Python script code UnitCells© [73] was developed prior to the project, which allowed for automatic generation of finite element models of the unit cells, with correct the imposition of the boundary conditions and assignment of the material properties, carrying out the analysis and extracting the effective properties.

As part of the present research, UnitCells© was substantially extended. It was previously a characterization tool for the effective thermoelastic properties of UD composites with regular fibre distribution and particle reinforced composites and there was only a limited capability for 2D woven composites. Through the extension carried out in the present project, the following areas have been covered. For the characterization of UD composites, it is capable to dealing with random fibre distribution over the cross section perpendicular to the fibres. Although the methodology was developed in [47], the implementation of the methodology for automated application is not a trivial exercise. In terms of the type of composites, it has included a large number of typical 2D and 3D textile composites. In terms of the types of analysis it has been extended from thermoselastic to thermal conductivity, electricity conductivity and effective strength. The most significant aspects are the developments into 3D textile composites and strength prediction. For the 3D textile composite models with complex architectures it can be extremely challenging to obtain a suitable geometry and mesh within a single piece of the conventional software. UnitCells© has been extended in this respect to take advantage of a number of other established codes to fulfil the task efficiently and effectively. To make this toolbox easy to use, a graphic user interface was created for users to input a small number of essential parameters in order to define to define the architecture of the textile preforms as well as the density of the meshes.

This chapter describes the stages of development of UnitCells©, and provides examples of it being applied for characterisation of various types of textile composites, after a review on the specific topic of the unit cells based on periodic boundary conditions in Section 3.2 followed by an overview of the implementation of the unit cells available in UnitCells© where pre-existing contents in UnitCells© before the present project and those developed as a part of the present project will be clearly identified without affecting the integrity of the presentation of the capability of UnitCells©.

3.2 Review of the Formulation for Unit Cells Based on Periodic Boundary Conditions

Idealisations are often necessary to represent realistic geometry micro/mesoscale architectures, which usually involves neglecting minor irregularities such that the micro/meso-architectures can be considered to be of regular patterns. Once a unit cell is identified, appropriate boundary conditions have to be applied to it so that it will represent the material of the micro/meso-structure where the unit cell is from. Only by doing this, the obtained effective material properties will be representative for the material concerned. Since the unit cell model has periodic geometry, the representative boundary conditions are called periodic boundary conditions [53].

Periodic boundary conditions result from the geometric periodicity of the microstructure [48, 54], while the periodic boundary conditions themselves may not necessarily show any periodicity in any way. In particular, in terms of displacement boundary conditions, the displacement field within in any unit cell is not periodic, while the obtained stress and strain fields are periodic. For FE analyses, periodic traction boundary conditions should not be imposed [54] and users can simply ignore their presence.

Periodic displacement boundary conditions are derived from geometric symmetries as present in the microstructure [43, 47, 48]. Symmetry is an important geometric characteristic and widely observed in crystals and composites. Theoretically, there are three typical symmetries: translational, reflectional and rotational ones. All these three symmetries have been widely used in the micromechanical analysis of composites. The reflectional symmetry is the most familiar one among the three. However, a reflectional symmetry can be validly applied only once to a particular direction and applying the same reflectional symmetry twice in the same direction in order to reduce the dimension to a finite extent in the direction concerned is a fundamentally flawed argument [74]. The correct way to extent the dimension in a direction is to use a translational symmetry [74, 75]. This does exclude the use of reflectional symmetries. In fact, within a period as defined by the translational symmetry, reflectional and rotational symmetries are often present and one can take advantage of them to reduce the size in this dimension [74, 75]. One is reminded that if a unit cell is established by using either the reflectional or rotational symmetries, it may not be applicable under the stress states which involve an arbitrary combination of the macroscopic stresses. This restriction could be removed by avoiding any reflectional or rotational symmetry transformations when establishing the unit cell [53]. In the present work, use has been made of the translational symmetries alone and the boundary conditions for the unit cells obtained are straightforward periodic boundary conditions. The relevant formulations were developed fully by Li et al. [75, 48, 54, 76]. As an illustration of the process of deriving the periodic boundary conditions, parallelepiped (specifically, a right prism with parallelogram base) packing is assumed, from which the unit cell is obtained which can represent a fibre-matrix assembly for a UD composite, a 2D or 3D woven or braided composites, etc. [16, 77]. The boundary conditions for this type of unit cell were obtained following the methodology proposed by Li [75].

3.2.1 Displacement field for unit cell model

Because of the periodic geometry, the stresses and strains distributions within the composites are periodic and identical from one unit cell to another as can be described in terms of translational symmetries. Moreover, the relative displacements are also periodic in the same manner, as is schematically depicted in Figure 3.1 where a rigid body rotation in the plane has been eliminated by constraining the rigid body rotation of the horizontal axis.

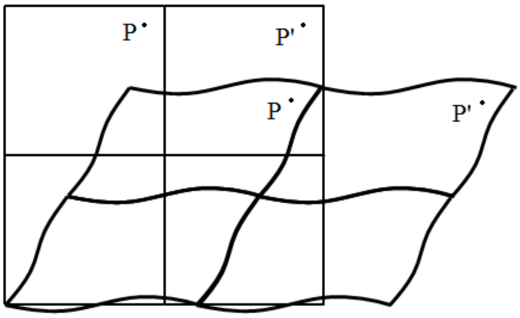

Figure 3.1 Schematic drawing showing the deformation of unit cells

In Figure 3.1, P is an arbitrary point in one unit cell and P' is the image of P in another unit cell. According to the principle of symmetry [78], the relative displacement field in each unit cell, e.g. to the bottom left corner O or O' of the unit cell remains periodic after deformation. Therefore, the relation between macroscopic strains and displacements at point P and P' can be described as follows.

$$\begin{cases} u^{'} - u = (x^{'} - x)\varepsilon_x^0 + (y^{'} - y)\gamma_{xy}^0 + (z^{'} - z)\gamma_{xz}^0 \\ v^{'} - v = (y^{'} - y)\varepsilon_y^0 + (z^{'} - z)\gamma_{yz}^0 \\ w^{'} - w = (z^{'} - z)\varepsilon_z^0 \end{cases} \tag{3-1}$$

where x, y and z are the coordinates of point P, u, v and w are the displacements at this point. Similarly, x', y' and z' are the coordinates of point P', u', v' and w' are the displacements at this point, and ε_x^0, ε_y^0, ε_z^0, γ_{yz}^0, γ_{xz}^0 and γ_{xy}^0 are the macroscopic strains.

In obtaining the strain field as represented in Equation (3-1), rigid body degrees of freedom should be constrained. Firstly, the three translational degrees of freedom are constrained at an arbitrary point by prescribing the following at that point:

$$u = v = w = 0 \tag{3-2}$$

The rigid body rotational degrees of freedom should also be constrained in the model, this could be achieved by constraining the rigid body rotations of the x axis about the y and z axes and the y axis about the x axis at $x = y = z = 0$, i.e.

$$\frac{\partial w}{\partial x} = \frac{\partial v}{\partial x} = \frac{\partial w}{\partial y} = 0 \tag{3-3}$$

However, this is not the only way to constrain the rigid body degrees of freedom, hence, the Equation (3-1) will vary according to the constraining method. It is worth noting that different expressions so obtained different from Equation (3-1) may result in different presentations for periodic boundary conditions, but they should lead to identical strain field, hence obtain the same effective material properties.

Equation (3-1) will be used throughout this illustration. Obviously Equation (3-3) could be automatic met as they have been absorbed in Equation (3-1) already and thus no constrain for the rigid body rotational degrees of freedom will need to be applied to the unit cell model.

3.2.2 Translational symmetries in a parallelepiped packing

A sectional view of a parallelepiped packing is shown in Figure 3.2, from which translational symmetry could be observed. Take one of the shaded parts as a unit cell. By using translational symmetry transformations only, this unit cell could cover the whole structure perfectly [76].

A schematic drawing of the unit cell for the parallelepiped packing system is shown in Figure 3.3. In this model, edge lengths $l_1 \neq l_2 \neq l_3$, and for simplicity, the edges of length l_3 are assumed to be perpendicular to those edges with length l_1 and l_2, respectively, while the edges with length l_1 are not necessarily perpendicular to those with length l_2. The six faces of this unit cell could be grouped into three pairs： A→B, C→D and E→F. In each pair, the two faces are parallel and opposite to each other. For a tidy sketch, this figure only shows the three visible faces A, C and F, while their counterparts B, D and E have been hidden.

In order to minimize the variable parameters of periodic boundary conditions, the origin of the coordinate system was placed at the geometric centre of the unit cell, and the z-axis was placed perpendicular to faces E and F, while faces are not necessarily perpendicular to the x-axis and y-axis (see Figure 3.3). Moreover, the angle between y-axis and face B is exactly half of the angle between faces D and B (see Figure 3.2). By setting the coordinate system like this, only four variables l_1, l_2, l_3 and 2θ need to be introduced into the model, for representing the coordinate of the unit cell (see Figure 3.2).

According to translational symmetry, each unit cell in the model can be obtained by applying translational symmetry transformations to a single origin. For an arbitrary point $P(x, y, z)$ in the origin, the corresponding point $P'(x', y', z')$ in another unit cell can be obtained by applying translational symmetry transformations to point P (see Figure 3.2). In the $\mathrm{x}-\mathrm{y}$ plane, the mapping from origin P to its corresponding point P' could be characterized by two independent translations in the (ξ, η) coordinate system. Within this (ξ, η) coordinate system, the ξ-axis and η-axis are parallel to the edges of the unit cell (see Figure 3.2). In $\mathrm{x}-\mathrm{z}$ and $\mathrm{y}-\mathrm{z}$ plane, the mapping from P to P' could be characterized by translation along the z-axis. Define i, j and k as the spaces from P to P', along the ξ-axis, η-axis and the z-axis respectively. If the direction of translation is opposite, a negative value should be used. In the case of Figure 3.2, $i = 3$, $j = 1$ and $k = 0$.

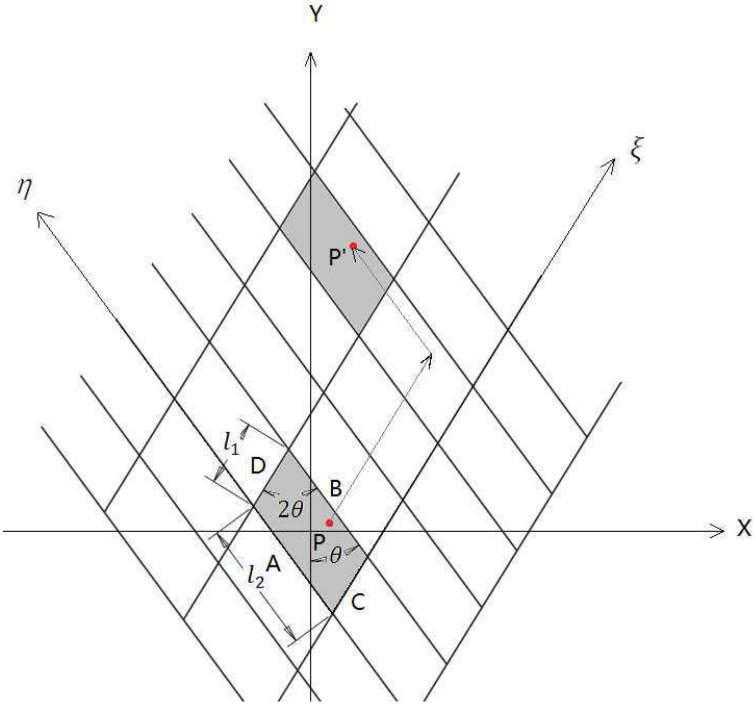

Figure 3.2 Translational symmetry transformation from a unit cell containing a representative point P to another in a parallelepiped packed micro/meso-structure

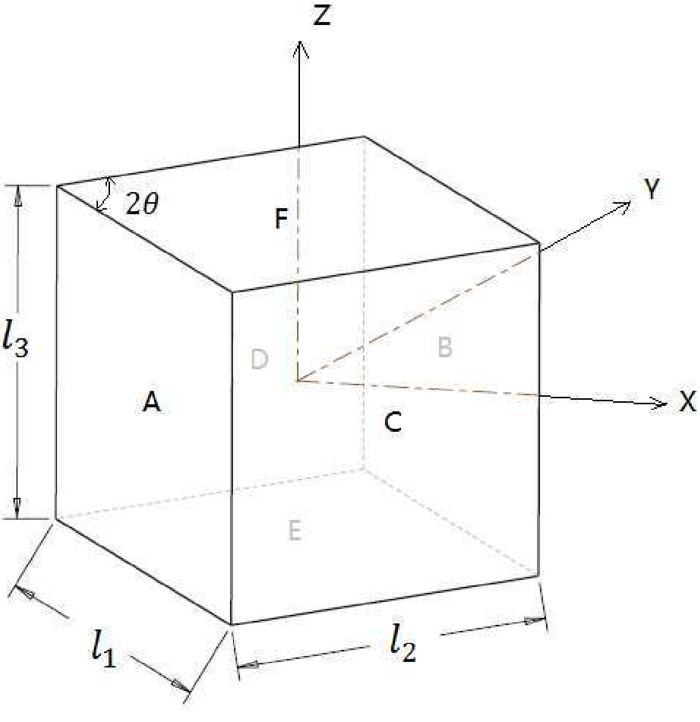

Figure 3.3 Illustration of a unit cell of parallelepiped packing

The coordinates of point $P(x, y, z)$ and $P'(x', y', z')$ are related as follows.

$$\begin{cases} x' = x + l_1 \cdot i \cdot sin\theta - l_2 \cdot j \cdot sin\theta \\ y' = y + l_1 \cdot i \cdot cos\theta + l_2 \cdot j \cdot cos\theta \\ z' = z + l_3 \cdot k \end{cases} \tag{3-4}$$

Equation (3-4) shows clearly how translational symmetry transformation is expressed in terms of the coordinates of corresponding point P': a translation along the ξ -axis by i spaces, a translation along the η- direction by j spaces and a translation along the ζ- direction by k spaces. Equation (3-4) can be rewritten as:

$$\begin{cases} x' - x = l_1 \cdot i \cdot sin\theta - l_2 \cdot j \cdot sin\theta \\ y' - y = l_1 \cdot i \cdot cos\theta + l_2 \cdot j \cdot cos\theta \\ z' - z = l_3 \cdot k \end{cases} \tag{3-5}$$

3.2.3 Expressions for periodic boundary conditions of parallelepiped packing unit cell

The equations for relative displacements between point P and its corresponding point P' are obtained by substituting Equation (3-5) into Equation (3-1). In fact, these three equations are the displacements boundary conditions for these two points. Such boundary conditions must be applied to all the surface points of the unit cell before any micromechanical analysis can be carried out.

In the unit cell model considered, there are three pairs of faces, A→B, C→D and E→F. Each face in the unit cell is shared by the neighbouring cell because of the continuity. Moreover, this face could also be obtained by applying following translational symmetry transformations on its counterpart face in the same pair:

$$\begin{cases} FaceA \rightarrow B: (i = 1, j = 0, k = 0) \\ FaceC \rightarrow D: (i = 0, j = 1, k = 0) \\ FaceE \rightarrow F: (i = 0, j = 0, k = 1) \end{cases} \tag{3-6}$$

The boundary conditions for the unit cell model are obtained as follows. Appropriate values of i, j and k, as specified in Equation (3-6), are substituted into Equation (3-5), which are next substituted into Equation (3-1) yields the equations of the boundary conditions as follows.

Face A→B (i = 1, j = 0, k = 0):

$$\begin{cases} x_B - x_A = l_1 \cdot sin\theta \\ y_B - y_A = l_1 \cdot cos\theta \\ z_B - z_A = 0 \end{cases} \tag{3-7.1}$$

$$\begin{cases} u_B - u_A = l_1 \cdot sin\theta \cdot \varepsilon_x^0 + l_1 \cdot cos\theta \cdot \gamma_{xy}^0 \\ v_B - v_A = l_1 \cdot cos\theta \cdot \varepsilon_y^0 \\ w_B - w_A = 0 \end{cases} \tag{3-7.2}$$

Abbreviated as $U_B - U_A = F_{AB}$, where U_B is the displacement of the points on face B, it can be expressed as $(u_B, v_B, w_B)^T$, U_A is the displacement of the points on face A, it can be expressed as $(u_A, v_A, w_A)^T$, F_{AB} is the relation between U_B and U_A, in this case it can be expressed as $(l_1 \cdot sin\theta \cdot \varepsilon_x^0 + l_1 \cdot cos\theta \cdot \gamma_{xy}^0,\ l_1 \cdot cos\theta \cdot \varepsilon_y^0,\ 0)^T$.

Face C→D (i = 0, j = 1, k = 0):

$$\begin{cases} x_D - x_C = -l_2 \cdot sin\theta \\ y_D - y_C = l_2 \cdot cos\theta \\ z_D - z_C = 0 \end{cases} \tag{3-8.1}$$

$$\begin{cases} u_D - u_C = -l_2 \cdot sin\theta \cdot \varepsilon_x^0 + l_2 \cdot cos\theta \cdot \gamma_{xy}^0 \\ v_D - v_C = l_2 \cdot cos\theta \cdot \varepsilon_y^0 \\ w_D - w_C = 0 \end{cases} \tag{3-8.2}$$

Abbreviated as $U_D - U_C = F_{CD}$

Face E→F (i = 0, j = 0, k = 1):

$$\begin{cases} x_F - x_E = 0 \\ y_F - y_E = 0 \\ z_F - z_E = l_3 \end{cases} \tag{3-9.1}$$

$$\begin{cases} u_F - u_E = l_3 \cdot \gamma_{xz}^0 \\ v_F - v_E = l_3 \cdot \gamma_{yz}^0 \\ w_F - w_E = l_3 \cdot \varepsilon_z^0 \end{cases} \tag{3-9.2}$$

Abbreviated as $U_F - U_E = F_{EF}$

Equation (3-7.1) gives the coordinate changes between all corresponding points on face A and B while through translational symmetry transformations. The notation x_A and x_B indicate the x coordinates of all corresponding points (excluding the points on the edges and vertexes, these points will be treated separately later) on faces A and B.

Equation (3-7.2) is the displacement boundary conditions for the face pair A→B. The notations u_A and u_B are relative displacements of all corresponding points (excluding the points on the edges and vertices) on faces A and B. These notations will be used throughout this work. Similarly, the boundary conditions for other face pairs are defined as in the above Equation (3-8) and (3-9).

In order to derive the boundary conditions for the edges of unit cell, the twelve edges of unit cell were grouped into different sets. The grouping rule is: each edge of one set is independent of the edges in the rest of the sets. In other words, any edge in one set could be obtained by performing translational symmetry transformations on other edges in the same set, but cannot be obtained by translate of the edges in other sets. According to the grouping rule, three sets were identified from the twelve edges (Figure 3.4). Set 1 includes edges I, II, III and IV. Set 2 includes edges V, VI, VII and $VIII$. Set 3 includes edges IX, X, XI and XII.

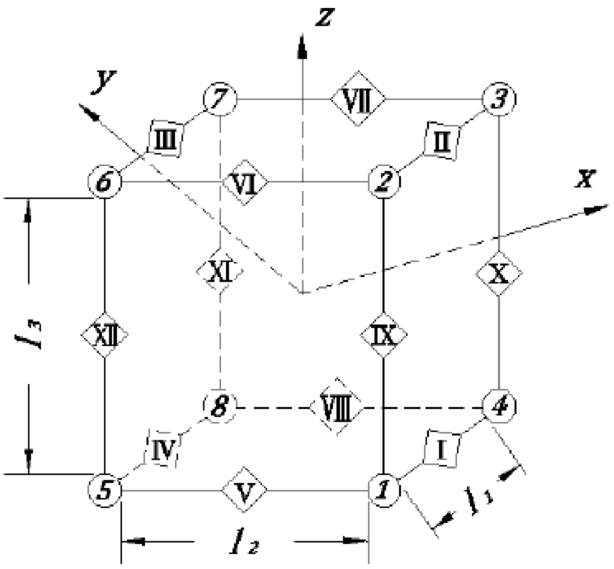

Figure 3.4 Edges and vertices of the unit cell

For Set 1, edges II, III and IV could be obtained by performing translational symmetry transformations on the edge I. The transformation could be defined as follows.

$$\begin{cases} EdgeI \ \rightarrow II: (i = 0, j = 0, k = 1) \\ EdgeI \ \rightarrow III: (i = 0, j = 1, k = 1) \\ EdgeI \ \rightarrow IV: (i = 0, j = 1, k = 0) \end{cases} \tag{3-10}$$

One group of i, j and k value is selected from the above Equation (3-10), and substituted into Equation (3-5). The boundary conditions for edges in Set 1 could then be obtained by substituting the assigned Equation (3-5) into Equation (3-1). The results are giving as follows.

$$\begin{cases} U_{II} - U_I = F_{EF} \\ U_{III} - U_I = F_{CD} + F_{EF} \\ U_{IV} - U_I = F_{CD} \end{cases} \tag{3-11}$$

It is worth noting that Equation (3-11) actually defines three sets of conditions which constrain the displacements between different edges. Taking $U_{II} - U_I = F_{EF}$ for example, the $U_{II} - U_I$ notation indicates the displacements boundary conditions for edge I and II. This could be fully expanded as follows.

$$\begin{cases} u_{II} - u_I = l_3 \cdot \gamma_{xz}^0 \\ v_{II} - v_I = l_3 \cdot \gamma_{yz}^0 \\ w_{II} - w_I = l_3 \cdot \varepsilon_z^0 \end{cases} \tag{3-12}$$

The rest two sets of equation in Equation (3-11) could also be expanded in the same way, the details will not be given here. These notations will be used throughout this work.

Similarly, boundary conditions for Set 2 and 3 could be obtained. The results are giving as follows.

$$\begin{cases} U_{VI} - U_V = F_{EF} \\ U_{VII} - U_V = F_{AB} + F_{EF} \\ U_{VIII} - U_V = F_{AB} \end{cases} \tag{3-13}$$

$$\begin{cases} U_X - U_{IX} = F_{AB} \\ U_{XI} - U_{IX} = F_{AB} + F_{CD} \\ U_{XII} - U_{IX} = F_{CD} \end{cases} \tag{3-14}$$

Similarly, the displacement boundary conditions for unit cell vertices should also be established separately and independently. It could be found in Figure 3.4 that each vertex of the unit cell could be obtained by vertex 1 through translational symmetry transformations. For example, the transformation from vertex 1 to vertex 2 could be defined as: Vertex 1-2: (i = 0, j = 0, k = 1). Thus boundary conditions for the eight vertexes could be established, by using the similar method as used to obtain the Equation (3-11), Equation (3-13) and Equation (3-14). The results are as follows.

$$\begin{cases} U_2 - U_1 = F_{EF} \\ U_3 - U_1 = F_{AB} + F_{EF} \\ U_4 - U_1 = F_{AB} \\ U_5 - U_1 = F_{CD} \\ U_6 - U_1 = F_{CD} + F_{EF} \\ U_7 - U_1 = F_{AB} + F_{CD} + F_{EF} \\ U_8 - U_1 = F_{AB} + F_{CD} \end{cases} \tag{3-15}$$

The unit cell for distorted 3D braided composites with parallelepiped packing has been established. Periodic displacements boundary conditions for the faces, edges and vertexes of this unit cell have also been obtained. They are defined in Equation (3-7)-(3-9), Equation (3-11) and Equation (3-13)-(3-15).

The periodic displacement boundary conditions for other types of unit cells such as cubic and hexagonal can be derived by using the same method.

3.2.4 Extraction of the effective properties

Macroscopic strains ε_x^0 , ε_y^0 , ε_z^0 , γ_{yz}^0 , γ_{xz}^0 and γ_{xy}^0 as appearing in the boundary conditions are physical entities, which can be assigned independent node numbers and treated as ordinary nodes or degrees of freedom. The nodal ‘displacements’ (dimensionless) at these special degrees of freedom give the corresponding macroscopic strains directly, eliminating the need to obtaining them by averaging strains from all elements. Concentrated ‘forces’, F_x , F_y , F_z , F_{yz} , F_{zx} and F_{xy} of a dimension of force × length can be prescribed to them as the ‘loads’, which are related to the average macroscopic stresses σ_x^0,σ_y^0, σ_z^0, τ_{yz}^0, τ_{zx}^0 and τ_{xy}^0 as follows.

$$\begin{aligned} &\sigma_x^0 = F_x / V && \tau_{yz}^0 = F_{yz} / V \\ &\sigma_y^0 = F_y / V && \tau_{xz}^0 = F_{xz} / V \\ &\sigma_z^0 = F_z / V \quad \text{and} && \tau_{xy}^0 = F_{xy} / V \end{aligned} \tag{3-16}$$

where V is the volume of the unit cell. Again, this eliminates the need to obtain macroscopic stresses by averaging stresses from all elements. The method for extracting average stress and strain offer extremely useful means to simplify the post-processing of the FE analysis of unit cells, bearing in mind the post-process of averaging stresses and strains is not usually available directly from commercial FE codes. The approach and relationships apply to all unit cells universally provided that the unit cell has been appropriately formulated based on rational considerations of symmetries. Details can be found in [43, 48, 75]. These special degrees of freedom ε_x^0, ε_y^0, ε_z^0, γ_{yz}^0, γ_{xz}^0 and γ_{xy}^0 are called key degrees of freedom (key dofs) and they apparently extremely useful. Similar key dofs are introduced in the analysis for thermal and electric conductivities. These key dofs are not a part of the unit cell as far as the geometry of the unit cell is concerned and therefore their locations can be arbitrary. Their coordinates can all collapse at the origin, if one chooses. In the terminology of Abaqus CAE, these key dofs have been introduced as ‘reference points’. The key dofs representing the macroscopic strains as described above appear in the equation constraints through which they become physical entities as a part of the unit cell.

With the macroscopic stresses being expressed in terms of ‘forces’ applied to unit cells, it is straightforward to obtain all effective properties of the materials represented by the unit cells in terms of the key degrees of freedom, ε_x^0, ε_y^0, ε_z^0, γ_{yz}^0, γ_{xz}^0 and γ_{xy}^0, and the applied loads, F_x,F_y,F_z,F_{yz}, F_{zx},F_{xy} and ΔT, where ΔT is the temperature difference imposed to obtain the effective thermal expansion coefficients for the materials. The effective properties can be obtained as follows from the analysis of the unit cells, where only elastic constants are shown as an illustration while thermal and electric conductivities can be expressed in a similar fashion. According to Li’s research [79], most of the composite model characterised are orthotropic material but, if the macroscopic orthotropy was not present, it would be straightforward to evaluate other coupling coefficients in a similar manner.

$$\begin{aligned}
&E_x^0 = \sigma_x^0 / \varepsilon_x^0 = F_x / V\varepsilon_x^0, \quad \text{when } F_y = F_z = F_{yz} = F_{zx} = F_{xy} = \Delta T = 0\\
&\nu_{xy}^0 = -\varepsilon_y^0 / \varepsilon_x^0, \quad \text{when } F_y = F_z = F_{yz} = F_{zx} = F_{xy} = \Delta T = 0\\
&\nu_{xz}^0 = -\varepsilon_z^0 / \varepsilon_x^0, \quad \text{when } F_y = F_z = F_{yz} = F_{zx} = F_{xy} = \Delta T = 0\\
&E_y^0 = \sigma_y^0 / \varepsilon_y^0 = F_y / V\varepsilon_y^0, \quad \text{when } F_x = F_z = F_{yz} = F_{zx} = F_{xy} = \Delta T = 0\\
&\nu_{yz}^0 = -\varepsilon_z^0 / \varepsilon_y^0, \quad \text{when } F_x = F_z = F_{yz} = F_{zx} = F_{xy} = \Delta T = 0\\
&E_z^0 = \sigma_z^0 / \varepsilon_z^0 = F_z / V\varepsilon_z^0, \quad \text{when } F_x = F_y = F_{yz} = F_{zx} = F_{xy} = \Delta T = 0\\
&G_{yz}^0 = \tau_{yz}^0 / \gamma_{yz}^0 = F_{yz} / V\gamma_{yz}^0, \quad \text{when } F_x = F_y = F_z = F_{zx} = F_{xy} = \Delta T = 0\\
&G_{xz}^0 = \tau_{xz}^0 / \gamma_{xz}^0 = F_{xz} / V\gamma_{xz}^0, \quad \text{when } F_x = F_y = F_z = F_{yz} = F_{xy} = \Delta T = 0\\
&G_{xy}^0 = \tau_{xy}^0 / \gamma_{xy}^0 = F_{xy} / V\gamma_{xy}^0, \quad \text{when } F_x = F_y = F_z = F_{yz} = F_{zx} = \Delta T = 0\\
&\alpha_x^0 = \varepsilon_x^0 / \Delta T, \quad \text{when } F_x = F_y = F_z = F_{yz} = F_{zx} = F_{xy} = 0\\
&\alpha_y^0 = \varepsilon_y^0 / \Delta T, \quad \text{when } F_x = F_y = F_z = F_{yz} = F_{zx} = F_{xy} = 0\\
&\alpha_z^0 = \varepsilon_z^0 / \Delta T, \quad \text{when } F_x = F_y = F_z = F_{yz} = F_{zx} = F_{xy} = 0
\end{aligned} \tag{3-17}$$

In obtaining each of the above properties, it is essential that the corresponding stress state is obtained. Although for a given material, represented by a unit cell, many of the properties in Equation (3-17) are related, calculating them individually from the unit cell analysis and finding out whether the relationships among them are obtained properly can serve as valuable checks on the unit cell, in particular, the correct application of all the boundary conditions before the unit cell is employed in a more sophisticated level of application.

3.3 Microscale Unit Cell for UD Composites

On a microscale level, a lamina of a laminated composite, or a yarn within the fibre-reinforced textile composite, can be regarded as UD composites. The effective material properties of UD composites can be predicted based on UD unit cell or RVE modelling, where the former one is applicable for UD composites with regular fibre distribution, while the latter one represents the UD composites with random fibre distribution.

3.3.1 UD composite model with a regular fibre distribution

Typical idealised packing scheme of UD composites are hexagonal and square arrangement [48] as shown in Figure 3.5. Both of these have relatively simple geometries, and can be readily meshed using a Python Script executable in Abaqus. For this type of analysis in UnitCells©, users only need to input the fibre volume fraction and material properties of fibre and matrix, while all the following analysis process is executed automatically. It is the user's choice which of the two arrangements should be used. Internally, half-sized unit cells are used inside UnitCells© to reduce the computational effort. The boundary condition imposed for this is based on a central reflectional symmetry condition [80].

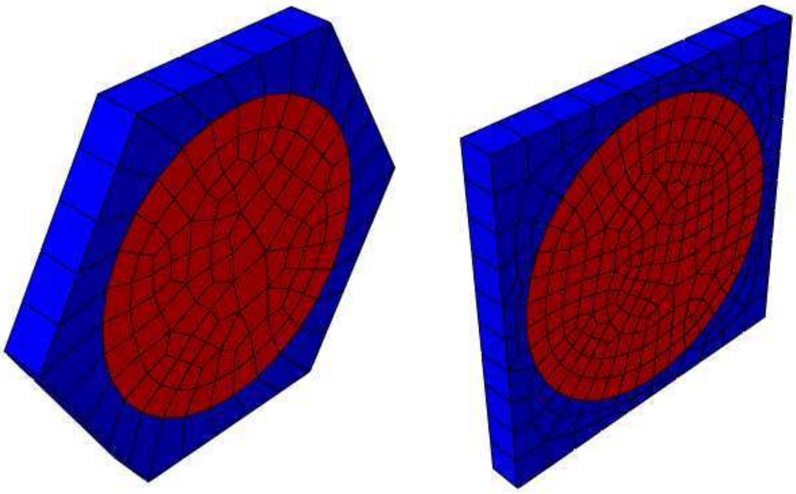

(a) Hexagonal arrangement (b) Square arrangement

Figure 3.5 Regular unit cells for UD composites

The accuracy of these two types of unit cells can be verified by comparing the UnitCell© calculations with the analytical predictions.

According to the rule of mixtures, the equivalent elastic properties, namely, longitudinal (E_1) transverse (E_2) and shear (G_{12}) moduli, as well as and thermal expansion coefficients, α_1 and α_2, of UD composites can be calculated as follows [81]. Since the rule of mixtures provides an upper bound estimate for the longitudinal stiffness and lower bound estimate for the transverse stiffness [31], it is only used here as some kind of references. More accurate methods [32, 33, 34, 35, 36, 37] are available that give more accurate predictions at varying levels of complexity.

$$
\begin{aligned}
&E_1 = E_m V_m + E_f V_f \\
&E_2 = \frac{E_f E_m}{V_m E_f + V_f E_m} \\
&G_{12} = \frac{G_f G_m}{V_m G_f + V_f G_m} \\
&\alpha_1 = \frac{\alpha_f E_f V_f + \alpha_m E_m V_m}{E_f V_f + E_m V_m} \\
&\alpha_2 = V_f\left(1 + \nu_f\right)\alpha_f + V_m(1 + \nu_m)\alpha_m - (\nu_f V_f + \nu_m V_m)\alpha_1
\end{aligned}
\tag{3-18}
$$

where V_m and V_f are the volume fractions, E_m and E_f are the Young's moduli , G_m and G_f are the shear moduli, ν_m and ν_f are the Poisson's ratios, α_m and α_f are the coefficients of thermal expansion. Subscripts "m" and "f" denote matrix and fibre constituents, respectively.

Alternatively, these properties can be obtained using the square and hexagonal unit cells representing the UD composites. Material parameter values for the matrix and the fibre in this case are listed in Table 3.1.

Table 3.1 Material property of fibre and matrix for UD composites

	Fibre	Matrix
E (GPa)	76	3.5
υ	0.2	0.35
α (10^{-6}°C^{-1})	5	60

The elastic and thermal properties of the UD composite were obtained over a range of fibre volume fractions through the unit cell modelling. These predictions are presented in Figure 3.6 alongside with those calculated using analytical expressions (3-18).

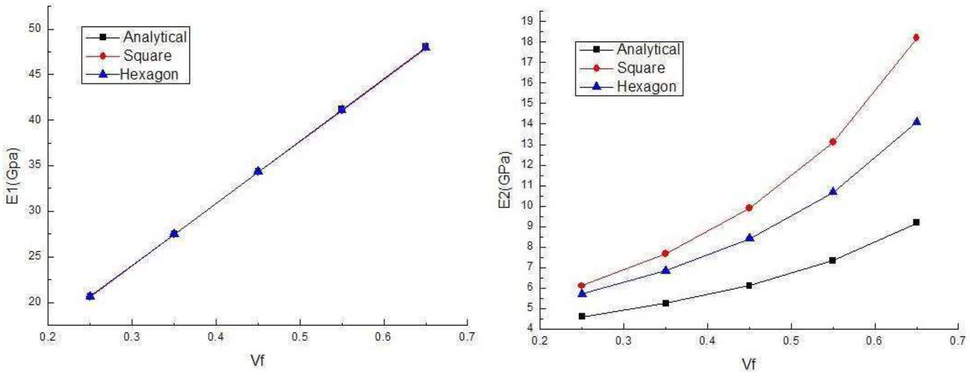

(a) E_1 (b) E_2

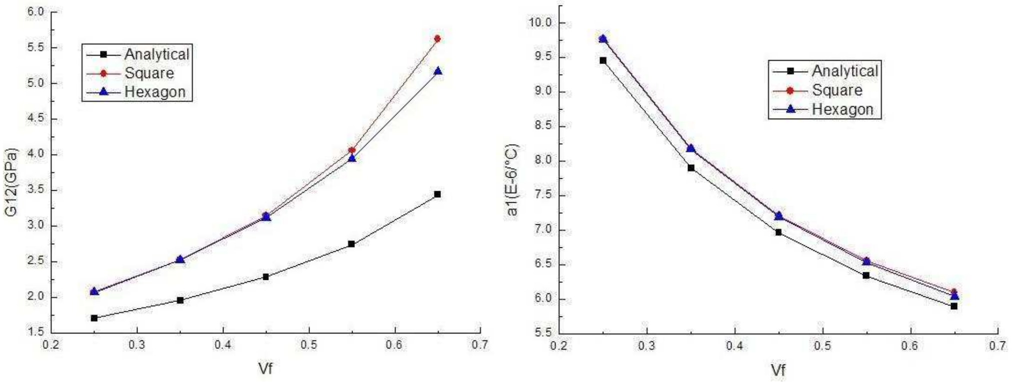

(c) G_{12} (d) α_1

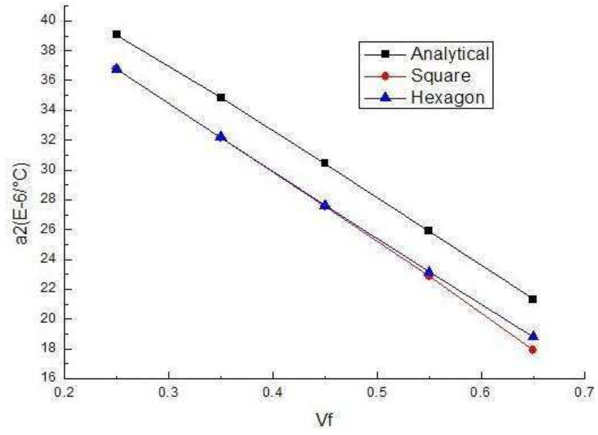

(e) α_2

Figure 3.6 Comparison of the equivalent properties calculated with UnitCells© with those calculated using rule of mixtures

The comparison shows that the Unit Cells tool calculations and analytical predictions agree reasonably well. Some discrepancy between the two sets of predictions is presented. However, considering that the rule of mixtures provides just an estimate for either the upper or the lower bound, some discrepancies between the predicted and analytical results are reasonable and can be expected.

To illustrate the difference between hexagonal and square unit cell predictions, a set of hexagonal and square unit cell models have been analysed. Fibre and matrix were defined as isotropic materials, with their properties (elastic constants and thermal expansion coefficients) listed in Table 3.1.

All the unit cells were set to have the same fibre volume fraction (60%). Their effective properties obtained by UnitCells© are summarised in Table 3.2.

Table 3.2 Effective properties of unidirectional composites (V_f=60%)

	Square	Hex
E_1 (GPa)	46.905	46.969
E_2 (GPa)	15.534	12.304
E_3 (GPa)	15.534	12.304
υ_{12}	0.25	0.252
υ_{23}	0.262	0.4
G_{12} (GPa)	4.755	4.519
G_{23} (GPa)	3.386	4.394
$\frac{E_2}{2(1+\upsilon_{23})}$	6.156	4.394
α_1 ($10^{-6}{}^{\circ}\mathrm{C}^{-1}$)	6.955	6.895
α_2 ($10^{-6}{}^{\circ}\mathrm{C}^{-1}$)	29.246	30.084

As can be seen, the parameter values obtained with the hexagonal and square unit cell are different to some extent, especially those in the transverse direction. The difference will be more pronounced if the Young's modulus in the 45° direction to the principal axis in the transverse plane to the fibre is evaluated [48].

Since the UD composites, in which fibres are distributed at random over their cross sections, usually exhibit transversely isotropic characteristics in a statistical sense, hexagonal packing captures this feature better than square packing. This was reflected by comparing the values of E_2 and E_3 and those of G_{23} and $\frac{E_2}{2(1+\upsilon_{23})}$. For a transversely isotropic material, each of the two pairs should share an identical value.

In order to assess the sensitivity of the mesh size on the predictions, a hexagonal UC model of UD composite was created, where the fibre volume fraction was fixed at 60%, and the material properties of the fibre and matrix were as specified in Table 3.1. Several cases were generated, where the model was meshed with elements of different sizes, so that all the models had different number of elements. The effective longitudinal and transverse stiffnesses calculated with those models are shown in Figure 3.7 (a) and (b), respectively.

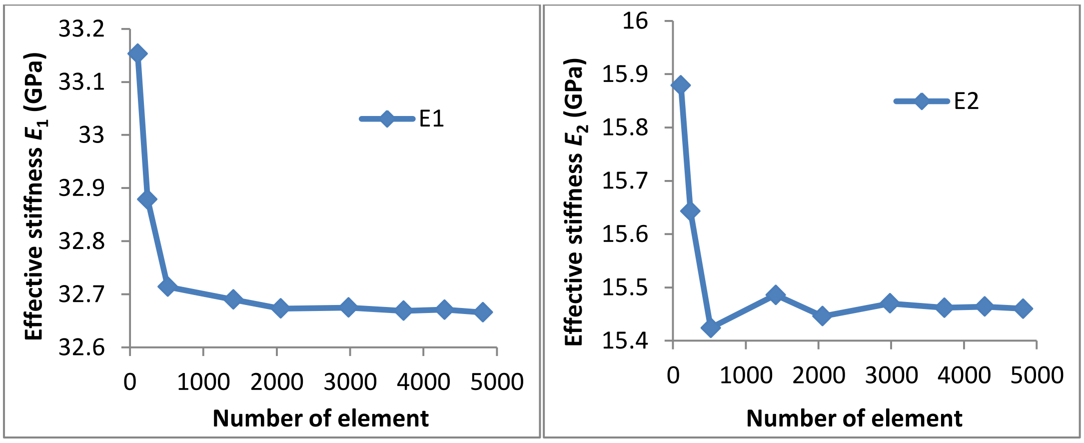

(a) Effective longitudinal stiffness (b) Effective transverse stiffness

Figure 3.7 Effective stiffness calculated from UC with different mesh size

It can be seen that the mesh size does affect the effective stiffness predictions, however, convergence of the stiffness predictions was obtained when the mesh was sufficiently fine.

3.3.2 UD composite model with a random fibre distribution

In real UD composites, the fibre distribution over the cross section perpendicular to the fibres is random, as can be seen from the microscopy image of the UD composites shown in Figure 3.8 [47]. The methodology of formulating appropriate representative volume elements (RVEs) for micromechanical finite element analysis has been established in [47]. As a part of the present project, the analysis has been incorporated in UnitCells© such that the analysis and the extraction of the effective properties can be made in an automated manner with minimal intervention from the user.

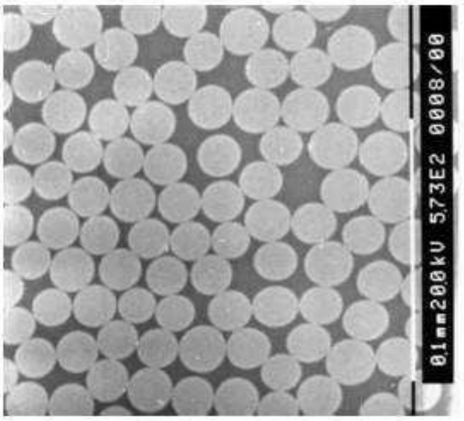

Figure 3.8 Microscopy image showing random fibre distribution in UD composite [47]

In order to create a RVE for the UD composites with random fibre distribution, two different methods were attempted.

The first method is referred to as 'insert fibre' method, and it involves random insertion of fibres to blank area. This method is easy to implement, however its limitation is that the maximum fibre volume fraction that can be achieved with method is relatively low. This is due to the presence of large gaps between fibres, which are, however, not large enough to accommodate a new fibre. In particular, in a typical example shown in Figure 3.9 it was about 40%, which was much lower than that in a conventional UD composite material.

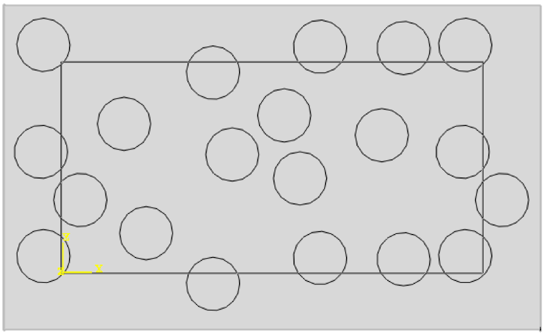

Figure 3.9 Random fibre distribution generated using ‘insert fibre’ method

Another method is referred to as a ‘move fibre’ method, which was proposed in [47]. It involves applying a random move function to a regular fibre distribution, to move each fibre along a random orientation to a random distance (Figure 3.10). This procedure was repeated several times until the fibre volume fraction in the middle range becomes equal to the overall fibre volume fraction [47]. Note that this method allows a fibre volume fraction up to 90.6%, giving regular hexagonal packing as the limit. An example of random fibre distribution generated with ‘move fibre’ method is shown in Figure 3.11.

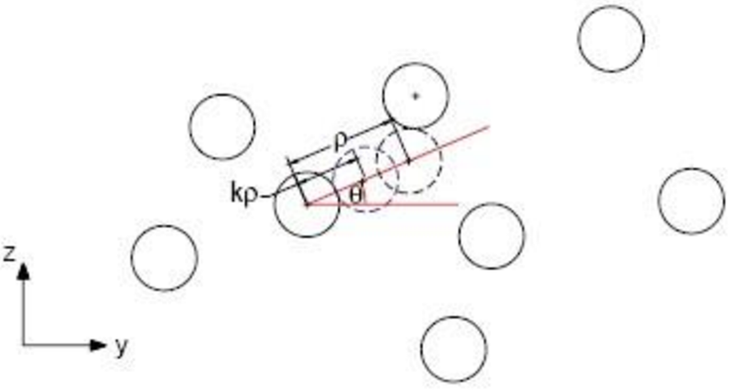

Figure 3.10 Illustration of a “move fibre” process [47]

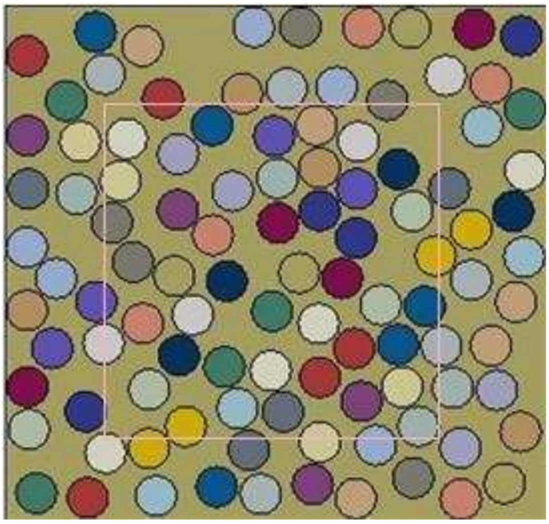

Figure 3.11 Random fibre distribution generated using 'move fibre' method

To verify this functionality, the results obtained with the regular and random fibre distribution models were compared. A set of regular unit cells and random RVEs were created and the equivalent properties of UD composites for these models were calculated. The materials properties of fibre and matrix are summarized in Table 3.3. The fibre volume fractions for all types of models were kept constant at 60%.

Table 3.3 Material properties of Silenka E-glass 1200 tex and epoxy resin [82]

	Matrix	Fibre
E (GPa)	3.35	74
υ	0.35	0.2

The RVE model input interface for random UD composites is shown in Figure 3.12 (a). Both the fibre and the matrix are defined as isotropic materials. If necessary, they can be chosen as transversely isotropic or orthotropic as desired. The constituent material properties input interface is shown in Figure 3.12 (b).

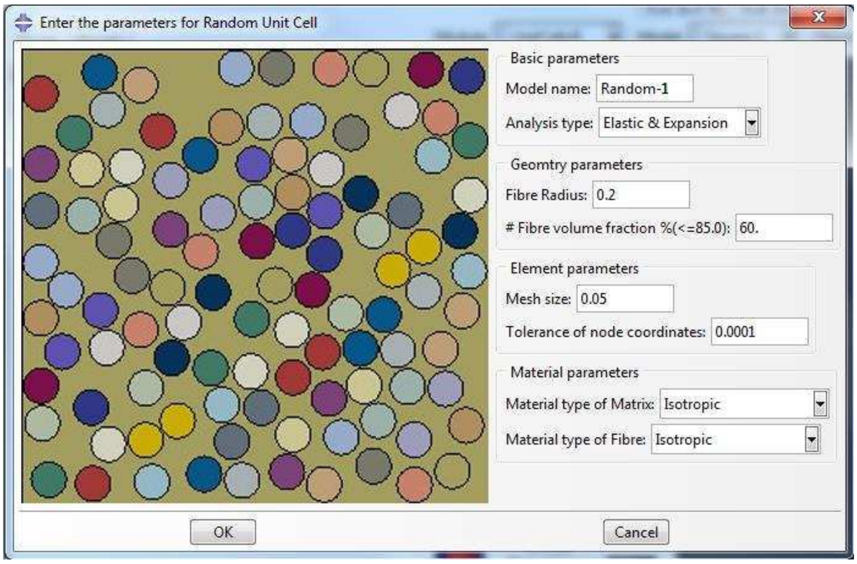

Basic parameters
Model name: Random-1
Analysis type: Elastic & Expansion
Geomtry parameters
Fibre Radius: 0.2
Fibre volume fraction %(<=85.0): 60.
Element parameters
Mesh size: 0.05
Tolerance of node coordinates: 0.0001
Material parameters
Material type of Matrix: Isotropic
Material type of Fibre: Isotropic

(a) Model parameters

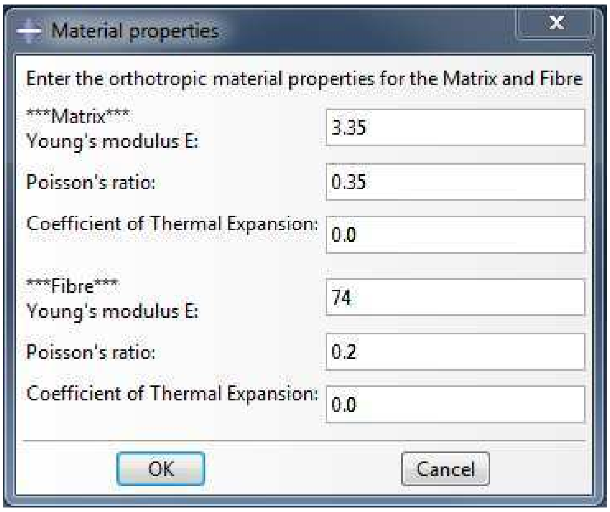

Enter the orthotropic material properties for the Matrix and Fibre
Matrix
Young's modulus E: 3.35
Poisson's ratio: 0.35
Coefficient of Thermal Expansion: 0.0
Fibre
Young's modulus E: 74
Poisson's ratio: 0.2
Coefficient of Thermal Expansion: 0.0

(b) Material properties of the constituents

Figure 3.12 User input for the thermo-mechanical analysis performed with UD RVE model with random fibre distribution

After the model parameters and material properties of matrix and fibre are defined, a random RVE shown in Figure 3.11 is generated automatically. Material properties for fibre and matrix are assigned automatically as well. Next, a uniaxial loading is applied to the RVE, and the stresses and strains for every element are calculated.

The results are post-processed automatically as follows. Properties are calculated based on the elements within the area marked by the pink frame (Figure 3.11) to avoid boundary effects. The fibre volume fraction within this area is the same as that of the whole RVE, which is equal to the predefined fibre volume fraction. Therefore, the calculated effective properties should be representative of the properties of the UD composite with the same fibre volume fraction. The extraction of the effective properties of UD composites is based on strains and stresses obtained for volume weighted average to be correct.

Here, three models with random fibre distribution were considered, which were generated based on the same set of parameters (see Figure 3.12(a)). The images of the finite element models with random fibre distribution are shown in Figure 3.13.

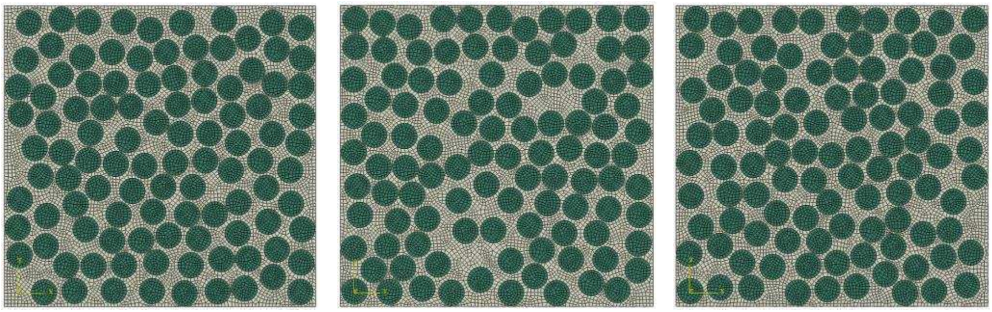

(a) Random 1 (b) Random 2 (c) Random 3

Figure 3.13 Finite element models from which RVEs with random fibre distribution are obtained

The effective properties predicted with these models are summarised in Table 3.4, along with the predictions of the UC models with regular fibre distribution, and the experimental results from [82].

Table 3.4 Effective properties of UD composites (V_f=60%)

	E_1 (GPa)	E_2 (GPa)	E_3 (GPa)	υ_{12}	υ_{23}	G_{12} (GPa)	G_{23} (GPa)	$\frac{E_2}{2(1+\upsilon_{23})}$
Experimental [82]	45.6	16.2		0.278	0.4	5.83	5.786	5.785
Square	45.6	14.9	14.9	0.250	0.261	4.56	3.245	5.916
Hexagonal	45.7	11.8	11.8	0.252	0.401	4.33	4.215	4.215
Random 1	45.6	12.4	12.8	0.265	0.377	4.61	4.580	4.513
Random 2	45.1	12.9	12.3	0.251	0.368	4.68	4.453	4.703
Random 3	45.6	12.5	13.4	0.251	0.387	4.71	4.646	4.517

Comparing the values of the effective properties in Table 3.4, it is easy to see that the effective material properties from the RVE models give reasonable representation of the transverse isotropy. Hexagonal packing produces perfect transverse isotropy, while the square packing leads to the most severe transverse anisotropy. The higher value of E_2 as obtained for the square unit cell is closer to the experimental value, but it is at the cost of transverse anisotropy and a much lower transverse Young's modulus in the 45° direction, along the diagonal of the square packing [48]. This can be confirmed by comparing the values of G_{23} and $\frac{E_2}{2(1+\upsilon_{23})}$.

Except those from the square unit cell, which tend to present a false image as discussed above, the rest of properties obtained from random packing show improvement to the regular packing.

It should be pointed out that due to the randomness in fibre distribution and the finite size of the RVE, different cases generated do not produce identical results. This discrepancy can be reduced by using RVEs of larger sizes that contain more fibres.

3.4 Building the Geometric Model for the Mesoscale UC with Texgen for Textile Composites.

In contrast to the UD composites, for which the microscale unit cell model has a relatively simple geometry, textile composites have complicated yarn architecture. It is not straightforward to create the geometry model for textile composites within FEM software which was Abaqus in the present development. A systematic method was needed to be developed to represent the realistic yarns properly. A micro-CT image of glass fibre reinforced 3D woven composites is shown in Figure 3.14 [83]. This development constituted a significant part of the efforts made in the present project as it was previously unavailable in UnitCells©.

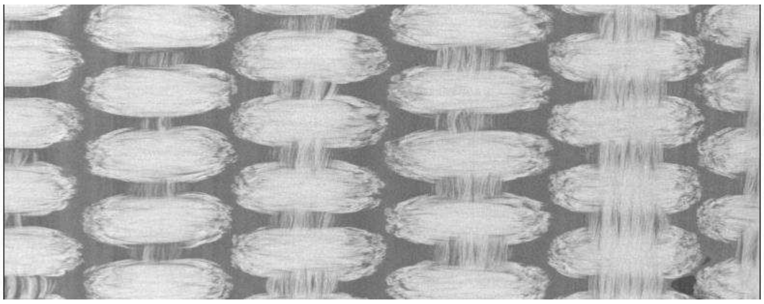

(a) Top view

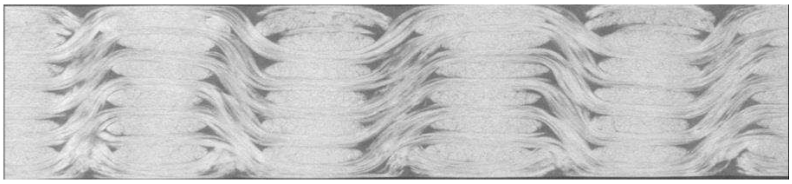

(b) Weft direction view

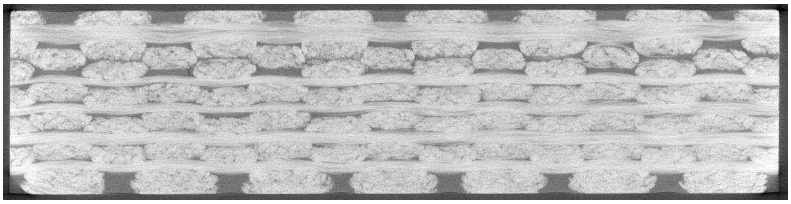

(c) Warp direction view

Figure 3.14 Micro-CT image of 3D woven fabric

It is easy to see that the cross sections of yarns are variable and the paths of weft yarns are curved. The open source software TexGen was applied to generate variable cross section and curved path yarn easily. The Python script interface and internal functions of TexGen make it compatible with other software, such as Abaqus and Hypermesh. An example the yarn generated using a Python script in TexGen is shown in Figure 3.15.

Figure 3.15 Model of the yarn with curved path and variable cross-section

This yarn was generated by sweeping several predefined cross sections, and the path of yarn was defined by the centre points of each cross section. The cross section was defined by a power ellipse function, which is available in Texgen. It employs several parameters allowing for more realistic representation of the cross section. The explicit expression of the power ellipse function is as follows [84].

$$X(t) = \begin{cases} \left(\frac{w}{2} + \Delta\, x\right)\cos(2\pi t) + \Delta\, x, & \text{if } 0.25 \le t \le 0.75 \\ \left(\frac{w}{2} - \Delta\, x\right)\cos(2\pi t) + \Delta\, x, & \text{if } t < 0.25 \; or \; t > 0.75 \end{cases}$$
$$Y(t) = \begin{cases} \frac{h}{2}(\sin(2\pi t))^n, & \text{if } 0 \le t \le 0.5 \\ -\frac{h}{2}(-\sin(2\pi t))^n, & \text{if } 0.5 \le t \le 1 \end{cases} \quad (3\text{-}19)$$

where w and h are the width and height of the cross section, n is a power which can be used to adjust the shape, namely, the cross section becomes elliptic when n=1 and it becomes rectangular when n =0. The parameter $\Delta\, x$ defines the offset of the cross section along horizontal direction. $X(t)$ and $Y(t)$ are the coordinates of the points on the power ellipse. The parameter t varies between zero at zero angle and unity at angle 2π. Three typical shape of cross section defined by power ellipse function are shown in Figure 3.16.

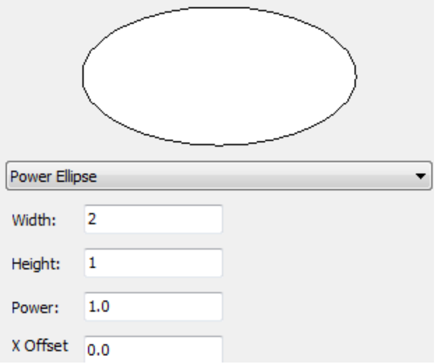
Power Ellipse
Width: 2
Height: 1
Power: 1.0
X Offset 0.0

(a) Case 1

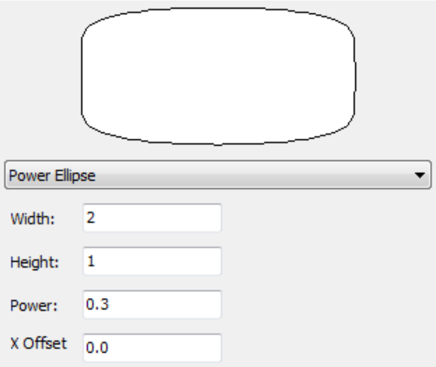
Power Ellipse
Width: 2
Height: 1
Power: 0.3
X Offset 0.0

(b) Case 2

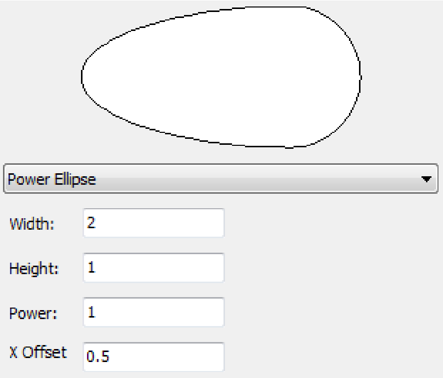
Power Ellipse
Width: 2
Height: 1
Power: 1
X Offset 0.5

(c) Case 3

Figure 3.16 Definition of yarn cross-sections as power ellipses at different parameters

With the Python script interface and internal functions of TexGen, parametric modelling of mesoscale unit cells can be achieved. By modifying the values of the parameters and copying, moving and rotating the yarns, numerous types of textile architectures can be created, where yarns can have variable cross sections and curved paths. This makes the unit cell models more realistic and allows to achieve reasonable yarn volume fractions. As an illustration, some unit cell models generated in TexGen using Python scripts are shown in Figure 3.17.

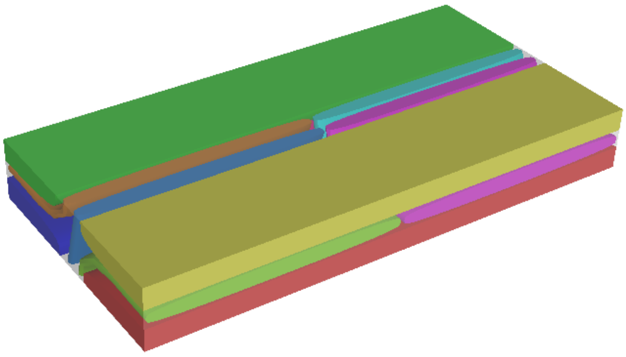

(a) Straight interlock weave (Yarn volume fraction: 78.5%)

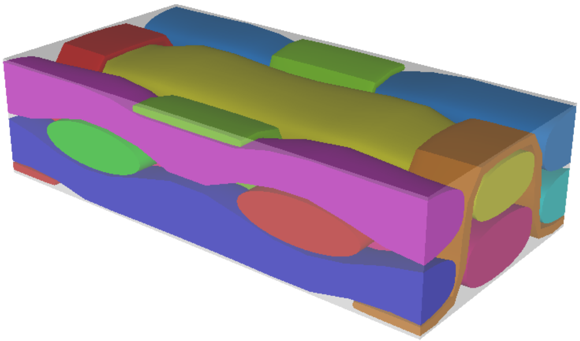

(b) Two layers warp yarn orthogonal weave (Yarn volume fraction: 60.9%)

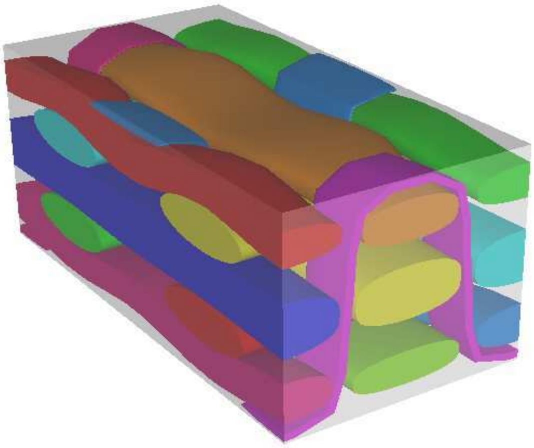

(c) Three layers warp yarn orthogonal weave (Yarn volume fraction: 60.68%)

Figure 3.17 Weave geometries for three types of unit cells generated by Python scripts

The unit cell models in Figure 3.17 have curved warp yarn paths, variable cross sections of the yarns and realistic yarn volume fraction, which suggests this method be applicable to representing the geometry of 3D textile composites efficiently.

3.5 Periodic Mesh for Mesoscale Model

Since the geometric models of 3D textile composites are complex and irregular, the greatest challenge in generating the unit cells for these materials is the meshing. Because of the complex yarn structures, it is not straightforward to ensure the correspondence of the nodes in a pair of opposite faces, which is the basic requirement for applying the periodic boundary condition.

Three different mesh methods were integrated in UnitCells© toolbox. The methods satisfy different precision requirements, for example, voxel mesh is suitable for stiffness predictions, but not suitable for predicting the stress field. A specific meshing method can be selected by the user and prior to analysis.

3.5.1 Voxel mesh generation in TexGen

An approximate voxel mesh (Figure 3.18) can be exported from TexGen directly. Since the yarn paths in 3D textile composite model are curved, and the material behaviour within the yarns is transversely isotropic, it is necessary to define the local coordinate system for the yarns at every point. In TexGen, the local coordinate system within the yarns is defined automatically once the geometry was created. The local coordinate system for every element is recorded to a file when the voxel mesh is exported to an Abaqus input file.

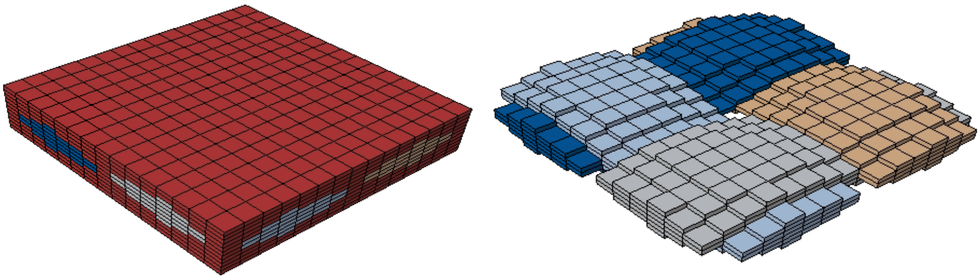

Figure 3.18 Voxel mesh for plain weave model

A Unit cell model with voxel mesh makes it possible to calculate the effective elastic properties with reasonable accuracy. However, it becomes inapplicable when analysis is extended to effective strength calculations, as described in Chapter 4. The stress distribution at the yarn/matrix interface is unrealistic, because the surfaces are not smooth. Therefore, the unit cell model with voxel mesh cannot predict the realistic stress concentration at the interface, which leads to an underestimation of the effective strengths. An example of non-smooth stress distribution within the unit cell model of a plain weave composite under uniaxial tensile loading along the *x*-direction is shown in Figure 3.19.

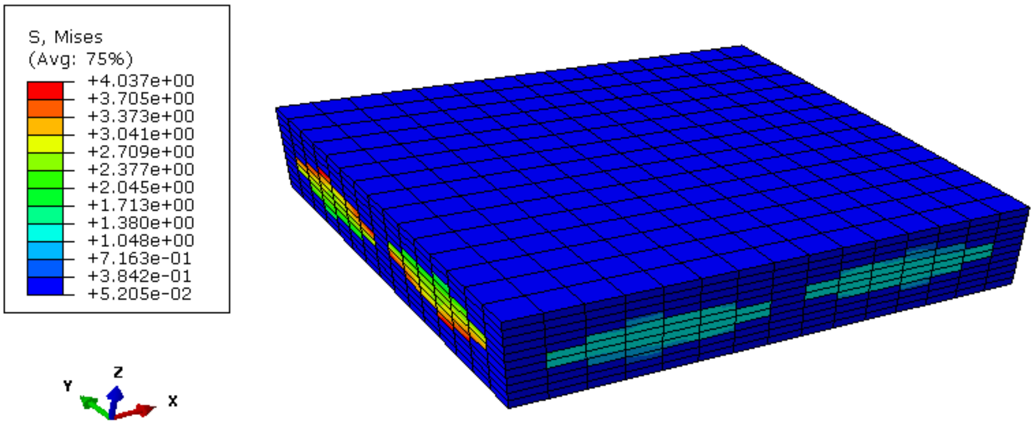

Figure 3.19 Stress distribution within a voxel meshed unit cell model under uniaxial tensile loading in the *x*-direction

3.5.2 Tetrahedral mesh generation with Hypermesh

A method of generating periodic mesh has been developed employing the advanced meshing capability of Hypermesh in order to achieve a smooth yarn/matrix interface within a unit cell. The geometric model as generated in TexGen was imported and meshed using command file of Hypermesh following the steps as outlined below.

First, a periodic 2D mesh was created on the surfaces of the unit cell. In order to create identical meshing on the opposite surfaces of the unit cell, the mesh generated on one face was projected on the opposite face. The identical 2D mesh generated on one pair of faces is shown in Figure 3.20.

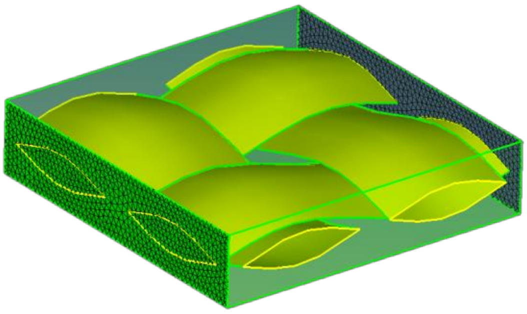

Figure 3.20 2D mesh applied on the opposite faces of the unit cell representing the plain weave composite

Next, the 3D mesh was generated based on the periodic 2D mesh, after which the 2D mesh was deleted. Before being exported to Abaqus, the 3D mesh was divided into several components according to the geometric structure, to separate the individual yarn and matrix constituents. An example of the periodic 3D mesh for the plain weave composite unit cell is shown in Figure 3.21.

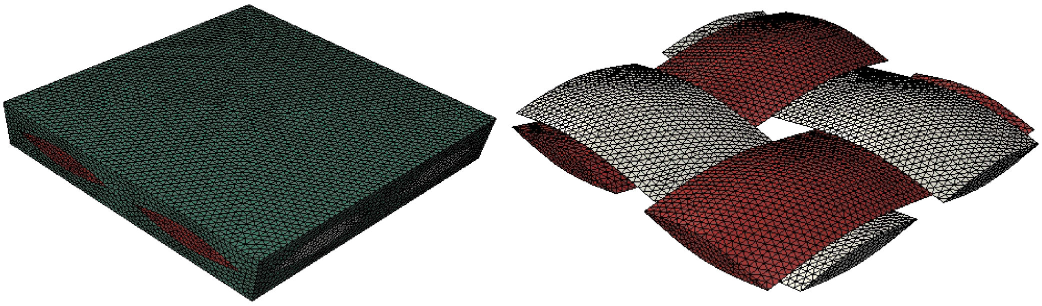

(a) Full model (b) Yarns

Figure 3.21 Periodic tetrahedral mesh applied to the unit cell representing the plain weave composite

The periodic tetrahedral mesh model has smooth yarn/matrix interfaces, hence it represents more realistic composite structure than that obtained with the voxel mesh. The stress distribution within the unit cell within periodic tetrahedral mesh under uniaxial tensile loading along *x*-direction is shown in Figure 3.22.

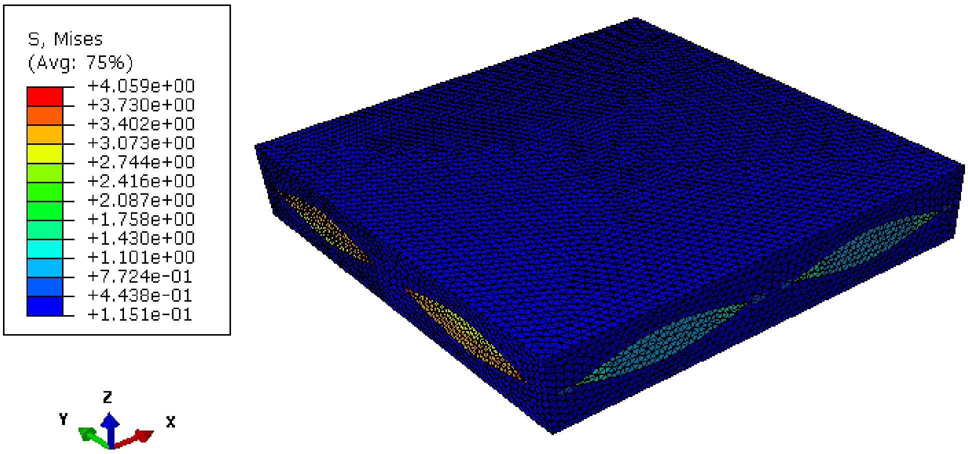

Figure 3.22 Stress distributions within periodic tetrahedral mesh unit cell model under uniaxial tensile loading in the *x*-direction

Comparing the contour plots of von Mises stress shown in Figure 3.22 and Figure 3.19, it is easy to see that the stress values are close, which suggests that effective stiffnesses predicted with the models with tetrahedral mesh and voxel mesh are similar.

Since the elements for the periodic tetrahedral mesh model are created in Hypermesh, the local coordinate system for the mesh cannot be defined directly, because of the complicated yarn architecture of textile composites. This issue was tackled by developing a method of incorporating an appropriate functionality of TexGen, which can return local coordinate system for a material point according to its coordinates. After the tetrahedral mesh was generated in Hypermesh, the coordinates of the centroid of every element were calculated and recorded into a file. Next, a Python script was run in TexGen to define the local coordinate system for every element and output to an orientation file. This was linked to the Abaqus input file before it was submitted to analysis. All the mesh generation process as described above is executed automatically in UnitCells© toolbox.

3.5.3 Smooth hexahedral mesh

The method of periodic mesh generation, as introduced in the previous section, allows defining smooth matrix/yarn interface. However, within Hypermesh, only tetrahedral element meshing can be applied together with the 2D mesh projection method. These elements have a lower accuracy than the hexahedral elements. Therefore, a method of applying hexahedral element meshing to the mesoscale unit cells has been developed.

For that, a mesh smoothing algorithm was applied to transfer a voxel mesh into a smooth hexahedral mesh. Specifically, an automatic mesh smoothing method proposed by Boyd and Müller [85] was adapted and extended. It is based on computationally efficient fairing technique developed for smoothing the polygonal surfaces [86, 87], and it was extended here to the finite element meshes.

The process can be divided into two steps, signal processing and smoothing processing.

1) Signal processing

In the signal processing, all the neighbourhoods (connected nodes) of each node will be identified. According to the number of neighbourhoods and the material type of neighbourhoods, all nodes in the 3D mesh are labelled in a hierarchical order. The nodes can be classified as four main groups (Figure 3.23): (1) fixed nodes at the corners of the unit cell, (2) interior nodes of the unit cell, (3) nodes at the matrix/ yarn interface and (4) surface nodes on the sides of the unit cell.

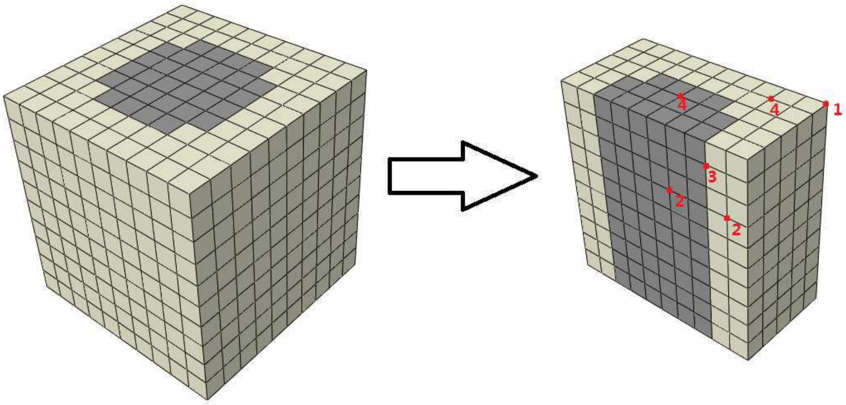

Figure 3.23 Illustration of nodes belonging to different node groups

Some of the nodes belong to both surface and interface, these nodes have to be classified as a new group. Finally, all the nodes can be divided into ten sub groups based on the four main groups as follows.

1---fixed nodes

2---interior nodes

3---interface nodes

4---surface nodes

5---interface and Xsurfaces nodes

6---interface and Y surfaces nodes

7---interface and Z surfaces nodes

8---interface and X- direction edges nodes

9---interface and Y- direction edges nodes

10---interface and Z- direction edges nodes

2) Smoothing processing

Based on the neighbourhood group definition, a Laplacian smoothing operator was defined for each node with weights w_{ij} for each related neighbour, resulting in a set of displacements:

$$\Delta x_i = \sum_{j \in i^*} w_{ij}(x_j - x_i) \tag{3-20}$$

where weights w_{ij} are non-negative numbers that add up to unity for each node:

$$\sum_{j \in i^*} w_{ij} = 1 \tag{3-21}$$

If all the nodes all treated as having the same importance, the weight w_{ij} can be defined as:

$$w_{ij} = \frac{1}{|i^*|} \tag{3-22}$$

where $|i^*|$ is the number of nodes which related to the current node i^*.

Displacements Δx_i form the signal to which low pass filtering via Laplacian smoothing can be applied. The Laplacian transfer function is $x_i' = x_i + \lambda \Delta x_i$, where λ is a scaling factor, $0 < \lambda < 1$, can be applied a number of times (N) to achieve a desired degree of smoothness.

Although Laplacian smoothing is a linear operation and it is efficient for large meshes, it sometimes results in over-smoothing and hence undesirable mesh shrinkage. The solution to this problem is the key of Taubin's fairing approach [86], where the transfer function is modified to:

$$x_i' = \begin{cases} x_i + \lambda \Delta x_i, & \text{if } N \text{ is an even number} \\ x_i + \mu \Delta x_i, & \text{if } N \text{ is an odd number} \end{cases} \tag{3-23}$$

Through careful selection of λ and μ an effective band-pass frequency for the transfer function is set by applying a number of smoothing iterations. This result in a low pass filters which does not cause polygonal mesh shrinkage. The restriction on choice of λ and μ proposed in [86] is as follows.

$$k_{PB} = \frac{1}{\lambda} + \frac{1}{\mu} > 0 \tag{3-24}$$

The values of λ, μ and k_{PB} have been chosen as follows [86].

$$\lambda = 0.631, \qquad \mu = -0.673, \qquad k_{PB} = 0.1 \tag{3-25}$$

The larger the number of smoothing iterations executed, the smoother the mesh. However, this makes the process more computationally expensive. In present work, after trial and error on the effects of the outcomes, it was concluded that 500 iterations were sufficient for obtaining a sufficiently smooth mesh. As an illustration, the shrinking and non-shrinking meshes after repeating the smoothing process 500 times are shown as Figure 3.24.

(a) Voxel mesh (b) Shrinking mesh (c) Non-shrinking mesh

Figure 3.24 Illustration of shrinking and non-shrinking smooth mesh

With the mesh smoothing algorithm, voxel meshes for all types of mesoscale unit cells can be converted to smooth hexahedral mesh automatically. Some examples are shown in Figure 3.25 to illustrate the capability of this mesh smoothing method.

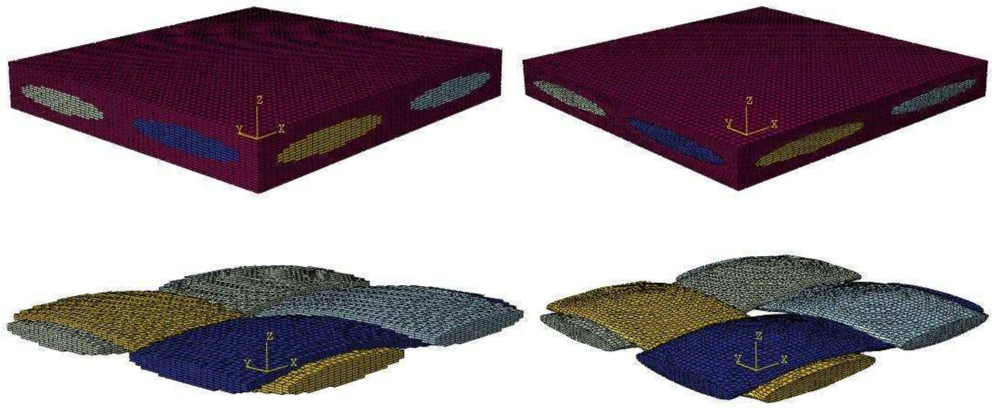

(a) Plain weave model

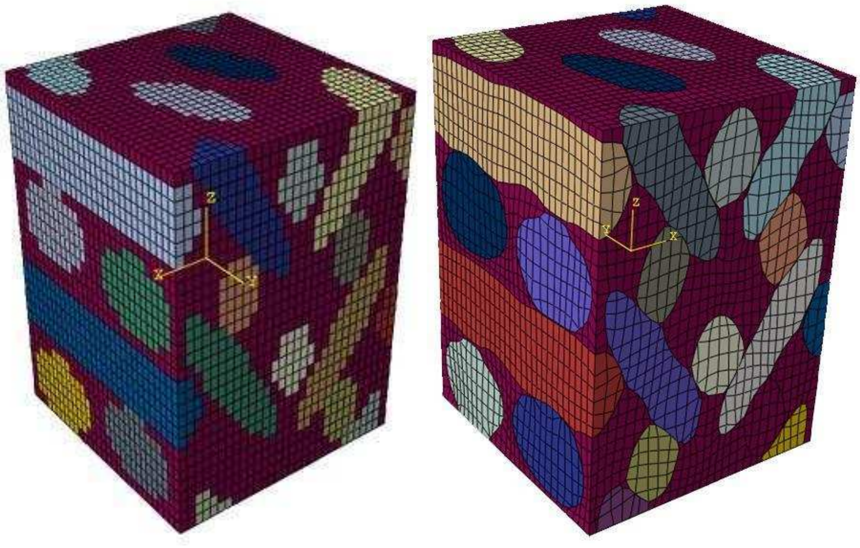

(b) 5-axial 3D braided model

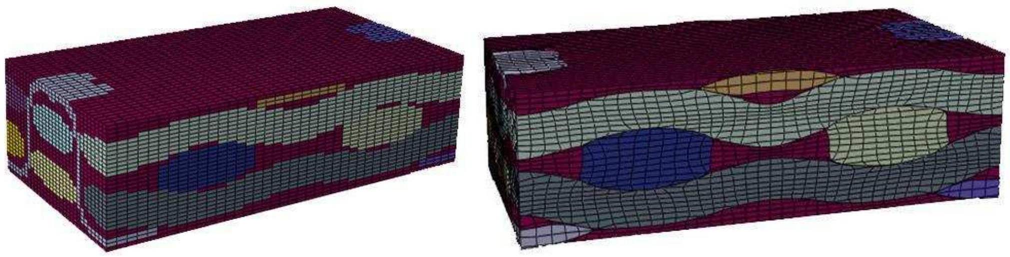

(c) Orthogonal interlock model

Figure 3.25 Voxel mesh and smooth hexahedral mesh

It can be concluded that the mesh smoothing algorithm introduced in this section is applicable for generating meshes for the unit cell models of composites with complex textile architectures.

3.6 Development of UnitCells©

To facilitate the unit cell modelling process, an automatic multi-scale composite material characterisation Python script code UnitCells© [73, 88, 89, 90] was adopted and extended. Initially, the Python script code UnitCells© were created by Li and Jeanmeure [89, 90] for carrying out unit cell modelling and subsequent composite material characterisation. These covered hexagonal and square unit cells representing the UD composites, and cubic unit cell for particle reinforced composites, with a primitive attempt made to the plain weave textile composite. The scripts ran on Abaqus [91] to calculate the effective stiffnesses and coefficients of thermal expansion.

In the current research, these analyses were further extended to a substantial range of textile composites based on various types of woven and braided reinforcements. The analysis types were extended to strength analysis, flexural analysis, heat conduction analysis and electric conduction analysis.

Using Abaqus as a platform and its Python script programming [91] facility as a vehicle, UnitCells© has been established as a fully automated composites characterization tool. Moreover, it is capable of drawing relevant functions from TexGen [45], an open source code for generating textile composite architectures, to generate the desirable textile preform configurations and from Hypermesh [92], a commercial FE pre-processor, to generate the appropriate meshes. In an automated manner, correct periodic boundary conditions are imposed and precise loads are applied before a complete material characterisation simulation. The effective material properties of the composite are readily obtained from simulation using this tool. The characterisation process is also fully controllable through the visual interfaces to define relevant geometric and material parameters. It can also be used for multi-scale modelling in the sense that different phases can be characterised in a length scale below, e.g. yarns in a textile composite as UD composites. The flow chart of UnitCells© is given in Figure 3.26.

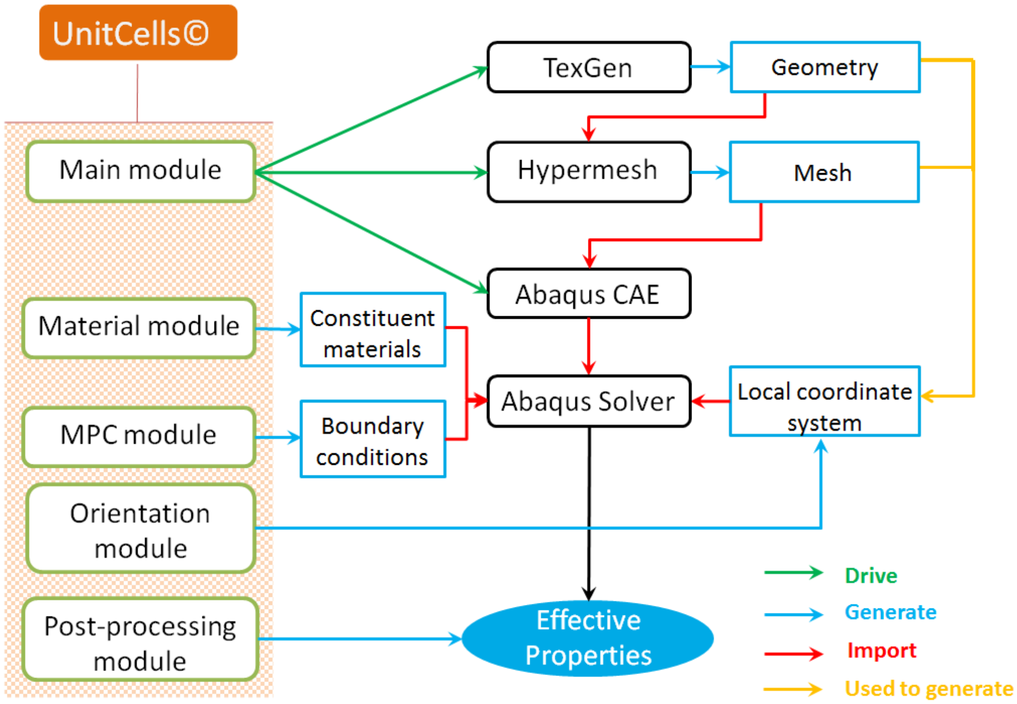

Figure 3.26 Flow chart of UnitCells©

This automatic multi-scale composites characterisation toolbox UnitCells© can be used to calculate the effective properties of UD composites, particulate-reinforced composites, laminate composites, 2D woven composites, 2D braided composites, 3D woven composites and 3D braided composites. These effective properties include stiffness, thermal expansion, quasi-static strength, thermal conductivity and electrical conductivity.

In terms of user access, a new module called ‘UnitCells’ was added to the existing list of modules in Abaqus. The main window of UnitCells© is shown in Figure 3.27. Various buttons can be found on the left hand side of the window. They can be clicked to select the type of the unit cell to be created for the characterisation of the composites it represents. Once the type of the unit cell has been selected, the user is prompted by various pop-up windows to define the details of the architecture of unit cell and the properties of the constituent materials. These are all carried out in an interactive manner. User can also use the menu or buttons in the main window to open user manual and refresh the screen. Any created unit cell can also be saved for retrieving on a later date, although the current set up as user exit from UnitCells©

will always be kept as the default value for next access to the same type of unit cell. None of the existing functionalities of Abaqus is affected by the installation of UnitCells©.

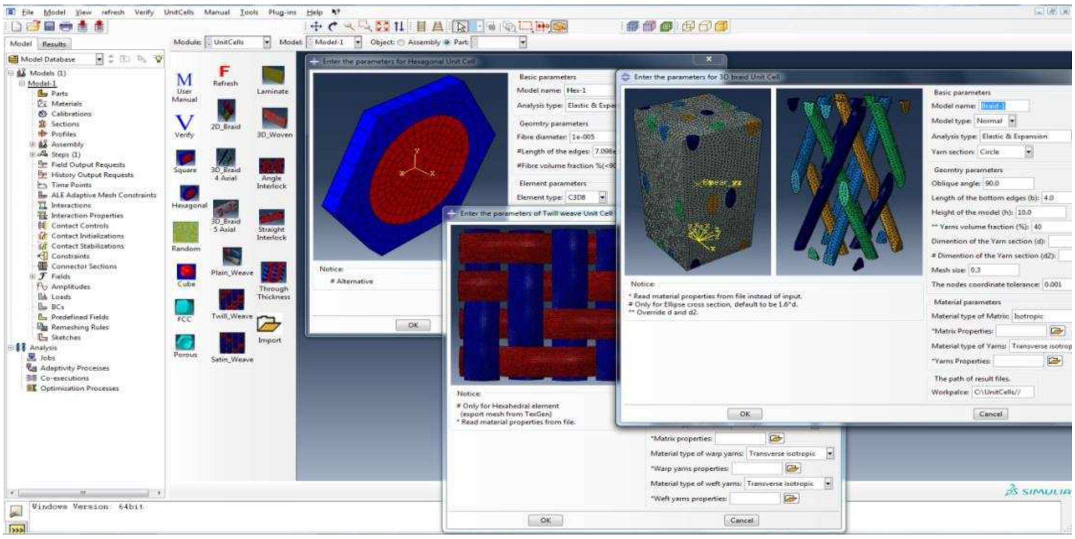

Enter the parameters for Hexagonal Unit Cell

Basic parameters
Model name: Hex-1
Analysis type: Elastic & Expa
Geomtry parameters
Fibre diameter: 1e-005
#Length of the edges: 7.098e
#Fibre volume fraction %(<90
Element parameters
Element type: C3D8

Notice:
Alternative

Enter the parameters of Twill weave Unit Cell

Notice:
Only for Hexahedral element
(export mesh from TexGen)
* Read material properties from file.

*Matrix properties:
Material type of warp yarns: Transverse isotropic
*Warp yarns properties:
Material type of weft yarns: Transverse isotropic
*Weft yarns properties:

Enter the parameters for 3D braid Unit Cell

Notice:
* Read material properties from file instead of input.
# Only for Ellipse cross section, default to be 1.6*d.
** Override d and d2.

Basic parameters
Model name: Braid-1
Model type: Normal
Analysis type: Elastic & Expansion
Yarn section: Circle
Geomtry parameters
Oblique angle: 90.0
Length of the bottom edges (b): 4.0
Height of the model (h): 10.0
** Yarns volume fraction (%): 40
Dimention of the Yarn section (d):
Dimention of the Yarn section (d2):
Mesh size: 0.3
The nodes coordinate tolerance: 0.001
Material parameters
Material type of Matrix: Isotropic
*Matrix Properties:
Material type of Yarns: Transverse isotrop
*Yarns Properties:
The path of result files.
Workpalce: C:\UnitCells//

Figure 3.27 Main window of UnitCells©

In order to make this toolbox easy to update, a verification program was included. The verification program will run to check each analysis type of all the unit cells when the user clicks the verification button.

3.7 Sanity Checks as Means of Verification

Verification is needed when a new version of a model is established. For UnitCells©, the verification process is used to ensure that the mesh generated has met the requirements, the boundary conditions have been imposed to the unit cell precisely, the stress states have been applied correctly and the data extraction (post-processing) is performed logically.

Sanity checks are essential for verifying the formulation and implementation of the unit cells, ensuring acceptability of mesh, strict imposition of boundary conditions, correct application of stress states and logical performance of data extraction (post-processing). They are carried out for all the unit cells for all types of the analysis, which usually help to eliminate most of the mistakes in analyses of unit cells. The procedure is summarised as follows.

1) With the exception of the unit cells for porous materials, all unit cells have undergone 'sanity checks' with all phases involve being given the same material properties.

2) Perfectly uniform stress and strain fields are obtained.

3) The uniform stresses or strains coincide with the stress states as prescribed, e.g. the prescribed values, a uniaxial stress state, and the strains corresponding to a uniaxial stress state.

4) These stresses and strains are related to each other according to the material properties assigned to, e.g. Young's moduli, shear moduli and Poisson's ratios.

5) The obtained effective properties are identical to those used to define the material as input.

As an illustration for the procedure of sanity check, unit cell models of 4-axial and 5-axial 3D braided composites were generated using UnitCells© toolbox, and a thermo-mechanical analysis was performed with them. The unit cell models for these composites are shown in Figure 3.28.

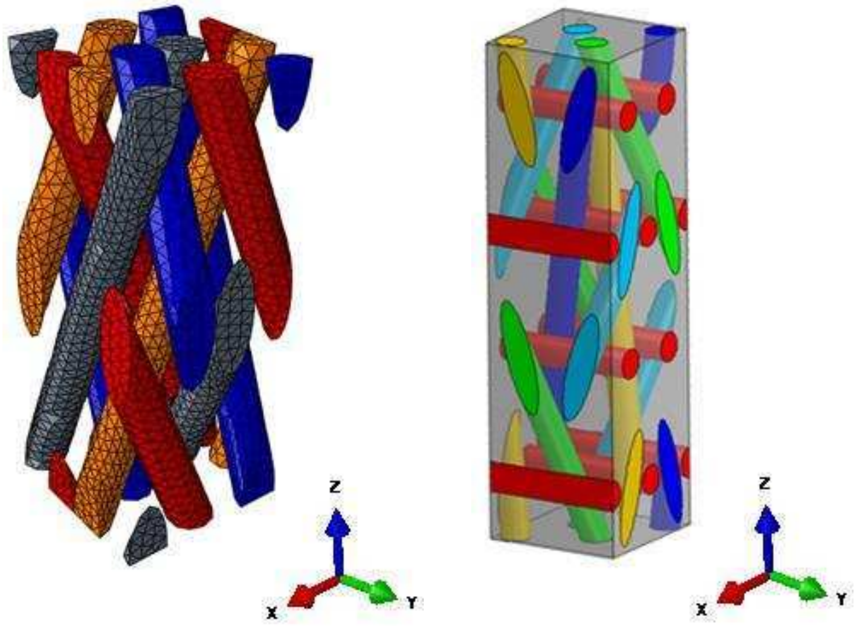

(a) 4-axial 3D braided (b) 5-axial 3D braided

Figure 3.28 UCs of 3D braided composites (braiding angle=21.8°, V_f=60%)

Both the matrix and the fibre phases of the unit cells were assigned the same assumed material properties as given in Table 3.5.

Table 3.5 Assumed material properties as the input for sanity checks

E (GPa)	3.01
υ	0.3
α (10^{-6}°C^{-1})	60

To run the analysis process, the user only needs to input some necessary parameters to generate the model, such as geometry parameters and material properties for matrix and yarn. The model parameters and material properties for this sanity check are given in Figure 3.29.

Seven loading cases are considered, six of them being uniaxial stress states of unity stress magnitude, and a temperature loading case corresponding to a uniform temperature increase of 1°C.

Under loading with macroscopic uniaxial stress $\sigma_1^0 = 1$, the obtained microscopic stress field should be completely uniform. Therefore, the predicted values of stress components should be precisely $\sigma_1 = 1$ and $\sigma_2 = \sigma_3 = \tau_{23} = \tau_{13} = \tau_{12} = 0$ as plotted in Figure 3.30 and one has to make sure that any discrepancy is no more than the rounding errors as shown in the τ_{12} contour plot. It is worth noting that the multicolour stress or strain contour plots obtained in the sanity checks usually suggest modelling issues, unless the plot legend indicates that the variation over the colour bar is truly negligible. Similarly, the microscopic strain field should be uniform, with values given by $\varepsilon_1 = \sigma_1 / E$, $\varepsilon_2 = \varepsilon_3 = -\nu\sigma_1 / E$ and $\gamma_{23} = \gamma_{13} = \gamma_{12} = 0$. The predictions for the remaining five load cases are assessed in exactly the same way. Under the temperature loading, all microscopic stresses should vanish, as well as the shear strains. At temperature increase of 1^{o}C, the magnitudes of the direct strains should be equal to the input values of the thermal expansion coefficient. The predicted effective properties are shown in Figure 3.31 and they should be equal to the input parameters.

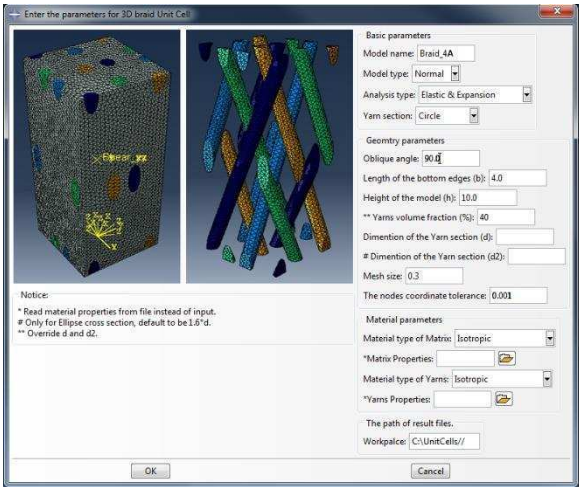

Basic parameters

Model name: Braid_4A

Model type: Normal

Analysis type: Elastic & Expansion

Yarn section: Circle

Geomtry parameters

Oblique angle: 90.0

Length of the bottom edges (b): 4.0

Height of the model (h): 10.0

** Yarns volume fraction (%): 40

Dimention of the Yarn section (d):

Dimention of the Yarn section (d2):

Mesh size: 0.3

The nodes coordinate tolerance: 0.001

Material parameters

Material type of Matrix: Isotropic

*Matrix Properties:

Material type of Yarns: Isotropic

*Yarns Properties:

The path of result files.

Workpalce: C:\UnitCells//

Notice:

* Read material properties from file instead of input.
\# Only for Ellipse cross section, default to be 1.6*d.
** Override d and d2.

(a) Model parameters for 4-axial 3D braided unit cell

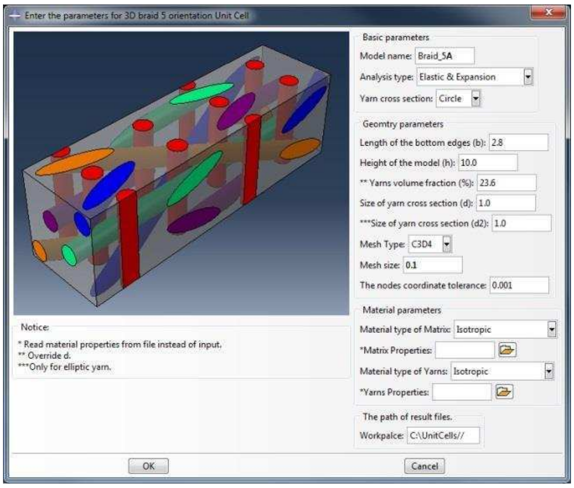

Basic parameters

Model name: Braid_5A

Analysis type: Elastic & Expansion

Yarn cross section: Circle

Geomtry parameters

Length of the bottom edges (b): 2.8

Height of the model (h): 10.0

** Yarns volume fraction (%): 23.6

Size of yarn cross section (d): 1.0

***Size of yarn cross section (d2): 1.0

Mesh Type: C3D4

Mesh size: 0.1

The nodes coordinate tolerance: 0.001

Material parameters

Material type of Matrix: Isotropic

*Matrix Properties:

Material type of Yarns: Isotropic

*Yarns Properties:

The path of result files.

Workpalce: C:\UnitCells//

Notice:

* Read material properties from file instead of input.
** Override d.
***Only for elliptic yarn.

(b) Model parameters for 5-axial 3D braided unit cell

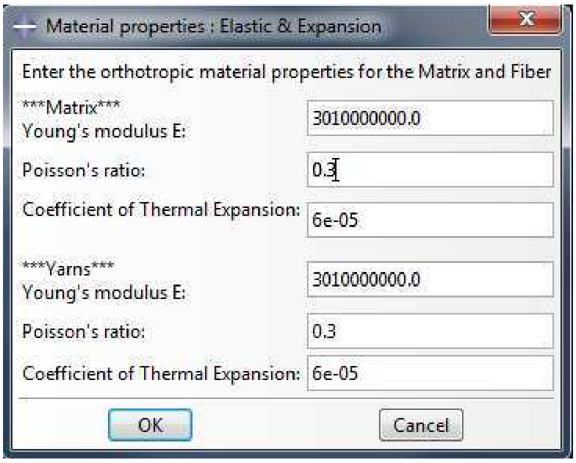

Enter the orthotropic material properties for the Matrix and Fiber

Matrix
Young's modulus E: 3010000000.0

Poisson's ratio: 0.3

Coefficient of Thermal Expansion: 6e-05

Yarns
Young's modulus E: 3010000000.0

Poisson's ratio: 0.3

Coefficient of Thermal Expansion: 6e-05

(c) Material properties for 4-axial and 5-axial 3D braided unit cells

Figure 3.29 Input data for sanity checks of thermo-mechanical analysis

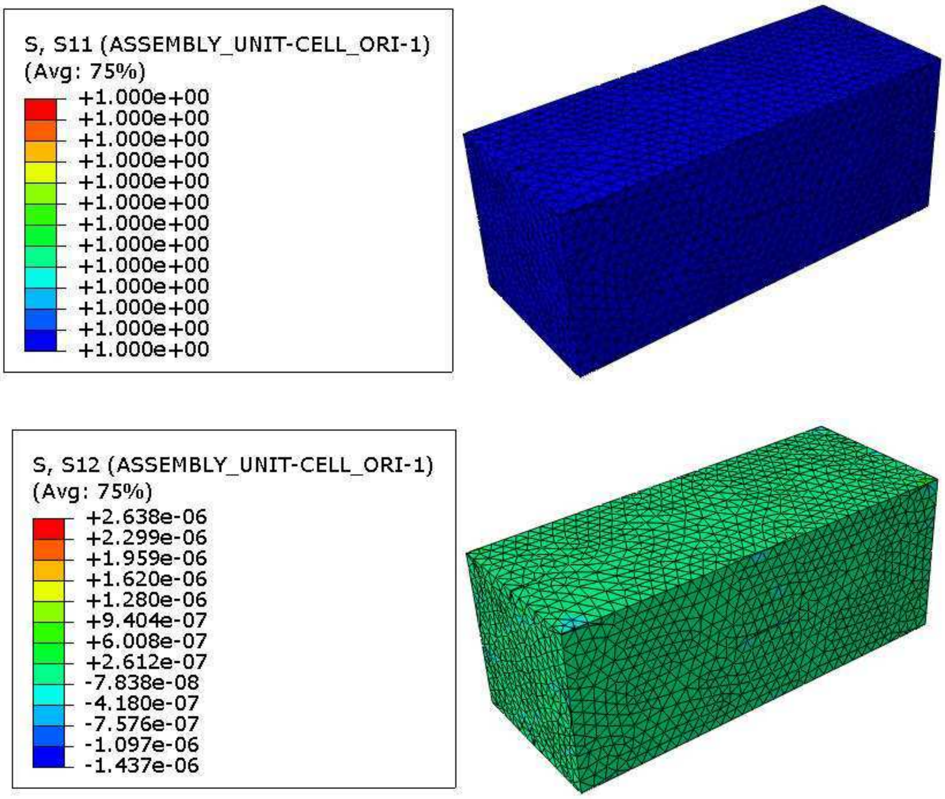

Figure 3.30 Some of the distributions of stresses over the 4-axial 3D braided unit cell

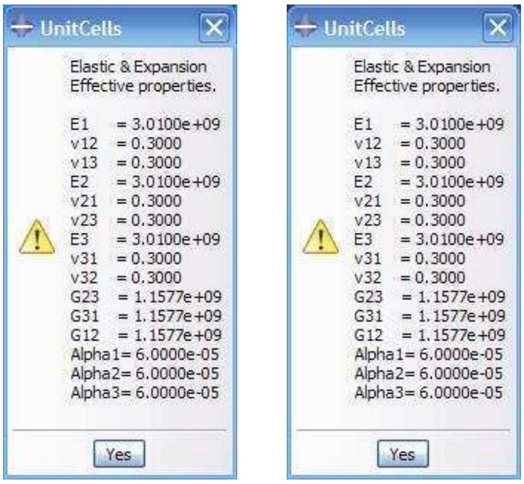

Elastic & Expansion
Effective properties.

E1 = 3.0100e+09
v12 = 0.3000
v13 = 0.3000
E2 = 3.0100e+09
v21 = 0.3000
v23 = 0.3000
E3 = 3.0100e+09
v31 = 0.3000
v32 = 0.3000
G23 = 1.1577e+09
G31 = 1.1577e+09
G12 = 1.1577e+09
Alpha1= 6.0000e-05
Alpha2= 6.0000e-05
Alpha3= 6.0000e-05

Elastic & Expansion
Effective properties.

E1 = 3.0100e+09
v12 = 0.3000
v13 = 0.3000
E2 = 3.0100e+09
v21 = 0.3000
v23 = 0.3000
E3 = 3.0100e+09
v31 = 0.3000
v32 = 0.3000
G23 = 1.1577e+09
G31 = 1.1577e+09
G12 = 1.1577e+09
Alpha1= 6.0000e-05
Alpha2= 6.0000e-05
Alpha3= 6.0000e-05

(a) 4-axial 3D braided (b) 5-axial 3D braided

Figure 3.31 Effective properties predicted in sanity check

The sanity checks will to a large extent to ensure that the following aspects have been dealt with correctly.

a) The input data have been taken in and processed correctly;

b) The mesh has been correctly generated topologically;

c) The mesh generated is suitable for the application of periodic boundary conditions;

d) Periodic boundary conditions have been imposed correctly;

e) Loads have been applied correctly;

f) The output has been post-processed correctly.

The following aspects are NOT covered by the sanity checks.

a) Whether or not the input data themselves are accurate;

b) Whether or not the mesh has been sufficiently fine or efficient;

c) Whether or not the microstructure employed reflects the physical material;

d) Whether or not the volume fractions are correct.

These should be verified or validated through other means, such as comparing with common sense, analytical results when available, e.g. those from the rule of mixtures and ultimately results from carefully conducted experiments.

Passing the sanity checks is a necessary step for the establishment of any unit cell. Before this has been achieved, any attempt at comparison with experimental results is futile, no matter how closely the comparisons might be in one respect or another.

3.8 Effective Stiffness of the Textile Composite

At present, the UnitCells© toolbox incorporates unit cells models for 3D textile composites based on three types of woven and two types of braided reinforcement architectures. All the models have passed the necessary sanity checks. To generate some meaningful verification cases with realistic material properties for fibre and matrix, effective elastic properties were calculated for each of them. Material properties of the fibre and resin used in this study are listed in Table 3.6.

Table 3.6 Elastic properties of PRIME^{TM} 20LV epoxy resin and IM7 carbon fibre

	Resin (PRIME^{TM} 20LV) [93]	Fibre (IM7) [94]
ρ (kg/m^3)	1140	1780
E_1 (GPa)	3.5	276
E_2 (GPa)	3.5	19
υ_{12}	0.35	0.28
υ_{23}	0.35	0.45
G_{12} (GPa)	1.3	9.5

A hexagonal unit cell was used to calculate the effective properties of the impregnated yarn. The fibre volume fraction within the yarns was set to as 90%. Based on these parameter values, the effective properties of yarns were obtained as specified in Table 3.7.

Table 3.7 Elastic stiffness properties of IM7 CF yarn (V_f=90%)

ρ (kg/m^3)	E_1 (GPa)	E_2 (GPa)	υ_{12}	υ_{23}	G_{12} (GPa)
1720	248.2	15.4	0.29	0.45	7.4

With the effective properties of yarns determined, all five types of textile composites as described above were characterised employing appropriate unit cell models for woven and braided composites, as shown in Figure 3.32 and Figure 3.28, respectively.

In order to carry out a meaningful comparison of the effective properties of the materials considered, all five models were set to have the same yarn volume fractions.

Note that for 3D braided composites, yarn volume fraction and yarn angle can be specified in the input panel. The warp and weft yarn volume fractions for the 3D woven composites cannot be defined explicitly, yet can be obtained as an output of the analysis, hence the desirable and also practical yarn volume fractions can be defined by adjusting the geometric parameters accordingly. The detailed discussion regarding the definition of geometric parameters for the layer-to-layer interlock unit cell model is presented in Chapter 8. The user input for model parameters and material properties are shown in Figure 3.33.

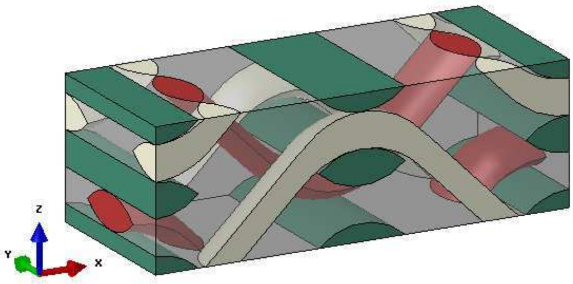

(a) Layer-to-layer angle interlock

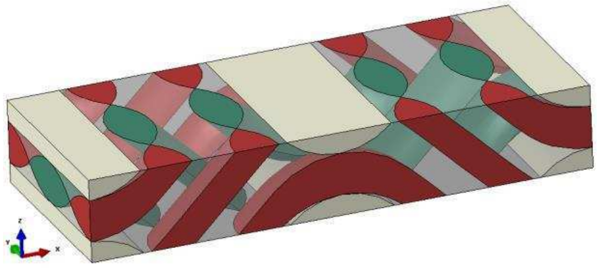

(b) Layer-to-layer interlock

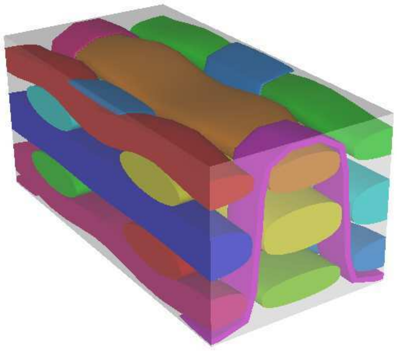

(c) Orthogonal interlock

Figure 3.32 3D woven composites (warp: weft yarn volume fraction= 35%:25%)

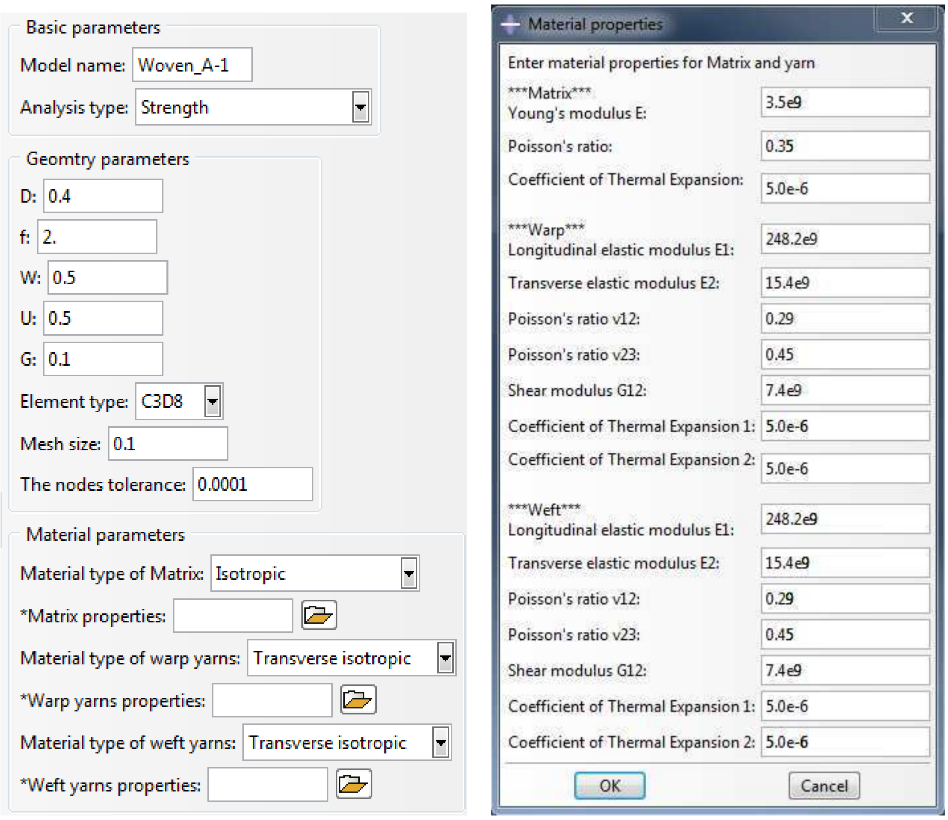

Basic parameters

Model name: Woven_A-1

Analysis type: Strength

Geomtry parameters

D: 0.4

f: 2.

W: 0.5

U: 0.5

G: 0.1

Element type: C3D8

Mesh size: 0.1

The nodes tolerance: 0.0001

Material parameters

Material type of Matrix: Isotropic

*Matrix properties:

Material type of warp yarns: Transverse isotropic

*Warp yarns properties:

Material type of weft yarns: Transverse isotropic

*Weft yarns properties:

Material properties

Enter material properties for Matrix and yarn

Matrix

Young's modulus E: 3.5e9

Poisson's ratio: 0.35

Coefficient of Thermal Expansion: 5.0e-6

Warp

Longitudinal elastic modulus E1: 248.2e9

Transverse elastic modulus E2: 15.4e9

Poisson's ratio v12: 0.29

Poisson's ratio v23: 0.45

Shear modulus G12: 7.4e9

Coefficient of Thermal Expansion 1: 5.0e-6

Coefficient of Thermal Expansion 2: 5.0e-6

Weft

Longitudinal elastic modulus E1: 248.2e9

Transverse elastic modulus E2: 15.4e9

Poisson's ratio v12: 0.29

Poisson's ratio v23: 0.45

Shear modulus G12: 7.4e9

Coefficient of Thermal Expansion 1: 5.0e-6

Coefficient of Thermal Expansion 2: 5.0e-6

(a) Model parameters input panel; (b) Elastic properties input panel

Figure 3.33 Input panels for stiffness predictions in UnitCells©

Effective elastic properties predicted with these composite models are summarised in Table 3.8, along with the properties of aluminium, which were included for the reference.

Table 3.8 Comparison of the elastic properties predicted for various types of textile composites

	Aluminium	Layer-to-layer angle interlock	Layer-to-layer interlock	Orthogonal interlock	4-axial 3D braided	5-axial 3D braided
ρ (kg/m^3)	2850	1485.6	1485.6	1485.6	1485.6	1485.6
E_1 (GPa)	72.39	12.543	63.503	35.176	9.4352	15.517
E_2 (GPa)	72.39	67.934	67.819	62.798	9.4362	60.998
E_3 (GPa)	72.39	21.077	10.164	20.405	93.224	75.519
G_{12} (GPa)	27.21	3.7247	3.874	3.2766	2.8255	5.0297
G_{13} (GPa)	27.21	3.5255	8.3736	3.0695	11.321	10.022
G_{23} (GPa)	27.21	3.4287	3.3747	3.0066	11.327	9.9816
v_{12}	0.33	0.0601	0.0019	0.0599	0.3269	0.1127
v_{13}	0.33	0.2307	0.4717	0.2468	0.0767	0.1475
v_{23}	0.33	0.1429	0.4335	0.1816	0.0767	0.0914

Analysing the predictions, it is easy to see that 3D woven composites and 5-axial 3D braided composite have stiffnesses along the Y-direction (E_2) similar to that of aluminium. This shows that these types of textile composites can be suitable for constructing fan blade casings. Although the effective stiffnesses along other directions are lower than those of aluminium, the main load in the fan casing is directed along the circumferential direction, which is coincident to the Y-direction of textile composites, therefore having high stiffness in this direction is crucial.

More importantly, the analysis as presented here suggests that the use of textile composites should make the engine more efficient, as the density of textile composite is nearly half of the density of aluminium.

3.9 Summary

This chapter introduced a piece of software UnitCells© for micro/meso/macro level analysis of unit cells representing composites of various micro/meso/macro-architectures. UnitCells© is a previously created Python script code, and it was extended extensively within the present research. A graphical user interface was created for ease of applications by users. The available models have been extended to included randomly packed UD composites and 3D textile composites, the analysis types have been extended to cover analyses for effective strengths, thermal conductivity and electricity conductivity. Building on the platform of Abaqus, extensions have also been made in the present project to draw a range of facilitating functionalities from other established codes including Texgen and Hypermesh for mesoscopic architectures of textile composites and mesh generations. A high level of automated operations has been achieved. The effective properties of the composites concerned can be obtained as the direct outcomes of the highly automated analysis. The capabilities of UnitCells© have been illustrated through a range of typical examples, including models for UD composites, 3D braided and 3D woven composites.

A systematic verification method 'sanity check' was introduced and illustrated using 3D braided composites as an example. The methodology introduced was verified by running a sanity check. This indicates that the unit cell modelling toolbox works properly.

The effective stiffness of different types of 3D textile composites were calculated and compared. The results suggest that the effective stiffnesses of 3D textile composites along the circumferential direction are similar with that of aluminium, while the density of textile composite is nearly half of the density of aluminium. Therefore, it is expected that the use of textile composites should make the engine more efficient.

Chapter 4 Effective Strength Prediction of Textile Composites at Quasi-Static Stress state

4.1 Introduction

Applications of textile composites in various fields of mechanical engineering require the strength properties of these materials. While standard experiments can be carried out to determine some of them, it is impractical to support the phase of development on selection of materials and determination of key parameter, as there is a vast number of experiments to be conducted. It is therefore essential to have the capability of predicting them theoretically, provided that the predicted values are of a reasonable accuracy. The methodology for predicting the elastic properties based on unit cell modelling, as presented in Chapter 3, is reasonably well established. It is the objective of the present chapter to tackle the effective strengths. Specifically, strength predictions can be affected by the local stress distribution and the stress concentration between the fibre and matrix. The location of stress concentration will vary with the stress states. In other words, textile composites have different failure mechanisms at different stress states. This makes strength prediction of textile composites complicated. Furthermore, the damage of the material at a local material point results in the stress redistribution during the loading process, which makes the strength prediction more challenging.

In this chapter, a multiscale modelling methodology developed for predicting the effective strength of textile composites is presented.

The failure criteria used in this research for predicting localised failure within a unit cell are from open literature. A review of the failure criteria was given in the next section as a part of the development before an acceptable criterion was adopted.

4.2 Review of Failure Criteria

While for homogeneous isotropic materials, the failure criteria, such as von Mises failure criteria and Mohr's failure criterion [95], are well-established, the failure analysis for composite materials is far from straightforward. Many useful theories for prediction the failure of laminates can be found from World-Wide Failure Exercise

(WWFE-I and WWFE-II) [96, 97], some of them will be reviewed in next sub section, in addition to other well-known criteria often cited in the literature.

Generally, the failure criteria for composites can be divided into two groups, the local criteria and the non-local criteria.

It should be pointed out that all phenomenological failure criteria are meant to be applicable to homogenous UD composites in principle. Any extrapolation to materials other than UD composites, such as a laminate as a material, or a textile composite, without appropriate justification represents an abuse of these criteria and should be rejected. The failure criteria reviewed below are all meant to be applicable to UD composites although the objective of the present research is to obtain something applicable to textile composites. Obviously the prediction of the failure of textile composites is no longer possible to be presented analytically in terms of failure functions. Instead, multiscale modelling has to be resorted to in a numerical manner. However, at the lowest length scale, i.e. the yarns of a textile composite which can be treated as a UD composite, an appropriate phenomenological failure criterion can be applicable to facilitate the failure prediction at this length scale. Other approaches, such as element deletion, will be employed at higher length scales in analyses in the corresponding length scale.

4.2.1 Local failure criteria

Local failure criteria predict failure based on the stresses or strains at a material point. In FE analyses, they are applied at each integration point. Once the stress or strain components at the integration point are calculated, the combination of these components as specified by the formulation of a failure criterion is compared with the critical value, typically, 1. The material point is considered to have failed once the value exceeds the critical one.

The difference between these criteria is the formulation of stress or strain combination, or the failure functions. The simplest form of failure criterion is the maximum stress (strain) criterion, which suggests that the material failure occur once the maximum of the ratios the stresses and strains in the material's principal axes to their respective strengths exceeds 1. Since there is only one stress (strain) component involved in the failure function in this criterion, although the failure function is applied to each stress component individually, it is mainly applicable to failure predictions for problems without strong interaction between stress components, i.e. there is only one dominant ratio of the stress and strain in the material's principal axes to its respective strength while all others are insignificant.

Under the general stress states, multiple stress (strain) components can contribute to the failure of the material. The failure mechanisms vary greatly with material properties and the stress state.

In contrast to the maximum stress/strain criterion, the von Mises criterion includes all six stress components [98]. However, it has been developed for predicting the failure (yield) initiation in ductile isotropic materials, hence it is not directly applicable to composites.

Hill [99] modified the von Mises criterion by adding weights to each stress component, to make it applicable for defining yielding initiation conditions in ductile metals with anisotropy. Tsai adapted this criterion to orthotropic composite material [100]. The difference between the strengths along different orientations was reflected by changing the coefficients of stress terms. A limitation of this criterion is that it does not distinguish directly between tensile and compressive strengths.

Azzi and Tsai [101] applied the Tsai-Hill criterion to predict the failure of transversely isotopic material such as UD composites.

Specifically for UD composites, Tsai and Wu developed a criterion [102], employing a quadratic failure function of all stress components. It has the capability to account for the difference between tensile and compressive strengths. This failure criterion is widely applied for strength predictions, although it failed to associate the predicted failure with its failure mode as if the failure mode made no difference to the failure.

Hoffman [103, 104] suggested a modification to the anisotropic yield criterion of Hill [99] through inclusion the linear terms of stresses to the quadratic failure function in order to allow different strengths between tensile and compressive direct stresses.

The Tsai-Wu and Hoffman criteria allow for predicting the strength and failure of composites effectively in some cases. The main drawback of these criteria is that they do not distinguish between different failure modes. Since the composite materials contain two or more constituent materials with very different properties, the stress and strain fields, hence the failure mechanisms within each phase can vary drastically from stress state to stress state.

To distinguish between different modes of failure in a transversely isotropic fibre reinforced UD composite, Christensen [105] suggested a failure criterion based on seven invariants of the stress tensor. For UD composites two failure modes are distinguished, one being matrix dominated, and another being fibre dominated. For the matrix dominated mode, the matrix failure was mainly affected by transverse stresses and shear stresses, while the longitudinal stress was ignored. For the fibre dominated mode, the failure of fibre was caused by longitudinal stress only.

Rotem [106, 107] proposed another failure criterion for UD composites, which also divides the failure of UD composites into fibre failure and matrix failure. However, the matrix failure in Rotem’s failure criteria is controlled by all the stress components.

Hashin [108] developed quadratic failure criteria, which account for four types of failure, namely, fibre tensile and compressive, as well as matrix tensile and compressive failure. In Hashin’s failure criteria, the failure of fibre was mainly caused by longitudinal stress. The matrix failure is controlled by two transverse stresses and three shear stresses, but the formulations for tension and compression are different.

The Hashin failure criteria were also adopted to predict the failure of fibre reinforced polymeric laminae in composite laminates under low energy impact by Batra et al. [109]. For impact analysis they added a lamina crush failure mode. They argued that the lamina crush mode occurs when the compressive stress in the through-thickness direction is larger than a critical value.

Puck and Schürmann [110, 111] proposed failure criteria for the UD composites identify fibre failure and inter-fibre (matrix) failure. According to the criteria formulation, two modes are associated with the fibre failure, the first being a tensile failure, and the second being a compressive "fibre kinking" failure. For inter-fibre failure at in-plane stress states, three different inter-fibre failure modes have been identified, referred to as modes A, B, and C. These inter-fibre failure modes are distinguished by the orientation of the fracture planes. Mode A corresponds to a fracture angle of 0°. The criterion is invoked if the transverse stress in the composites is positive. Mode B failure occurs due to the combined contribution of the transverse compressive stress and a longitudinal shear stress, which is below a fracture resistance. Mode C failure is initialled by a transverse compressive stress and a longitudinal shear stress, which is large enough to cause fracture on an inclined plane parallel to fibre direction.

The failure criteria reviewed above are summarized in Table 4.1.

Table 4.1 Summary of failure criteria

Tsai-Hill [99, 100]

$$F(\sigma_{11}-\sigma_{22})^2+G(\sigma_{22}-\sigma_{33})^2+H(\sigma_{33}-\sigma_{11})^2+2L\sigma_{23}^2+2M\sigma_{13}^2+2N\sigma_{12}^2=1$$

In which, *F*, *G*, *H*, *L*, *M*, *N* are material properties.

Azzi-Tsai [101]

$$\sigma_{11}^2-\sigma_{11}\sigma_{22}+\frac{X^2}{Y^2}\sigma_{22}^2+\frac{X^2}{T^2}\sigma_{12}^2=X^2$$

In which, X is the strength in the fibre direction, Y is the strength in the transverse direction, T is the in-plane shear strength.

Tsai-Wu [102]

$$F_{11}\sigma_{11}^2+F_{22}\sigma_{22}^2+F_{33}\sigma_{33}^2+F_{44}\sigma_{23}^2+F_{55}\sigma_{13}^2+F_{66}\sigma_{12}^2+2F_{12}\sigma_{11}\sigma_{22}+$$
$$2F_{13}\sigma_{11}\sigma_{33}+2F_{23}\sigma_{22}\sigma_{33}+F_1\sigma_{11}+F_2\sigma_{22}+F_3\sigma_{33}=1$$

In which, $\mathrm{F_i}$ are material properties as follows.

$$F_{11}=\frac{1}{S_{Xt}S_{Xc}},\qquad F_{22}=F_{33}=\frac{1}{S_{Yt}S_{Yc}},\qquad F_{44}=\frac{1}{{S_{23}}^2},\qquad F_{55}=F_{66}=\frac{1}{{S_{12}}^2}$$

$$F_{12}=F_{13}=-\frac{1}{2}\sqrt{F_{11}F_{22}},\qquad F_{23}=-\frac{1}{2}\sqrt{F_{22}F_{33}},$$

$$F_1=\frac{1}{S_{Xt}}-\frac{1}{S_{Xc}},\qquad F_2=F_3=\frac{1}{S_{Yt}}-\frac{1}{S_{Yc}}$$

Hoffman [103,104]

$$C_1(\sigma_{11}-\sigma_{22})^2+C_2(\sigma_{22}-\sigma_{33})^2+C_3(\sigma_{33}-\sigma_{11})^2+C_4\sigma_{11}+C_5\sigma_{22}+C_6\sigma_{33}+$$
$$C_7\sigma_{23}^2+C_8\sigma_{13}^2+C_9\sigma_{12}^2=1$$

where the constants C_i, i =1, 9, are nine independent material parameters which can be uniquely determined from six uniaxial tension and compression tests and three shear tests.

Christensen [105]

Matrix dominated mode:

$$\alpha k\sigma_{ij} + \left(\frac{1}{2} + \alpha\right)\left[-\frac{\sigma_{ij}^2}{2} + \sigma_{ij}\sigma_{ij}\right] + \sigma_{1i}\sigma_{1i} \le k^2 \qquad i, j = 2{,}3$$

In which, $\alpha = \frac{1}{2}\left(\frac{S_{Yc}}{S_{Yt}} - 1\right)$, $k = \frac{S_{Yc}}{2}$

Fibre dominated mode:

$$-\alpha k\sigma_{11} + \frac{1}{2}\left(\frac{1}{2} + \alpha\right)\sigma_{11}^2 - \frac{(1+\alpha)^2}{2}\sigma\sigma_{11} \le k^2$$

In which, $\alpha = \frac{1}{2}\left(\frac{S_{Xt}}{S_{Xc}} - 1\right)$, $k = \frac{S_{Xt}}{2}$, $\sigma = \frac{\sigma_{22}+\sigma_{33}}{2}$

Rotem [106, 107]

Fibre failure:

$$\sigma_{11} \ge S_{Xt} \ \ or \ -\sigma_{11} \ge S_{Xc}$$

Matrix failure:

$$\left(\frac{E_m\varepsilon_{ft}}{\pm S_m}\right)^2 + \left(\frac{\sigma_{22}}{\pm S_{Yft}}\right)^2 + \left(\frac{\sigma_{12}}{S_{12}}\right)^2 \ge 1$$

where E_m is the Young's modulus of matrix, ε_{ft} is the tensile failure strain of fibre, S_m is the strength of matrix, S_{Yft} is the transverse tensile strength of fibre.

Hashin [108]

Fibre tensile mode $\sigma_{11} > 0$:

$$f_1 = \left(\frac{\sigma_{11}}{S_{Xt}}\right)^2 + \frac{1}{S_{12}^2}(\sigma_{12}^2 + \sigma_{13}^2) = 1 \ or \ f_1 = \frac{\sigma_{11}}{S_{Xt}} = 1$$

Fibre compressive mode $\sigma_{11} < 0$:

$$f_2 = \frac{|\sigma_{11}|}{S_{Xc}}$$

Matrix tensile mode $\sigma_{22} + \sigma_{33} > 0$:

$$f_3 = \frac{1}{{S_{Yt}}^2}(\sigma_{22} + \sigma_{33})^2 + \frac{1}{S_{23}^2}(\sigma_{23}^2 - \sigma_{22}\sigma_{33}) + \frac{1}{S_{12}^2}(\sigma_{12}^2 + \sigma_{13}^2) = 1$$

Matrix compressive mode $\sigma_{22} + \sigma_{33} < 0$:

$$f_4 = \frac{1}{S_{Yc}}\left[\left(\frac{S_{Yc}}{2S_{23}}\right)^2 - 1\right] + \frac{1}{4S_{23}^2}(\sigma_{22} + \sigma_{33})^2 + \frac{1}{S_{23}^2}(\sigma_{23}^2 - \sigma_{22}\sigma_{33}) + \frac{1}{S_{12}^2}(\sigma_{12}^2 + \sigma_{13}^2) = 1$$

Puck [110,111]

Fibre tensile failure:

$$\frac{1}{\varepsilon_{Xt}}\left(\varepsilon_{11}+\frac{\upsilon_{f12}}{E_{f1}}m_{\sigma f}\sigma_{22}\right)=1$$

Fibre compressive failure:

$$\frac{1}{\varepsilon_{Xc}}\left|\varepsilon_{11}+\frac{\upsilon_{f12}}{E_{f1}}m_{\sigma f}\sigma_{22}\right|=1-(10\gamma_{12})^{1}$$

Inter-fibre failure mode A:

$$\sqrt{\left(\frac{\sigma_{12}}{S_{12}}\right)^2+\left(1-p_{\perp\parallel}^{(+)}\frac{S_{Yt}}{S_{12}}\right)^2\left(\frac{\sigma_{22}}{S_{Yt}}\right)^2}+p_{\perp\parallel}^{(+)}\frac{\sigma_{22}}{S_{12}}=1-\left|\frac{\sigma_{11}}{\sigma_{1D}}\right|$$

Inter-fibre failure mode B:

$$\frac{1}{S_{12}}\left(\sqrt{{\sigma_{12}}^2+\left(p_{\perp\parallel}^{(-)}\sigma_{22}\right)^2}+p_{\perp\parallel}^{(-)}\frac{\sigma_{22}}{S_{12}}\right)=1-\left|\frac{\sigma_{11}}{\sigma_{1D}}\right|$$

Inter-fibre failure mode C:

$$\frac{1}{2\left(1+p_{\perp\perp}^{(-)}\right)}\left(\left(\frac{\sigma_{12}}{S_{12}}\right)^2+\left(\frac{\sigma_{22}}{R_{\perp\perp}^{A}}\right)^2\right)\frac{R_{\perp\perp}^{A}}{-\sigma_{22}}=1-\left|\frac{\sigma_{11}}{\sigma_{1D}}\right|$$

In which, ε_{11} and γ_{12} are the longitudinal uniaxial strain and longitudinal shear strain, $\varepsilon_{Xt}$and ε_{Xc} are the longitudinal tensile and compressive failure strain, υ_{f12} is longitudinal Poisson's ratio of the fibre, E_{f1} is longitudinal tensile modulus of the fibre, $m_{\sigma f}$ intended to capture the differences in the transverse stresses in the fibre and matrix, $p_{\perp\parallel}^{(+)}$, $p_{\perp\perp}^{(-)}$ and $p_{\perp\parallel}^{(-)}$ are the slopes of the $(\sigma_{22},\sigma_{12})$ fracture envelope,$R_{\perp\perp}^{A}$ is fracture resistance of the stress action plane against its fracture due to transverse/ transverse shear stressing, σ_{1D} is a "degraded" stress in the composite allowing for pre-fibre failure breakage of individual fibres.

In Table 4.1, σ_{ij} are the stress components expressed in the local material coordinates of the yarn, S_{Xt} (S_{Xc}) the axial tensile (compressive) strength along the longitudinal direction, S_{Yt} (S_{Yc}) the axial tensile (compressive) strength along the transverse direction, S_{12} and $S_{23}$the shear strengths in the longitudinal and transverse planes, respectively.

4.2.2 Non-local failure criteria

The local failure models may result in underestimation of the strength of the composites. For instance, the experiment for plates with an open hole subjected to tensile loading revealed that the maximum stress criterion underestimated the tensile strength [112]. Since composite materials have a complex microstructure, complicated concentrations of the stresses and strains are present. The existence of voids and micro cracks in the composite also leads to stress concentrations. The stress within the composite may locally exceed the strengths at stress concentrations points, such as voids and micro cracks, yet the material would not fail.

To take into account the influence of the stress concentrations (or strain gradients) within the composites, non-local failure criteria based on the mean values determined over a characteristic range were introduced.

The basic idea of this approach is to replace a local variable (e.g. stress, strain, energy release rate) by its mean value average over a characteristic range [113, 114, 115, 116]. The characteristic range can be a length, an area or a volume.

For example, the simple criterion based on the maximum stress $\sigma_{ij} < \sigma_{ij_{max}}$ is replaced by the maximum mean stress calculated over the characteristic volume $\bar{\sigma}_{ij} = \frac{1}{V}\int_V \sigma_{ij} \cdot dV$ and $\bar{\sigma}_{ij} < \sigma_{ij_{max}}$. Any local failure criteria can be applied here, including more complex ones, such as the Hashin [108] failure criteria.

A number of studies employing various kinds of non-local criteria for predicting the strength of composite materials have been reported in the literature.

Chen et al. [117] introduced a ‘characteristic length’ concept to account for the effect of a stress concentration caused by a notch. It was assumed that failure occurs when the stress in the 0° plies in a composite laminate over some distance away from the notch is equal to or greater than the longitudinal ultimate tensile or compressive strength of a unidirectional laminate. They suggested that the value of this ‘characteristic length’ be determined by fitting the predictions against the experimental data.

Hochard et al. [115, 116] proposed a non-local criterion for laminated structures based on woven plies. Three internal damage variables were introduced, being related to the associated thermodynamic force. Instead of applying a failure criterion at a single material point, the mean of the associated force over a characteristic volume was used. The characteristic volume was defined as a cylinder in [115]. Its height was equal to the ply thickness and the diameter was defined as the characteristic length. The value of the characteristic length was regarded as a material property, which is independent to laminate configuration, geometry and stress distribution.

Pyttel et al. [118] presented a non-local failure criterion for laminated glass subjected to an impact. It postulates that a critical energy threshold must be reached over a finite region before failure can occur. The finite region is a circle on the point of first impact.

Instead of using mean average, some non-local criteria adopted weighted average. Zhu et al. [119] proposed a micromechanics-based non-local anisotropic failure criterion for brittle materials based on energy release rate. The basic idea implemented consists in replacing the local energy release rate for each micro crack by its weighted average over a representative volume of the material centred at a given point.

It can be concluded that the definitions of the characteristic range can be different from case to case: it can be a length, an area or a volume. It can also be determined by the geometry and stress distribution [113]. In a one-dimensional bar, the characteristic range should be a line segment, the length of which is the characteristic length [113]. In laminate composite model [116], the characteristic range can be defined as a cylinder. For a normal 3D composite model, the characteristic range can be a sphere.

It should be noted that the rational definition for the size of the characteristic range is rarely given by the authors of such studies. Moreover, the shape of the characteristic range is sometimes not specified [114]. Nevertheless, some common conclusions can be made. The characteristic length (size of the characteristic range) is a material property which must be determined by comparing the results of experiments and numerical simulations. Next, the characteristic length is related to the level of material in homogeneity (level of stress concentration). As a compromise, characteristic length can be determined by comparing the FEM results with experimental data. However, experimental data fitting is not an efficient method for determining the characteristic length, as it would vary once the geometric/material parameters are changed.

Apart from the definition of the characteristic length, another challenge of using non-local failure criteria is applying those in finite element modelling. Incorporating non-local criteria into a material model is substantially more complicated than applying a local criterion. Since non-local criteria are based on an average value, the criterion has to be applied at the end of a computational step after every Gauss point is calculated. Hence an average calculation step has to be added after each original incremental calculation step.

When applying FEM for the analysis of composite materials with non-local criteria, the size of the mesh must be smaller than the range in which the mean value is calculated. In particular, Hochard et al. [115] reported that even in the high stress gradient zones around 10 integration points in the characteristic range are required in order to make the mean value stable.

The non-local criteria make it possible to obtain mesh-independent results, even in structures with high stress gradients, which is not the case with most of the conventional methods. When a local criterion is used, the force at failure depends on the size of the element, and it does not converge if the solution is singular. It should be noted that with the local criterion, the results do not match the experimental data whatever the size of element used. An experiment of saw cut plate illustrated the mesh-independent results of non-local criterion [115].

The main challenge of applying non-local criteria is determining the value of the characteristic length. No rational method for calculating the characteristic length for 3D textile composite model could be found in the literature. As a compromise, in the model development as presented here, local criteria were adopted.

4.3 Failure criteria for multiple scales modelling

The strength prediction of textile composites is based on multiple scales modelling process. At a microscale, a UD unit cell model is used to predict the effective properties of yarn. These are assigned to mesoscale unit cell model to predict effective properties of textile composites. In both micro- and mesoscale unit cell models, failure criteria have to be applied to define the damage initiation within the constituent materials. Since unit cell models at different length scales have different damage mechanisms, the failure criteria for micro- and mesoscale unit cell models should also vary.

4.3.1 Failure criteria for microscale unit cell model

For a microscale UD unit cell model, material properties of fibre and matrix were used to predict effective properties of yarn. For the matrix, which can be regarded as an isotropic material, von Mises and maximum stress failure criteria were applied to define the damage initiation conditions. Since the definition of the von Mises failure criterion involves all the stress components, it is suitable for failure predictions under most of the stress states. However, it does not distinguish tensile and compressive failure modes, while for the most resins, the material strengths under tension and compression may be quite different. To cover this limitation of von Mises failure criterion, the maximum stress failure criterion was applied as follows.

$$f = max\left(\frac{\sigma_1}{S_t}, \frac{-\sigma_3}{S_c}\right) \geq 1 \tag{4-1}$$

where σ_1 is the first principal stress, σ_3 is the third principal stress, S_t is tensile strength, S_c is compressive strength.

On the other hand, the fibre can only fail under longitudinal tensile or compressive loading. Therefore, the maximum stress failure criterion as described by the Equation (4-1) was applied to define the damage onset stress within the fibres.

4.3.2 Failure criteria for mesoscale unit cell model

For the mesoscale unit cell model, considering the complicated composite structure and the stress distribution within it, the failure mechanisms are very complex.

On the other hand, the failure in UD fibre reinforced composites is understood reasonably well. Since a yarn within the textile composites has transversely isotropic material properties, it can be treated as a UD composite. Therefore, any failure criteria suitable for UD composites can be applied to the yarns within the textile composite, such as Tsai-Wu failure criterion [102, 120, 121], or Hashin failure criteria [108].

Since the Tsai-Wu criterion does not distinguish between the different failure modes, the Hashin failure criteria were considered to be more applicable for predicting failure within the yarns. The elements in the mesoscale unit cell models are under a 3D stress state, therefore the full 3D formulation of the criteria was used. The explicit expressions defining the four modes of failure for the Hashin failure criteria are shown in Table 4.1. Damage is initiated when either of the conditions in the equations is satisfied.

The matrix in the mesoscale unit cell model has the same material properties and failure mechanism as the matrix in the microscale unit cell model, therefore the same failure criterion can be applied to define matrix failure in the mesoscale model.

4.3.3 Verification of failure criteria within user material subroutine

The failure criteria for every component were implemented as user-defined material subroutines, UMAT for Abaqus/Standard, and VUMAT for Abaqus/Explicit. In order to verify the failure criteria implementation, the predictions obtained with the UMAT subroutine are compared with those of the Abaqus/Standard in-built models.

To verify the von Mises and maximum stress failure criteria subroutines, a homogeneous unit cell model was created and loaded under the stress combination of σ_3=100 MPa, σ_2=273 MPa, τ_{23}=50 MPa. The von Mises and maximum principal stress distributions were calculated by the UMAT subroutine and compared to those calculated by Abaqus/Standard as part of stress output. The von Mises and maximum principal stress contour plots are shown in Figure 4.1 and Figure 4.2, respectively.

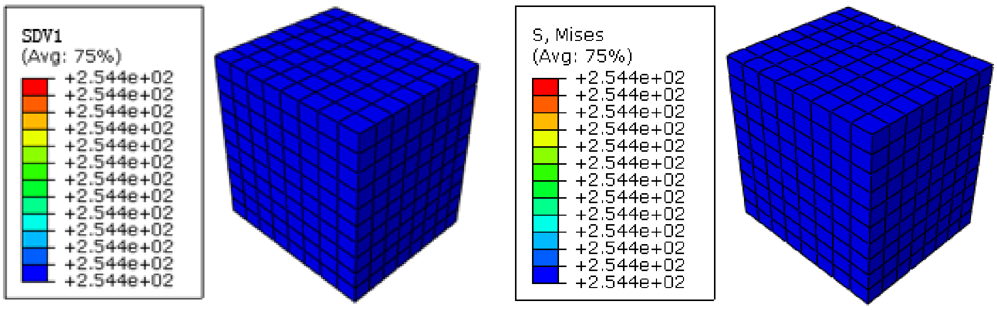

Figure 4.1 Von Mises stress from UMAT (left) and Abaqus/Standard (right)

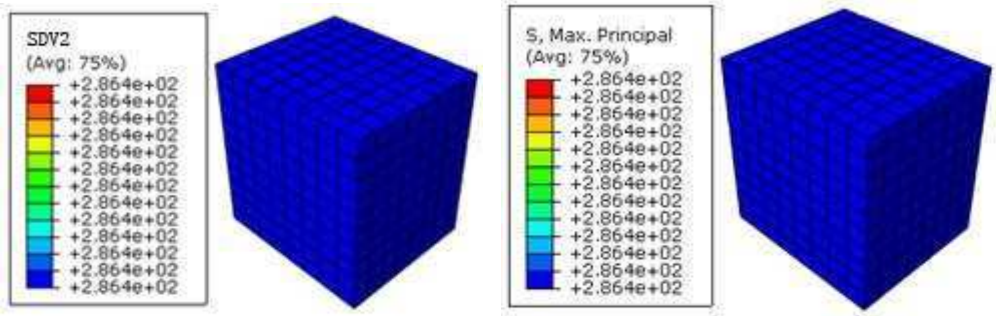

Figure 4.2 Maximum principal stress from UMAT (left) and Abaqus/Standard (right)

In each case, the predictions obtained with the UMAT subroutine are identical to the values calculated by Abaqus/Standard. This verifies the implementation of these two failure criteria as a user defined materials subroutine.

The Hashin failure criteria subroutine predictions were compared against those of the Abaqus in-built model. The formulation of Hashin failure criteria as available in Abaqus/Standard only applies to the plane stress problems, hence a FE model meshed with shell elements was generated in Abaqus/Standard to represent the UD lamina under plane stress. On the other hand, the complete 3D failure criteria formulation was implemented as a user-defined subroutine, hence, in order to make the comparison of predictions meaningful, only in-plane stress loading was applied to the solid element model representing the 3D composite. Both models were assigned the same material properties. The strengths of IM7 carbon fibre [94] were assigned to the FE model.

$$S_{Xt} = 5670 \text{ MPa}, S_{Xc} = 4260 \text{ MPa}, S_{Yt} = 290 \text{ MPa}, S_{Yc} = 215 \text{ MPa} \qquad (4\text{-}2)$$

The models were consecutively loaded in tension and compression in longitudinal and transverse material directions. For each loading case, the stresses predicted by both models were compared, along with the failure indicators, which should assume a value of unity once the failure criterion is satisfied. Legends of contour plot for stresses and failure indicator at tensile loading in longitudinal direction are shown in Figure 4.3. For both models, once the tensile stress reached a critical value 5670 MPa, the failure indicators assumed the value of unity. The same agreement between predictions of two models has been achieved by comparing stresses and failure indicator values in three remaining loading cases (longitudinal compression, transverse tension and transverse compression), from which it can be concluded that the two formulations are equivalent.

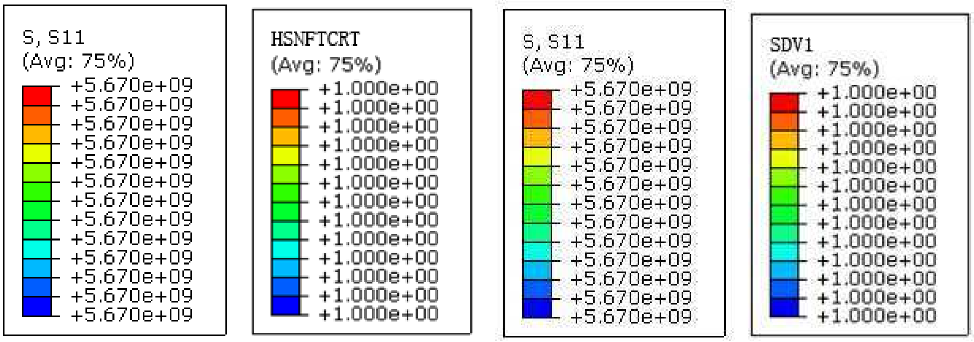

(a) Abaqus/Standard model (b) User-defined subroutine

Figure 4.3 Stress distribution and failure indicator for tensile loading in fibre direction

4.4 Damage Evolution Modelling

Once the failure in the yarns is initiated, the material still retains some of its residual stiffness before ultimate failure occurs. Therefore, a damage evolution law is needed to estimate the value of the residual stiffness. The approach to modelling damage evolution was developed based on the damage evolution law proposed by Matzenmiller et al. [122], and the stiffness degradation can be represented as follows.

$$E = E_0 \cdot (1 - \omega)$$
$$\omega = 1 - exp\left[\frac{1 - f^m}{m}\right] \tag{4-3}$$

where E and E_0 are the residual and original tangent modulus, respectively, $\omega$is the damage variable, f is the mode-related failure variable, and m is a material constant. The rate and tendency of stiffness degradation is controlled by m. The stiffness degradation methods with different m value are shown in Figure 4.4.

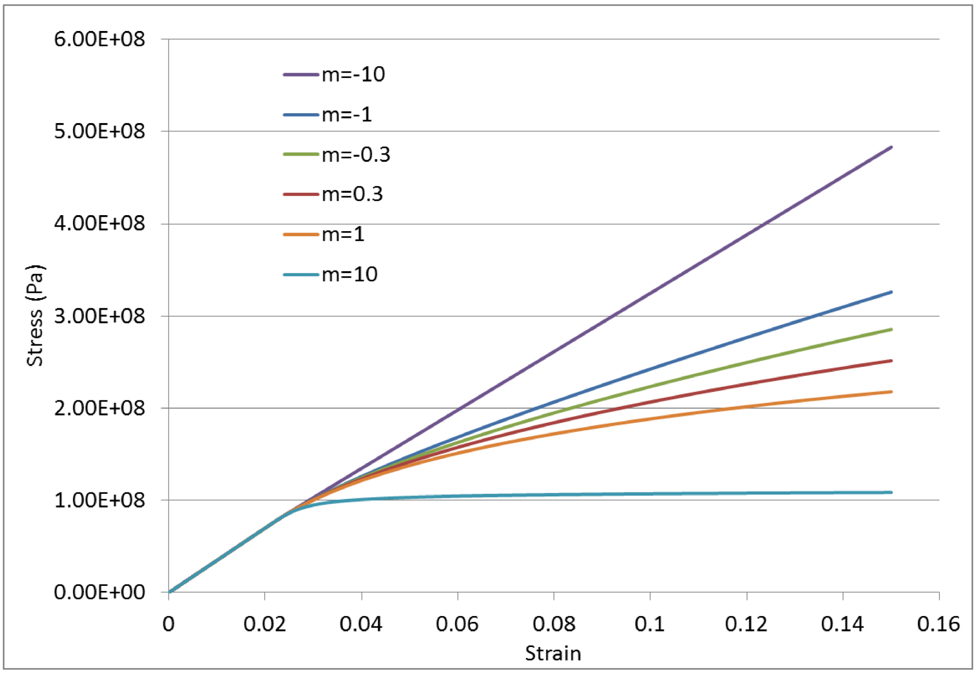

Figure 4.4 Effect of damage evolution parameter *m* on stiffness degradation

For matrix, because it has isotropic material properties, only one stiffness parameter is needed to update (E), this damage evolution law can be applied directly, f for matrix can be calculated using Equation (4-1).

The final failure of the matrix is defined in terms of an indicator as follows.

$$fail = \begin{cases} 1 & (\omega \geq 0.95) \\ 0 & else \end{cases} \tag{4-4}$$

For the fibre in the microscale unit cell model, the maximum stress failure criterion in Equation (4-1) is used, therefore there is only one failure variable f. The stiffness degradation of fibre was represented by the same damage variable as follows.

$$\overline{E_i} = E_i^0 \cdot (1-\omega), E_i = E_1, E_2, E_3, G_{12}, G_{13}, G_{23}$$
$$\omega = 1 - exp\left[\frac{1-f^m}{m}\right] \tag{4-5}$$

The final failure of fibre is also defined by the indicator of Equation (4-4).

For yarn within mesoscale unit cell model, since the stiffness degradation mechanism in the yarns is more complicated and depends on the failure mode, an updated damage evolution law was developed. Instead of calculating damage variables directly, the failure variables $Q_i$were calculated first.

$$Q_i = 1 - exp\left[\frac{1-{f_i}^m}{m}\right], (i = 1, 2, 3, 4), f_i \geq 1 \tag{4-6}$$

Using the failure variables $f_1 - f_4$ calculated from the Hashin failure criteria described in Table 4.1, damage variables related to different failure modes can be obtained as follows.

$$\omega_1 = max(Q_1, Q_2)$$
$$\omega_2 = \omega_3 = \omega_6 = max(Q_3, Q_4) \tag{4-7}$$
$$\omega_4 = \omega_5 = max(Q_1, Q_2, Q_3, Q_4)$$

Then the effective stiffness can be updated based on these damage variables using the following relation.

$$\overline{\langle E \rangle} = D \cdot \langle E \rangle \tag{4-8}$$

In which,

$$\langle E \rangle = \{E_1, E_2, E_3, G_{12}, G_{13}, G_{23}\}$$
$$D = \langle (1-\omega_1), (1-\omega_2), (1-\omega_3), (1-\omega_4), (1-\omega_5), (1-\omega_6) \rangle \tag{4-9}$$

The yarn failed only if the fibre within the yarn failed, thus the final failure of yarn is defined by using an indicator as follows.

$$fail = \begin{cases} 1 & (Q_i \geq 0.95, i = 1,2) \\ 0 & else \end{cases} \tag{4-10}$$

In micro- and mesoscale unit cell model, the element will be regarded as utility failed when the indicator $fail$ equal to 1. There are two different ways to represent the final failure of element in Abaqus/Explicit user material subroutine VUMAT and Abaqus/Standard user material subroutine UMAT.

Within Abaqus/Explicit, the failed element is deleted directly by setting the element deletion related state variable to 0.

Since the element deletion option is not available in Abaqus/Standard, stresses of the element are reduced to zero instead of delete the element explicitly. However, reducing stresses to zero in a sudden will cause convergence problem. Therefore, the stresses were reduced to zero step by step as follows.

If $fail = 1, \overline{\sigma_i} = 50\% \cdot \sigma_i\ ,\ i = 1 - 6$ (4-11)

4.5 Effective Strength Prediction Module in UnitCells©

With the failure criteria and stiffness degradation expressions defined and implemented as Abaqus user material subroutines, the effective strengths of textile composites can be predicted. The periodic boundary conditions have been assigned and a single load (tensile, compressive or shear) has been applied to the unit cell model through the ‘reference points’ until the macroscopic strain reached a prescribed value (this value depends on the failure strain of the material). The displacement and reaction force of the ‘reference points’ are used to calculate average stress-strain curves for a complete unit cell model according to the formulation described by Equation (3-16). The effective strength in each particular loading direction was defined as the maximum stress value on the average stress-strain curve calculated for this particular loading case. The gradient of the curve calculated at the first time increment is the effective elastic modulus of the model along this direction. The illustration of a typical stress-strain curve was shown in Figure 4.5.

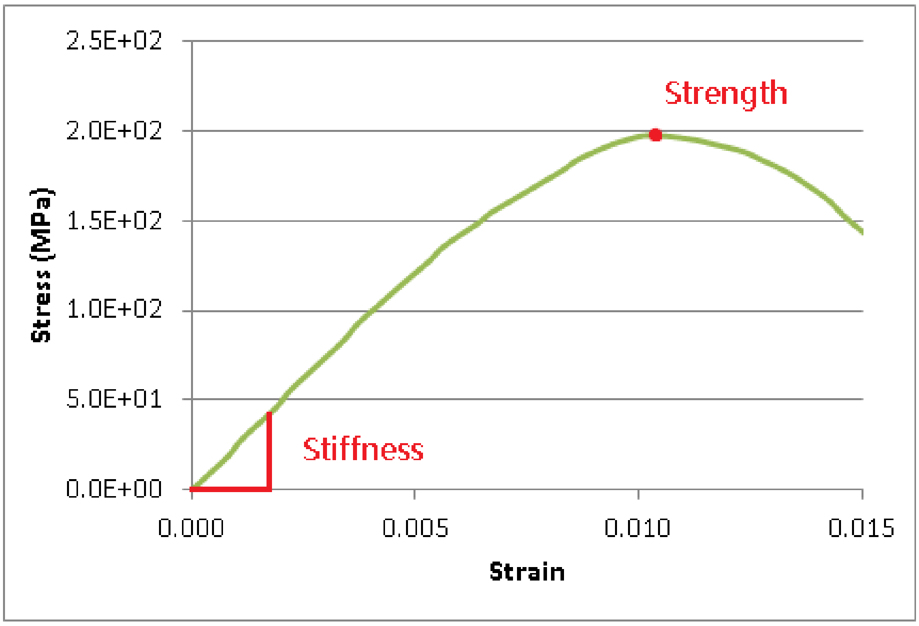

Figure 4.5 Illustration of a stress-strain curve calculated with a unit cell model

Strength predictions with unit cell modelling method are strictly based on the assumption of microscopic homogeneity in damage distribution. In absence of this, e.g. in the late stages of the damage process, the localisation takes place and the approach becomes no longer inapplicable. It is reasonable to expect that the failure prediction obtained should be of a conservative nature.

To process strength prediction analysis automatically, a strength analysis module was integrated in UnitCells©, and it can be activated prior to analysis. The process of strength analysis in UnitCells© is similar to that of stiffness analysis. The user needs to input the model parameters and material properties of the constituents through the input windows. UnitCells© will create a geometry model, generate periodic mesh, assign periodic boundary conditions, assign material properties for constituent components, apply the loads, submit the job and extract effective properties automatically. The difference between stiffness prediction and strength prediction is that for strength prediction the material behaviour of constituents, incorporating damage initiation criteria and damage evolution law proposed in Sections 4.3 and 4.4, are defined via the user material subroutines.

To predict the strength at different stress states, the software automatically generates nine single loading cases (three tensile, three compressive and three shear), which are applied to the unit cell model one by one, and average stress-strain curve for each case is calculated. An example of nine average stress-strain curves for a unit cell model of layer-to-layer interlock 3D woven composites is shown in Figure 4.6. As can be seen, all the stress-strain curves are initially linear, which corresponds to the elastic response of the material. Beyond the linear elastic regime, softening of the stress-strain behaviour occurs, which is associated with the matrix damage. Once the stress reaches a certain point, fibre failure is triggered, following which the stress values reduce rapidly under the applied loading, typically, beyond the maximum point, as observed in stress-strain curves obtained under both tension and compression in Y-direction, which is due to the failure of the warp yarn.

The calculation results suggest that the effective stiffnesses and strengths of the model are different along the different directions. This should be expected for the layer-to-layer interlock 3D woven composites, which has orthotropic effective properties. At the same time, the peak of stress-strain curve for shear in the XZ plane much higher than the other two types of shear loading. This result is also reasonable, because the crimped warp yarn improves the material resistance to shear in XZ plane.

After loading and generating nine stress-strain curves, UnitCells© extracts the effective stiffnesses and strengths from these curves and records them to a report file automatically.

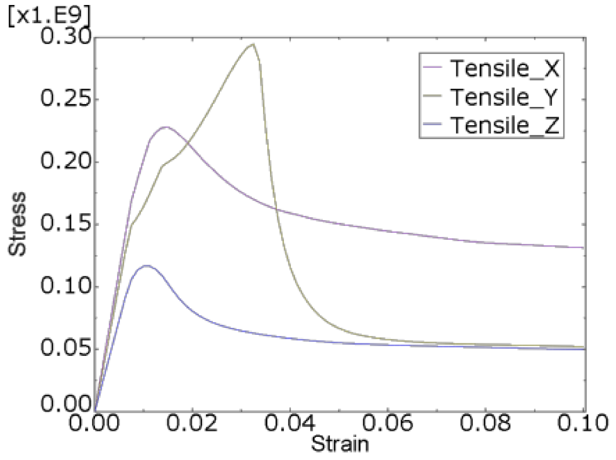

(a) Stress-strain curves of tensile loading

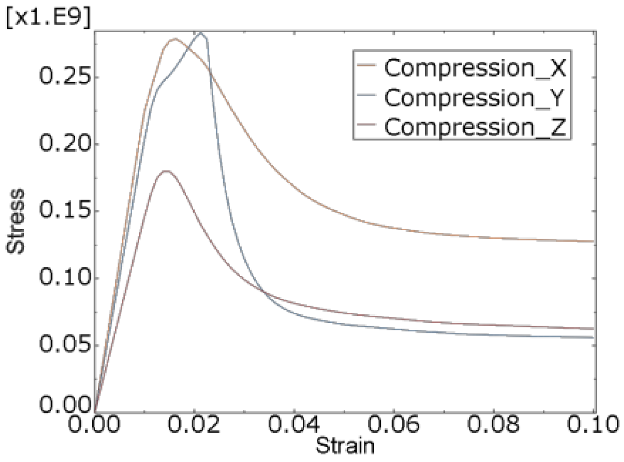

(b) Stress-strain curves of compressive loading

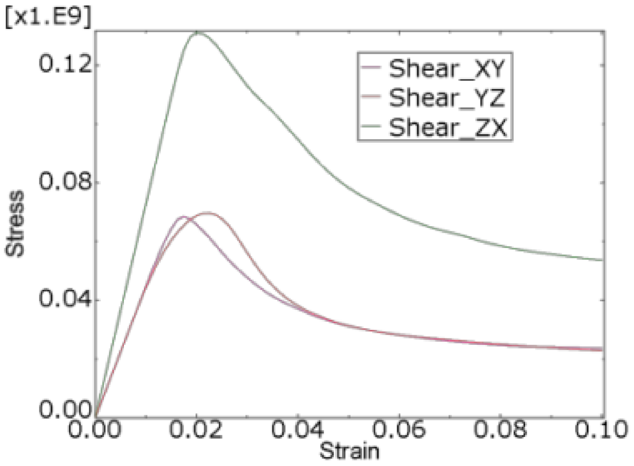

(c) Stress-strain curves of shear loading

Figure 4.6 Nine average stress-strain curves calculated with a unit cell model

4.6 Effective Strength of 3D Textile Composites

The strength prediction module of UnitCells© has been applied to predict the effective strengths of three types of 3D woven composites and two types of 3D braided composites, for which the elastic analysis can been carried out in Chapter 3 (see Figure 3.28 and Figure 3.32). For effective strength prediction analysis, elastic properties input has been kept the same (Table 3.6), and it was supplemented with strength properties of the constituents as specified in Table 4.2.

Table 4.2 Strength properties of PRIME™ 20LV epoxy resin and IM7 CF

	Resin (PRIME™ 20LV) [93]	Fibre (IM7) [94]
S_t (MPa)	73.0	5600
S_c (MPa)	120.0	3500
m	0.3	0.3

The first step of the analysis involved definition of the effective stiffnesses and strengths of the yarns based on UD unit cell modelling. The average stress-strain curves of the UD unit cell model calculated for nine uniaxial loading cases are shown in Figure 4.7.

The calculation was based on a hexagonal unit cell, which is transversely isotropic within the elastic range. Beyond that range, the stress-strain curves along the Y- and Z-directions may no longer be identical. The average value along these two directions was used to represent the properties in the transverse direction. The predicted strengths of the yarns are summarised in Table 4.3.

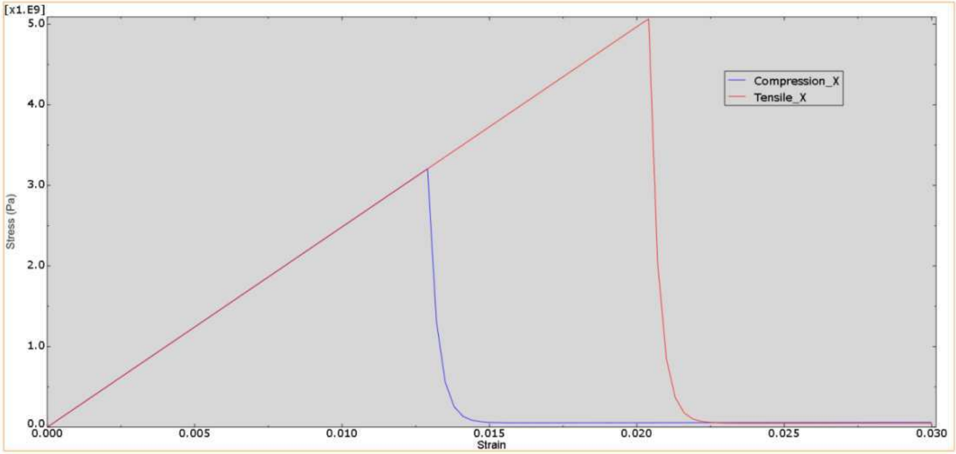

(a) Longitudinal tension and compression

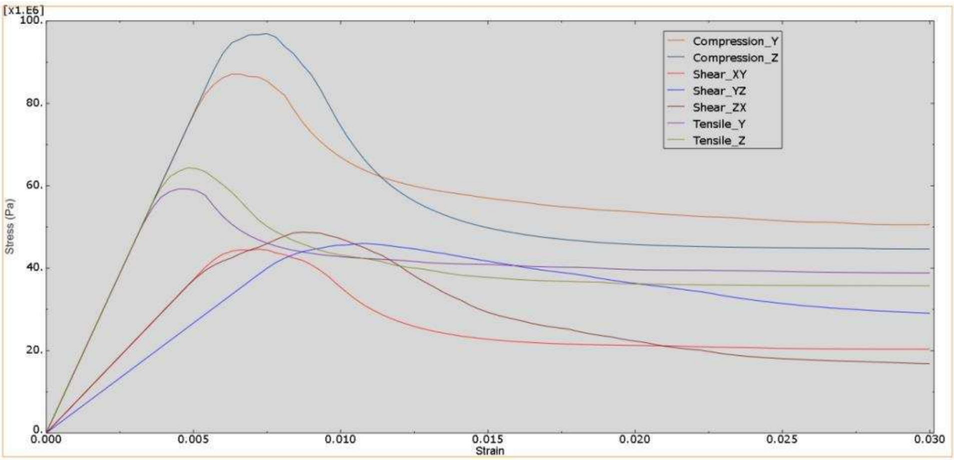

(b) Shear and transverse direction loading

Figure 4.7 Stress-strain curves for calculated for UD unit cell model

Table 4.3 Effective strengths of IM7 CF yarn (V_f=90%)

S_{Xt} (MPa)	S_{Xc} (MPa)	S_{Yt} (MPa)	S_{Yc} (MPa)	S_{xy} (MPa)	S_{yz} (MPa)	m
5090.9	3130.3	68.5	106.0	52.7	52.2	0.3

In the mesoscale unit cell, the constitutive behaviour of the yarns and the matrix was represented by a user defined material subroutine, incorporating the failure criteria and damage evolution law as described in Section 4.3 and Section 4.4. The effective properties of the yarns and matrix were defined as the input properties for the user defined material subroutine.

In this case, the Hashin [108] failure criteria was used to predict damage initiation in yarns and the maximum stress failure criteria was used to predict the damage initiation in the matrix. The damage evolution law extended from Matzenmiller's [122] theory was used to represent the stiffness degradation of both matrix and yarn. If the failure criteria and damage evolution law changes to a different one, the predicted result will be different. The interfaces of strength prediction are similar to the interfaces of stiffness prediction (Figure 3.33) but with two more input panels to define the failure criteria and strength properties for matrix and yarn, which are shown in Figure 4.8**.**

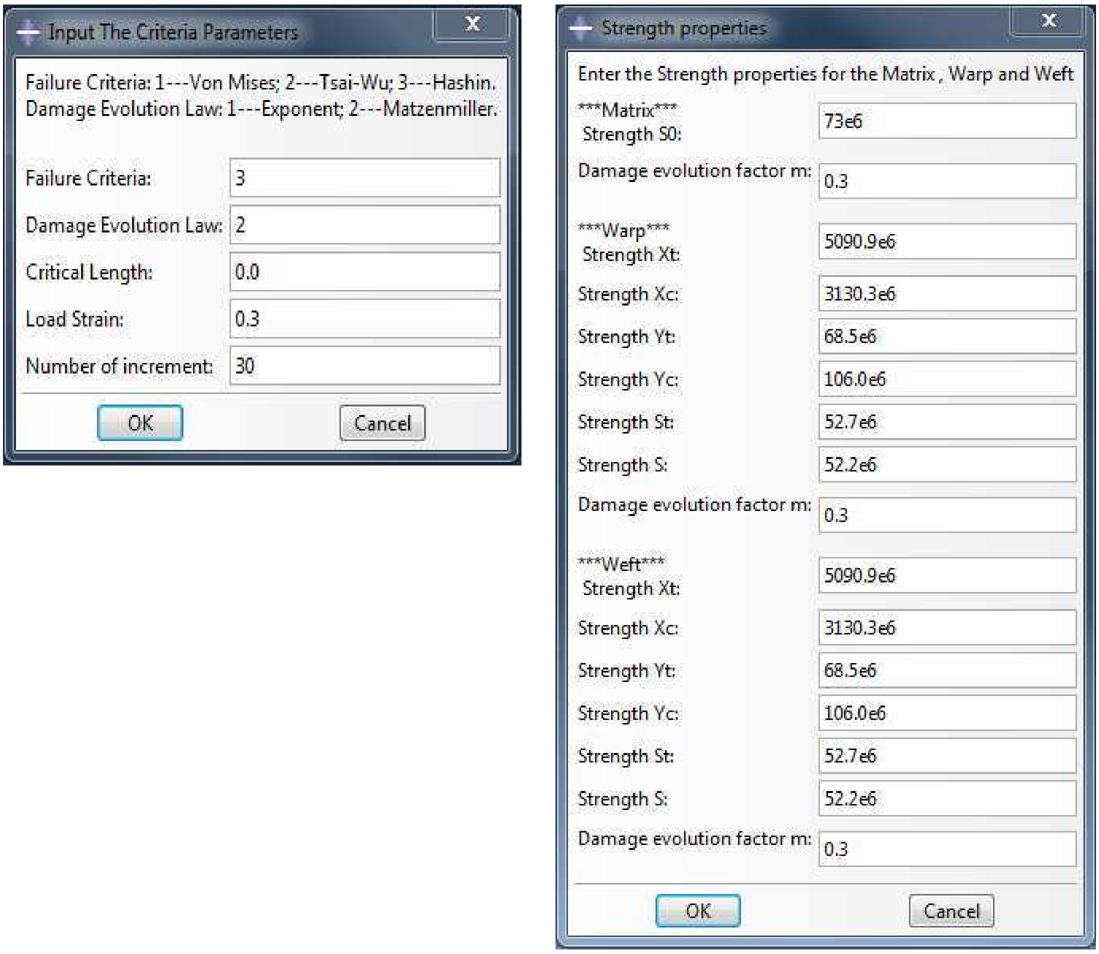

Failure Criteria: 1---Von Mises; 2---Tsai-Wu; 3---Hashin.
Damage Evolution Law: 1---Exponent; 2---Matzenmiller.

Failure Criteria: 3
Damage Evolution Law: 2
Critical Length: 0.0
Load Strain: 0.3
Number of increment: 30

Enter the Strength properties for the Matrix , Warp and Weft

Matrix
Strength S0: 73e6
Damage evolution factor m: 0.3

Warp
Strength Xt: 5090.9e6
Strength Xc: 3130.3e6
Strength Yt: 68.5e6
Strength Yc: 106.0e6
Strength St: 52.7e6
Strength S: 52.2e6
Damage evolution factor m: 0.3

Weft
Strength Xt: 5090.9e6
Strength Xc: 3130.3e6
Strength Yt: 68.5e6
Strength Yc: 106.0e6
Strength St: 52.7e6
Strength S: 52.2e6
Damage evolution factor m: 0.3

(a) Criteria parameters input panel (b) Strength properties input panel

Figure 4.8 Input interface panels for strength analysis in UnitCells©

Nine unidirectional loading cases were simulated for the mesoscale unit cell model, and the calculated stress-strain curves were processed in the same way as the UD unit cell. The predicted strength values are summarised in Table 4.4.

Table 4.4 Strengths predicted for different types of 3D textile composites

Type	Aluminium	Layer-to-layer angle interlock	Layer-to-layer interlock	Orthogonal interlock	4-axial 3D braided	5-axial 3D braided
S_{Xt} (MPa)	350	65.63	433.51	633.59	68.21	61.18
S_{Xc} (MPa)	350	92.40	389.72	571.89	104.77	113.12
S_{Yt} (MPa)	350	1486.30	1486.30	1321.10	68.17	1218.40
S_{Yc} (MPa)	350	1170.40	1166.10	1082.90	104.72	1002.70
S_{Zt} (MPa)	350	87.53	52.10	90.26	910.20	825.16
S_{Zc} (MPa)	350	103.19	109.87	142.25	579.95	562.62
S_{xy} (MPa)	250	37.91	40.35	36.74	42.80	84.02
S_{xz} (MPa)	250	40.95	49.79	38.58	170.16	142.45
S_{yz} (MPa)	250	38.09	35.80	37.55	171.64	173.68

From Table 4.4 it is easy to see that the strength of 3D textile composites along the Y-direction (S_{Yt}) is larger than that of aluminium, except for 4-axial 3D braided composites. The main load in the fan casing during a FBO event is directed along the circumferential direction, which is coincident to the Y-direction of textile composites. This means it is more efficient by using 3D textile composites to replace aluminium in fan blade casing of aircraft engine.

4.7 Summary

This chapter introduced the method of predicting the effective static strength of textile composites under unidirectional loading.

The maximum stress failure criterion was adapted to indicate damage initiation of the matrix and fibre in the microscale unit cell model. The Hashin failure criteria were adopted to represent the start of stiffness degradation of yarns in mesoscale unit cell model.

Damage evolution laws were developed based on Matzenmiller's research to represent the stiffness degradation of matrix, fibre and yarn.

Failure criteria and damage evolution laws were implemented as Abaqus user subroutine and verified by comparing with Abaqus/Standard in-built models. Based on these Abaqus user subroutines, strength prediction module were added to UnitCells© toolbox.

As an application of strength prediction modulus, the effective strength of three types of 3D woven composites and two types of 3D braided composites were calculated using UnitCells© toolbox and compared with aluminium.

Chapter 5 Strain Rate Sensitivity Study of Textile Composites

5.1 Introduction

When considering constitutive behaviour of textile composites under dynamic loading, it is necessary to take into account the strain rate sensitivity of these materials. Even assuming that the fibres and matrix involved in the composite are free from rate sensitivity, the undulations and the interlacing in the textile reinforcement alone can cause the composite to exhibit noticeable effective rate sensitivity [62]. In the modelling framework presented here, mechanical properties of constituent materials are used explicitly, i.e. once rate dependency of a constituent is known, it is assigned to mechanical properties of this constituent at micro- and mesoscale levels.

To determine the rate sensitivity of the yarns within textile composites, a microscale analysis is employed, where a UD unit cell is loaded at eight different strain rates, effective properties are calculated, and rate sensitivity parameters related to moduli and strengths of yarns are extracted. Effective material properties so obtained at the microscale are assigned to the yarns in a mesoscale model, along with the rate-dependent properties of the resin, and same analysis is carried out to quantify the rate-dependency of the material at a mesoscale.

For the carbon fibre reinforced 3D textile composites, some of the published research [123] indicates that the rate-sensitive behaviour exhibited mainly in the resin, whereas the carbon fibre can be treated as a rate-independent. On the other hand, the rate dependency of glass fibres has been confirmed experimentally [124]. If required, it can be incorporated into the models of 3D textile composites by applying the same method as was developed here for the resin. The method of assigning rate dependency to the fibres has been implemented through appropriate material subroutines and made available to users. However, in this chapter, all the analyses presented were carried out under the assumption that the fibre properties are independent of strain rate.

5.2 Mechanical Testing of the Epoxy Resin

To determine the rate sensitivity of the resin, appropriate experiments have been carried out with pure resin samples under compression at quasi-static and high strain rate loading.

The pure resin samples were produced with the PRIME^{TM} [93] epoxy resin system supplied by Gurit [125]. The same resin system was used when manufacturing carbon and glass fibre reinforced textile composite samples, which were mechanically tested to validate the predicted material properties as will be presented in Chapters 7. The PRIME^{TM} 20LV resin and PRIME^{TM} slow hardener [93] were mixed in a weight ratio of 100:26 and degassed before being poured into aluminium tubes with inner diameter of 19mm, as shown Figure 5.1 (a). After being cured in an oven at 65°C for 7 hours, the resin rods as shown in Figure 5.1 (b) were extracted from the tubes, and cut into 20 mm and 8 mm thick disks as the test specimens, respectively for different types of tests.

(a) Aluminium tubes filled with the resin (b) Cured resin samples

Figure 5.1 Preparation of resin samples

Six specimens of 20 mm thickness were tested under quasi-static compression at a strain rate of 0.0004 s^{-1}. The experimental set-up is shown in Figure 5.2. The compressive load was applied by a 50 kN Instron machine. The axial force was measured by the load cell located in the upper cross head. The displacement measurements were taken by two LVDT probes, positioned on either side of the specimen. These devices were interfaced with a PC. The measured force and displacement data were processed to give the compressive behaviour of the resin in terms of stress–strain curves for the quasi-static stress state. The sample was assumed to be a perfect cylinder. To ensure good contact between the upper and the lower surfaces of the sample and the loading platens of the testing machine, the two ends of the sample were polished with a sample polishing machine and 240 grit sand paper. RS® High Temperature Grease was applied on the specimen to reduce the fiction between the sample and the loading platens of the testing machine.

Figure 5.2 Quasi-static compression test experimental setup

The quasi-static experimental stress-strain curves are shown in Figure 5.3. For each test, Young's modulus was determined as the gradient of the linear part of the curve, and the strength was determined as the maximum stress value. Among the tests, Case 1 differs from the rest in terms of the initial phase which might be because of the improper preparation of the specimen, e.g. the loading surfaces were not sufficiently parallel to each other. However, this should not affect the Young's modulus as it was extracted from the part of the stress-strain curve away from the initial phase.

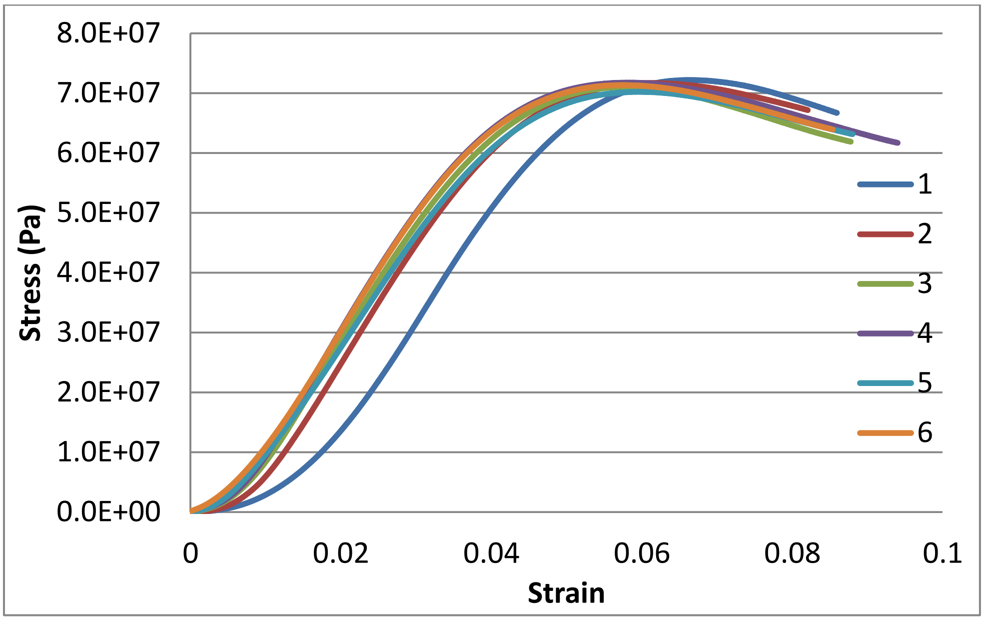

Figure 5.3 Experimental stress-strain curves obtained in quasi-static compression test

The Young's moduli and strengths determined in all six experiments are summarized in Table 5.1. As can be seen from Fig. 5.3 and Table 5.1, the experimental data are consistent, as there is little variation within stiffness and strength values measured in all the tests.

Table 5.1 Young's modulus and strength of the resin determined under quasi-static compression

NO.	1	2	3	4	5	6	Mean	STDEV
E (GPa)	1.928	1.934	1.829	1.767	1.778	1.874	1.852	0.066
S_c (MPa)	72.208	71.706	71.026	71.773	70.243	71.361	71.386	0.688

To investigate the rate-dependent behaviour of the resin at high strain rates, the resin samples were tested with standard Split Hopkinson Pressure Bar (SHPB) set-up [126]. In this case, the 8 mm thick disk specimens were used. The specimens were polished using a sample polishing machine and 240 grit sand paper. RS® High Temperature Grease was applied to reduce the fiction between the specimens and the pressure bars in a similar way as in the quasi-static tests. A photograph of SHPB system used in the tests is shown in Figure 5.4.

Figure 5.4 Photograph of SHPB

A total of sixteen 8 mm thickness samples were tested at strain rates in the range from 763 s^{-1} to 2543 s^{-1}. The measured Young's modulus and strength values are summarised in Table 5.2 along with the quasi-static test data. The procedure of SHPB experiment and the data processing procedures are described in Appendix 1 [127].

Analysing the experimental data, it is easy to see that a relatively low rate dependency of the Young's modulus has been observed. Comparing to the strength measurements, a larger scatter in the Young's modulus measurements arises from the complexity in extracting this quantity from the SHPB test data. On the other hand, compressive strength of the material shows a clearly increasing trend with the strain rate.

Table 5.2 Compressive Young's modulus and strengths of the resin measured at different strain rates

NO.	$\dot{\varepsilon}$ (s^{-1})	E (GPa)	S_c (MPa)
Static	4×10^{-4}	1.85	71.39
1	763	2.15	99.54
2	1046	2.52	142.48
3	1158	2.15	159.38
4	1180	2.90	192.34
5	1326	2.38	181.76
6	1552	2.61	218.92
7	1698	1.84	190.65
8	1843	2.45	219.80
9	1884	2.26	188.96
10	1920	2.28	222.71
11	1990	2.82	230.43
12	2033	2.09	219.11
13	2041	2.65	227.77
14	2451	2.86	210.45
15	2543	2.48	225.11
16	2920	2.79	248.02

5.3 Representation of Strain Rate Sensitivity

To identify an appropriate method for assigning rate sensitivity to the material properties of the resin, a literature review has been carried out as presented in Chapter 2. It was concluded that phenomenological and empirical models are often used for this purpose, where the experimental data are fitting to an appropriate function. For the applications in this project, three such models were considered which suggest logarithmic or exponential dependency of the elastic and strength properties on the strain rate as follows, each involve three material constants to be determined.

Model 1 [72]: $$A_{rt}(\dot{\varepsilon}) = A_0\left[1 + C_A \ln(\frac{\dot{\varepsilon}}{\dot{\varepsilon}_0})\right] \quad (5\text{-}1)$$

Model 2 [71]: $$A_{rt}(\dot{\varepsilon}) = A_0\left[1 + \left(\frac{\dot{\varepsilon}}{C}\right)^{\frac{1}{P}}\right] \quad (5\text{-}2)$$

Model 3 [60]: $$A_{rt}(\dot{\varepsilon}) = a + b\dot{\varepsilon}^{c} \quad (5\text{-}3)$$

where A_{rt} can be the Young's modulus or strength as a function of strain rate, A_0 is the quasi-static value of the appropriate parameter and$\dot{\varepsilon}$the current effective strain rate, $\dot{\varepsilon}_0$ a reference strain rate. Quantities C_A in Equation (5-1), C and P in Equation (5-2) and a, b and c in Equation (5-3) are the parameters of the models, which are determined by fitting the experimental data to the respective expressions.

The Matlab curve fitting toolbox was applied to fit the measured elastic and strength properties of the resin with Equations (5-1)-(5-3). The fitted Young's modulus and strength data are shown in Figure 5.5 (a) and (b), respectively. Two of the models, model 2 and model 3, suggest an exponential strain rate dependence as defined by Equation (5-2) and (5-3), respectively. The expressions are very similar, hence the curves obtained by fitting these two equations to the same set of experimental data are very similar, too.

The accuracy of the fitting obtained with each of the models was assessed by calculating the coefficient of determination, R^2, and Root Mean Square Error (RMSE). The RMSE allows comparing between the accuracy of the fitting for different models. The lower the RMSE, the more accurate the data fitting to the formula. On the other hand, the R^2 provides an absolute measure of the error, where $R^2 = 1$ indicates a perfect fit, while R^2 close to zero suggests a poor fit.

Comparing value of R^2 and RMSE presented in Table 5.3 for the three models, it is easy to see that all the models have a similar accuracy for the Young's modulus while for the strength Models 2 and 3 appear to outperform Model 1, which can be expected as the former ones have more fitting parameters than the last. However, despite providing a better fit within the data range considered, models 2 and 3 suggest an exponential dependency on the strain rate, hence are likely to overestimate the material properties beyond this range, because the exponential growth is rapid. To avoid this, the logarithmic dependence as defined in Equation (5-1) was adopted to represent the rate sensitivity of the Young's modulus and strength of the resin, which is a relatively conservative approach in comparison with the other two.

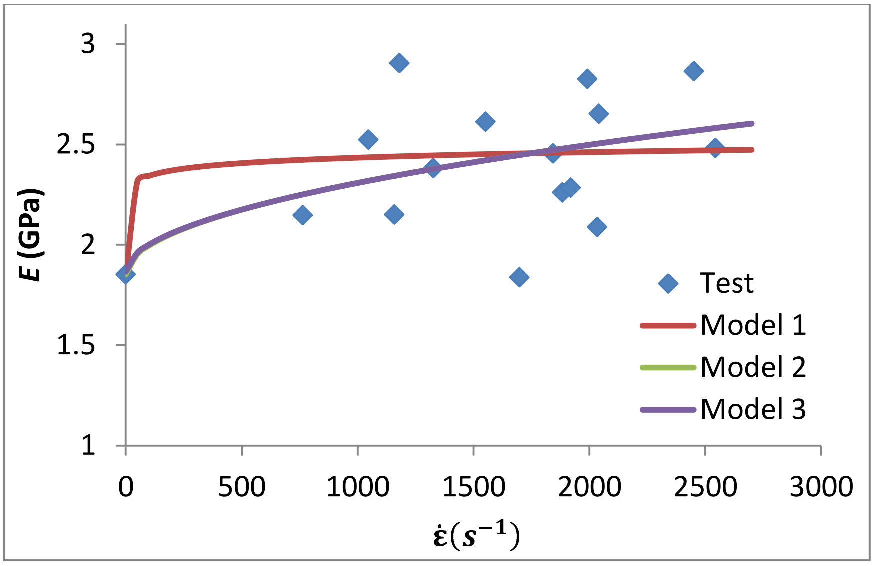

(a) Rate dependency of Young's modulus of the resin

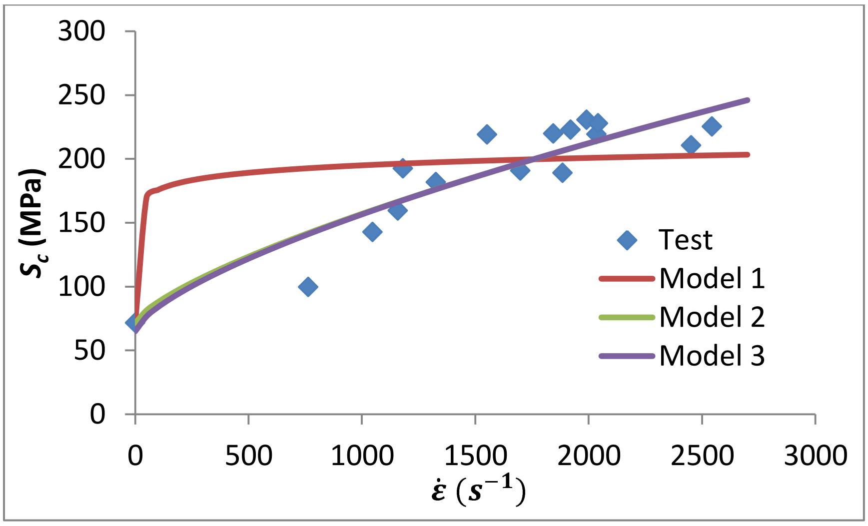

(b) Rate-dependency of the resin compressive strength

Figure 5.5 Curve fitting of rate-dependent material properties of the resin determined from SHPB tests

Table 5.3 Estimated errors in the curve fitting

	For Young's modulus E (GPa)			For compressive strength S_c (MPa)		
	Model 1	Model 2	Model 3	Model 1	Model 2	Model 3
R^2	0.2097	0.2695	0.2696	0.489	0.8426	0.8438
RMSE	0.2974	0.2953	0.3057	34.48	19.77	20.38

Since the quasi-static testing of resin samples was carried out at a strain rate of 0.0004 s^{-1}, this was defined as the value of a quasi-static reference strain rate, $\dot{\varepsilon}_0$. The strain rate scaling constant for Young's modulus and strength, C_E and C_S, respectively, were determined by fitting the experimental data to expression (5-1).

According to equation (5.1) the normalised stiffness/strength is linearly dependent on the logarithm of the normalised strain rate. The scaling constants for stiffness and strength can then be defined as the gradients of the linearly fitted lines as shown in Figure 5.6. The intersections of fitted linear functions with the ordinate axis were set to 1, so that at the reference strain rate the models would be capable of representing the quasi-static properties. For stiffness, the models reproduce the linear trend reasonably well. In terms of approximation of the strength properties, the data trend was not captured very well. The data points which were not represented properly by the fitted straight line were obtained at relatively lower strain rates, at which very limited number of tests were conducted. In the present work, the models developed were to be applied to simulate the impacts cases, which generate strain rates beyond this range. Therefore, this discrepancy was not expected to cause any problem. The fitting can be potentially improved by carrying out testing of the resin samples over a larger range of strain rates. However, at present it might not be possible due to limitations of the experimental equipment.

The values of scaling coefficients C_E and C_S were determined as follows.

$$C_E = 0.0213 \quad \text{and} \quad C_S = 0.1175 \tag{5-4}$$

Since the resin is an isotropic material, the rate dependence needs to be assigned only to a single elastic property, Young's modulus, *E*. Note that Poisson ratio, ν, is considered to be unaffected by the strain rate. The rate dependence of the shear modulus, *G*, can be obtained from the isotropy, i.e. $G=E/2(1+\nu)$. Failure of the resin was defined by the maximum stress failure criterion, hence the rate dependency was also assigned to tensile and compressive strengths, S_t and S_c. The impact response of the resin under the tension and compression was assumed to be the same, hence the same value of the scaling coefficient, C_S, was used to prescribe the rate sensitivity to the tensile and compressive strengths.

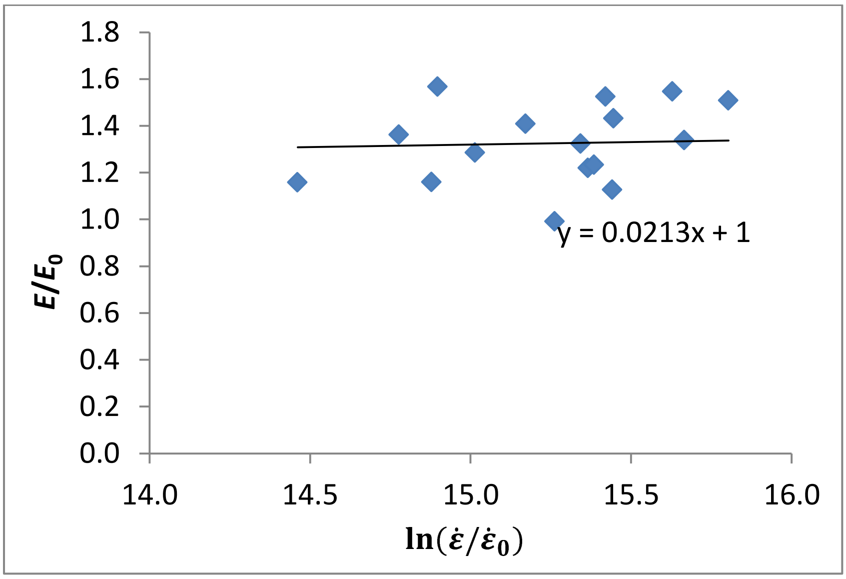

(a) Young's modulus

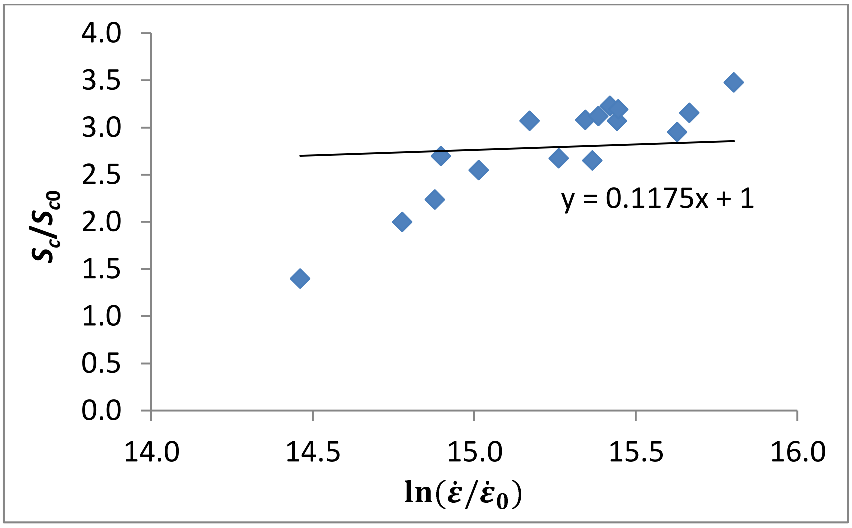

(b) Compressive strength

Figure 5.6 Strain rate sensitivity of epoxy resin

Under the general stress states, the stiffness and strength were scaled with respect to the maximum strain rate.

$$\dot{\varepsilon}_m = \max\{|\dot{\varepsilon}_1|, |\dot{\varepsilon}_2|, |\dot{\varepsilon}_3|, |\dot{\gamma}_{12}|, |\dot{\gamma}_{13}|, |\dot{\gamma}_{23}|\} \tag{5-5}$$

Then, the explicit expressions for Young's modulus and strength as functions of the strain rate become:

$$\begin{gathered} E_{rt}(\dot{\varepsilon}_m) = E_0\left[1 + C_E \ln\left(\frac{\dot{\varepsilon}_m}{\dot{\varepsilon}_0}\right)\right], G_{rt}(\dot{\varepsilon}_m) = \frac{E_{rt}(\dot{\varepsilon}_m)}{2(1+\nu)} \\ S_{rt}(\dot{\varepsilon}_m) = S_0\left[1 + C_S \ln\left(\frac{\dot{\varepsilon}_m}{\dot{\varepsilon}_0}\right)\right] \end{gathered} \tag{5-6}$$

With rate-dependent properties of the resin known, the rate-dependency of 3D textile composites can be predicted by applying FEM at micro- and mesoscales as presented in the subsequent subsections.

5.4 Rate sensitivity study at the microscale

At the microscale, the strain rate-dependent response of the yarns was defined based on the unit cell modelling of UD composites that was described in Chapters 3 and 4. The static analysis was extended by assigning the rate dependency defined by Equations (5-5) and (5-6) to the elastic and strength properties of the matrix and the also the fibre if required. A number of loading cases had been generated, when the unit cell model was loaded at a range of constant strain rates. These could not be defined directly in Abaqus, hence a variable displacement, or variable velocity, was prescribed in each case in order to simulate the loading at a constant strain rate. Given the logarithmic definition of the strain, the explicit expression of the variable velocity is as follows.

$$v = l_0 \dot{\varepsilon}_0 e^{\dot{\varepsilon}_0 t} \tag{5-7}$$

where v is the velocity, t is the time, l_0 is the original length of the unit cell along the loading direction and $\dot{\varepsilon}_0$ is the constant strain rate. It should be noted that, because of the updated Lagrangian strain formulation adopted in Abaqus, constant strain rate cannot be achieved simply by loading the unit cell at a constant velocity. The strain rate curves calculated at a constant and variable velocity are shown in Figure 5.7. As can be seen is Figure 5.7, the variable velocity loading as defined by Equation (5-7) results in a constant average strain rate.

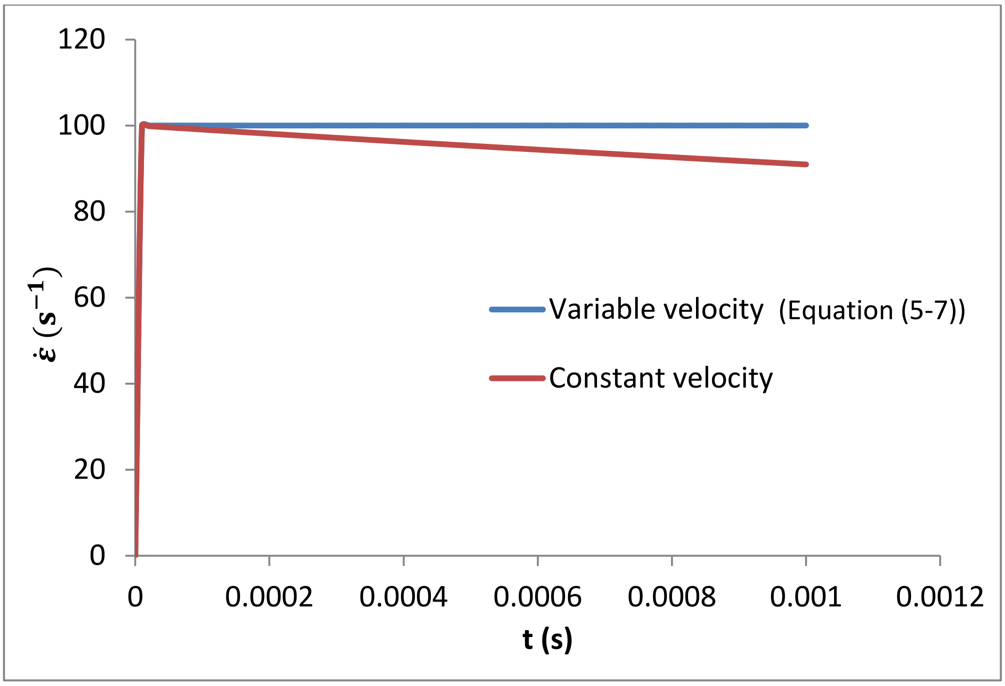

Figure 5.7 Strain rate time history calculated with two different loading methods

The rate dependency expressed in terms of material properties was assigned to the resin via a user-defined subroutine UMAT for the microscale model. The subroutine incorporates a function representing the strain rate effects for both the stiffness and the strength of the resin.

As a sanity check of the subroutine predictions, a homogeneous unit cell model was generated, where the rate-dependent material properties were defined by the user-defined subroutine UMAT for the microscale model. Within this UMAT, the Equation (5-5) and Equation (5-6) were adopted to represent the strain rate sensitivity of stiffness and strength. The static stiffness and strength were assumed to be the same as those for the resin, *E*=1.85 GPa and *S*=71.76 MPa. The values of scaling coefficients for stiffness and strength are given in Equation (5-4).

The model was loaded at a range of strain rates and the average strain and stress was recorded at each increment. The average stress-strain curves calculated at different strain rates are shown in Figure 5.8.

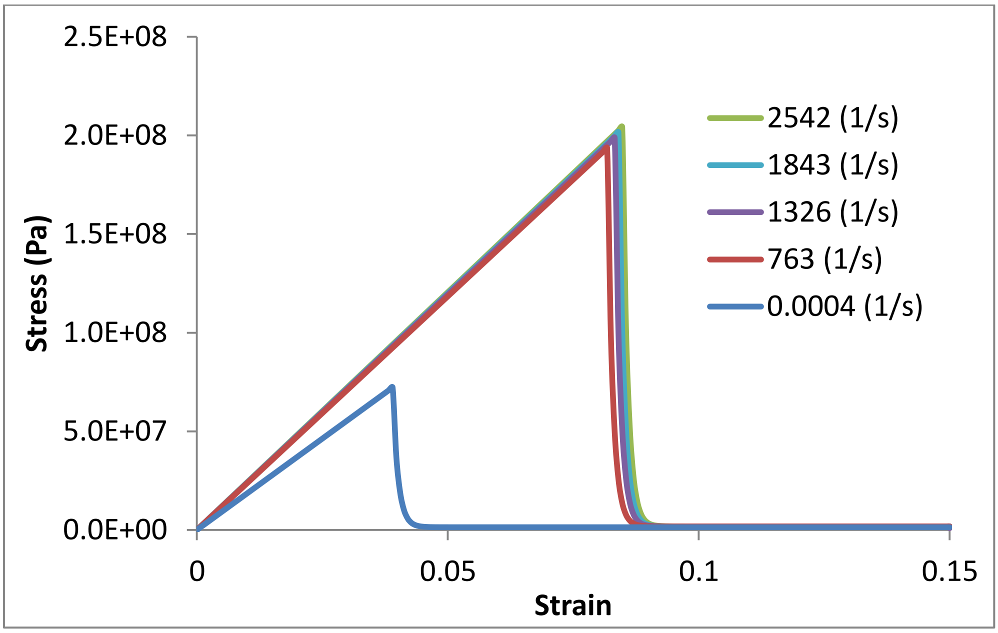

Figure 5.8 Average stress-strain curves calculated at different strain rates assuming the resin properties for both of the constituents in the UC

The values of Young's modulus and strengths extracted from these curves are listed in Table 5.4 along with the values calculated from Equation (5-1).

Table 5.4 Young's modulus and strength of the resin at different strain rates

	$\dot{\varepsilon}$ (s^{-1})	4×10-4	763	1326	1843	2543
E (GPa)	from Equation (5-1)	1.85	2.36	2.38	2.40	2.41
	from UMAT	1.85	2.36	2.38	2.40	2.41
S (MPa)	from Equation (5-1)	71.76	192.69	197.32	200.08	202.78
	from UMAT	71.76	192.69	197.32	200.08	202.78

As can be seen, the properties matched identically, which confirms that the user-defined material subroutine has passed a sanity check in representing the strain rate-dependent material properties.

As a verification case on the rate sensitivity analysis at a microscale, the rate-dependent properties of the T300 carbon fibre yarn have been determined with a UD unit cell model similar to the model shown in Figure 3.5 (a). The fibre volume fraction within the yarn was defined as 78.6%.

The UMAT subroutine for the microscale model was used to represent the material properties of the matrix and T300 carbon fibre. The T300 carbon fibre was defined as a rate-independent material, while the matrix was defined as a strain rate-dependent material. Material properties of matrix and T300 carbon fibre in this analysis are listed in Table 5.5, and the values of scaling coefficients for resin stiffness and strength are given in Equation (5-4).

Table 5.5 Material properties of PRIME^{TM} 20LV epoxy resin and T300 carbon fibre

	Matrix (PRIME^{TM} 20LV)	T300 carbon fibre [82]
ρ (kg/m^3)	1140	1780
E_x (GPa)	3.5	230
E_y (GPa)	3.5	15
ν_{xy}	0.35	0.2
ν_{yz}	0.35	0.0714
G_{xy} (GPa)	1.3	15
S_t (MPa)	73.0	2500
S_c (MPa)	120	2000
m	0.3	0.3

The UD unit cell model was loaded at various strain rates, and the effective stiffness and strength calculated each at strain rate were extracted and listed in Table 5.6. Next, Equation (5-1) was applied to fit each effective property in order to express it as a function of the strain rate. In all the cases, the reference strain rate was defined as $\dot{\varepsilon}_0$ =0.0004 s^{-1}. The calculated strain rate scaling parameters *C* for every stiffness and strength component are listed in Table 5.6 as well.

Table 5.6 Effective properties of UD model at different strain rates (V_f=78.6%)

	Load 1	Load 2	Load 3	Load 4	Load 5	Load 6	Load 7	Load 8	*C*
$\dot{\varepsilon}$ (s^{-1})	4×10^{-4}	4×10^{-3}	4×10^{-2}	4×10^{-1}	4×10^{0}	4×10^{1}	4×10^{2}	4×10^{3}	
E_x (GPa)	181.32	181.36	181.39	181.43	181.46	181.5	181.53	181.56	0.0001
E_y (GPa)	10.67	10.83	10.98	11.12	11.26	11.4	11.52	11.64	0.0058
E_z (GPa)	10.67	10.83	10.98	11.12	11.26	11.4	11.52	11.64	0.0058
G_{xy} (GPa)	6.63	6.79	6.94	7.09	7.23	7.37	7.5	7.62	0.0095
G_{xz} (GPa)	6.63	6.79	6.94	7.09	7.23	7.36	7.5	7.62	0.0095
G_{yz} (GPa)	4.35	4.42	4.49	4.55	4.62	4.68	4.74	4.79	0.0065
S_{Xt} (MPa)	2067.09	2067.48	2067.87	2068.26	2068.65	2069.04	2069.43	2069.81	0.0001
S_{Xc} (MPa)	1631.92	1632.22	1632.53	1632.84	1633.14	1633.45	1633.76	1634.06	0.0001
S_{Yt} (MPa)	70.89	86.64	102.66	119.4	135.56	150.86	168.32	184.38	0.0990
S_{Yc} (MPa)	112.16	137.89	166.41	192.48	217.76	247.41	273.15	301.53	0.1041
S_{Zt} (MPa)	62.46	76.62	92.84	107.51	122.1	136.97	152.1	167.65	0.1041
S_{Zc} (MPa)	99.66	123.44	147.23	170.22	195.97	221.16	245.85	272.44	0.1061
S_{xy} (MPa)	71.08	85.56	101.44	117.78	133.03	148.69	164.74	179.79	0.0949
S_{xz} (MPa)	63.68	77.63	90.49	103.46	117.32	132.32	144.33	159.23	0.0924
S_{yz} (MPa)	50.04	62.16	74.38	86.96	98.88	111.74	124.69	137.49	0.1076

The fitted values for parameter *C* were employed to define the strain rate dependency for each effective stiffness and strength property. Since transverse isotropy from the hexagonal unit cells is present only up to the limit of linear elasticity, the effective strengths along Y- and Z- directions are not identical. However, since the yarn was assumed to be transversely isotropic, the average values of the properties along Y- and Z-direction were used to represent the transverse properties of yarn. The calculated strain rate dependent effective properties of the carbon fibre yarn are summarised in Table 5.7, where the Poisson's ratios are assumed to be independent of strain rate.

Table 5.7 Strain rate-dependent properties of T300 carbon fibre yarn (V_f=78.6%)

	Quasi-static value	Strain rate constant, C
E_x (GPa)	181.32	0.0001
E_y (GPa)	10.67	0.0058
v_{xy}	0.2291	N/A
v_{yz}	0.2285	N/A
G_{xy} (GPa)	6.63	0.0095
S_{Xt} (MPa)	2067.09	0.0001
S_{Xc} (MPa)	1631.92	0.0001
S_{Yt} (MPa)	66.68	0.1016
S_{Yc} (MPa)	105.91	0.1051
S_{xy} (MPa)	67.38	0.0937
S_{yz} (MPa)	50.04	0.1076

From Table 5.7 it is easy to see that the effective properties in the direction transverse to the fibres are more rate-dependent than those in the longitudinal direction along the fibres. This should be expected, since in the longitudinal direction, the properties of the yarn are similar to those of the fibres, which were defined as strain rate-independent, while the transverse properties of the yarns are mainly determined by rate-sensitive material properties of the matrix.

The rate-dependent effective material properties of the yarn as obtained here can now be applied in the mesoscale model to characterize the strain rate-dependent response of 3D textile composites.

5.5 Rate sensitivity study at the mesoscale

In the mesoscale UC models for textile composites, both the yarn and the matrix are modelled as strain rate-dependent materials. Similar to the microscale model, the matrix within the mesoscale model is also defined as an isotropic material, for which the strain rate effect on stiffness and strength is prescribed via the Equations (5-5) and (5-6).

The rate-sensitivity of the effective properties of the yarns was established following the analysis as presented in Section 5.4, where values of the rate scaling parameters were determined for all the properties. Generally, the yarn is transversely isotropic, therefore three stiffness (E_x, E_y, G_{xy}) and six strength parameters ($S_{Xt}, S_{Xc}, S_{Yt}, S_{Yc}, S_{xy}, S_{yz}$) should be defined for it. During the FE analysis at mesoscale, at each integration point within the yarns all six components of strain rate (3 direct and 3 shears) are calculated based on the current strain level and the current simulation time. From these values maximum strain rate values is determined according to Equation (5-5).

At each integration point, the strain rate scaling of the stiffness (longitudinal, transverse and shear) is performed using the same logarithmic dependence on the maximum strain rate, where the values of strain rate scaling constants are different for longitudinal, transverse and shear stiffnesses:

$$\begin{aligned} E_1^{rt}(\dot{\varepsilon}_m) &= E_1^0\left[1 + C_{E_1}\ln\left(\frac{\dot{\varepsilon}_m}{\dot{\varepsilon}_0}\right)\right] \\ E_2^{rt}(\dot{\varepsilon}_m) &= E_2^0\left[1 + C_{E_2}\ln\left(\frac{\dot{\varepsilon}_m}{\dot{\varepsilon}_0}\right)\right] \\ G_{12}^{rt}(\dot{\varepsilon}_m) &= G_{12}^0\left[1 + C_{G_{12}}\ln\left(\frac{\dot{\varepsilon}_m}{\dot{\varepsilon}_0}\right)\right] \end{aligned} \tag{5-8}$$

Similarly, the strain rate scaling of all strength values (longitudinal tensile and compressive, transverse tensile and compressive and longitudinal and transverse shear) is carried out using the same equation but with individual rate related constant:

$$S_i^{rt}(\dot{\varepsilon}_m) = S_i^0\left[1 + C_{s_i}\ln\left(\frac{\dot{\varepsilon}_m}{\dot{\varepsilon}_0}\right)\right], i = 1, \dots .6 \tag{5-9}$$

To demonstrate how the rate-dependent material properties are defined for a mesoscale model, a unit cell model for layer-to-layer interlock 3D woven composite shown in Figure 5.9 was created and the effective stiffnesses and strengths were calculated at different strain rates.

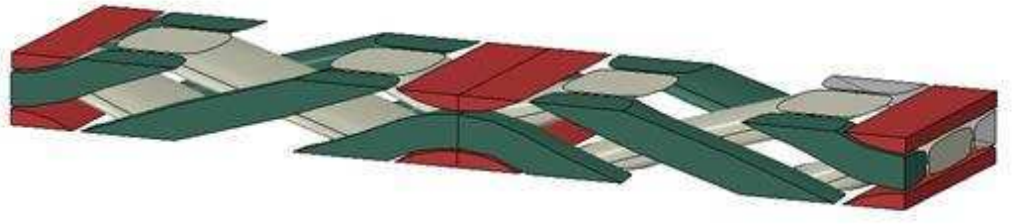

Figure 5.9 Unit cell for layer-to-layer interlock 3D woven composite

The volume fractions of warp and weft yarn were 38% and 28%, respectively. The warp yarn weaving angle was 27.34°. The matrix was assigned the same material properties as were specified in Table 5.5 for the matrix in the microscale model. The material properties of the yarns are determined from the UD composite unit cell model analysis as described in Section 5.5 (Table 5.7).

The load was applied to the model at different strain rates, and the effective stiffness and strength values at each strain rate were calculated. These properties are presented in Table 5.8. Since the layer-to-layer interlock 3D woven composites are orthotropic, the stiffness and strength components obtained under all uniaxial stress states and pure shear stress states are independent. Therefore, for different stiffness and strength components, the strain rate scaling parameters *C*'s can assume different values. The values of these parameters are presented as the rightmost column of Table 5.8

Table 5.8 Effective properties calculated with layer-to-layer interlock 3D woven composite UC model at different strain rates

	Load 1	Load 2	Load 3	Load 4	Load 5	Load 6	Load 7	Load 8	C
$\dot{\varepsilon}$ (s^{-1})	4×10^{-4}	4×10^{-3}	4×10^{-2}	4×10^{-1}	4×10^{0}	4×10^{1}	4×10^{2}	4×10^{3}	
E_x (GPa)	51.19	51.53	51.85	52.17	52.48	52.78	53.08	53.36	0.0027
E_y (GPa)	55.73	55.86	56.00	56.13	56.26	56.39	56.52	56.65	0.0010
E_z (GPa)	8.10	8.31	8.51	8.71	8.91	9.11	9.31	9.50	0.0108
G_{xy} (GPa)	4.26	4.37	4.48	4.59	4.69	4.80	4.91	5.02	0.0118
G_{xz} (GPa)	4.94	5.04	5.15	5.26	5.36	5.46	5.57	5.67	0.0092
G_{yz} (GPa)	3.17	3.26	3.34	3.43	3.52	3.60	3.69	3.77	0.0111
S_{Xt} (MPa)	424.26	506.34	584.31	655.96	717.60	745.96	766.47	778.89	0.0615
S_{Xc} (MPa)	421.79	504.86	586.37	659.97	719.37	751.02	761.49	766.91	0.0619
S_{Yt} (MPa)	719.80	724.18	730.90	748.60	770.55	774.67	777.18	779.10	0.0058
S_{Yc} (MPa)	699.02	712.14	714.01	715.79	717.56	719.29	721.03	722.73	0.0025
S_{Zt} (MPa)	61.56	75.92	91.17	107.46	123.53	137.63	153.23	171.13	0.1087
S_{Zc} (MPa)	118.24	147.57	176.87	207.05	237.39	267.99	299.31	329.58	0.1103
S_{xy} (MPa)	43.86	53.60	63.88	74.43	84.38	94.63	105.10	115.43	0.0888
S_{xz} (MPa)	50.60	61.46	72.16	83.17	94.14	104.91	115.74	126.62	0.0932
S_{yz} (MPa)	38.98	46.78	55.03	62.78	70.88	78.74	86.71	94.98	0.1008

The strain rate-dependent properties of layer-to-layer interlock 3D woven composites can now be applied to generate a macroscale model of a textile composite and perform a structural analysis. The macroscale model development is described in detail in Chapter 6. As a result of the composite material homogenisation at a macroscale, the composite can be represented as a monolithic material, for which a FE model can be generated, with its constitutive behaviour being represented via an appropriate user material subroutine. To verify the capability on that subroutine to accurately predict the rate-dependent material behaviour, a homogeneous unit cell model was generated and loaded along warp (X-) direction at different strain rates.

The calculated average stress-strain curves for each loading case are shown in Figure 5.10.

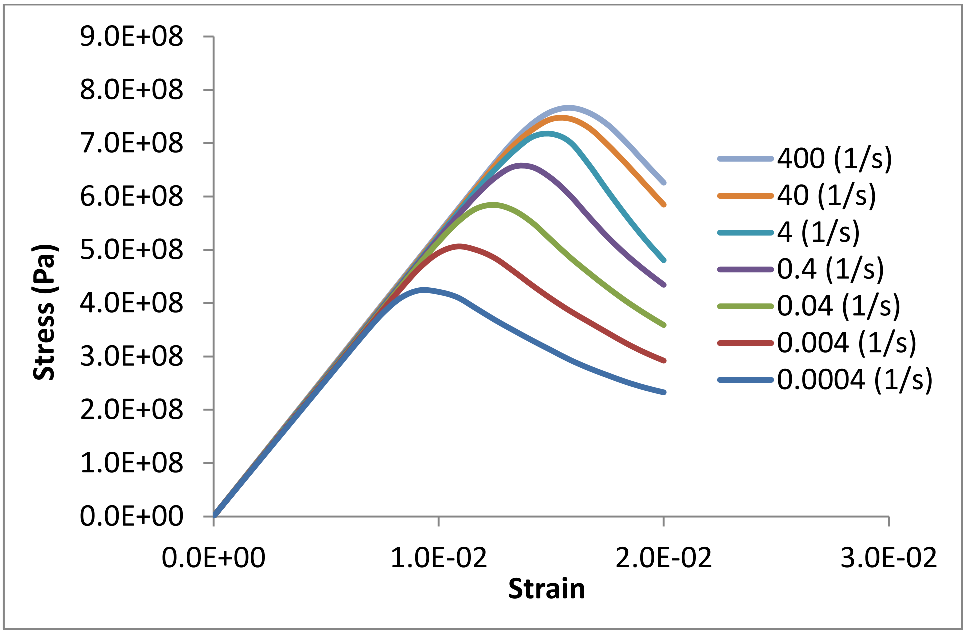

Figure 5.10 Average stress-strain curves for homogenised macroscale model at different strain rates under loading along the warp direction

The effective strength of the homogenised macroscale model (defined as the maximum stress points) from the stress-strain curves in Figure 5.10 agree well with the calculated values of mesoscale unit cell model as specified in Table 5.8. This confirms that the macroscale user material subroutine is capable of representing the strain rate-dependent properties of layer-to-layer interlock 3D woven composites.

5.6 Summary

The multi scale modelling methodology of accounting for the strain rate sensitivity of textile composites has been established and presented in this chapter.

To evaluate the strain rate sensitivity of the matrix, mechanical properties of the epoxy resin were determined experimentally at the quasi-static and high strain rate loading. The experimental data were approximated by a logarithmic model. In this way, the parameters of the model were determined and they are applied to represent the strain rate sensitivity of epoxy resin.

Based on this logarithmic model, the representation of strain rate sensitivity of matrix and yarn were developed and implemented as UMAT user subroutines.

This multi scale modelling methodology was verified through systematic sanity checks and its application to composites has been demonstrated by predicting the strain rate dependent effective properties of T300 carbon fibre reinforced layer-to-layer interlock 3D woven composites.

Chapter 6 Modelling Composites Based on Artificial Neural Networks

6.1 Introduction

Failure of 3D textile composites is an aspect upon what conventional failure criteria have not yet touched. To define a failure envelope for a material of this kind in a multi-dimensional stress space, conventional strength properties as obtained when the material is subjected to uniaxial stresses would be far from sufficient. Conventional strength criteria aim to construct failure envelopes using a minimum set of strength properties. While there have been huge amounts of effort made in this respect with some achievements published in the literature [128], their applicability has been restricted primarily to UD laminae. There is not yet any phenomenological failure criterion, i.e. having the composites treated as monolithic materials, which is directly applicable to 3D textile composites. While waiting for failure criteria suitable for textile composites to become available, an attempt has been made to move forward via a pragmatic approach as presented in this thesis.

In absence of any obvious definition of the minimum set of strength properties for 3D textile composites in general, and simple analytical functions to construct the failure criteria, one would expect that failure under general stress states can be reasonably captured only if a sufficient, usually very large, number of data points for failure could be collected under all possible stress states. Apparently, it is impossible to exhaust all possible combinations of stress states. With an appropriate sampling process, however, one might expect that the space can be reasonably covered with a finite set of data points through a certain interpolation process. The artificial neural network (ANN) systems [129] offer as an ideal methodology for this purpose.

The next question is the generation of sufficient number of data points. For the coverage to be reasonable, a very large number of sampling points will be required, which could easily run into millions, if not more. Experimental means of generating them are simply unthinkable. Numerical testing is the way forward, which needs to be appropriately validated by designated experiments. Mesoscale unit cells (UCs) for 3D textile composites, as presented in Chapter 3 and Chapter 4 offers a practical platform for such numerical testing [73].

In this chapter, a methodology to predict failure of 3D textile composites under general stress states is presented.

6.2 Overview of Artificial Neural Network

Artificial neural network (ANN) [130, 131] is an advanced interpolation method inspired by biological neural networks. ANN is generally presented as a system of interconnected neural elements, which are the basic units of ANN. Each neural element has several inputs and one output. A schematic drawing of the neural element is shown in Figure 6.1.

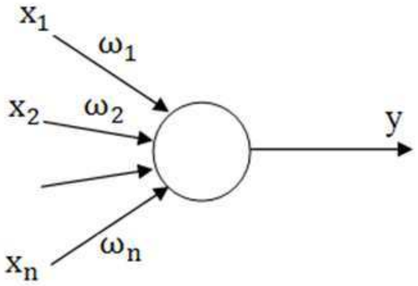

Figure 6.1 A neural element

The relation between inputs and output of a neural element can be defined by a linear or nonlinear function [132] as follows.

$$y = f\left(\sum_{i=1}^{n} \omega_i x_i - \theta\right) \tag{6-1}$$

where x_1,x_2,$\dots x_n$ signify the inputs, y is the output, w_i are the weight coefficients, θ is the threshold and $f(x)$ is the response function, which can be linear or non-linear.

For example, consider relationship between inputs and output as follows.

$$z = \sum_{i=1}^{n} \omega_i x_i - \theta \tag{6-2}$$

Let the response function be defined as a signum function, i.e.

$$sgn(x) = \begin{cases} 1, & x > 0 \\ 0, & x \leq 0 \end{cases} \tag{6-3}$$

Then

$$y = f(z) = \begin{cases} 1, & \sum_{i=1}^{n} \omega_i x_i > \theta \\ 0, & \sum_{i=1}^{n} \omega_i x_i \leq \theta \end{cases} \tag{6-4}$$

A full ANN has numerous neural elements allocated to several layers. Generally, the layers of ANN can be classified into three different types, they are input layer, hidden layer and output layer. An ANN should have one input layer and one output layer. Hidden layers were used to improve the capability of ANN. The number of hidden layers and the number of neural elements in each hidden layers can be determined by trial and error. The connection between the neural elements can vary and therefore there are several types of ANNs [133, 134], which have different architectures and properties. The ANN applied here is a feed-forward artificial neural network (FFANN) [135, 136], which has a simple architecture and provides an acceptable accuracy of predictions. The neural elements in the same layer are independent, while the neural elements in neighbouring layers are connected sequentially. There are no cycles or loops in this neural network. The value of the connected neural elements is transferred through a weight coefficient. The topology of three layers of FFANN is schematically shown in Figure 6.2.

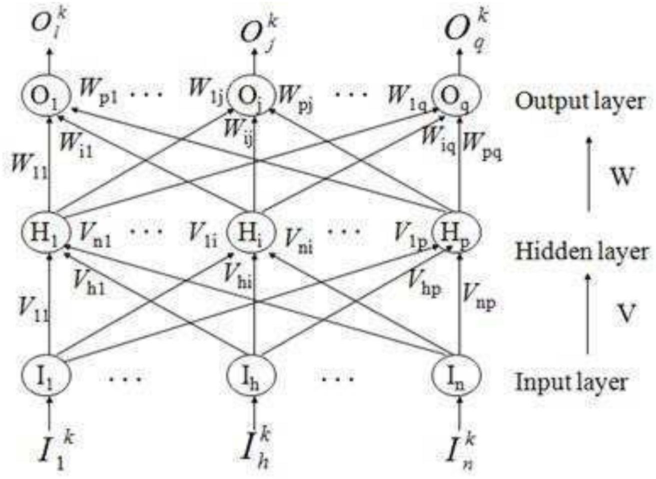

Figure 6.2 Structure of an ANN

The weights and thresholds of ANN can be determined based on a large number of known inputs and corresponding outputs. This process is called training, and a set of known inputs and outputs is called a training case. The training process is a mathematical optimization process, for which various algorithms have been developed [137, 138]. The most widely used one is backpropagation (BP) method [139]. It calculates the gradient of an error function with respects to all the weights in the network. The gradient is fed back to the optimization method to update the weights, in an attempt to minimize the error function. Training process is the most demanding step of ANN development, which can be substantially simplified by employing an ANN toolbox in Matlab. It allows for constructing and training the ANN relatively easily. A user needs to write an appropriate Matlab script to set up the training case and parameters of the ANN toolbox following the format as defined in Matlab, and most of the complicated mathematical manipulations are processed within Matlab automatically [140, 141].

ANNs are widely used in many research fields, such as pattern recognition, control, data processing, function approximation and artificial intelligence [142, 143]. ANNs were also used to predict the mechanical strengths of materials and structures [144, 145].

For polymer composites, ANNs method has shown its capability of predicting certain properties [130, 146]. In particular, the ANN method was applied to predict the fatigue life of glass fibre reinforced UD composites [147] and of carbon/glass fibre reinforced laminate [148]. Some success has been achieved by using ANN to predict the tribological properties of polymer composites [149, 150, 151, 152]. Zhang et al. [153] employed ANN to evaluate the dynamic mechanical properties of polymer composites, such as the storage modulus and damping. Al-Haik et al. [154] applied ANN to investigate the viscoplastic behaviour of composites. ANNs were also used by researchers to conduct the optimization of the manufacturing process [155, 156, 157] and design [158] of polymer composites.

One of the first studies where ANN was employed to define the stress-strain behaviour of composites was that of Pidaparti and Palakal [159]. A back-propagation neural network was developed to predict the stress-strain behaviour of graphite-epoxy laminates. The inputs of this ANN were the fibre angle, the initial stress and the stress increment, while the output was total strain. Reasonable accuracy of prediction was obtained with this ANN.

Labossière and Turkkan [160] applied ANN to predict the failure of composite under plane stress loading conditions. The three in-plane stress components, σ_1, σ_2 and τ_{12}, were treated as the inputs of the ANN and the indicator for the failure was regarded as an output. A failure envelope for a typical fibre-reinforced composite material was obtained using this ANN.

Lee et al. [161] applied an ANN to predict the failure of cross-ply T300 carbon/epoxy composite tubes under combined loading conditions. A failure envelope was plotted based on the ANN and then compared with the Tsai-Wu criterion and experimental results. The failure envelope calculated using ANN showed a better agreement with the experimental results than that obtained with the Tsai-Wu criterion.

ANN has a unique capability of solving problems which have no explicit relations between the inputs and outputs. In textile composites, as in the conventional materials, the failure is related to the strain or stress state of the material. However, there is no explicit expression available to relate the failure to strain or stress states. Therefore, this relationship can be established by applying the ANN methodology.

6.3 Using ANN for Composite Material Characterization

With ANN, the effective constitutive relationships of composites can be predicted which is applicable for any combinations of loading cases. The road map of the method is schematically presented in Figure 6.3, and the procedure is as follows.

Step 1: A large number of stress-strain relationships for the unit cell model are generated by running a Python script in Abaqus. These stress-strain relationships are regarded as the training samples for the ANN.

Step 2: An ANN is created in Matlab. Its parameters are determined from training and the parameter values are recorded in a results file.

Step 3: The structure of the trained ANN is implemented as user-defined material subroutines of Abaqus or LS-Dyna.

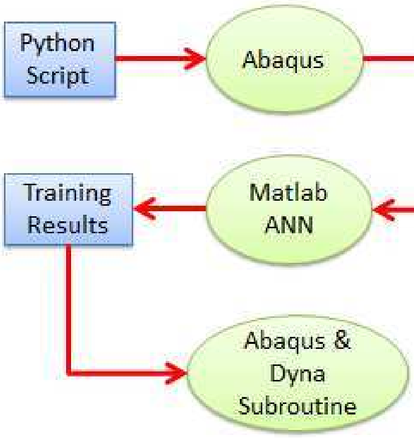

Figure 6.3 Road map of using ANN

This method is suitable for all types of composite materials and can be applied at any length scale. Here, it was primarily developed to represent the constitutive behaviour of 3D textile composites at the macroscale level.

The procedure of applying the ANN method to represent the constitutive behaviour of textile composites is shown in a flowchart form in Figure 6.4. The process is from microscale to macroscale level. At the microscale, the effective properties of the yarns are predicted based on the material properties of matrix and fibre. Then the predicted yarn properties and original matrix property serve as an input for mesoscale unit cell analysis, which is carried out to generate training cases for ANN. With the training cases, the ANN is constructed and trained. The output of the ANN is a database which includes all the parameters of the ANN. The database is accessed by the user material subroutine of Abaqus [91] or LS-Dyna [162] to reconstruct the ANN. In the macroscale model, the textile composite is modelled as a monolithic material with its constitutive behaviour being prescribed via the ANN related user material subroutine.

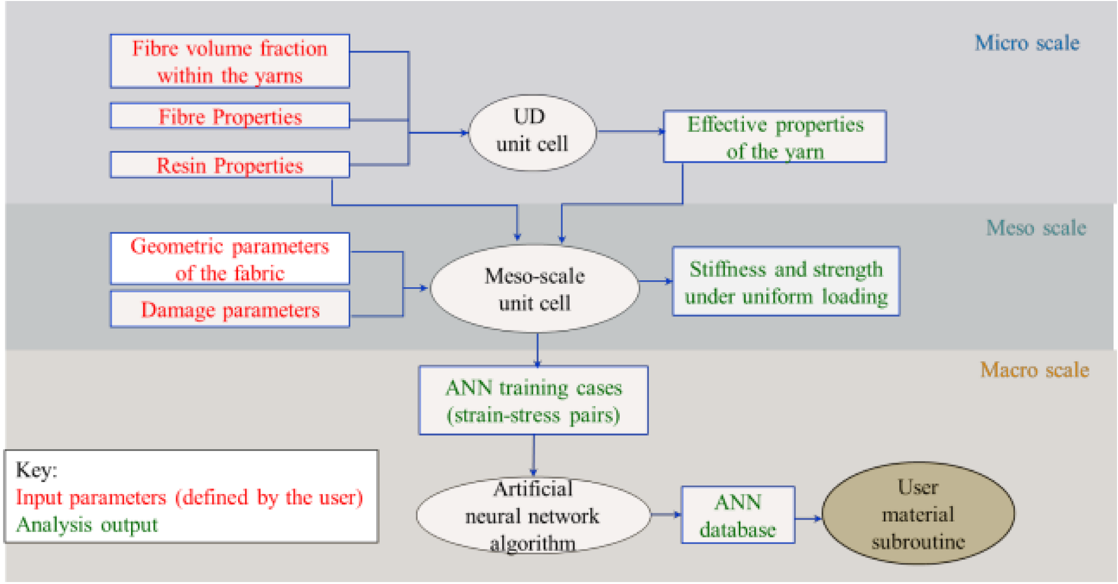

Figure 6.4 Flow chart for using ANN system in textile composites

6.4 Verification of ANN System

To assess the accuracy of ANN predictions and illustrate the capability of ANN, ANNs have been established and applied to the composites at micro-, meso- and macroscale.

6.4.1 Neural network for the UD composites with damage

At the microscale, an ANN was generated to define the material response of the UD composite, where progressive damage of the material is defined based on the damage representation and evolution model developed by Li et al. [163, 164]. For simplicity, properties of the undamaged material as given in Table 6.1 were kept fixed for all the loading cases.

Table 6.1 Virgin material properties for the composite material model accounting for the damage evolution

E_1 (MPa)	E_2 (MPa)	G_{12} (MPa)	G_{23} (MPa)	ν_{12}	ω_0	K
237000	23700	15000	8172	0.29	0	0.4
S_{mt} (MPa)	S_{ms} (MPa)	μ_I	μ_{II}	S_{ft} (MPa)	S_{fc} (MPa)	
300	180	0.0496	0.2	4000	2000	

The inputs of ANN were defined as a combination of six strain components ε_1, ε_2, ε_3, γ_{12}, γ_{13} and γ_{23}. The outputs of ANN are the six stress components σ_1, σ_2, σ_3, τ_{12}, τ_{13} and τ_{23}.

The homogenised UD composite model was loaded at various stress combinations, and the strain and stress components were recorded at every increment. Since the stress in the fibre direction is not subjected to the progressive damage, the loading cases were defined as a combination of five stress components, taking three equally spaced values over desirable ranges as follows.

σ_2: [0.0, 180.0, 360.0]

σ_3: [0.0, 180.0, 360.0]

τ_{12}: [0.0, 125.0, 250.0]

τ_{13}: [0.0, 125.0, 250.0]

τ_{23}: [0.0, 165.0, 330.0]

As an illustration, 242 loading cases were used, with 200 increments defined for each loading case, which results in 48400 pairs of stress-strain combination. Half of these stress-strain combination pairs were used to train the ANN, and half were used to verify the outcomes of the ANN. For more serious applications, more sampling points should be introduced into the ranges as defined above in order to obtain a more faithful representation of the behaviour of the material.

An ANN with two hidden layers was generated in Matlab, and the numbers of neural elements in two hidden layers were 26 and 20, respectively. The illustration of the ANN is shown in Figure 6.5 on Matlab.

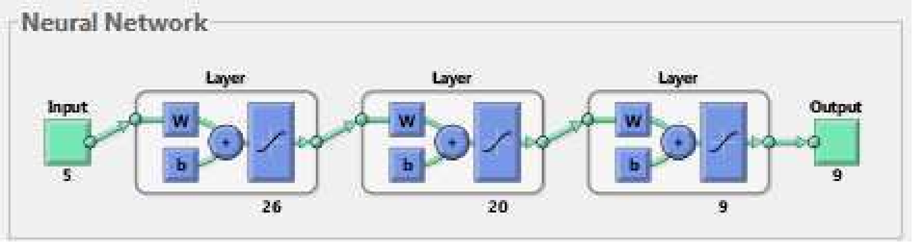

Figure 6.5 Artificial Neural Network for UD composite model

This ANN was trained with the training cases. A screenshot of the progress of the training process is shown in Figure 6.6.

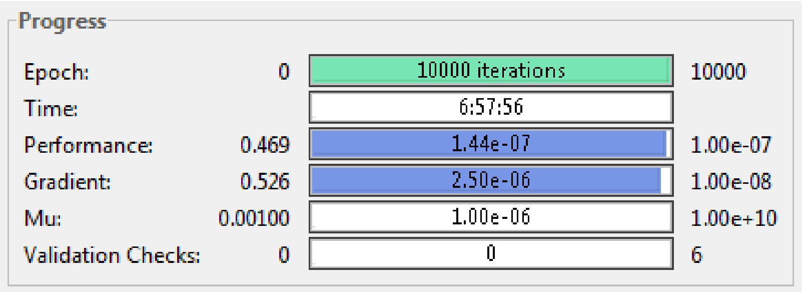

Progress

Epoch:	0	10000 iterations	10000
Time:		6:57:56	
Performance:	0.469	1.44e-07	1.00e-07
Gradient:	0.526	2.50e-06	1.00e-08
Mu:	0.00100	1.00e-06	1.00e+10
Validation Checks:	0	0	6

Figure 6.6 Progress of neural network training

The training output is a dataset of the values of all ANN parameters, which is written into a data file.

In order to verify the trained ANN, it was applied to the testing cases. In Table 6.2, the normalized effective stress components σ_1 and σ_2 calculated with ANN are presented alongside with those calculated directly with the damage model. As can be seen, in most of the cases presented, the error is below 1%, which indicates that the ANN is capable of accurate representation of the damage model.

Table 6.2 Verification of trained ANN for UD composites

Normalised σ_1			Normalised σ_2		
damage model	ANN	error	damage model	ANN	error
0.0657	0.0662	-0.806%	0.0589	0.0594	-0.906%
0.0509	0.0515	-1.223%	0.0404	0.0407	-0.802%
0.0432	0.0433	-0.349%	0.0308	0.0306	0.444%
-0.0261	-0.0260	0.566%	-0.0558	-0.0563	-0.765%
-0.0359	-0.0358	0.393%	-0.0681	-0.0685	-0.691%
-0.0460	-0.0458	0.365%	-0.0806	-0.0811	-0.571%
-0.0563	-0.0561	0.397%	-0.0936	-0.0940	-0.428%
-0.0670	-0.0667	0.432%	-0.1069	-0.1072	-0.291%
-0.0780	-0.0776	0.432%	-0.1206	-0.1208	-0.188%

The trained ANN was implemented as Abaqus UMAT and VUMAT subroutines. The parameters of ANN are automatically transferred to the subroutine through user defined material properties via the Python script, which has been automated on Abaqus/Standard. A segment of the user-defined material properties input for ANN is shown as a screenshot in Figure 6.7.

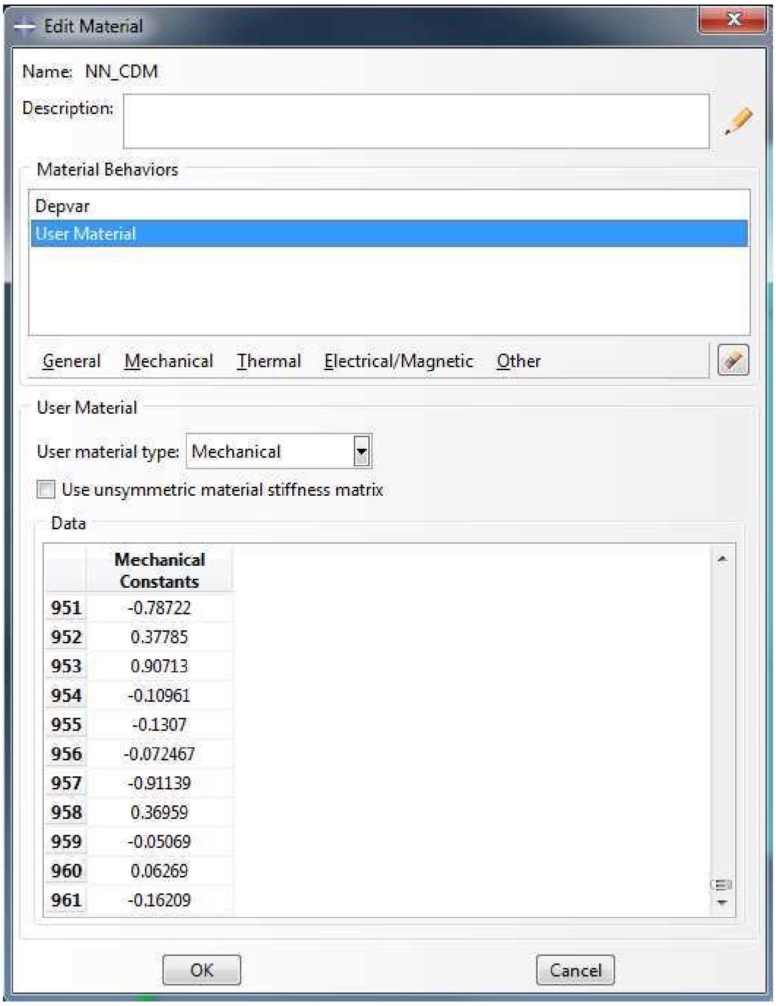

Name: NN_CDM

Description:

Depvar

User Material

User material type: Mechanical

☐ Use unsymmetric material stiffness matrix

	Mechanical Constants
951	-0.78722
952	0.37785
953	0.90713
954	-0.10961
955	-0.1307
956	-0.072467
957	-0.91139
958	0.36959
959	-0.05069
960	0.06269
961	-0.16209

Figure 6.7 ANN database transferred into the user-defined material properties via Python script

In the Abaqus VUMAT subroutine, only the stress components should be updated. Since the input and output of ANN are the strain and stress components, the stress can be updated by calling ANN with current strain directly.

As for Abaqus UMAT subroutine, both stress and the Jacobian matrix (DDSDDE) should be updated. The central difference method was used to calculate the

DDSDDE matrix from current strain and stress through ANN. The step by step description of the process of applying the central difference method to update DDSDDE matrix in Abaqus UMAT is as follows.

Within the user defined material subroutine UMAT, at each increment, the Abaqus solver provides the current value of the stresses and the strains. Denote $\vec{\varepsilon}_0$ and $\vec{\sigma}_0$ as the current strains and the current stresses in their contracted form, respectively, each having six components for a general 3D stress state.

Step 1: An increment was added to the first component of the strain vector as follows.

$$\vec{\varepsilon}_1 = \vec{\varepsilon}_0 + \Delta\varepsilon * \begin{Bmatrix} 1 \\ 0 \\ 0 \\ 0 \\ 0 \\ 0 \end{Bmatrix} \tag{6-5}$$

where $\Delta\varepsilon$ is a strain perturbation specified by a user, the appropriate magnitude of which depends on the sensitivity of the ANN as will be briefly discussion later.

Step 2: The neural network is called to evaluate stresses $\vec{\sigma}_1 = \vec{\sigma}_1(\vec{\varepsilon}_1)$, which are then used to obtain the stress increment $\Delta\vec{\sigma}_1 = \vec{\sigma}_1 - \vec{\sigma}_0$.

Step 3: Repeat step 1 and step 2 with $\vec{\varepsilon}_2 = \vec{\varepsilon}_0 + \Delta\varepsilon * \begin{Bmatrix} 0 \\ 1 \\ 0 \\ 0 \\ 0 \\ 0 \end{Bmatrix}$ to obtain $\Delta\vec{\sigma}_2$. The procedure is repeated to obtain $\Delta\vec{\sigma}_3$, $\Delta\vec{\sigma}_4$, $\Delta\vec{\sigma}_5$ and $\Delta\vec{\sigma}_6$, for which the third, fourth, fifth and sixth component of the strain vector is perturbed respectively by the comment value of $\Delta\varepsilon$ accordingly.

Step 4: The Jacobian matrix or tangential stiffness matrix, $\frac{\partial\Delta\sigma}{\partial\Delta\varepsilon}$, can be approximately expressed as follows.

$$\frac{\partial\Delta\sigma}{\partial\Delta\varepsilon} = \frac{1}{\Delta\varepsilon}[\Delta\vec{\sigma}_1, \Delta\vec{\sigma}_2, \Delta\vec{\sigma}_3, \Delta\vec{\sigma}_4, \Delta\vec{\sigma}_5, \Delta\vec{\sigma}_6] \tag{6-6}$$

The magnitude of $\Delta\varepsilon$ dictates degree of the approximation of the Jacobian obtained in two conflicting way. When expression (6-6) is considered as a finite difference, then the smaller the $\Delta\varepsilon$, the better the approximation to the Jacobian. On the other hand, as $\Delta\varepsilon$ reduces, numerical errors tend to build up and significant accuracy is lost in the evaluation of differences, such as $\Delta\vec{\sigma}_1 = \vec{\sigma}_1 - \vec{\sigma}_0$. After some careful parametric study, a value of 0.0001 for $\Delta\varepsilon$ was found to be able to strike a balance in the application of the ANN in present work.

Uniaxial stress-strain curves along the transverse direction calculated using Abaqus UMAT and VUMAT subroutines based on material model defined by ANN are plotted in Figure 6.8 along with the curve calculated directly with the damage model subroutine.

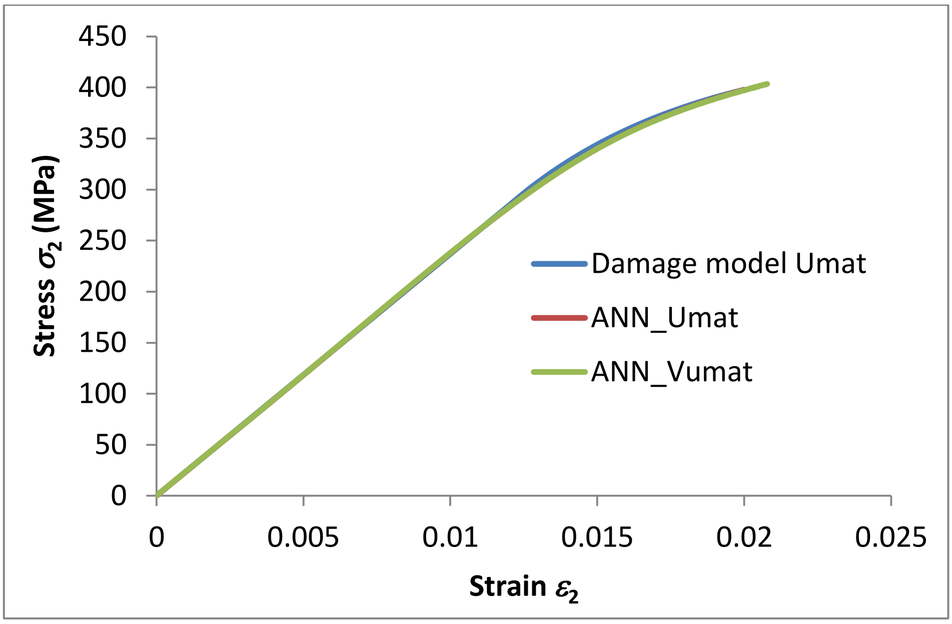

Figure 6.8 Comparison of the stress-strain curves calculated using ANN system and those predicted with the original damage model

In this case, the UD composite unit cell was loaded along the transverse direction. As can be seen, prior to damage initiation (at 300 MPa) the stiffness predictions are identical for all three models, while there is a marginal discrepancy in stress predictions past this point. This indicates a highly accurate prediction as the ANN-based material model.

6.4.2 Neural network for 3D textile composites

At the mesoscale, an ANN for 4-axial 3D braided composites with progressive damage was generated and implemented as Abaqus UMAT and VUMAT subroutines. The unit cell shown in Figure 3.28 (a) was applied to conduct the analysis.

In this example, only six stress components were treated as inputs, while parameters, V_f=60% and braiding angle=27°, as well as the material properties of fibre (Table 3.6) and matrix (Table 4.2), were kept fixed. The fibre volume fraction within the yarn was assumed as 90%. Effective properties of the yarn calculated with UD unit cell model are listed in Table 3.7 and Table 4.3.

The mesoscale unit cell model for 4-axial 3D braided composites that was introduced in Section 4.6 of Chapter 4 was applied to generate the training cases for ANN. As mentioned above, the inputs of the ANN are the six strain components, and the outputs are the stress combinations corresponding to each of those strain combinations. Therefore, a combination of six strain components was applied to mesoscale unit cell model, and the output stress combinations were recorded at each increment. To ensure that ANN is capable of representing the constitutive behaviour of the material over a sufficiently large strain range, the six strains components, ε_1, ε_2, ε_3, γ_{12}, γ_{13}, and γ_{23}, were assigned values from the set [-0.3,0.0, 0.3]. This resulted in total of 728 strain combinations. These 728 load cases were calculated using UnitCells© toolbox, where 30 increments was defined for each loading case. This results in 21840 stress-strain pairs being generated from the unit cell model. Half of them were treated as a training cases and the other half were treated as a testing cases. An ANN with two hidden layer was generated in Matlab and the number of neural elements in two hidden layers were 46 and 38, respectively.

Comparison of the normalized effective stress components σ_2 and τ_{23} in Table 6.3 shows good the agreement between the predictions obtained with trained ANN material model and those obtained directly from the unit cell model. This verifies the applicability of the ANN approach in this case.

Table 6.3 Verification of ANN for 3D braided composite model

Normalised σ_2			Normalised τ_{23}		
UC	ANN	error	UC	ANN	error
-0.0226	-0.0225	0.084%	0.0043	0.0043	0.496%
-0.0162	-0.0162	0.051%	0.0078	0.0078	0.201%
-0.0099	-0.0099	-0.054%	0.0113	0.0113	0.160%
-0.0035	-0.0035	-0.155%	0.0148	0.0148	0.083%
0.0028	0.0028	0.665%	0.0183	0.0183	0.081%
0.0092	0.0092	0.319%	0.0219	0.0218	0.042%
0.0155	0.0155	0.204%	0.0254	0.0254	0.044%
0.0219	0.0219	0.189%	0.0289	0.0289	0.019%
0.0282	0.0282	0.189%	0.0324	0.0324	0.023%
0.0346	0.0345	0.148%	0.0359	0.0359	0.003%

The trained ANN was then implemented as Abaqus UMAT and VUMAT subroutines. These subroutines can now be applied to define the constitutive behaviour of the material at a macroscale. As a verification case, 3D braided composite model was loaded along X-direaction. The average stress-strain curves calculated with UMAT and VUMAT subroutine material models are plotted simultaneously in Figure 6.9 along with the stress-strain curve obtained directly from original unit cell model.

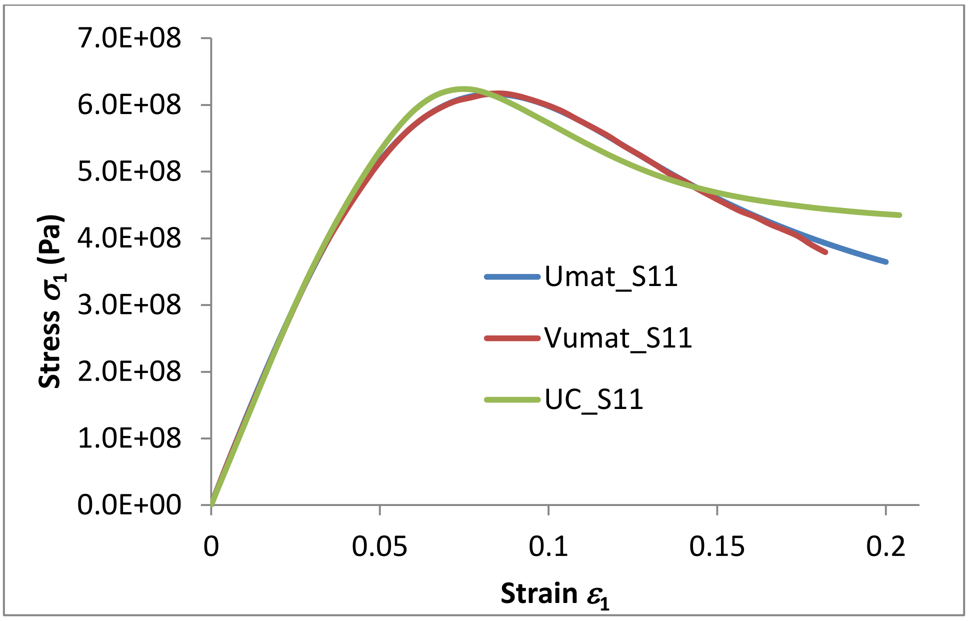

Figure 6.9 Comparison of the stress-strain curves of calculated with ANN and those predicted directly from the UC analysis

Close agreement between the curves verifies the applicability of the ANN approach. The ANN-based model is capable of reflecting the effects of damage initiation and evolution in the mesoscale textile composite model. The accuracy can be improved by introducing more sampling points to the ANN training case within the given range of strains, which was from -0.3 to 0.3 in the present analysis.

The ultimate goal of ANN model is to predict the failure of the textile composites. As was previously explained, the failure is defined here as the initiation of the localised deformation at macroscale which corresponds to the state soon after the tangential stiffness matrix for the unit cell as a representative volume of the material loses its positive definitiveness. In order to achieve this, an appropriate failure criterion is required in the mesoscale modelling. As a conservative measure, a material point is considered to have failed and will be deleted from the mesh when the Jacobian matrix (DDSDDE) at this integration point becomes singular. The tangential stiffness reduces gradually as the damage in the material evolves, and the determinant of tangential stiffness matrix monotonically decreases to zero. As soon as the value of determinant becomes zero, the Jacobian matrix becomes singular and is considered to have lost its positive definitiveness.

This criterion has been implemented within Abaqus UMAT and VUMAT ANN subroutines. Within the VUMAT, an indicator was used to indicate the status of each element. The value of the indicator changes from zero to unity when the element deletion condition was activated. The time histories of average stress and the element deletion indicator are shown in Figure 6.10. As can be seen, stress predicted with UMAT ANN subroutine reduces smoothly after the maximum point, while that calculated with VUMAT ANN subroutine drops to zero because of the use of element deletion. As can be seen from Figure 6.10, the DDSDDE matrix becomes singular and element deletion condition is activated when stress reaches its maximum, which is consistent with the definition of the failure as is used here.

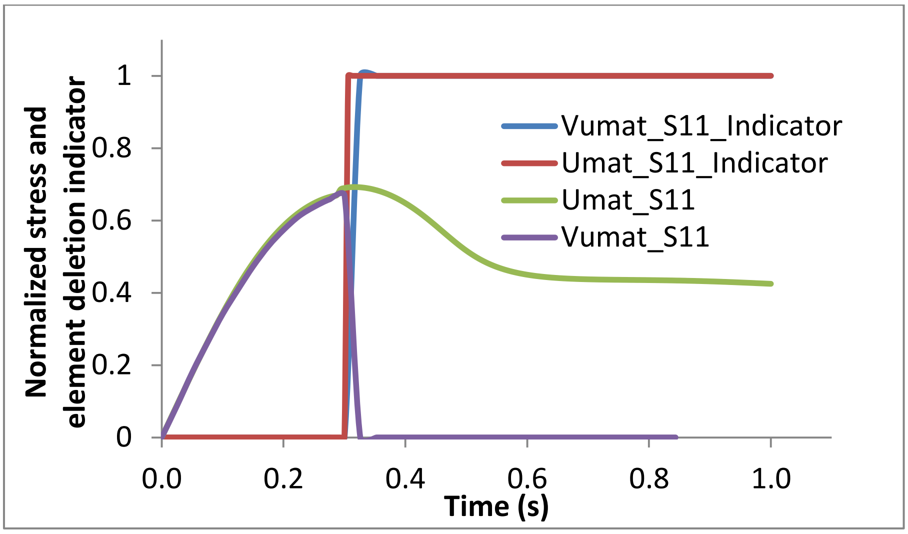

Figure 6.10 Stress and element deletion indicator output calculated with UMAT and VUMAT

With this ANN, the failure envelope for 3D braided composites under different stress combination were predicted and plotted in Figure 6.11 as a verification case for ANN related to this type of textile composites.

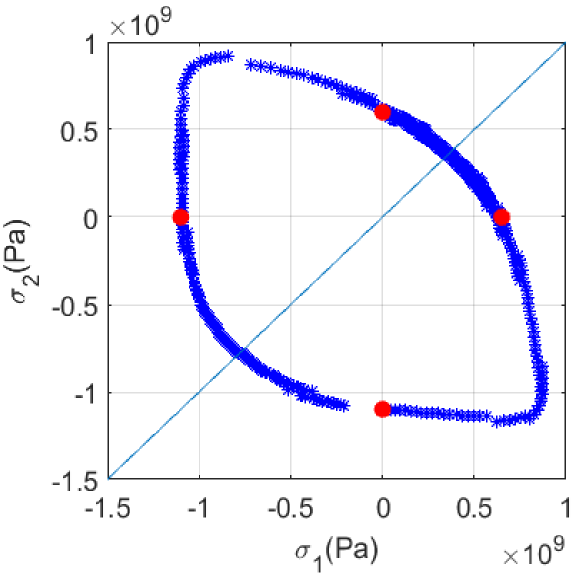

(a) σ_1-σ_2

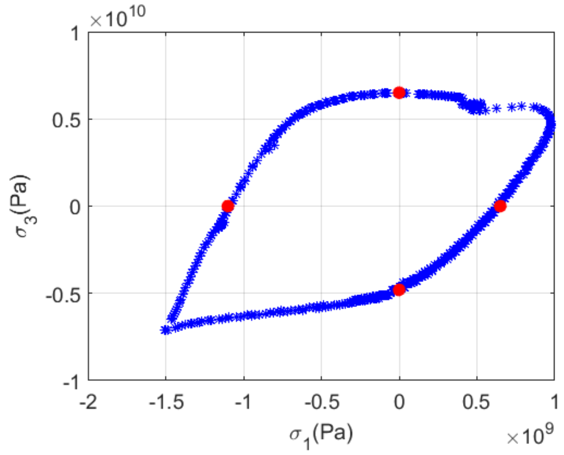

(b) σ_1-σ_3

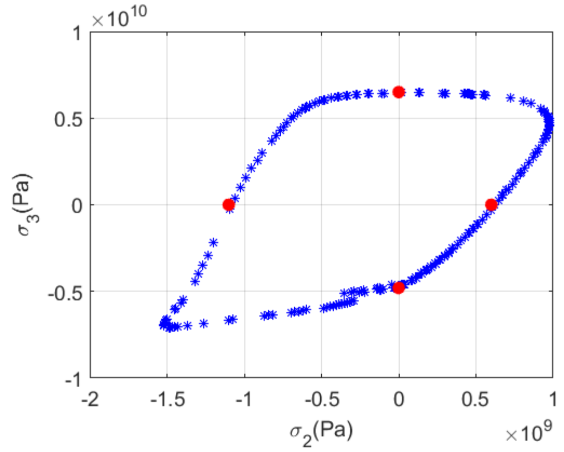

(c) σ_2-σ_3

Figure 6.11 Failure envelopes for 3D braided composites calculated employing ANN systems (Red points are predictions made with the mesoscale unit cell model; blue points were calculated with ANN)

The failure envelopes of σ_1-σ_3 and σ_2-σ_3 should be identical in theory and they are similar enough here as an approximation, since the unit cell model of 3D braided composites is of identical structure in the X and Y directions. Moreover, the failure envelope of σ_1-σ_2 should be symmetric about the axis in 45° direction. The red points in Figure 6.11 are the uniaxial loading strengths calculated from mesoscale unit cell model. These strengths are well captured by the failure envelopes produced based on ANN.

6.4.3 Neural network for the laminate

At the macroscale, the ANN method was applied to conduct the failure analysis for a laminate. In accordance with this methodology, the laminate is treated as a monolithic material, rather than a stack of individual laminae.

In order to verify the model developed, the failure envelopes were constructed and compared with those obtained following a conventional laminate analysis, which is based on classical laminate theory. In this case, failure is assessed by applying the failure criteria to each lamina as a UD composite. A large variety of failure criteria is available [165] for UD composites, among which some of the most commonly used are the Tsai-Wu failure criterion [102], Hashin failure criteria [108] and Chang-Chang failure criteria [166]. It is worth noting that these criteria are only applicable for predicting the failure in UD composites. In absence of appropriate failure criterion for composites of more sophisticated architecture, e.g. textile composites, users might be tempted to extend the criteria for UD composites blindly. An example will be shown below how erroneous it could be if a lamina-based failure criterion is applied to the entire laminate. It results in arbitrary failure predictions, which in some cases can be reasonable by chance, while in other cases would differ substantially from those obtained by applying the failure criteria at the lamina level.

To demonstrate the disparity, the analysis has been carried out for a laminate of [0°/90°/90°/0°] lay-up of four plies of T300 carbon fibre reinforced UD composite (V_f =60%), with the material properties given in Table 6.4. The stress state within each layer was calculated at various stress states based on classical laminate theory. Within each layer, the stress state was checked against the Tsai-Wu failure criterion, which is defined for the 2D stress state as follows.

$$F_1\sigma_1 + F_2\sigma_2 + F_{11}\sigma_1^2 + F_{22}\sigma_2^2 + F_{66}\tau_{12}^2 + 2F_{12}\sigma_1\sigma_2 = 1$$

$$F_1 = \frac{1}{S_{Xt}} - \frac{1}{S_{Xc}}, \quad F_2 = \frac{1}{S_{Yt}} - \frac{1}{S_{Yc}}, \quad F_{11} = \frac{1}{S_{Xt}S_{Xc}} \tag{6-7}$$

$$F_{22} = \frac{1}{S_{Yt}S_{Yc}}, \quad F_{66} = \frac{1}{{S_{xy}}^2}, \quad F_{12} = -\frac{1}{2}\sqrt{F_{11}F_{22}}$$

The failure envelopes for the laminate have been obtained, where strength is defined by the first instance of failure in any lamina of the laminate.

Table 6.4 Material properties of T300 carbon fibre reinforced UD composite with DY063 epoxy matrix (V_f=60%) [82]

E_1 (GPa)	138
E_2 (GPa)	11
ν_{12}	0.28
G_{12} (GPa)	5.5
S_{1t} (MPa)	1500
S_{1c} (MPa)	900
S_{2t} (MPa)	27
S_{2c} (MPa)	200
S_{12} (MPa)	80

The macro strengths calculated with this method were S_{Xt}= 148 MPa; S_{Xc}= 629 MPa; S_{Yt}= 148 MPa; S_{Yc}= 629 MPa; S_{xy}= 65 MPa. With these macro strengths, if the Tsai-Wu failure criterion was applied to the entire laminate model, where the laminate was treated as a monolithic material, a failure envelope would be obtained which was an ellipse determined by the four points on the axes as shown according to Equation (6-7). It is plotted alongside with the failure envelope based on lamina in Figure 6.12.

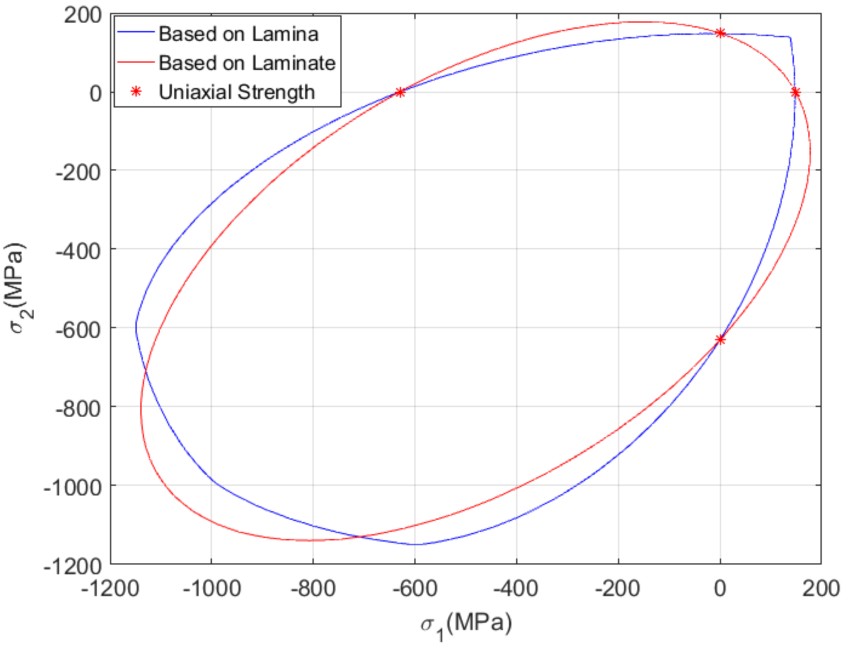

Figure 6.12 Failure envelopes of T300 carbon fibre laminate predicted based on lamina- and laminate-based failure criterion

It can be seen that in this case, the failure envelopes based on lamina and laminate bear some similarities. The analysis has next been made for the laminate of same lay-up, where the individual plies were assigned the properties of glass-fibre composite, as defined in Table 6.5.

Table 6.5 Material properties of E-glass 21xK43 Gevetex UD composite with DY063 epoxy matrix (V_f=62%) [82]

E_1 (GPa)	53.48
E_2 (GPa)	17.7
ν_{12}	0.278
G_{12} (GPa)	5.83
S_{1t} (MPa)	1140
S_{1c} (MPa)	570
S_{2t} (MPa)	35
S_{2c} (MPa)	114
S_{12} (MPa)	72

Failure envelopes calculated by applying Tsai-Wu failure criterion on laminate and lamina level are plotted in Figure 6.13. As can be seen, in this case, the failure envelopes are drastically different. This confirms the importance of consistent modelling of failure in composites, where failure models applicable to the UD composites should not be extended blindly to anything other than UD.

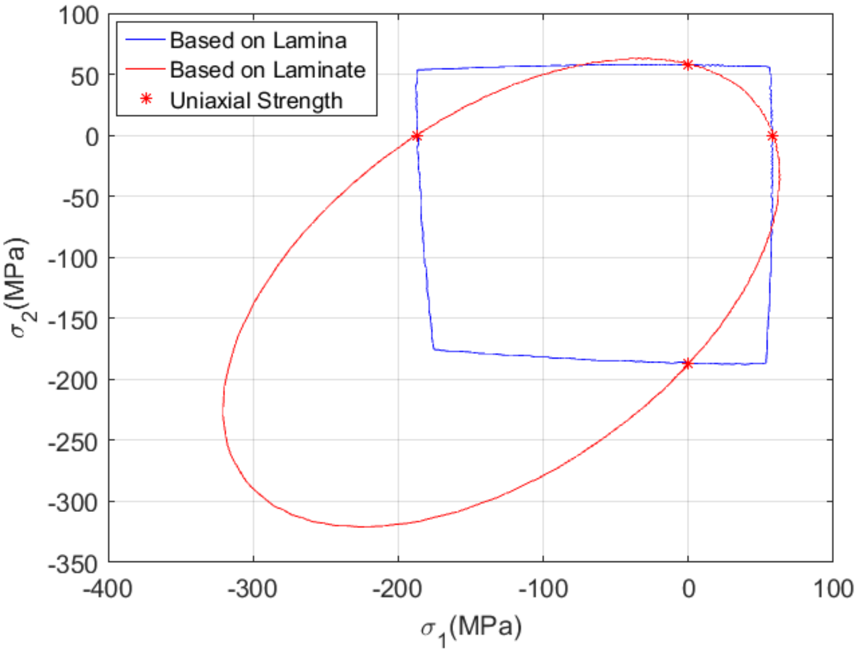

Figure 6.13 Failure envelopes of E-Glass fibre laminate predicted based on lamina- and laminate-based failure criterion

At the same time, modelling the lamina explicitly and applying failure criteria to each layer is relatively more complicated and computationally demanding. Failure criterion that is applicable to the whole laminate can facilitate the failure analysis more conveniently. However, it cannot be achieved in the way as shown above, as it is apparently misleading. The ANN method offers a solution to this problem. To demonstrate the applicability of this method, it was applied to construct the macroscale failure envelope for the whole laminate.

The ANN training cases were generated for the GF laminate as in the previous example. The laminate model was loaded at 728 different macro stress combinations. Within each layer, the stress state at every increment of every stress combination was checked and compared with the Tsai-Wu failure criterion. The laminate was regarded as have failed if any layer failed according to the Tsai-Wu failure criterion. In this case, an indicator '1' was output for this increment; otherwise, an indicator '0' was output. An ANN was generated and trained, where the macro stress components of every increment were treated as input of the training case for ANN, while the indicator was treated as output.

The same GF laminate model as was used when the training case was created and loaded at different ratios of two macro stress components σ_1 and σ_2. The failure of the laminate was determined by the macro stress components via the ANN instead of applying the Tsai-Wu failure criterion to each layer. The failure envelope for the entire laminate based on the ANN is shown in Figure 6.14.

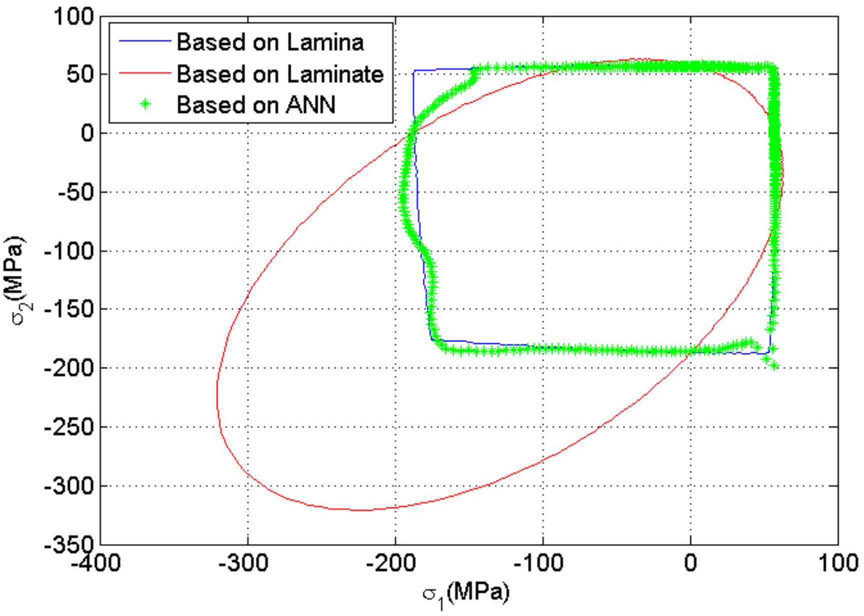

Figure 6.14 Failure envelopes predicted using lamina- and laminate-based failure criterion, and calculated employing ANN system

As can be seen, the failure envelope that was calculated applying ANN method agrees reasonably well with that constructed by explicitly applying the failure criterion at the ply level. The accuracy can be improved as more sampling points are incorporated into the ANN training. The explicit method can therefore be replaced by an ANN method, for which laminated composites are modelled as monolithic materials. This verifies the method developed and suggests that it can be extended for the analysis of textile composites.

The verification cases in this section have confirmed the capability of the ANN system to accurately represent the behaviour of composites at the microscale, mesoscale and laminate levels. However, in the present work, the main purpose of developing the ANN systems was to apply them for the definition of the constitutive behaviour of textile composites at the macroscale level. The examples of such applications are given in Chapter 7.

6.5 Summary

A multiscale modelling methodology has been developed to define the constitutive behaviour of the textile composites, incorporating elastic behaviour, progressive damage and an ultimate failure. It employs the ANN method to define the constitutive behaviour of textile composites at the macroscale. With the ANN system, the strength of textile composites at multi-axial stress states can be predicted. As an illustration, the failure envelopes of a 4-axial 3D braided composites and a laminate were created.

This ANN system was implemented as Abaqus user material subroutines (UMAT and VUMAT) to represent the properties of textile composite model at meso- and macroscales as a fictitiously monolithic material. Sanity checks have been carried out at each stage and scale of the analysis to verify the method. The capability of the methodology has been demonstrated through a simulation of rigid ball impact of a 3D braided composite flat panel.

Chapter 7 Validation and Application

7.1 Introduction

The multiscale modelling methodology as established in Chapter 6 needs to be validated before it can be applied to solve practical problems. The validation process is carried out to ensure that the predictions of the model are reasonable and have an acceptable accuracy. For validation, the multi scale unit cell models were used to predict the effective stiffness of 3D braided and 3D orthogonal woven composites and compared with published data. Furthermore, the unit cell and ANN modelling method were used to predict the effective static and dynamic stiffness and strength and critical velocities of glass and carbon fibre reinforced layer-to-layer interlock 3D woven composites. The predicted results agreed well with the experimental results from a parallel PhD project [127]. To demonstrate the capability of the established method to predict the response of the textile composite materials at a component level which is at a macro-scale, a finite element simulation of the impact of the containment casing was carried out as presented and discussed in Section 7.4.

7.2 Validation against Published Data

In addition to the extensive verification exercises as described in Chapter 3 and Chapter 4, UnitCells© has also been partially validated against the limited experimental data available in the open literature. In this section, the effective properties obtained with UnitCells© for different types of composites are compared with those from [40, 82, 167, 168, 169].

7.2.1 Effective properties of UD composites

As a validation of stiffness and strength predictions of UD composites, four types of unidirectional laminae were characterised employing the unit cell modelling. The predictions were compared with the experimental data [82]. Typical data for the properties of four fibres and epoxy resins are summarised in Table 7.1 and Table 7.2. These serve as the input material properties for the analysis.

Table 7.1 Mechanical properties of four types of the fibres [82]

Fibre type	AS4	T300	Gevetex E-glass 21xK43	Silenka E-glass 1200tex
E_{f1} (GPa)	225	230	80	74
E_{f2} (GPa)	15	15	80	74
G_{f12} (GPa)	15	15	33.33	30.8
ν_{f12}	0.2	0.2	0.2	0.2
G_{f23} (GPa)	7	7	33.33	30.8
X_{fT} (MPa)	3350	2500	2150	2150
X_{fC} (MPa)	2500	2000	1450	1450
ε_{f1T} (%)	1.488	1.086	2.687	2.905
ε_{f1C} (%)	1.111	0.869	1.813	1.959

Table 7.2 Mechanical properties of four types of the epoxy resins [82]

Matrix type	3510-6 epoxy	BSL914C epoxy	LY556/HT907 / DY063 epoxy	MY750/HY917/ DY063 epoxy
E_m (GPa)	4.2	4	3.35	3.35
G_m (GPa)	1.567	1.481	1.24	1.24
ν_m	0.34	0.35	0.35	0.35
Y_{mT} (MPa)	69	75	80	80
Y_{mC} (MPa)	250	150	120	120
S_m (MPa)	50	70		
ε_{mT} (%)	1.7	4	5	5

Table 7.3 Mechanical properties of four unidirectional laminae [82]

Fibre type	AS4		T300		Gevetex E-glass 21xK43		Silenka E-glass 1200tex	
Matrix type	3510-6 epoxy		BSL914C epoxy		LY556/HT907/ DY063 epoxy		MY750/HY917/ DY063 epoxy	
V_f	0.6		0.6		0.62		0.6	
	Test	UnitCells©	Test	UnitCells©	Test	UnitCells©	Test	UnitCells©
E_1 (GPa)	126	136.62	138	139.54	53.48	50.87	45.6	45.74
E_2 (GPa)	11	9.55	11	9.44	17.7	16.34	16.2	14.99
G_{12} (GPa)	6.6	4.7	5.5	4.52	5.83	4.96	5.83	4.58
ν_{12}	0.280	0.252	0.280	0.256	0.278	0.246	0.278	0.250
ν_{23}	0.40	0.26	0.40	0.27	0.40	0.25	0.40	0.26
X_T (MPa)	1950	2049.23	1500	1548.85	1140	1339.28	1280	1292.42
X_C (MPa)	1480	1557.42	900	1213.96	570	930.99	800	905.63
Y_T (MPa)	48	50.9	27	54.04	35	44.13	40	44.96
Y_C (MPa)	200	177.66	200	106.14	114	64.76	145	67.44
S_{12} (MPa)	79	42.29	80	45.64	72	44.61	73	45.45
ε_{1T} (%)	1.38	1.5	1.087	1.11	2.132	2.7	2.807	2.91
ε_{1C} (%)	1.175	1.14	0.652	0.87	1.065	1.83	1.754	1.98
ε_{2T} (%)	0.436	0.54	0.245	0.6	0.197	0.27	0.246	0.3
ε_{2C} (%)	2	1.86	1.818	1.14	0.644	0.42	1.2	0.45
γ_{12u} (%)	2	0.9	4	1.02	3.8	0.9	4	1.02

The effective properties of the unidirectional laminates were calculated and compared with the experimental data in Table 7.3. Reasonable agreements have been achieved between the predicted effective stiffnesses and the experimental results except for the odd ones which will be justified below. The same conclusion can be made comparing the measured and predicted tensile strength and tensile failure strain along both the longitudinal and transverse directions. At the same time, the predicted values of the compressive strength in the longitudinal directions are larger than those determined experimentally. This is due to the fibre buckling that occurred in the experiments prior to the ultimate compressive failure. Fibre buckling is not accounted for in the unit cell model, hence the predicted strength values are expected to be larger than the measured ones. Under transverse compressive loading and shear loading, the predicted strength values are lower than the measured ones. These types of failure are dominated by matrix failure, hence within unit cell analysis, the material is considered to have failed when matrix failure occurred. However, in the real-life tests, the fibres can come into contact with each other and can sustain more load even after the matrix has failed. Because of that, the strength predictions under the shear and compressive tensile loading in the transverse direction are expected to be conservative.

7.2.2 Effective properties of textile composites

To validate the material characterisation methodology for textile composites, a 4-axial 3D braided composite was considered. Some of the effective properties for this composite were calculated employing four different methods, namely, multi-unit cell model with rule of mixtures for the yarn (MUCM1) [40], multi-unit cell model with the bridging model [170] for the yarn (MUCM2) [40], weighted average model (WAM) [168] and hybrid stress element model (HYB) [167]. Some experimental results can be found in [40], where these were compared with the predictions made with the methods as proposed in [167, 168].

In accordance with the multi-scale modelling methodology, the effective properties of the yarns were calculated first. These are presented in Table 7.4, where the properties of the constituent materials, as were used in [40], are also reproduced. The microscale analysis was carried out by UnitCells©, where the UD composite with fibre volume fraction of 80% was represented by a hexagonal UC (Figure 3.5 (a)).

Table 7.4 Properties of AS4 carbon fibre, epoxy resin [40] and UD composites

	Fibre (AS4 carbon fibre)	Matrix (epoxy resin)	UD composites (V_f=80%)
E_1 (GPa)	234.6	2.94	188
E_2 (GPa)	13.8	2.94	9.61
G_{12} (GPa)	13.8	1.176	6.00
G_{23} (GPa)	5.50	1.176	3.59
ν_{12}	0.20	0.25	0.226

At the mesoscale, the material characterisation was carried employing the unit cell of a 4-axial 3D braided composite (see Figure 3.28 (a)), which is available in UnitCells©. Six unit cell models were generated in total, each having the same braiding angles and fibre volume fractions as those in [40]. The braiding angles and fibre volume fractions are listed in Table 7.5. With a fixed fibre volume fraction for the yarns, the specified fibre volume fractions can be achieved by selecting appropriate yarn volume fractions in the corresponding unit cells which can be done analytically [73]. It can be shown that moderate exchange between the fibre volume fraction in the yarns and the yarn volume fraction in the unit cell makes no significant difference to the predicted results. The same conclusion applies to other unit cells (see section 8.3 in Chapter 8).

At the mesoscale, the effective properties of UD composites listed in Table 7.4 were used to represent the material properties of yarns. The material properties of the matrix were the same as those of the epoxy resin in Table 7.4. Mesoscale material characterisation has been carried out for all six models, and the predicted longitudinal and transverse elastic moduli were compared with those from [40] in Table 7.5 and Table 7.6, respectively, where such data was available. Note that UnitCells© allows calculation of all the effective elastic properties, and for the sake of completeness, these are presented in Table 7.7, even though no experimental data were available for comparison.

From Table 7.5 and Table 7.6 it is easy to see that the values of the elastic moduli predicted with UnitCells© agree well with the experimental data, as well as with the values calculated via other mathematical models. Particularly good agreement has been achieved in terms of predictions of the longitudinal effective stiffness.

Table 7.5 Effective longitudinal stiffness values obtained with different methods in [40] and calculated with UnitCells©

Specimen No.	1	2	3	4	5	6
Braiding angle θ	0	17	17	20	22	25
V_f	0.28	0.38	0.4	0.46	0.44	0.29
Experiment (GPa)	66.9	43.6±1.9	45.9±1.2	48.0±3.0	38.5±2.4	21.2±1.8
MUCM1 (GPa)	66.2	45.2	47.4	46.5	40.3	24.1
MUCM2 (GPa)	66.2	43.9	46	45.3	39.1	23
WAM[168] (GPa)	68.8	48.3	50.7	47	38.6	21.6
HYB[167] (GPa)	69.2	46	46.9	44.8	38.1	23.8
UnitCells© (GPa)	67.7	42.5	43.3	46.8	37.2	23.9

Table 7.6 Effective transverse stiffness values obtained with different methods in [40] and calculated with UnitCells©

Specimen No.	1	2	3	4	5	6
Experiment (GPa)	N/A	6.21±0.41	N/A	N/A	6.02±0.3	N/A
MUCM1 (GPa)	N/A	5.81	N/A	N/A	6.39	N/A
MUCM2 (GPa)	N/A	5.62	N/A	N/A	6.14	N/A
WAM[168] (GPa)	N/A	5.74	N/A	N/A	6.21	N/A
HYB[167] (GPa)	N/A	6.22	N/A	N/A	6.54	N/A
UnitCells© (GPa)	4.54	5.48	6.09	6.95	6.78	5.72

All effective properties are summarised in Table 7.7 for many of which experimental data were not available.

Table 7.7 All effective properties predicted using UnitCells©

Specimen No.	1	2	3	4	5	6
E_1 (GPa)	67.7	42.5	43.3	46.8	37.2	23.9
E_2=E_3 (GPa)	4.54	5.48	6.09	6.95	6.78	5.72
G_{12}=G_{13} (GPa)	1.78	5.22	5.9	8.07	8.43	6.64
G_{23} (GPa)	1.54	1.9	2.08	2.29	2.17	1.68
ν_{23}	0.48	0.37	0.36	0.31	0.29	0.29
$\nu_{12}=\nu_{13}$	0.3	0.57	0.58	0.69	0.74	0.73

Another example is for non-crimp fabric (NCF, referred to as 3D orthogonal woven) composites. The fabric architecture and experimental results can be found in [169]. The total fibre volume fraction was given as 51.1%. A hexagonal unit cell similar to that shown in Figure 3.5(a) was used to predict the effective properties of the yarns as UD composites, but the fibre volume fraction within the yarns was assumed to be 70%. The NCF composite architecture (Figure 7.1) was defined using UnitCells© such that the geometric parameters employed resulted in a yarn volume fraction of 73%, gives the desired overall fibre volume fraction of 51.1%. The volume ratio of the warp, weft and binder yarns in the fabric was chosen to be the same as that given in [169] at 46.12:51.24:2.64%. Because of the limitation in model generation, the binders have 1.37% through thickness and 1.27% as ‘Z-crown’ [169], respectively, as opposed to 1.34% and 1.30% as in [169]. Such a minor disparity would not be expected to result in much difference in the results. The yarn cross sections were chosen as a power ellipse, and the mesh for the yarns involved in the unit cell model is shown in Figure 7.1.

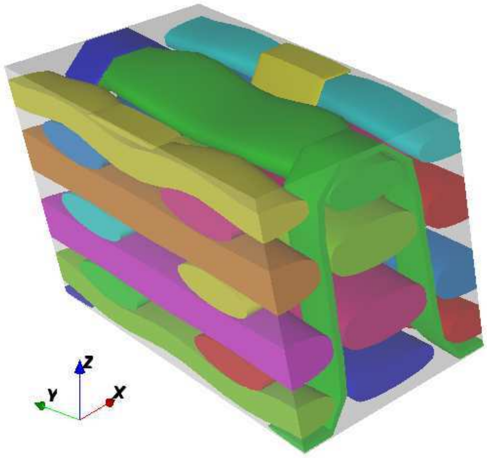

(a) Geometry generated using TexGen

(b) Yarn mesh generated by HyperMesh (only those for the yarns are shown)

Figure 7.1 Unit cell for 3D orthogonal woven composites

The properties of the fibre and matrix were not provided in [169]. However, according to the types of fibre and matrix specified in [169], the relevant properties were obtained from their suppliers' web sites as listed in Table 7.8 [171, 172], while the obtained results are shown in Table 7.9. The same composite with simple rectangular yarn cross sections with straight yarn paths and binders bending at right angles was also attempted, and the results are included in Table 7.9 in the row marked 'Rectangle', where the Z-binder split was 1.62 and 1.02%, a bit further away from the ratio given in [169]. Again, no major error is expected in the results. In fact, the lack of differences between the results from 'Rectangle' and 'Power ellipse' yarn cross sections as shown in Table 7.9 suggests that effective elastic properties are not extremely sensitive to detailed geometric parameters while the dominant factors are the fibre volume fractions in the principal directions.

Table 7.8 Properites of the epoxy resin and Toho Tenax carbon fibre

Fibre (Toho Tenax) [171]	E_1 (GPa)	237.0
	E_2 (GPa)	23.7
	G_{12} (GPa)	15.0
	ν_{23}	0.45
	ν_{12}	0.29
Matrix	E (GPa)	3.98
(105 epoxy 209 extra slow hardener) [172]	ν	0.33

Table 7.9 Comparison of the effective stiffnesses of NCF textile composites

		E_1 (GPa)	E_2 (GPa)	E_3 (GPa)
Experimental [169]		60.0	67.0	N/A
Yarn cross section used in UnitCells©	Rectangular	60.88	67.30	25.52
	Power elliptic	60.27	67.35	26.62

The two examples shown above indicate that the effective properties predicted by using unit cell models agreed well with the experimental results. This means the developed multiple scale unit cell model has reasonable accuracy in predicting the effective properties of 3D textile composites.

7.3 Validation against the Experiments

The comparisons of the effective properties predicted using UnitCells© and the published experimental data in Section 7.2 should validate the unit cells involved to a certain extent. Further validation was carried out by comparing the predicted and measured properties of the textile composites with 3D layer-to-layer interlock woven reinforcement. The mechanical testing of the composites was carried out by a different researcher from the team of the larger project on the simulation methodology for impact damage in composite components of aero-engines [83, 127]. The experimental program involved both coupon tests at quasi-static and dynamic stress states (SHPB), as well as ballistic impact tests on the composite panels. The specimen manufacturing, experimental procedures and data processing techniques are reported in detail in [127]. Here, the quasi-static and dynamic properties determined in the tests are employed for the validation of the modelling methodology.

7.3.1 Static stiffness and strength of 3D woven composites

The static stiffness and strength predictions were validated for two types of E-glass fibre reinforced layer-to-layer interlock composites and two types of carbon fibre reinforced layer-to-layer interlock composites. The resin transfer moulding (RTM) method was applied to form the fabric into the panel shape [83]. The specimens machined from the cured panels were used in the experiments, which were designed to determine the stiffnesses and strengths in the in-plane material principal directions under quasi-static loading [127]. Photographs of the glass fibre and carbon fibre composite samples in quasi-static tensile tests are shown in Figure 7.2 (a) and (b), respectively.

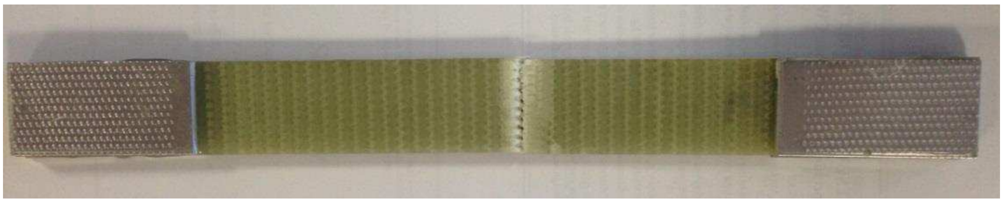

(a) E-glass fibre

(b) Carbon fibre

Figure 7.2 Composite specimens in quasi-static tensile tests

The Multi-scale modelling approach has been applied for characterising the composite materials based on woven textile reinforcements. The mesoscale unit cell as shown in Figure 5.9 is employed, which explicitly defines the complex geometry of the fabric weave structure in a textile composite. The input parameters as required in order to follow the modelling process are categorised into three groups as follows.

1) Material properties: elastic and strength properties as available from material suppliers and some special parameters introduced by various theories.

2) Processing related parameters: fibre and yarn volume fractions.

3) Geometric dimensions: definition of the textile architecture, e.g. the weaving angle of warp yarn and the size of the yarns cross sections.

Measurements of the geometric parameters were carried out by processing the micro-CT images of the fabrics [83]. Four types of preforms were analysed, with brief description of these fabrics being given in Table 7.10.

Table 7.10 Four types of layer-to-layer angle interlock reinforced textile composites applied in material characterization study

Notation	Fibre material	Yarn volume fraction ratio (warp:weft)	Fibre volume fraction ratio (warp:weft)	Thickness (mm)
GF1	E-glass fibre	48.99%:13.24%	38.51%:9.88%	4.0
GF2	E-glass fibre	42.62%:23.39%	33.50%:17.46%	4.0
T300 CF	T300 carbon fibre	38.02%:28.41%	29.88%:22.33%	4.2
IM7 CF	IM7 carbon fibre	42.25%:27.85%	33.21%:20.79%	4.2

Within the first stage of modelling, the effective properties of the yarns were predicted via a UD unit cell analysis. The input parameters were the material properties of the fibre and the resin, and the fibre volume fraction, V_f, within warp and weft yarns. The properties of the fibres and the resin are given in Table 7.11 and Table 7.12, while the fibre volume fractions in the warp (78.6%) and weft (74.65%) yarns were estimated by analysing the micro-CT images of the fabric. The predicted density, elastic and strength properties of the yarns are summarised in Table 7.13 and Table 7.14.

Table 7.11 Mechanical properties of the constituent materials (resin and glass fibre)

	ρ (kg/m^3)	E (GPa)	ν	S_t (MPa)	S_c (MPa)
Resin (PRIME^{TM} 20LV)	1140	3.5	0.35	73	120
E-glass fibre	2570	74	0.22	2000	1080

Table 7.12 Mechanical properties of the constituent materials (T300 and IM7 carbon fibre)

	ρ (kg/m^3)	E_x (GPa)	E_y (GPa)	G_{xy} (GPa)	ν_{xy}	ν_{yz}	S_t (MPa)	S_c (MPa)
T300 carbon fibre	1780	230	15	15	0.20	0.07	2500	2000
IM7 carbon fibre	1780	276	19	9.5	0.28	0.45	5600	3500

Table 7.13 Predicted density and effective elastic properties of the yarns

	ρ (kg/m^3)	E_x (GPa)	E_y (GPa)	G_{xy} (GPa)	ν_{xy}	ν_{yz}
Warp yarn (GF1&GF2)	2264.0	58.86	22.93	8.39	0.24	0.33
Weft yarn (GF1&GF2)	2207.5	56.08	19.62	7.13	0.25	0.34
Warp yarn (T300 CF)	1643.0	181.32	10.62	6.54	0.23	0.23
Weft yarn (T300 CF)	1617.8	172.39	10.01	5.77	0.23	0.25
Warp yarn (IM7 CF)	1643.0	217.42	12.21	5.29	0.29	0.45
Weft yarn (IM7 CF)	1617.8	206.64	11.34	4.80	0.30	0.46

Table 7.14 Predicted effective strength properties of the yarns

	S_{Xt} (MPa)	S_{Xc} (MPa)	S_{Yt} (MPa)	S_{Yc} (MPa)	S_{xy} (MPa)	S_{yz} (MPa)
Warp yarn (GF1&GF2)	1580.7	894.6	55.8	88.3	56.7	33.7
Weft yarn (GF1&GF2)	1506.6	824.2	57.8	89.1	58.7	35.6
Warp yarn (T300 CF)	1930.8	1150.0	37.0	220.0	84.0	48.8
Weft yarn (T300 CF)	1835.7	1093.4	39.0	223.0	88.0	50.0
Warp yarn (IM7 CF)	4435.4	2804.7	63.1	103.1	66.2	47.8
Weft yarn (IM7 CF)	4215.5	2665.7	62.9	101.6	64.5	46.6

To characterize the material at the mesoscale, the analysis was carried out for the UC as shown in Figure 5.9. In this case, the input parameters were the properties of resin as in Table 7.11, and parameters of the yarns were determined in the microscale analysis. In addition to that, the geometric parameters of the weave need to be specified. These include the width and height of the cross-sections of the warp and weft yarns, and the distance between two adjacent weft yarns. These were determined by processing the micro-CT images of the fabrics (see Figure 3.14 [83]). Image processing software ImageJ [173] was utilised to measure the dimensions of the yarns and their spacing at various locations within the fabric. The average values and the standard deviations of the geometric parameters of the fabric as presented in Table 7.15 were determined based on approximately 20 measurements of each parameter. It can be seen that the measured geometric parameters are scattered due to the inherent variability of the weave geometry. This introduces errors in the predicted results. However, the scatter of the geometric parameters does not affect the predictions of the mechanical properties significantly, as long as the fibre volume fraction and the weaving angle are close enough to those of the real material. Influence of geometric properties of the weave on variation of the mechanical properties is investigated in a parametric study presented in Section 8.2 of Chapter 8.

Table 7.15 Measured geometric parameters of the fabrics

Type	GF 1	GF 2	T300 CF	IM7 CF
Weft yarn space (mm)	4.52±0.4	4.35±0.3	3.75±0.5	4.52±0.14
Weft yarn width (mm)	1.45±0.5	2.48±0.2	2.3±0.2	2.26±0.16
Weft yarn thickness (mm)	0.36±0.05	0.42±0.06	0.36±0.05	0.37±0.03
Warp yarn width (mm)	1.31±0.1	1.31±0.1	1.25±0.14	1.28±0.09
Warp yarn thickness (mm)	0.38±0.05	0.37±0.15	0.4±0.1	0.37±0.04
Warp yarn weaving angle	23°~27°	38°~43°	23°~34°	29°~35°
Weft yarn layers	6	6	7	7

With the input parameters defined as described above, the mesoscale UC analysis was carried out. The stress-strain curves in each loading case were calculated and the effective elastic and strength of the UC were extracted from the stress-strain curves. Some typical stress-strain curves are shown in Figure 7.3.

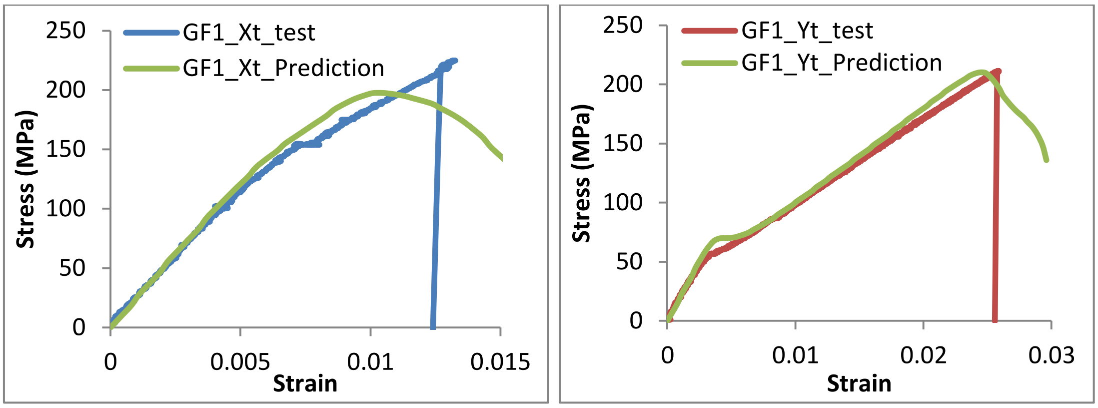

(a) Warp tension of GF1

(b) Weft tension of GF1

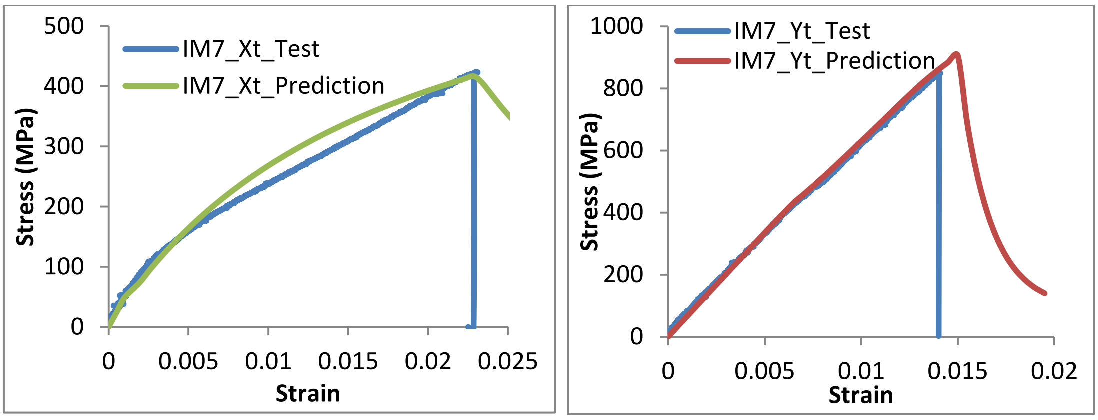

(c) Warp tension of IM7

(d) Weft tension of IM7

Figure 7.3 Comparison of the calculated and experimental stress-strain curves of GF1 and IM7 composites

As can be seen, there is a good agreement between the measured and the predicted stress-strain curves. The stress-strain curves obtained under warp tension show more nonlinearity than those under the weft tension. Since the weft yarns are straight, the material has higher stiffness in this direction, which is not affected much by the damage and failure in matrix constituent. The local reduction of the weft stiffness following the damage onset point in GF1 is due to the transverse failure of the warp yarn. This feature is not observed in the stress-strain curve of IM7 under weft tension, because the transverse stiffness of warp fibres is much lower than the longitudinal stiffness of the weft fibres. Therefore, the transverse failure of warp yarn does not significantly influence the properties in the weft direction.

The predictions of the effective elastic and strength properties are summarised in Table 7.16 and Table 7.17, respectively. Mesoscale unit cells can be used to represent the material under uniform stress states; hence the predictions can be directly compared with the experimental data obtained in standard coupon tests, through which the accuracy of the predictions are assessed and the modelling approach is validated.

Table 7.16 Effective elastic properties predicted from the mesoscale UC analysis

	E_x (GPa)	E_y (GPa)	E_z (GPa)	G_{xy} (GPa)	G_{xz} (GPa)	G_{yz} (GPa)	ν_{xy}	ν_{xz}	ν_{yz}
GF1, predicted	24.61	19.81	10.23	4.95	5.38	3.70	0.14	0.51	0.35
GF1, measured	24.77	17.24		4.03					
GF2, predicted	20.61	22.94	10.69	4.73	4.94	3.80	0.12	0.48	0.33
GF2, measured	21.83	25.67		4.06					
T300 CF, predicted	51.66	56.99	8.08	4.19	4.91	3.20	0.01	0.77	0.32
T300 CF, measured	48.68	55.16		3.81					
IM7 CF, predicted	48.56	67.24	9.06	3.44	5.19	2.95	0.01	0.96	0.43
IM7 CF, measured	45.00	68.00		3.62					

Table 7.17 **Effective strengths predicted for composites with various textile reinforcements**

	S_{Xt} (MPa)	S_{Xc} (MPa)	S_{Yt} (MPa)	S_{Yc} (MPa)	S_{Zt} (MPa)	S_{Zc} (MPa)	S_{xy} (MPa)	S_{xz} (MPa)	S_{yz} (MPa)
GF1, predicted	185.16	184.85	223.16	185.08	48.74	70.03	35.89	43.49	27.34
GF1, measured	223.49	173.33	206.46	199.07			28.57		
GF2, predicted	210.48	242.39	443.30	329.67	84.73	109.49	55.68	61.52	50.51
GF2, measured	213.21	167.50	336.79	323.18			38.28		
T300 CF, predicted	327.27	296.87	512.21	422.45	32.38	171.31	50.51	50.62	35.12
T300 CF, measured	335.53	197.30	485.29	386.22			39.41		
IM7 CF, predicted	439.37	167.15	941.74	294.92	46.74	122.77	42.49	44.72	35.22
IM7 CF, measured	421.36	113.13	832.11	296.52			42.81		

Comparison of the measured and predicted stiffness and strength values shows that a good agreement was achieved between predictions of the effective elastic properties and the experimental data. In this case, the error between the measured and predicted values is within 10%. On the other hand, at present, the predictions of the effective strengths are less accurate. This discrepancy is due to the definition of the input parameters. The input parameters affecting the calculation of the effective elastic properties were the material properties of fibres and resin, as well as geometric parameters of the fabric, which were measured explicitly. Hence the values of these parameters represented the actual constituent materials and the weaving architecture of the composite. The effective strength is defined as a maximum stress value on the average stress-strain curve calculated under the unidirectional loading. Before the material fails, a gradual reduction of stiffness takes place due to the evolution of damage. On the analysis as presented in above, the parameters defining damage evolution were not based on measurements, and were assigned a single fixed value as a temporary measure to facilitate the development of the model. This affects the accuracy of predictions of stiffness degradation and hence the strengths of the material. A more important consideration is that effective elastic properties are overall measures of the material behaviour obtained in some kind of average sense while strengths are closely associated with local distribution of stresses which are sensitive to variations of geometric parameters.

7.3.2 Dynamic strength of 3D woven composites

As a validation of the dynamic properties predictions, the effective strength of IM7 carbon fibre composite with layer-to-layer interlock 3D woven reinforcement (IM7 CF in Table 7.10), calculated at different strain rates, were compared with the experimental data.

The method of assigning the rate sensitivity to the textile composite is described in detail in Chapter 5. For IM7 CF composite, the rate dependency was defined only for the matrix constituent, while the IM7 carbon fibre was considered to be strain rate independent. The material properties of matrix and IM7 carbon fibre are listed in Table 3.6 and Table 4.2. Following the methodology as presented in Chapter 5, strain rate scaling coefficients for the elastic and strength properties were calculated with the UD unit cell models representing the warp and the weft yarns. The determined values of the scaling coefficients are listed in Table 7.18 alongside with the quasi-static values of the corresponding material properties. Employing appropriate user-defined material subroutines, the rate-dependent effective material properties of the yarns were implemented in the mesoscale UC model. Applying the mesoscale UC analysis, the compressive strengths of the composite were calculated over a range of strain rates. In Table 7.19, the predictions are compared with the dynamic strength values obtained from SHPB tests [127].

Table 7.18 Strain rate dependent material properties of IM7 yarns

	Warp yarn (V_f=78.6%, ρ =1643.0 kg/m^3)		Weft yarn (V_f=74.65%, ρ=1617.8 kg/m^3)	
	Quasi-static value	Strain rate constant, C	Quasi-static value	Strain rate constant, C
E_x (GPa)	217.42	0.0001	206.64	0.0001
E_y (GPa)	12.21	0.0065	11.34	0.0078
v_{xy}	0.29		0.30	
v_{yz}	0.45		0.46	
G_{xy} (GPa)	5.29	0.0076	4.80	0.0088
S_{Xt} (MPa)	4435.39	0.0001	4215.51	0.0001
S_{Xc} (MPa)	2804.73	0.0001	2665.69	0.0001
S_{Yt} (MPa)	63.08	0.1042	62.95	0.0997
S_{Yc} (MPa)	103.12	0.1032	101.57	0.1033
S_{xy} (MPa)	66.18	0.0988	65.47	0.0969
S_{yz} (MPa)	47.78	0.1097	46.61	0.1093

Table 7.19 Compressive strength of IM7 CF composite at different strain rates

Warp compressive strength (MPa)			Weft compressive strength (MPa)		
$\dot{\varepsilon}$ (s^{-1})	Experimental	Predicted	$\dot{\varepsilon}$ (s^{-1})	Experimental	Predicted
Static	113.13	119.02	Static	296.52	294.92
1054	304	313.99	1033	490	474.06
2043	346	359.63	2023	544	572.87
2824	373	385.67	2591	645	621.67

The predicted compressive strengths at different strain rates agree well with the measured ones. This means the strain rate sensitivity model is reasonable and is capable to represent the strain rate sensitivity of 3D woven composites to some extent.

7.3.3 Impact resistance of 3D woven composites

The implementation of the ANN system was verified at micro-, meso- and laminate level in Chapter 6. As a validation of the ANN system, its capability to deliver reasonable predictions when applied for the analysis at a component level has been assessed. For that, the ballistic impact was simulated for three textile composites, GF1, GF2 and IM7 CF in Table 7.10, where the constitutive behaviour of the composite was prescribed by means of an appropriate ANN system. For all three composites, the critical velocities were calculated and compared with those determined based on the experimental data in [127].

The ANN system employed in the current analyses and associated developments have been presented in previous chapters. The inter-yarn debonding damage model developed in a companion project [174] has been incorporated in generating the training cases for the IM7 specimens as the effect of this mode of damage was rather pronounced.

In the experiments [127], the ballistic impact was performed on 150mm×150mm square composite panel. A typical test panel of GF2 composite is shown in Figure 7.4(a). The panel was fixed to the rig by a steel frame with a circular cut-out, leaving an exposed circular area of 100 mm in diameter. Because of that, in the FE simulations, the test panel was modelled by a circular plate with its boundary fixed. The FE model of the ballistic impact test is shown in Figure 7.4 (b). The composite was defined as a monolithic material with its constitutive behaviour being prescribed via the ANN UMAT subroutine. In the tests, the steel ball bearing with a radius of 6.35 mm was fired at the panels. In the FE simulations, it was modelled by a rigid ball.

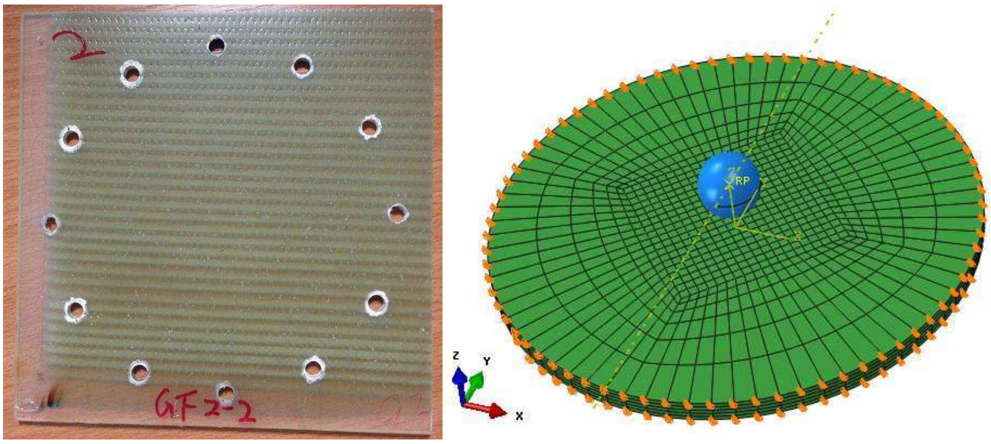

(a) Composite plate for ballistic impact test

(b) FE model for ballistic impact simulation

Figure 7.4 Composite sample and FE model for the ballistic impact simulation

In the simulations, the critical velocity was determined with the bisection method, the algorithm which is as follows.

Step 1: The iterative velocity range from V_1=0 m/s to V_2=300 m/s is defined, which covers the range of the impact velocities in the experiments.

Step 2: The panel is impacted at the initial velocity V_0= $(V_1+V_2)/2$. The time histories are taken for the acceleration, velocity and displacement of the rigid ball as the output.

Step 3: The residual velocity of the rigid ball is determined from the velocity curve. The deformation of the GF1 composite panel and the output curves (acceleration, velocity and displacement) obtained from the case with the initial velocity V_0=110 m/s are shown in Figure 7.5 and Figure 7.6, respectively. As can be seen, the velocity changes sign before settling at a nearly constant value again after impact, which indicates the rebounding of the projectile. The deformation of the GF1 panel and the output curves forV_0=140 m/s are shown in Figure 7.7 and Figure 7.8, respectively. In this case, the velocity of the projectile maintains the same sign throughout the simulation, which indicates the perforation of the target. If the panel was not penetrated, the lower boundary of the range of the velocities is updated as V_1= V_0. Otherwise, the upper boundary is updated as V_2= V_0.

Step 4: Step 2 and 3 are repeated until the absolute value of residual velocity of the projectile becomes smaller than 1 m/s. The impact velocity at this iterative step was regarded as the ballistic limit.

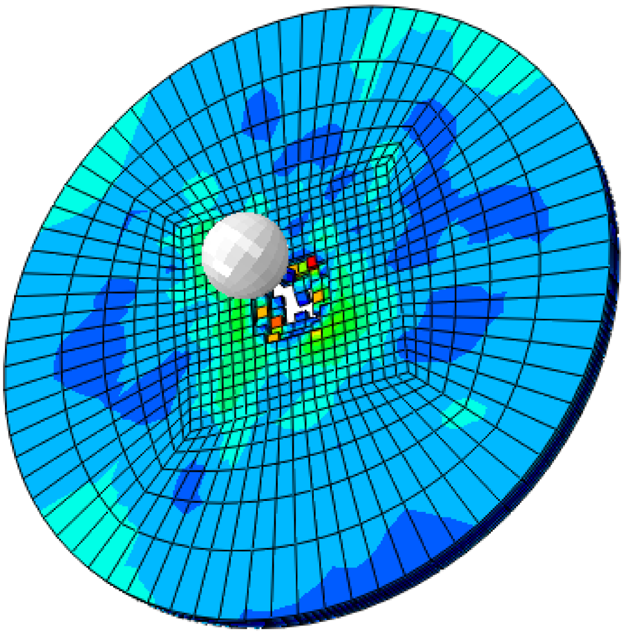

Figure 7.5 Deformation of GF1 composite panel in the impact simulation with initial velocity 110 m/s

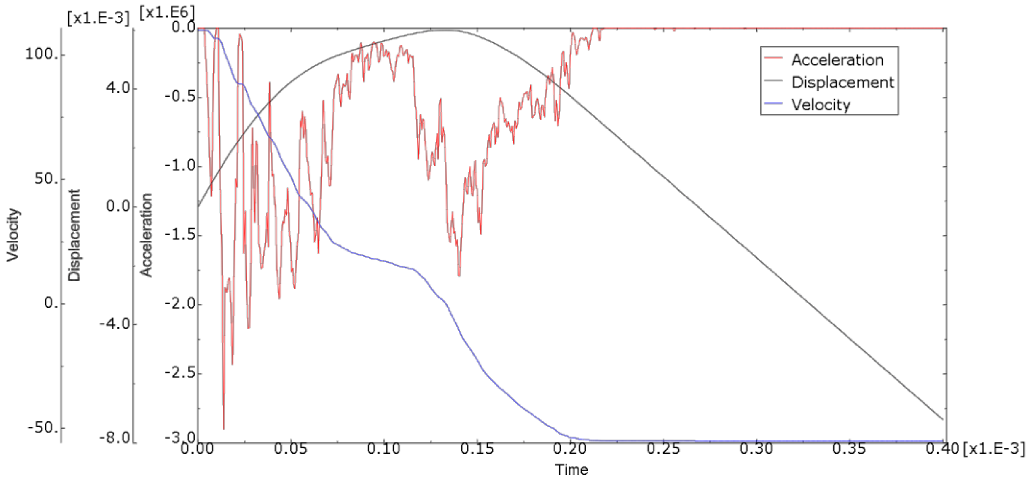

Figure 7.6 Output curves for the GF1 composite ballistic impact simulation with the initial velocity 110 m/s

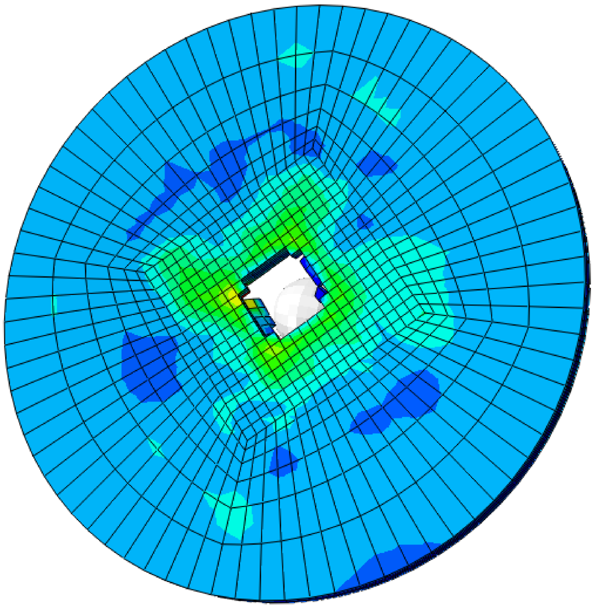

Figure 7.7 Deformation of the GF1 composite panel predicted by the impact simulation with initial velocity 140 m/s

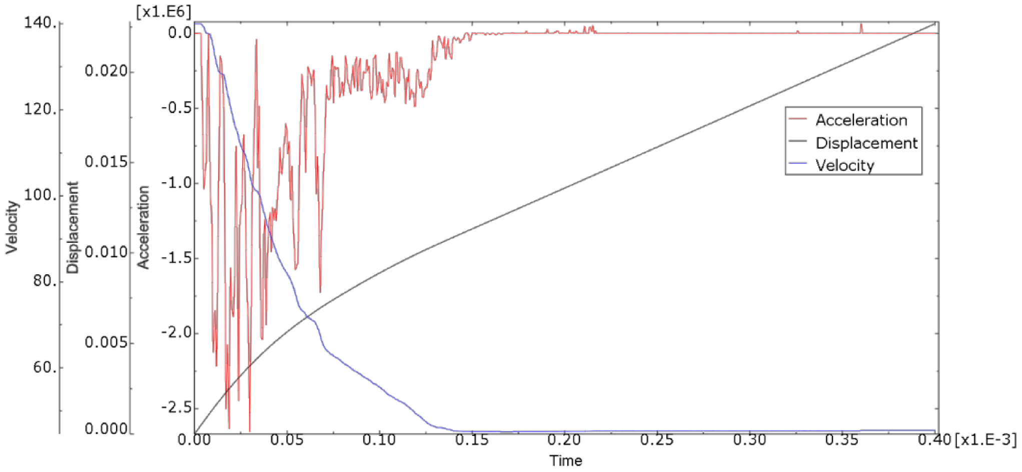

Figure 7.8 Projectile output curves calculated for GF1 composite impacted with initial velocity 140 m/s

It should be noted that the perforation hole in Figure 7.7 is not of a perfect circular shape. The reason for that is the mesh in the model being relatively coarse. A model with refined mesh is expected to deliver a more realistic prediction of the panel failure.

Additional information can be extracted analysing the acceleration time history. Once the acceleration reduces to zero, this indicates that the rigid ball is no longer in contact with the target plate.

The critical velocities for three types of textile composites determined with the bisection method are shown in Table 7.20.

In the experiments [127], the initial, V_i, and the residual, V_r, velocities of the projectile were recorded during the test for all the impact cases, and the critical velocities were obtained by post-processing the experimental data. The impact simulations were performed over a similar range of velocities, and the experimental and calculated V_i–V_r plots for each composite are presented in Figure 7.9. As can be seen, the predicted V_i–V_r curves generally show the same trend as the experimental ones, both below and above the ballistic limit.

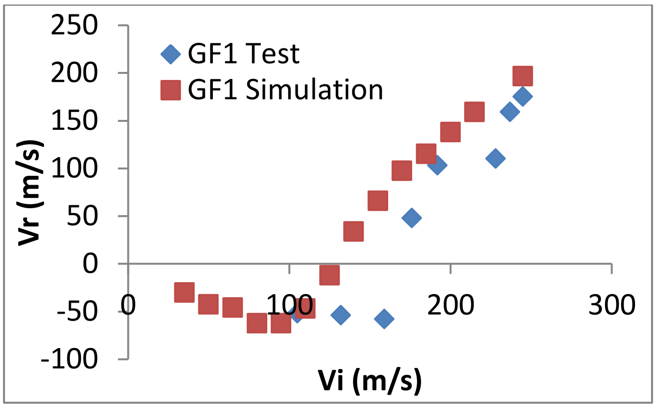

(a) V_i–V_r curve for GF1 composite

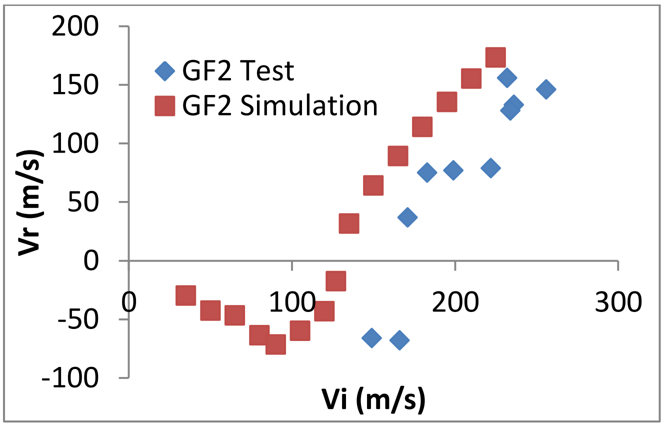

(b) V_i–V_r curve for GF2 composite

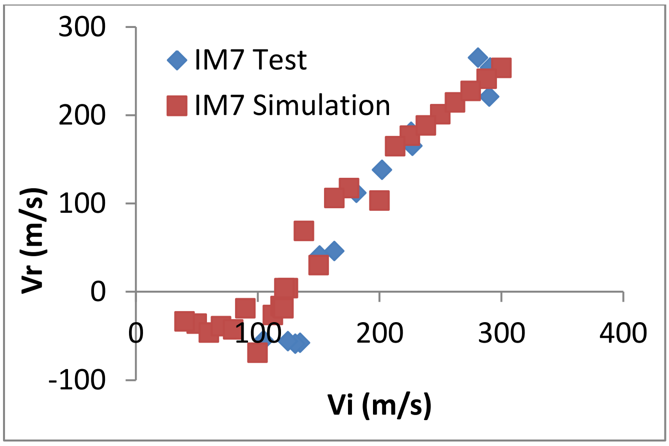

(c) V_i–V_r curve for IM7 composite

Figure 7.9 Initial and final velocity of ballistic test and simulation

To determine the critical velocity based on the experimental data, the experimental V_i–V_r curves were fitted employing the Matlab curve fitting tool. The fitting function was the Lambert-Jonas equation [175], which is commonly used for this purpose. It is applicable for the range of impact velocities at which panels were penetrated by the projectile. The explicit expression for Lambert-Jonas equation is as follows.

$$V_r^p = \beta^p (V_i^p - V_{50}^p) \tag{7-1}$$

where V_i is the initial velocity, V_r is the residualvelocity, V_{50} is the critical velocity which means there is 50% possibility to penetrate the panel by impact with this velocity, p and β are two parameters which need to be determined via fitting.

The fitted experimental V_i–V_r plots for all three composites tested are shown in Figure 7.10. The critical velocities are extracted from the fitted curves and presented in Table 7.20 alongside with the predicted critical velocity values.

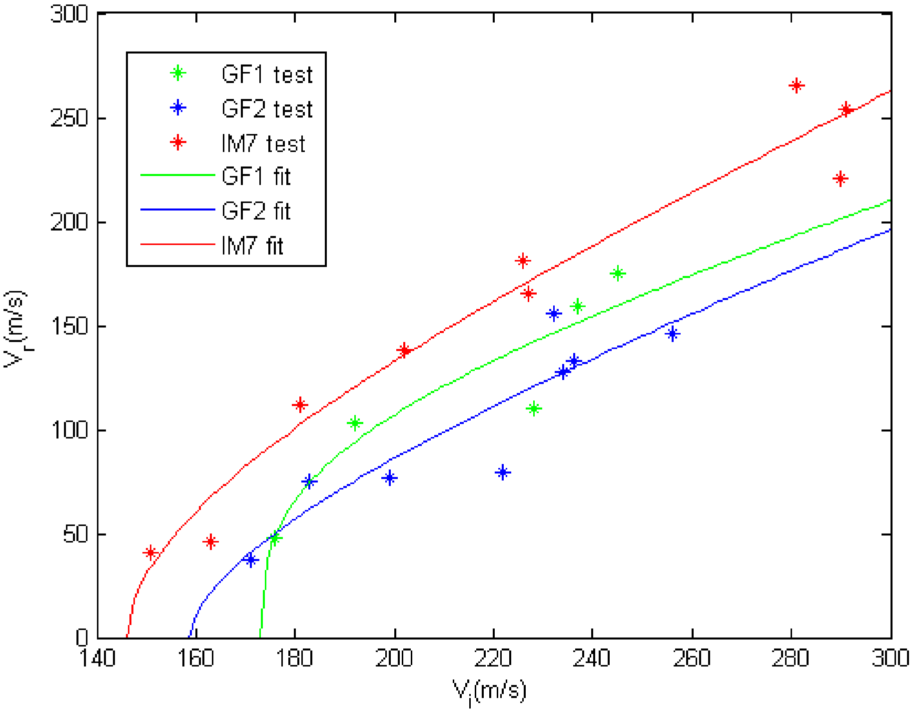

Figure 7.10 Fitted ballistic impact test data for three types of woven composites

Table 7.20 Comparison of the calculated and measured critical velocities for three types of woven composites

	Predicted (m/s)	Experimental (m/s)	Error
GF1	130.2	173.1	-24.78%
GF2	125.5	158.7	-20.92%
IM7 CF	121.5	149.0	-18.46%

As can be seen, the predicted values of the ballistic limit can be underestimated by up to 25%. In this case, material failure is defined based on an element deletion criterion. The material is assumed to fail once the Jacobian matrix (DDSDDE) becomes singular. This is a conservative criterion, as it does not account for the residual strength in the material. Therefore the predicted critical velocity should be on the conservative side of the experimental results.

7.4 Application of ANN on Simulation of Containment Casing

As a demonstration of the applicability of the ANN system to an analysis at component level, a model was generated to simulate a blade impact on a ring component represents a containment casing, which is assigned the same constitutive behaviour as IM7 composite, as defined in Section 7.3.3. The geometric properties of the blade and the containment ring were the same as in [19]. The model was simplified by modelling the blade as a steel plate, and not accounting for its failure and damage. The geometric and material parameters of the model are summarised in Table 7.21.

The FE models of blade and containment casing are shown in Figure 7.11. One edge of the ring component is fixed, while the other edge is left free. An initial angular velocity 1464 rad/s is assigned to the blade. General contact is defined between the blade and containment casing. Simulation was carried out with Abaqus/Explicit.

Table 7.21 Geometric properties of the blade and the containment ring [19]

Blade inner radius	213 mm
Blade outer radius	328 mm
Blade axial length	50 mm
Blade thickness	3.6 mm
Blade elastic modulus	200 GPa
Blade Poisson's ratio	0.3
Blade density	7810 kg/m^3
Blade initial angular velocity	1464 rad/s
Containment ring inner diameter	668 mm
Containment ring thickness	6 mm
Containment ring axial length	150 mm

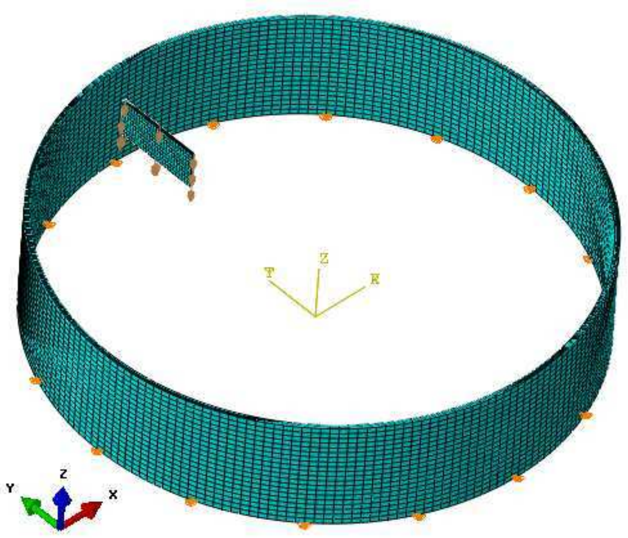

Figure 7.11 FE model of the blade and containment casing

The total step time is set to 0.002 s and the increment is automatic. The calculated time history of equivalent strain and deformation contour on the containment casing are shown in Figure 7.12.

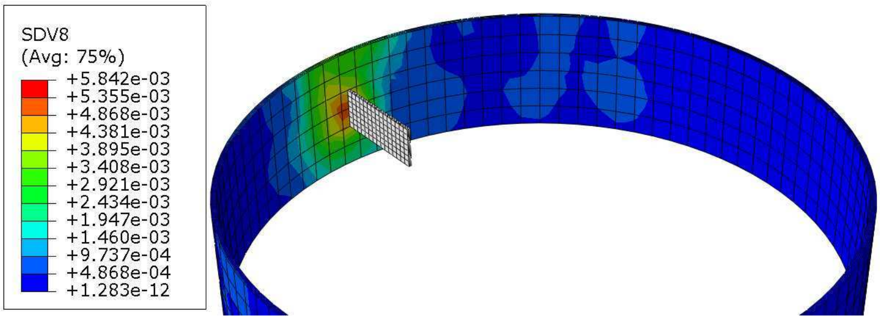

(a) *t* = 0.00015 s

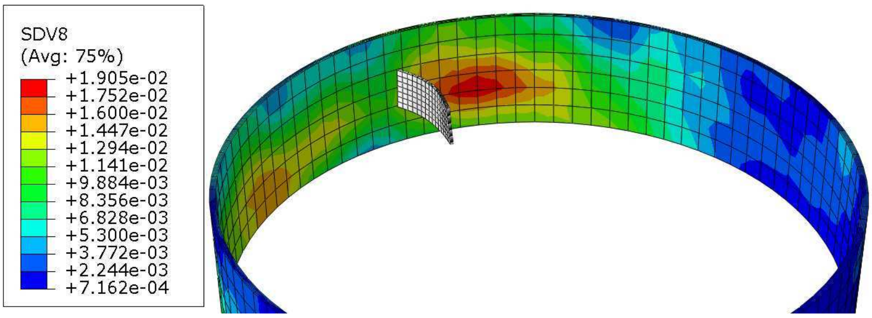

(b) *t* = 0.00036 s

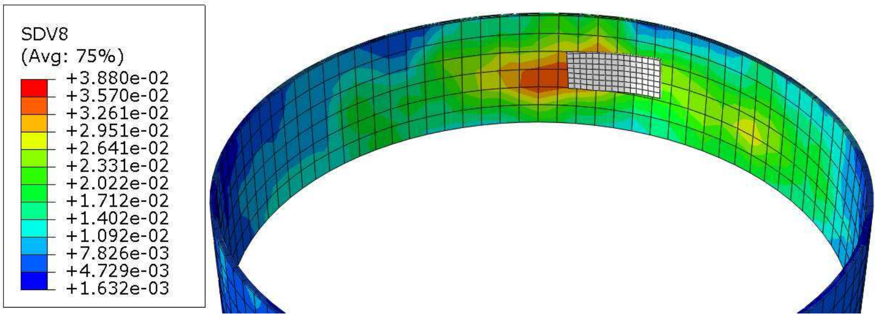

(c) *t* = 0.00105 s

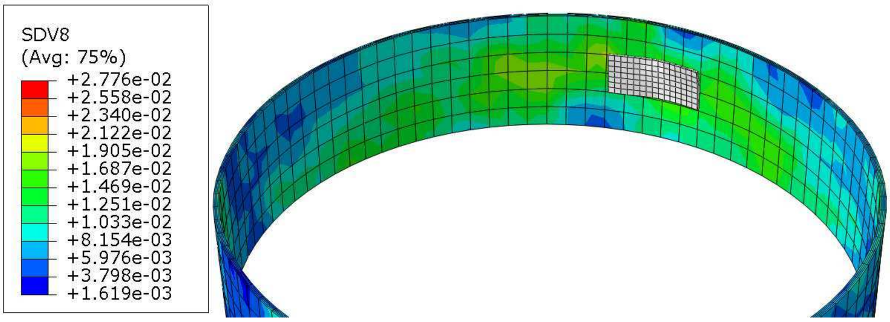

(d) *t* = 0.0012 s

Figure 7.12 Time history of deformation and strain contour on the containment casing

Considering the predicted deformation and failure modes of both the composite ring and the impactor, it can be concluded that the ANN system is capable of representing the constitutive relationship of 3D woven textile composite at a component level. As can be seen in Figure 7.12, the released blade impacted the containment casing twice, and it started to bend (see Figure 7.12 (b)) following the first impact. The second impact was more damaging (see Figure 7.12 (c)). Similar behaviour was also captured in [19], which suggests the impact scenario predicted with ANN system was reasonable.

On the other hand, the containment casing was not penetrated during the impact, which illustrated the high impact resistance of IM7 carbon fabric.

7.5 Summary

The modelling approach validation study as presented in this chapter confirmed that the predicted effective stiffnesses and strengths of both the UD composites and the 3D textile composites agreed well with the published data and with the experimental results. This indicates that the developed multi scale unit cell modelling method has acceptable accuracy in terms of the prediction of the effective properties.

Good correspondence has been achieved between the calculated impact resistance of 3D woven composites and the ballistic test results. This confirms that the macroscale modelling based of ANN has a powerful capability of homogenizing 3D textile composites with damage and failure effects being duly reflected.

The applicability of the ANN system for conducting the analysis at a macroscale has been demonstrated by carrying out the impact simulation of the composite component with 3D woven textile reinforcement.

Chapter 8 Parametric Study on Impact Resistance

8.1 Introduction

The objective of the current project is to develop a methodology for design, analysis and optimisation of textile composites. For the composites to be used in a fan blade containment casing, impact resistance is the dominant property. A parametric study has been carried out to demonstrate the effects of various the geometric parameters for textile composites on the impact resistance. A composite with a layer-to-layer interlock weave architecture, based on the material characterisation study in Chapters 3 and 4, was considered to be a feasible candidate for the application in fan blade containment casings. The parametric study was carried out with respect to three principal parameters: total fibre volume fraction, ratio of volume fraction of warp and weft yarns and weaving angle of warp yarns. ANN was generated for each combination of parameters and panel impact simulations were carried out to determine the critical velocity for each case. An optimized combination of the geometric parameters was proposed based on the comparison of the critical velocities.

8.2 Extraction of the Principal Parameters

The definition of the mesoscale unit cell model of textile composites has been described in Chapter 4 and Chapter 5. The model input requires a relatively large number of parameters to be specified, which can be grouped into several categories, as was shown in the flowchart in Figure 6.4. When designing a textile composite for a particular application, in order to obtain an optimal performance, decisions have to be made regarding the parameter choices within each category. Here, some rational considerations can be employed when selecting the constituent materials. In particular, for aerospace applications, it is practical to employ CF reinforcements. The type of the textile reinforcement as used here was chosen based on comparing the effective properties of the composites with various types of 3D textile reinforcements in Chapters 3 and 4 and manufacturing feasibility. Having selected the layer-to-layer interlock weave architecture, it is still not clear how the internal structure of the weave should be defined in terms of the dimensions of yarn cross-sections and spacings between the warp and the weft yarns. To make an informed decision in this respect, the effect of the weave geometry on the effective properties of the composite should be understood first.

When defining the geometry of the layer-to-layer interlock 3D woven composites, seven geometric parameters can be identified in order to generate a mesoscale unit cell model as illustrated in Figure 8.1 where strings are used instead of algebraic symbols for direct correspondence with the software developed. Carrying out the parametric studies that account for all possible combinations of these parameters would be time-consuming. To facilitate the parametric studies, a method of reducing the number of parameters is to be employed.

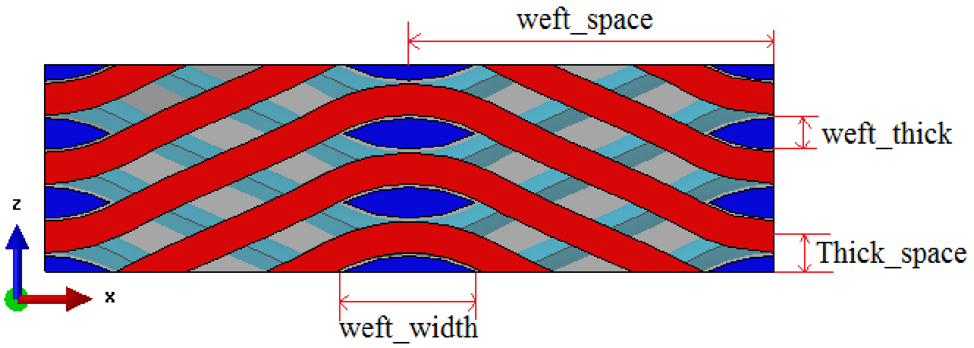

(a) Weft direction view

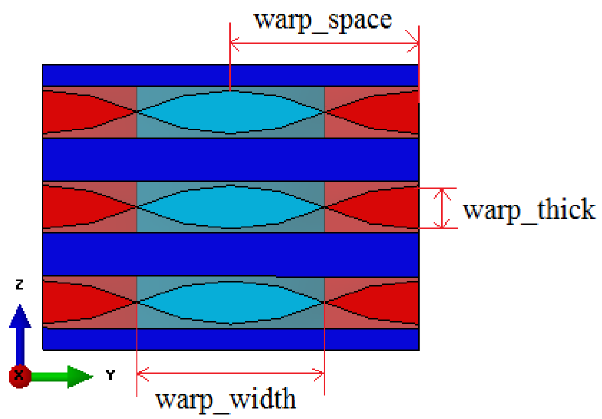

(b) Warp direction view

Figure 8.1 Geometric parameters of layer-to-layer interlock unit cell model

In order to investigate the effect of the geometric parameters on the effective properties, the material characterisation was carried out using UnitCells© for a range of layer-to-layer interlock 3D woven composites. As well as having the same type of reinforcement, all the UC models had the same properties of the constituents, as specified in Table 8.1. Geometric parameters of the weave for each model are listed in Table 8.2. Substantial ranges of variations have been given to various geometric parameters while keeping the warp yarn weaving angle and the warp and weft yarn volume fractions constant for all the models. The effective stiffness and strength properties calculated for all the cases considered are summarised in Table 8.3 and Table 8.4, respectively.

Table 8.1 Material properties of the epoxy resin and T300 CF yarn

Matrix (PRIME^{TM} 20LV)		Yarn (T300 CF, V_f =78.6%)	
E (GPa)	3.5	E_x (GPa)	181.32
v	0.35	E_y (GPa)	10.67
S_t (MPa)	73.0	v_{xy}	0.229
S_c (MPa)	120	v_{yz}	0.229
m	0.3	G_{xy} (GPa)	6.63
		S_{Xt} (MPa)	2067.1
		S_{Xc} (MPa)	1631.9
		S_{Yt} (MPa)	66.7
		S_{Yc} (MPa)	105.9
		S_{xy} (MPa)	67.4
		S_{yz} (MPa)	50.0
		m	0.3

Table 8.2 Geometric parameters of ten layer-to-layer interlock composite models

No.	Weft space	Warp space	Weft width	Weft thick	Warp width	Warp thick	Thick space	V_f Warp	V_f Weft	Angle	V_f Total
1	2.00	0.14	0.80	0.20	0.14	0.14	0.18	35.0%	15.0%	31.3°	50.0%
2	2.30	0.16	0.94	0.23	0.16	0.16	0.20	35.0%	15.0%	31.3°	50.0%
3	2.60	0.19	1.03	0.27	0.19	0.19	0.24	35.0%	15.0%	31.3°	50.0%
4	3.00	0.22	1.18	0.31	0.22	0.22	0.27	35.0%	15.0%	31.3°	50.0%
5	3.50	0.26	1.37	0.37	0.26	0.26	0.32	35.0%	15.0%	31.3°	50.0%
6	4.00	0.29	1.56	0.41	0.29	0.29	0.36	35.0%	15.0%	31.3°	50.0%
7	4.50	0.34	1.73	0.48	0.34	0.34	0.42	35.0%	15.0%	31.3°	50.0%
8	5.00	0.37	1.92	0.52	0.37	0.37	0.45	35.0%	15.0%	31.3°	50.0%
9	5.50	0.40	2.17	0.57	0.40	0.40	0.49	35.0%	15.0%	31.3°	50.0%
10	5.80	0.42	2.30	0.59	0.42	0.42	0.51	35.0%	15.0%	31.3°	50.0%

Table 8.3 Effective stiffness of ten layer-to-layer interlock composite models

No.	E_x (GPa)	E_y (GPa)	E_z (GPa)	G_{xy} (GPa)	G_{xz} (GPa)	G_{yz} (GPa)	ν_{xy}	ν_{xz}	ν_{yz}
1	42.44	33.24	7.25	3.16	7.26	2.75	0.0054	0.9639	0.3365
2	43.56	34.1	7.32	3.22	7.42	2.79	0.0048	0.9708	0.3344
3	40.94	33.17	7.24	3.11	7.4	2.76	0.0035	0.9835	0.3356
4	40.95	33.01	7.23	3.08	7.39	2.75	0.0036	0.9832	0.3356
5	40.2	33.14	7.25	3.1	7.44	2.77	0.0032	0.9872	0.3339
6	41.14	32.99	7.26	3.08	7.28	2.76	0.0046	0.9701	0.3371
7	39.36	32.65	7.23	3.05	7.42	2.76	0.0031	0.9873	0.3343
8	40.28	32.74	7.24	3.06	7.3	2.76	0.0042	0.9766	0.3360
9	41.21	33.6	7.28	3.09	7.38	2.78	0.0040	0.9773	0.3357
10	42.31	33.66	7.3	3.12	7.43	2.79	0.0038	0.9784	0.3362

Table 8.4 Effective strengths calculated with ten layer-to-layer interlock composite models

No.	S_{Xt} (MPa)	S_{Xc} (MPa)	S_{Yt} (MPa)	S_{Yc} (MPa)	S_{Zc} (MPa)	S_{Zc} (MPa)	S_{xy} (MPa)	S_{xz} (MPa)	S_{yz} (MPa)
1	316.79	296.68	392.12	396.71	54.99	93.73	36.52	61.62	30.79
2	331.19	307.32	402.65	407.55	54.96	94.93	36.42	61.98	30.68
3	285.47	272.54	397.48	400.86	54.23	93.96	38.53	61.73	30.45
4	285.41	269.9	398.03	397.29	53.92	93.16	40.32	62.12	30.63
5	276.20	264.73	396.97	400.19	53.57	92.81	38.62	62.41	30.11
6	289.50	276.23	395.77	398.41	53.55	93.95	38.18	62.47	30.02
7	266.23	250.54	396.52	396.66	54.20	91.91	38.17	63.29	30.95
8	275.69	267.08	394.56	394.36	52.94	92.21	38.19	61.54	29.93
9	289.01	275.49	404.33	406.35	53.41	93.54	38.36	61.39	30.22
10	299.27	283.23	407.14	407.95	53.48	94.10	38.20	61.63	31.47

Comparing the effective properties predicted with different models, it can be observed that, despite the substantial variations in the geometric parameters of the weave, the effective material properties vary only marginally. This suggests that the material response is primarily dependent on combination of three principal parameters: total fibre volume fraction, warp: weft yarn volume fraction ratio and weaving angle of warp yarns. To a large extent, these principal parameters capture the key trends of the variations caused by the seven individual geometric parameters.

Definition of the total fibre volume fraction is rather straightforward, as it has to be as high as can be achieved for a given type of reinforcement and the practical composite processing technology. Therefore, the maximum practically achievable fibre volume fraction should be the design value.

This reduces the number of parameters for the parametric study to two principal parameters, the yarn volume fraction ratio and the warp yarn weaving angle and they will be investigated in the sections to follow.

8.3 Volume Fraction Equivalency

For textile composites, there are a number of methods available for determining the total fibre volume fraction, such as the burn-off test. However, the procedure for determining the fibre volume fraction within the yarns is far less straightforward. A numerical study was undertaken to assess the effect the definition of fibre volume fraction within the yarns has on predictions of the effective properties of the composite.

Since the fibre within the yarn is not modelled explicitly in the mesoscale unit cell model, it can be represented by a homogeneous UD composite model. Two UD unit cell models, denoted as UC 1 and UC 2, were generated to represent the yarns with the fibre volume fractions of 66.4% (Figure 8.2 (a)) and of 80.1% (red area of Figure 8.2 (b)), respectively. Additional matrix material was added to the boundary of the model UC 2, which reduced the volume fraction in this model to 66.4%, same as that of UC 1.

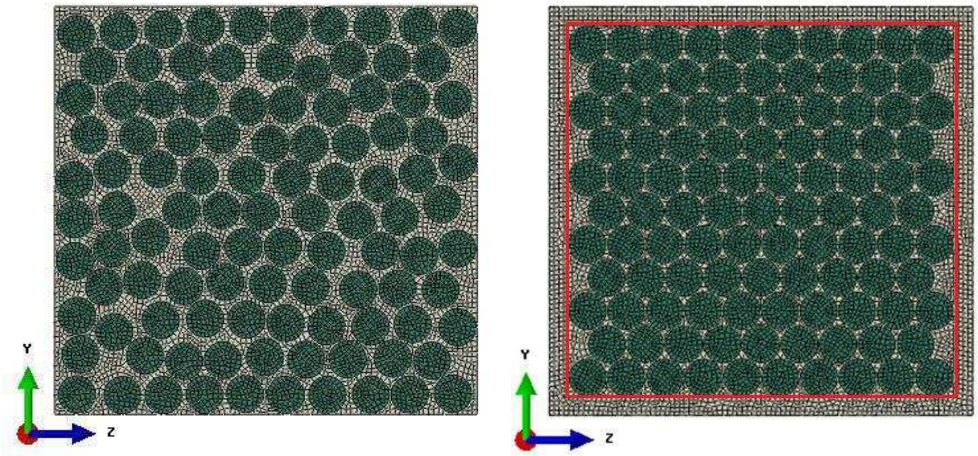

(a) UC 1 (V_f =66.4%) (b) UC 2 (V_f =80.1%→V_f =66.4%)

Figure 8.2 Unit cell model for UD yarn

Material properties of the matrix and the fibre as given in Table 8.5 were assigned to the two UD unit cell models. The effective stiffness and strengths calculated with the two models are summarised in Table 8.6 and Table 8.7, respectively.

Table 8.5 Material properties of PRIME^{TM} 20LV epoxy resin and T300 CF

	Matrix (PRIME^{TM} 20LV)	Fibre (T300 CF)
E_x (GPa)	3.5	230
E_y (GPa)	3.5	15
v_{xy}	0.35	0.2
v_{yz}	0.35	0.0714
G_{xy} (GPa)	1.3	15
S_t (MPa)	73.0	2500
S_c (MPa)	120	2000
m	0.3	0.3

Table 8.6 Effective stiffness values calculated with two types of UD composite UC models

	E_x (GPa)	E_y (GPa)	E_z (GPa)	G_{xy} (GPa)	G_{xz} (GPa)	G_{yz} (GPa)	ν_{xy}	ν_{xz}	ν_{yz}
UC 1	153.89	9.13	9.07	5.03	4.85	3.42	0.2448	0.2469	0.2831
UC 2	152.27	9.39	9.33	4.86	4.72	3.24	0.2459	0.2479	0.2889
error	1.1%	-2.9%	-2.9%	3.4%	2.7%	5.3%	-0.5%	-0.4%	-2.1%

Table 8.7 Effective strengths calculated with two types of UD composite UC models

	S_{Xt} (MPa)	S_{Xc} (MPa)	S_{Yt} (MPa)	S_{Yc} (MPa)	S_{Zc} (MPa)	S_{Zc} (MPa)	S_{xy} (MPa)	S_{xz} (MPa)	S_{yz} (MPa)
UC 1	1708.14	1338.82	52.22	80.83	49.68	78.65	39.40	40.19	39.37
UC 2	1690.20	1324.75	53.60	84.88	51.90	82.35	40.64	41.84	40.65
error	1.1%	1.1%	-2.6%	-5.0%	-4.5%	-4.7%	-3.2%	-4.1%	-3.3%

As can be seen, the effective properties of the two models are similar, despite the different distribution of the fibres. Therefore, it can be concluded that UC2 model, which had high fibre volume fraction within the yarn with some matrix surrounding it, can be equivalent to a yarn model with lower fibre volume fraction, as long as the total fibre volume fractions of the two models are the same. In other words, precise definition of the fibre volume fraction within the yarns is not essential in order to obtain acceptable predictions from a mesoscale model provided that the fibre contents in the warp and weft directions and overall fibre volume fraction are maintained. This is a very important conclusion as it would help to trivialise the need for precise fibre volume fractions in the yarn which difficult to measure on one hand and hard to simulation on the other hand. Advantages of this have been taken previously within the thesis where the fibre volume fractions were assumed at an unrealistic level of 90%. Comparing the effective properties of UC 1 and UC 2 demonstrates the validity of this assumption in the present application.

As a verification case, two layer-to-layer 3D woven unit cell models, Model 1 and Model 2, were generated and their effective stiffnesses and strengths were calculated. These unit cell models had the same weaving angle and the same fibre volume fraction of warp and weft yarns, but different fibre volume fractions within the yarns. The fibre and yarn volume fractions are specified in Table 8.8.

Table 8.8 Fibre volume fraction and yarn volume fraction

	Model 1	Model 2
Angle	31°	31°
Fibre volume fraction of warp yarn	23.73%	23.39%
Fibre volume fraction of weft yarn	12.52%	12.56%
Fibre volume fraction within yarns	69%	85%
Yarn volume fraction of warp yarn	34.39%	27.52%
Yarn volume fraction of weft yarn	18.14%	14.78%

The material properties that were assigned to the constituents, the matrix and the fibre, are specified in Table 8.5. The effective material properties of the yarns as given in Table 8.9 were calculated using UD unit cell models.

Table 8.9 Effective properties of the yarns with different fibre volume fractions

	Yarn (V_f =69%)	Yarn (V_f =85%)
E_x (GPa)	159.62	195.80
E_y (GPa)	9.21	11.72
v_{xy}	0.2429	0.2199
v_{yz}	0.2837	0.1881
G_{xy} (GPa)	4.92	8.32
S_{Xt} (MPa)	1771.77	2173.32
S_{Xc} (MPa)	1388.69	1703.42
S_{Yt} (MPa)	62.51	58.23
S_{Yc} (MPa)	100.81	93.62
S_{xy} (MPa)	62.32	50.70
S_{yz} (MPa)	42.52	45.50

The effective material properties of yarns were assigned to the two layer-to-layer interlock unit cell model to calculate the effective stiffness and strength as presented in Table 8.10 and Table 8.11, respectively.

Table 8.10 Effective stiffness values obtained with two types of layer-to-layer 3D woven composite models

	E_x (GPa)	E_y (GPa)	E_z (GPa)	G_{xy} (GPa)	G_{xz} (GPa)	G_{yz} (GPa)	ν_{xy}	ν_{xz}	ν_{yz}
Model 1	26.561	34.111	6.46	2.67	4.43	2.31	0.0028	0.9651	0.3530
Model 2	26.060	34.303	6.40	2.99	4.26	2.28	0.0036	0.9647	0.3506
error	1.9%	-0.6%	0.9%	-12.0%	3.8%	1.3%	-28.6%	0.0%	0.7%

Table 8.11 Effective strengths obtained with two types of layer-to-layer 3D woven composite models

	S_{Xt} (MPa)	S_{Xc} (MPa)	S_{Yt} (MPa)	S_{Yc} (MPa)	S_{Zt} (MPa)	S_{Zc} (MPa)	S_{xy} (MPa)	S_{xz} (MPa)	S_{yz} (MPa)
Model 1	208.91	194.14	404.68	415.42	56.17	105.66	41.64	42.87	40.24
Model 2	180.53	177.67	409.65	411.96	50.25	85.35	37.75	39.28	35.53
error	13.6%	8.5%	-1.2%	0.8%	10.5%	19.2%	9.3%	8.4%	11.7%

Comparing the predicted values of the effective properties, it can be seen that the fibre volume fraction within the yarns does not effect the effective material properties significantly, especially for the effective stiffness. For effective strength, although the results from two different models are not identical, the difference of strength is still in an acceptable range with the 16% difference in fibre volume fraction within the yarns. Therefore, by assuming a fibre volume fraction within the yarns in a realistic range, reasonable predictions of the effective stiffness and strength can be produced. Based on the information available in the open literature [176, 177], the maximum fibre volume fraction within the yarns in textile composites can be as high as 88.7%. In the parametric study process as presented here, fibre volume fraction within yarns was assumed to be 85%. This should not compromise the validity of the conclusions achieved while offering significant convenience in modelling.

8.4 Effect of Weft Yarn Offset on Effective Properties

The modelling framework as described in the previous sections was developed assuming an idealized regular structure of the reinforcement. In real textile composites, however, some degree of geometric variability is inherent within fibrous reinforcements. Geometric variability can potentially affect the forming process and the material performance. An initial study was carried out to investigate the influence of alignment of weft yarns on the mechanical behaviour of the composite. As can be seen from micro-CT image in Figure 8.3, in the weave, the weft yarn cross-sections were not aligned to the vertical axis, but to a slightly inclined line. Therefore, in addition to an idealised mesoscale UC model as shown in Figure 8.4, distorted UCs were generated, where weft yarns were offset horizontally for more realistic representation of the actual composite weaving structure. An example of UC with offset weft yarns is shown in Figure 8.5.

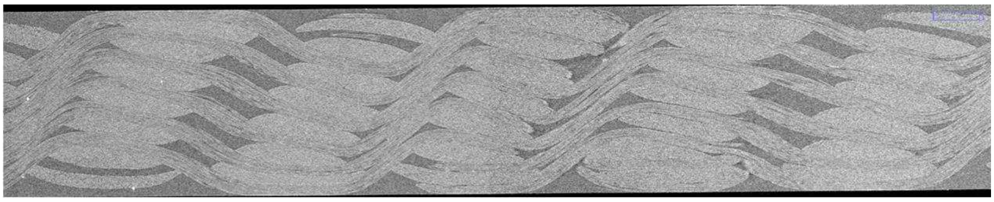

Figure 8.3 Micro CT image of carbon fibre reinforced textile composites

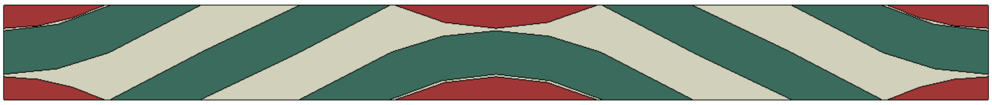

Figure 8.4 Idealized unit cell model of layer-to-layer interlock composites

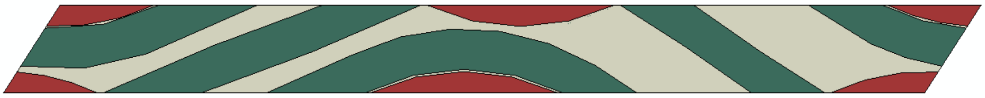

Figure 8.5 Unit cell model of layer-to-layer interlock composite with offset weft yarn

Due to the limitation of model generation, this analysis was carried out with mesoscale UCs which represent a textile composite based on the glass fibre reinforced fabric perform defined as GF1 in Table 7.10, the same input material and geometric parameters were used in all models. The material properties of matrix and yarn are listed in Table 7.11, Table 7.13 and Table 7.14. In total, four mesoscale UCs were generated with different degrees of weft yarn offset. For each model generated, the fibre and yarn volume fractions were calculated, and warp yarn weaving angles were evaluated. These are summarised in Table 8.12. As can be seen, introducing weft yarn offset alters primarily the weaving angle of the weft yarn, which takes different values on different sides of the weft yarn due to the offset as indicated in Table 8.12. The yarn volume fraction ratio and total fibre volume fraction within the UC are hardly affected.

Table 8.12 Weaving angle and yarn ratio at different degrees of weft yarn offset

Offset value	Angle	Yarn Ratio (Warp:Weft)	V	V_f
0.0×Weft_width	23.85°/23.85°	48.99%:13.24%	18.96	48.39%
0.1×Weft_width	22.30°/25.72°	49.05%:13.24%	18.96	48.44%
0.2×Weft_width	20.99°/28.06°	49.10%:13.24%	18.96	48.48%
0.3×Weft_width	19.86°/31.09°	49.16%:13.24%	18.96	48.52%

Predictions of the effective stiffnesses and strengths obtained for the models with different degrees of offset are summarised in Table 8.13 and Table 8.14, respectively.

Table 8.13 Elastic properties predicted at different degrees of weft yarn offset

Offset value	E_x (GPa)	E_y (GPa)	E_z (GP)	G_{xy} (GPa)	G_{xz} (GPa)	G_{yz} (GPa)	ν_{xy}	ν_{xz}	ν_{yz}
0.0×Weft_width	24.61	19.81	10.23	4.95	5.38	3.71	0.14	0.51	0.35
0.1×Weft_width	24.79	19.74	10.04	4.96	5.32	3.64	0.13	0.52	0.36
0.2×Weft_width	24.38	19.70	9.96	4.96	5.33	3.64	0.13	0.53	0.35
0.3×Weft_width	24.60	19.52	9.84	4.94	5.20	3.57	0.13	0.55	0.35

Table 8.14 Strength values predicted at different degrees of weft yarn offset

Offset value	S_{Xt} (MPa)	S_{Xc} (MPa)	S_{Yt} (MPa)	S_{Yc} (MPa)	S_{Zt} (MPa)	S_{Zc} (MPa)	S_{xy} (MPa)	S_{xz} (MPa)	S_{yz} (MPa)
0.0×Weft_width	185.16	184.85	223.16	185.08	48.74	70.03	35.89	43.50	27.34
0.1×Weft_width	184.32	186.39	203.87	180.69	49.80	72.17	36.00	43.23	27.87
0.2×Weft_width	186.38	187.00	233.85	187.13	52.21	74.46	35.59	45.38	28.35
0.3×Weft_width	183.85	185.70	232.26	186.17	55.36	75.50	36.24	50.78	29.07

The results presented in Table 8.13 and Table 8.14 suggests that the offset of weft yarn does not substantially affect the predicted effective stiffnesses and strengths. Having considered variability in terms of distortion in weave pattern, it can be concluded that idealised models would serve as a good basis to facilitate design activities, given the range of variability in the results due to this factor.

8.5 Parametric Study

Having excluded side issues, such as fibre volume fraction in yarns and variability in woven structure, attention can now be focused upon the principal parameters. A parametric study was carried out for a layer-to-layer interlock 3D woven composite material to determine the effects of warp yarn weaving angle and the yarn volume fraction ratio combination on the impact resistance of such composites.

For the parametric study of layer-to-layer interlock 3D woven composites, the parametric unit cell model was generated (Figure 8.1). The geometric parameters were adjusted to make sure the total yarn volume fraction of the unit cell models remained 60%, while the volume fraction ratio of the warp and the weft yarns and the warp yarn weaving angle were varied from case to case as specified in Table 8.15. In total, 17 different unit cell models were created to facilitate the parametric study.

In this study, the constituent materials were PRIME^{TM} 20LV epoxy resin and IM7 carbon fibre. Their properties are given in Table 3.6 and Table 4.2, respectively. The fibre volume fraction within the yarns was assumed to be 85%, resulting in a total fibre volume fraction of 51%. Following the methodology presented in Chapter 5, the strain rate dependent effective properties of yarn, as specified in Table 8.16, were calculated.

To represent the constitutive behaviour of the composite at the macroscale, the methodology as described in Chapter 6 was applied to generate the ANN systems for each of the cases in Table 8.15. For each composite configuration, the mesoscale UC was created, which was employed to generate the training cases for the ANN. The ANN was trained, and the generated ANN database was accessed by an appropriate user subroutine to define the composite material behaviour in the FE model.

Table 8.15 Geometric parameters of UC models in the parametric study

NO.	Weft space	Warp space	Thick space	Weft width	Weft thick	Warp width	Warp thick	Angle	Ratio, warp:weft
1	2.8	0.220	0.612	1.339	0.740	0.220	0.220	50°	40%:20%
2	3.1	0.130	0.599	1.717	0.770	0.130	0.130	50°	35%:25%
3	3.9	0.100	0.546	2.583	0.740	0.100	0.100	50°	30%:30%
4	2.7	0.220	0.596	1.040	0.650	0.220	0.220	45°	45%:15%
5	3.1	0.295	0.526	1.603	0.605	0.295	0.295	45°	40%:20%
6	3.9	0.310	0.512	2.350	0.635	0.310	0.310	45°	35%:25%
7	3.9	0.385	0.388	2.690	0.500	0.385	0.385	45°	30%:30%
8	3.4	0.100	0.551	1.484	0.560	0.100	0.100	40°	45%:15%
9	3.9	0.385	0.613	1.842	0.755	0.385	0.385	40°	40%:20%
10	3.5	0.190	0.477	1.949	0.635	0.190	0.190	40°	35%:25%
11	3.6	0.325	0.424	2.239	0.605	0.325	0.325	40°	30%:30%
12	3.1	0.325	0.489	1.215	0.545	0.325	0.325	35°	45%:15%
13	3.8	0.310	0.515	1.816	0.635	0.310	0.310	35°	40%:20%
14	3.2	0.370	0.371	1.745	0.500	0.370	0.370	35°	35%:25%
15	3.8	0.370	0.375	2.360	0.545	0.370	0.370	35°	30%:30%
16	3.9	0.385	0.476	1.640	0.500	0.385	0.385	30°	45%:15%
17	3.9	0.355	0.414	1.955	0.500	0.355	0.355	30°	40%:20%

Table 8.16 Effective properties of IM7 carbon fibre yarn (V_f=85%)

ρ (kg/m^3)	1680	Strain rate constant, C
E_1 (GPa)	234.8	0.0000
E_2 (GPa)	13.9	0.0046
v_{12}	0.288	
v_{23}	0.454	
G_{12} (GPa)	6.3	0.0053
S_{Xt} (MPa)	4787.0	0.0001
S_{Xc} (MPa)	3029.4	0.0000
S_{Yt} (MPa)	63.5	0.1031
S_{Yc} (MPa)	101.9	0.1048
S_{xy} (MPa)	61.3	0.0982
S_{yz} (MPa)	48.4	0.1124
m	0.3	

The impact resistance for different composite configurations was assessed by simulating the ballistic impact cases on the composite panels. The FE models in this study were identical to those employed in the model validation study in Section 7.3 of Chapter 7. Specifically, a 4 mm thick circular composite plate, 100 mm in diameter, was impacted by a rigid ball with radius of 6.35 mm and density of 7800.0 kg/m^3. The composite was modelled as a homogenous material, with its material properties being represented via the ANN user material subroutine. An initial impact velocity was assigned to the rigid ball. The velocity, displacement and acceleration of the rigid ball were plotted as outputs. Output curves of this kind were previously obtained for the plate impact simulation in Section 7.3.3 of Chapter 7 and those are shown in Figure 7.6 and Figure 7.8.

Two sets of simulations were carried out to assess the impact resistance of various configurations of the layer-to layer interlock composite. In one of them, an initial impact velocity of 200 m/s was assigned to the rigid ball, and the residual velocities were determined for each layer-to-layer interlock 3D woven composite model as specified in Table 8.17 in the column under ‘Residual velocity’.

The bisection method as described in Section 7.3.3 of Chapter 7 was applied to determine the critical velocities, the values are also shown in Table 8.17 under the column ‘Critical velocity’, which are presented as a narrow range as the director outcomes of the bisection analysis.

Table 8.17 Velocity predictions in the parametric study of layer-to-layer interlock 3D woven composites

NO.	Impact velocity (m/s)	Residual velocity (m/s)	Critical velocity (m/s)
1	200.0	138.28	[164.84, 165.63]
2	200.0	127.41	[174.22, 175.00]
3	200.0	81.75	[188.28, 189.06]
4	200.0	112.05	[192.19, 192.97]
5	200.0	105.57	[199.22, 200.00]
6	200.0	122.90	[178.91, 179.69]
7	200.0	-113.61	[202.34, 203.13]
8	200.0	160.26	[159.38, 160.16]
9	200.0	141.51	[167.19, 167.97]
10	200.0	133.08	[177.34, 178.13]
11	200.0	-135.28	[206.25, 207.03]
12	200.0	137.20	[179.69, 180.47]
13	200.0	144.00	[180.47, 181.25]
14	200.0	135.91	[179.69, 180.47]
15	200.0	105.81	[193.75, 194.53]
16	200.0	145.05	[182.03, 182.81]
17	200.0	-147.43	[203.91, 204.69]

To facilitate the assessment of data obtained in the parametric study, the graphic representation of the data was applied. The critical velocity was plotted as function of the warp yarn weaving angle in Figure 8.6 (a) where critical velocity was obtained at a range of weaving angles. Different values of the critical velocity were shown at each pre-designated weaving angle due to different warp to weft fibre volume fraction ratios. As can be seen, the highest value of the critical velocity was obtained with the composite configuration having the weaving angle of 40° at an appropriate warp to weft fibre volume fraction ratio.

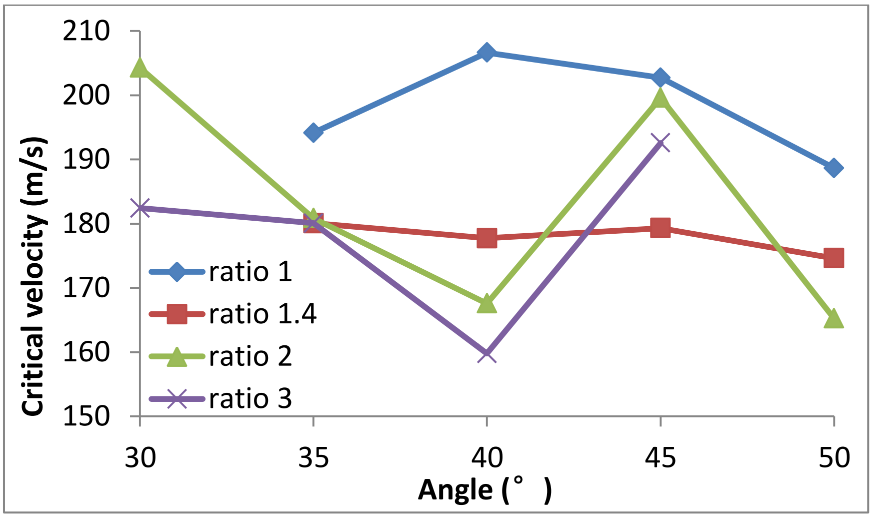

(a) Critical velocity plotted against the weaving angle

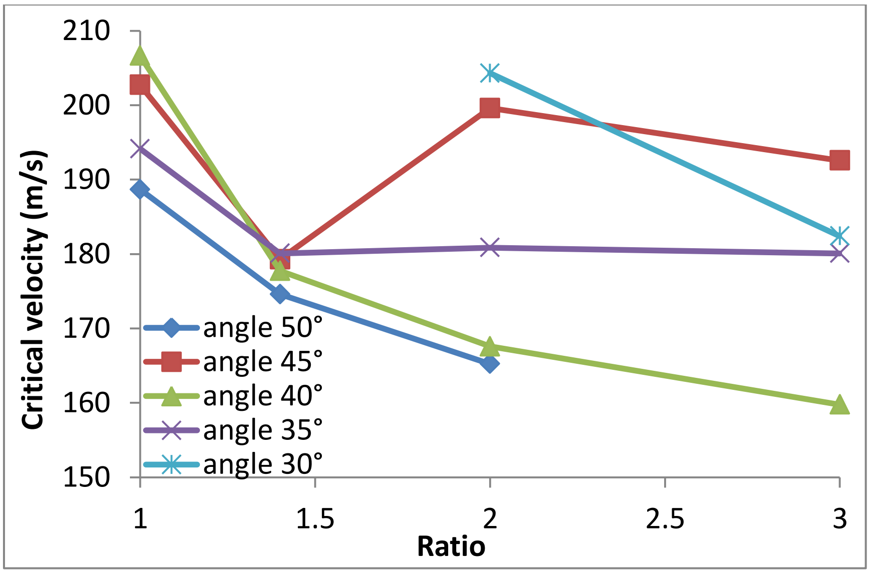

(b) Critical velocity plotted against the ratio of the warp and weft yarns

Figure 8.6 Critical velocity of model with different angle and volume fraction ratio

Similarly, plotting the critical velocity against the warp to weft yarn ratio in Figure 8.6 (b), it becomes apparent that the composite configuration with equal volume fractions of warp and weft yarns should have the best impact resistance out of all the cases considered. According to the data presented in Table 8.17, the composite configuration 11, which has and 30% warp and 30% weft yarn volume fraction satisfies both conditions. It should be pointed out that equal fibre volume fraction in warp and weft directions does not mean equal properties in these two directions at all. In fact, given the significant disparity between the undulating fibre path of the warp yarns and straight fibre path of the weft yarns, the effective properties of the composite in these two directions can be rather different. As an illustration, the effective properties of the parametric study unit cell models with the equal fibre volume fraction in the warp and weft directions are listed in Table 8.18.

Table 8.18 Effective properties of unit cell models (warp: weft=30%:30%)

No.	3	7	11	15
Angle (°)	50	45	40	35
E_x (GPa)	27.94	36.61	30.33	32.80
E_y (GPa)	80.98	80.09	80.61	81.72
E_z (GPa)	10.72	8.82	9.53	9.69
G_{xy} (GPa)	3.17	3.66	3.35	3.43
G_{xz} (GPa)	9.15	5.01	8.32	7.32
G_{yz} (GPa)	2.98	3.12	3.36	3.40
S_{Xt} (MPa)	917.58	1298.50	870.28	547.85
S_{Xc} (MPa)	755.02	941.44	754.65	762.85
S_{Yt} (MPa)	3337.50	3545.10	3367.80	3373.80
S_{Yc} (MPa)	5364.60	5347.60	5364.10	5376.90
S_{Zt} (MPa)	236.62	203.79	201.34	187.92
S_{Zc} (MPa)	694.77	769.75	729.95	661.00
S_{xy} (MPa)	242.22	281.31	266.75	251.44
S_{xz} (MPa)	339.25	270.46	326.19	311.17
S_{yz} (MPa)	245.12	241.82	272.47	255.81

8.6 Summary

A parametric study for textile composites has been carried out in this chapter. The process can be adapted as a methodology for preliminary optimisation as a part of material selection. It has been illustrated using a layer-to-layer interlock 3D woven composite. Three principal parameters were identified out of seven geometric parameters, namely the total fibre volume fraction, the ratio of warp and weft yarns volume fractions and the warp yarn weaving angle. The effects of fibre volume fraction within yarn and the weft yarn offset on effective material properties were studied and they were found to contribute only marginally to the behaviour of the composite and hence can be neglected in early stages of material selection and architecture design. Impact simulation of layer-to-layer interlock 3D woven composites with different principal parameters was performed in Abaqus/Explicit to evaluate the impact resistance of different models. From the analysis the conclusion can be made that the model with warp yarn weaving angle of 40° and 30% warp and 30% weft yarn volume fraction has the best impact resistance out of the present analysis, given the limited scope of factors taken into consideration.

Chapter 9 Conclusions and Future Work

9.1 Conclusions

The undertaken project aimed to develop a multiscale material characterisation methodology, which could be applied to textile composites for design, analysis and optimisation, in view of their application for the fan blade containment casings of civil aero-engine. The major achievements of this research were highlighted below.

9.1.1 Unit cell modelling toolbox UnitCells©

UnitCells© was a pre-existing code developed at the University of Nottingham automated specifically for composite characterisation based on multiscale and multi-physics modelling [73] but with rather limited functionality prior to the present project. It has been subjected to substantial and systematic development within the present project. The particular areas the present project contributed exclusively are the strength prediction and the mesoscale unit cells particularly relevant to textile composites. To enable the construction of mesoscale models, two important extensions have been made such that UnitCells© has the access to other established codes, TexGen for constructing textile architecture and Hypermesh for generating appropriate meshes for subsequent FE analysis of the unit cells. These are all in addition of the existing functionalities such as the imposition of periodic boundary conditions, extraction of effective properties. After the efforts through the present project, there are seven types of microscale models and eleven types of mesoscale models available in this toolbox. The macroscale characterisation is limited to a laminate level, where the constituent laminae properties can be either defined by the user or as the outcomes of a previous micro- or mesoscale analysis of a UD or textile composite. The basic output parameters from UnitCells© are the effective elastic properties, effective strength, thermal expansion coefficients and thermal and electric conductivities.

1) Types of applicable composites in UnitCells©

   a) The UD composites, such as a lamina in a composite laminate or a yarn in a textile composite.

  b) Particulate reinforced/moderated composites which may be applied to define the matrix in a fibre reinforced composite.

  c) Textile composites: braided (2D and 3D) and woven (2D and 3D).

  d) Laminated composites: laminae can be UD or textile composites obtained from the analysis of the lower scale composite types which are listed above.

2) Types of available unit cells in UnitCells©

  a) UD: square, hexagonal and random fibre distribution.

  b) Particulate reinforced: cubic (from simple cubic packing) and dodecahedral (for FCC face centred cubic packing).

  c) Porous materials: same as above with the particulate reinforcement replaced by void.

  d) 2D and 3D braided textile composites.

  e) 2D and 3D woven textile composites.

  f) Laminated composites.

3) Types of available analyses in UnitCells©

  a) Thermo-mechanical analysis: for determining the effective elastic properties and thermal expansion coefficients.

  b) Flexural analysis: for calculating the bending stiffness and effective flexural properties.

  c) Heat conduction analysis: for identifying the effective heat conductivities.

  d) Electric conduction analysis: for calculating the effective electric conductivities.

e) Strength analysis: for calculating the effective strength at quasi static loading.

The multi scale unit cell modelling toolbox UnitCells© has been verified via systematic sanity checks and other inspections of every observable perspective to iron out any inconsistency before any attempt at meaningful validation. The establishment of a comprehensive set of verification cases is one of the most important outcomes in terms of software development.

The predicted stiffness and strength was compared with experimental results to validate the accuracy of UnitCells©.

9.1.2 Strain rate sensitivity study

A method of accounting for the rate sensitivity in multi-scale modelling of textile composites has been developed and applied. The rate sensitivity of the stiffness and strength of the matrix (PRIME^{TM} 20LV epoxy resin in this study) was measured experimentally and the appropriate parameters were determined by processing to fit the experimental data. The UD unit cell modelling was applied to determine the strain rate-dependent material properties of the T300 carbon fibre (CF) yarns as a UD composite, assuming that the CF constituent is not rate-sensitive. With the strain rate-dependent material properties of yarns and matrix, a mesoscale unit cell model was applied to calculate the strain rate-dependent material properties of T300 carbon fibre reinforced 3D textile composite.

A similar exercise has also been conducted GF textile composites with the rate sensitivity of the fibres duly accounted for at the microscale level of modelling.

9.1.3 ANN system

The methodology for representing the constitutive behaviour of textile composites at a macroscale, which naturally incorporates the damage initiation, the stiffness degradation and the final failure, was proposed and applied. Since no failure criteria are readily available for textile composites, the method based on the ANN systems was proposed as an alternative. The ANN systems were verified for micro-, meso- and macroscale models, respectively.

At the microscale, the ANN system was applied to represent the response of UD composites. The training cases were generated by using a CDM model to account for material degradation at the microscale. The outcome of the ANN simulation allows the UD composite to be homogenised into a monolithic counterpart. The applicability of the approach has been verified by comparing the behaviour of the monolithic material through a model using a single finite element of a material as defined through the stress-strain relationship obtained from the ANN system that from original CDM model implemented through analysis of the microscale unit cell. The agreement achieved means the ANN system is sufficiently accurate to reflect the internal relationship between the inputs and outputs as brought in through all training cases.

At the mesoscale, the ANN system was used in the same fashion. Unit cell models with progressive damage have been used to generate large numbers of training cases sufficiently comprehensive to cover all characteristics of the material. The results demonstrate that the ANN system so obtained is capable of reflecting damage initiation and evolution in the textile composite models. To predict the final failure of the element, a failure criterion based on the singularity of the Jacobian matrix has been developed and incorporated into the ANN system. An indicator was output from the ANN system to signify the status of failure of the element. With the ANN, the failure envelopes for the 3D braided composites were generated as an example to illustrate the capability of the ANN system to represent the damage initiation, stiffness degradation and final failure of 3D textile composites.

As another example of applications of the ANN system at macroscale, it was applied to laminated composites to define the constitutive response of laminates, which are treated as homogenised monolithic materials. It has been demonstrated that, with the ANN system, failure envelopes could be constructed for the entire laminate, rather than for the individual plies. The results were verified against those obtained from conventional laminate analysis. This eliminates the need of modelling each layer explicitly when dealing with the simulation of large components. As a result, the modelling efforts and the computational costs can be reduced efficiently, provided that an appropriate ANN system is established prior to the structural simulation.

As a validation, the ANN system was used to predict the critical velocities of three types of layer-to-layer interlock 3D woven composite panel. The predicted results matched well with the experimental data.

Furthermore, as an illustration of its potential capability, the ANN system obtained for a type of 3D textile composite was applied to predict the impact behaviour of a component simulating the fan blade off scenario for the fan blade containment casing.

9.1.4 Parametric study on impact resistance

To explore the most important objective of this research, a parametric study based on ANN system was conducted to determine the effects of geometry parameters of the 3D textile composite on for their impact resistance. This was performed on a 3D woven layer-to-layer interlock composite. Three principal parameters related to the geometry of the weave were identified that affect the effective properties of the composite most significantly, the total fibre volume fraction, ratio of warp and weft yarns volume fraction and warp yarns weaving angle. The outcomes of the parametric study are informative for material selection and design optimisation and therefore are of significant practical implications.

Strain rate dependency can also be incorporated in the ANN system which was successfully applied to represent the constitutive behaviour of 3D woven layer-to-layer interlock composites. Impact simulations with different principal parameters were carried in Abaqus/Explicit to determine the critical velocity for different composite configurations. The obtained values of the geometric parameters at which the highest critical velocity was achieved would serve as an optimal set of parameters out of a preliminary material design exercise.

9.2 Future Work

1) In its present form, the mesoscale unit cells available in UnitCells© have a powerful capability in composite material characterisation. However, they can only be applied to predefined preform architectures within the toolbox, although geometric dimensions of various features are allowed to vary within practically meaningful ranges. This is the main limitation of applying this toolbox for textile composite material design. Application to any architecture of a new topology will

require the intervention of the developer by putting a new unit cell in position before use can be made of it for subsequent analysis and optimisation.

The developed toolbox, UnitCells©, can be potentially improved by supplementing it with a graphic user interface that allows the user to create new unit cells of different geometric models. At present, it only allows to modify the existing models in terms of the parametric input, mesh density, etc. Reference can be made to the interface of TexGen [45] where architecture can be created manually, although the actual provision of the interface of TexGen is limited to weaves. With such an interface, users should be able to create a geometric model with different yarn architecture easily by clicking some buttons. The main challenge in this development would be the automatic generation of the periodic mesh for the newly designed model. The current version TexGen can export periodic mesh of an acceptable quality for unit cells with a simple structure, while the mesh quality of the unit cells of complex structures is not acceptable. Therefore, a more powerful meshing module for TexGen is needed.

Until the meshing module of TexGen become available, the approach of employing Hypermesh script as has been established in the present project will be the way forward. The challenge will be the automatic generation of periodic meshes from the geometric mode created without users' intervention.

2) Since the inputs of the current ANN are the strain components and the outputs are the corresponding stress components, for a given strain state, the outputs of the ANN remain the same regardless whether it defines the material response during the loading or unloading of the material. However, once the damage is initiated in the material, its stiffness should reduce and during unloading the stress-stain curve should follow a different path. Therefore, a rational mechanism should be developed distinguish between loading, unloading and reloading of the material.

3) The current criterion for element deletion in the ANN system is that the element gets deleted at the state when its Jacobian matrix becomes singular, which makes the predicted result conservative. In order to improve the accuracy of failure predictions, a different criterion can be devised that accounts for the residual strengths the material beyond that point, although deformation localisation will

remain as the limit of applicability as defined by the use of unit cells which are based on the assumption of regularity in the meso-structures.

4) The parametric study as presented in Chapter 8 was carried out based on 17 combinations of parameters, which was limited in scope. A mathematical optimization method can be adopted to determine the best parameter combination. The main challenge here is that covering all possible parameter combination would require a substantial computational effort, and this will be in addition to ANN training and an impact simulation. Theoretically, an ANN system could include all geometric parameters as a part of the inputs (a full parameter ANN system). However, the demand on computing power might easily make it impractical. A more efficient computational method will have to be introduced to overcome this difficulty.

To make the full parameters ANN system feasible, the number of input parameters of ANN can be reduced by applying principal component analysis (PCA) [178]. PCA defines a set of new variables (principal components) of significantly reduced number, each as a combination of the original set of parameters. Successful application of PCA may offer a way forward when solving the problem of large inputs.

References

[1] Federal Aviation Administration (United States), Federal aviation regulation part 33, section 33.94-blade containment and rotor unbalance tests, 1984

[2] Fan case design with metal foam between Kevlar, United States patent application publication, US 6652222B1, Nov. 25, 2003

[3] Fan containment case, United States patent application publication, US 2011/0138769, 16 June 2011

[4] European Aviation Safety Agency, Certification Specifications for Engines CS-E 810 Compressor and Turbine Blade Failure,10 December 2007

[5] G. D. Roberts, J. M. Pereira, M. S. Braley, W. A. Arnold, J. D. Dorer, W. R. Watson, Design and Testing of Braided Composite Fan Case Materials and Components. NASA/TM—2009-215811, 2009

[6] E. R. Chapdelaine, B. C. Fenton, R. A. Delucia, Statistics on aircraft gas turbine engine rotor failures that occurred in US commercial aviation during 1989 (final report), DOT/FAA/CT-92/5, 1992

[7] R. A. Delucia, B. C. Fenton, J. Blake, Statistics on aircraft gas turbine engine rotor failures that occurred in US commercial aviation during 1987 (final report). DOT/FAA/CT-90/19, 1991

[8] K. S. Carney, J. M. Pereira, D. M. Revilock, P. Matheny, Jet engine fan blade containment using an alternate geometry, *International Journal of Impact Engineering*, 36:720–728, 2009

[9] T. Zhang, W. Chen, Y. Guan, D. Gao, Study on Titanium Alloy TC4 Ballistic Penetration Resistance Part I: Ballistic Impact Tests, *Chinese Journal of Aeronautics*, 25: 388-395, 2012

[10] C. L. Stotler, A. P. Coppa, Containment of Composite Fan Blades, Final Report, NASA CR–159544, 1979

[11] R. Karakuzu, E. Erbil, M. Aktas, Damage prediction in glass/epoxy laminates subjected in impact loading, *Indian Journal of Engineering & Materials sciences*, 17: 186-198, 2010

[12] ALBANY Engineered Composites. http://www.albint.com/business/aec/en-us/Production/Technologies/3D-Reinforced-Composites.aspx

[13] M. McClain, J. Goering, Rapid assembly of fibre performs using 3D woven components. Albany Engineered Composites, Inc. 2012

[14] Hexcel® Industrial selector guide, http://www.hexcel.com/Resources/SelectorGuides/Industrial_SelectorGuide.pdf

[15] L. Chen, X. M. Tao, C. L. Choy, On the microstructure of three-dimensional braided performs, *Composites Science and Technology*, 59: 391-404, 1999

[16] G. Fang, J. Liang, Q. Luo, B. Wang, Y. Wang, Investigation on the compressive properties of the three dimensional four-directional braided composites, *Composite Structures*, 93: 392–405, 2011

[17] D. Li, Z. Lu, L. Chen, J. Li. Microstructure and mechanical properties of three-dimensional five-directional braided composites, *International Journal of Solids and Structures*, 46:3422–3432, 2009

[18] F. Zhang, Z. Liu, Z. Wu, G. Tao, A New Scheme and Microstructure Model for 3D Full 5-directional Braided Composites, *Chinese Journal of Aeronautics*, 23: 61-67, 2010

[19] H. Xuan, R. Wu, Aero engine turbine blade containment tests using high-speed rotor spin testing facility, *Aerospace Science and Technology*, 10:501–508, 2006

[20] D. Naik, S. Sankaran, B. Mobasher, S. D. Rajan, J.M. Pereira, Development of reliable modelling methodologies for fan blade out containment analysis – Part I: Experimental studies, *International Journal of Impact Engineering*, 36:1–11, 2009

[21] G. T. Smith, Composite Containment Systems for Jet Engine Fan Blades, Thirty-sixth Annual Conference of the Reinforced Plastics/Composites Institute of the Society of the Plastics Industry, Inc. (NASA TM–81675),Washington, DC, Feb. 16–20, 1981

[22] G. D. Roberts, J. M. Pereira, M. S. Braley, W. A. Arnold, J. D. Dorer, W. R. Watson, Design and Testing of Braided Composite Fan Case Materials and Components. NASA/TM—2009-215811, 2009

[23] S. J. Lundin, R. B. Mueller, Advanced aircraft materials, engine debris penetration testing. DOT/FAA/R-03/37, 2005

[24] Z. Stahleckera, B. Mobashera, S. D. Rajana, J. M. Pereirab, Development of reliable modeling methodologies for engine fan blade out containment analysis. Part II: Finite element analysis, *International Journal of Impact Engineering*, 36: 447–459, 2009

[25] J. Aboudi, Micromechanical analysis of composites by the method of cells, *Applied Mechanics Reviews*, 42:193–221, 1989

[26] S. Nemat-Nasser, M. Hori, Micromechanics: overall properties of heterogeneous materials, Amsterdam: Elsevier Science Publishers, 1993

[27] ASTM D3039 / D3039M-14, Standard Test Method for Tensile Properties of Polymer Matrix Composite Materials, ASTM International, West Conshohocken, PA, 2014

[28] P. J. Minguet, M. J. Fedro, C. K. Gunther, Test Methods for Textile Composites, NASA Contractor Report 4609, 1994

[29] T. W. Clyne, P. J. Withers, An introduction to metal matrix composites, Cambridge University Press, 1993

[30] C. R. Barrett, W. D. Nix, A. S. Tetelman, The principles of engineering materials, Prentice-Hall, Englewood cliffs, NJ, 1973

[31] J. Aboudi, Mechanics of Composite Materials: A Unified Micromechanical Approach (Studies in Applied Mechanics), Elsevier, 1991

[32] Z. Hashin, B. W. Rosen, The elastic moduli of fiber-reinforced materials, *Journal of Applied Mechanics*, 31:223-232, 1964

[33] A. V. Hershey, The elasticity of an isotropic aggregate of anisotropic cubic crystals, *Journal of Applied Mechanics*, 21: 236-241, 1954

[34] B. Budiansky, On the elastic moduli of some heterogeneous materials, *Journal of the Mechanics and Physics of Solids*, 13:223-227, 1965

[35] T. Mori, K. Tanaka, Average stress in matrix and average elastic energy of materials with misfitting inclusions, *Acta Metallurgica*, 231:571-574, 1973

[36] R. M. Christensen, K. H. Lo, Solutions for the effective shear properties in three phase sphere and cylinder models, *Journal of the Mechanics and Physics of Solids*, 27:315-330, 1979

[37] R. Hill, Continuum micromechanics of elastoplastic polycrystals, *Journal of the Mechanics and Physics of Solids*, 13:89-101, 1965

[38] N. Pan, Analysis of woven fabric strengths: prediction of fabric strength under uniaxial and biaxial extensions, *Composites Science and Technology*, 56:311-327, 1996

[39] H. Sun, X. Qiao, Prediction of the mechanical properties of three-dimensionally braided composites, *Composites Science and Technology*, 57:623-629, 1997

[40] M. M. Shokrieh, M. S. Mazloomi, A new analytical model for calculation of stiffness of three-dimensional four-directional braided composites, *Composite Structures*, 94:1005–1015, 2012

[41] R. Haj-Alia, J. Aboudia, A new and general formulation of the parametric HFGMC micromechanical method for two and three-dimensional multi-phase composites, *International Journal of Solids and Structures*, 50:907–919, 2013

[42] R. Haj-Alia, J. Aboudia, Formulation of the high-fidelity generalized method of cells with arbitrary cell geometry for refined micromechanics and damage in composites, *International Journal of Solids and Structures*, 47:3447–3461, 2010

[43] S. Li, A. Wongsto, Unit cells for micromechanical analyses of particle-reinforced composites, *Mechanics of Materials*, 36:543-572, 2004

[44] T. Zeng, L. Wu, L. Guo, Mechanical analysis of 3D braided composites: a finite element model, *Composite Structures*, 64:399–404, 2004

[45] http://texgen.sourceforge.net/index.php/Main_Page

[46] P. Suquet, Elements of homogenization for inelastic solid mechanics, in: Homogenization Techniques for Composite Media. Sanchez-Palencia, E. and Zaoui, A. (Eds), Lecture Notes in Physics**,** Springer-Verlag, Berlin, 194–278, 1987

[47] A. Wongsto, S. Li, Micromechanical FE analysis of UD fibre-reinforced composites with fibres distributed at random over the transverse cross-section, *Composites Part A*, 36:1246–12663, 2005

[48] S. Li, General unit cells for micromechanical analyses of unidirectional composites, *Composites Part A*, 32:815-826, 2001

[49] G. Fang, J. Liang, Y. Wang, B. Wang, The effect of yarn distortion on the mechanical properties of 3D four-directional braided composites, *Composites Part A*, 40: 343–350, 2009

[50] K. Mehmet, V. Stepan, E. Alexander, M. Dmitri, I. Verpoest, Internal geometry evaluation of non-crimp 3D orthogonal woven carbon fabric composite, *Composites Part A*, 41:1301–1311, 2010

[51] D. Bigaud, P. Hamelin, Stiffness and failure modelling of 2D and 3D textile-reinforced composites by means of imbricate-type elements approaches, *Computers and Structures,* 80: 2253–2264, 2002

[52] L. Jiang, T. Zeng, S. Yan, D. Fang, Theoretical prediction on the mechanical properties of 3D braided composites using a helix geometry model, *Composite Structures*, 100: 511–516, 2013

[53] S. Li, Boundary conditions for unit cells from periodic microstructures and their implications, *Composites Science and Technology*, 68:1962–1974, 2008

[54] S. Li, On the nature of periodic traction boundary conditions in micromechanical FE analyses of unit cells, *IMA Journal of Applied Mathematics*, 77:441–450, 2012

[55] G. D. Roberts, R. K. Goldberg, W. K. Binienda , W. A. Arnold, J. D. Littell, L. W. Kohlman. Characterization of Triaxial Braided Composite Material Properties for Impact Simulation, NASA/TM—2009-215660, 2009

[56] A. Nia, M. Sadeghi, An experimental investigation on the effect of strain rate on the behaviour of bare and foam-filled aluminium honeycombs, *Materials and Design*, 52:748–756, 2013

[57] W. W. Chen, B. Song, Split Hopkinson (Kolsky) Bar: Design, Testing and Applications, Mechanical Engineering Series, DOI 10.1007/978-1-4419-7982-7_1, 2011

[58] J. Harding, E. O. Wood, J. D. Campbell, Tensile testing of materials at impact rates of strain, *Journal of Mechanical Engineering and Science*, 2:88-96, 1960

[59] R Foroutan, J. Nemes, H. Ghiasi, P. Hubert, Experimental investigation of high strain-rate behaviour of fabric composites, *Composite Structures*, 106:264–269, 2013

[60] M. Mahmood, J. Majid , Investigation of strain rate effects on in-plane shear properties of glass/epoxy composite, *Composite Structures*, 91:95–102, 2009

[61] Y. Hou, H. Hu, B. Sun, B. Gu. Strain rate effects on tensile failure of 3-D angle-interlock woven carbon fabric, *Materials and Design*, 46:857–866, 2013

[62] J. López-Puente, S. Li. Analysis of strain rate sensitivity of carbon/epoxy woven composites, *International Journal of Impact Engineering*, 48:54-64,2012

[63] W. Hufenbach, A. Langkamp, M. Gude, C. Ebert, A. Hornig, S. Nitschke, H. Böhm, Characterization of strain rate dependent material properties of textile reinforced thermoplastics for crash and impact analysis, *Materials Science*, 2:204–211, 2013

[64] C. Ebert, W. Hufenbach, A. Langkamp, M. Gude, Modelling of strain rate dependent deformation behaviour of polypropylene, *Polymer Testing*, 30:183–187, 2011

[65] A. Y. Malkin, A. I. Isayev, Rheology: Concepts, Methods, and Applications, ChemTec Publishing, 59–60, 2006

[66] D. Roylance, Engineering Viscoelasticity, Cambridge, MA 02139: Massachusetts Institute of Technology, 8–11, 2001

[67] M. Meyers, K. Chawla, Mechanical behaviour of Materials, Prentice Hall, 570–580, 1999

[68] D. Mohotti, M. Ali, T. Ngo, J. Lu, P. Mendis, Strain rate dependent constitutive model for predicting the material behaviour of pleurae under high strain rate tensile loading, *Materials and Design*, 53: 830–837, 2014

[69] I. Daniel, B. Werner, J. Fenner, Strain-rate-dependent failure criteria for composites, *Composites Science and Technology*, 71:357–364, 2011

[70] I. Daniel, J. Luo, M. Schubel, B. Werner, Interfibre/interlaminar failure of composites under multi-axial states of stress, *Composites Science and Technology*, 69: 764–771, 2009

[71] G. Cowper, P. Symonds, Strain hardening and strain-rate effects in the impact loading of cantilever beams, Tech. Rep., Brown University Division of Applied Mathematics, 1957

[72] C. Yen, Ballistic impact modelling of composite materials, 7th international Ls-Dynauser’s conference, Dearborn, Michigan, 2002

[73] UnitCells© User Manual, University of Nottingham, 2012

[74] S. Li, C. Zhou, H. Yu, L. Li, Formulation of a unit cell of a reduced size for plain weave textile composites, *Computational Materials Science*, 50:1770–1780, 2011

[75] S. Li, On the unit cell for micromechanical analysis of fibre-reinforced composites, *Proceedings of the Royal Society A*, 455:815-838, 1999

[76] S. Li, C. V. Singh, R. Talreja, A representative volume element based on translational symmetries for FE analysis of cracked laminates with two arrays of cracks, *International Journal of Solids and Structures*, 46:1793–1804, 2009

[77] P. Tan, L. Tong, G. P. Steven, Modelling for predicting the mechanical properties of textile composites—A review, *Composites Part A*, 28: 903–922, 1997

[78] X. Ding, structural mechanics, Aviation Industry Press, 1991 (In Chinese)

[79] S. Li, Symmetries and material characterisation, *20th International conference on composites material*, 2015

[80] S. Li, Z. Zou, The use of central reflection in the formulation of unit cells for micromechanical FEA, *Mechanics of Materials*, 43:824–834, 2011

[81] Q. Pan. Numerical simulation of thermal deformation of composite materials, Graduate design, NUAA, 2010

[82] P. D. Soden, M. J. Hinton, A. S. Kaddour, Lamina properties, lay-up configurations and stress states for a range of fibre reinforced composites laminate, *Composite Science and Technology,* 58:1011–1022, 1998

[83] X. Zhao, Defects generation in the manufacturing of composite materials, PhD thesis, University of Nottingham, 2016, in preparation

[84] M. Sherburn, Geometric and Mechanical Modelling of Textiles, PhD thesis, University of Nottingham, 2007

[85] S. K. Boyd, R. Müller, Smooth surface meshing for automated finite element model generation from 3D image data, *Journal of Biomechanics*, 39:1287–1295, 2006

[86] G. Taubin, A signal processing approach to fair surface design, *Siggraph'95 Conference Proceedings*, 351–358, 1995

[87] G. Taubin, Geometric signal processing on polygonal meshes, *Euro graphics: State of the Art Report*, 2000

[88] Q. Pan, S. Li, E. Sitnikova, Multi-scale modelling and characterization of 3D woven composites using unit cells, *The 16th European conference of composite material*, 2014

[89] Q. Pan, T. Yu, L. Jeanmeure, S. Li, An automated unit-cell modelling tool UnitCells© on Abaqus platform drawing functionalities from multiple external codes, *The 19th international conference of composite material*, 2013

[90] S. Li, L.F.C. Jeanmeure, Q. Pan, A composites characterisation tool: UnitCell©, *Journal of Engineering mathematics*, 95:279-293, 2015

[91] Abaqus/CAE User's Manual 6.11, USA, Dassault Systems company, 2011

[92] Altair HyperMesh User's Guide 11.0, www.altair.com

[93] PRIME™ 20LV datasheet: epoxy infusion system, Gurit, PDS-PRIME20LV-11-0614

[94] HexTow® IM7 product data, http://www.hexcel.com, 2010

[95] J. F. Labuz, A. Zang, The ISRM Suggested Methods for Rock Characterization, Testing and Monitoring, 2007-2014, Springer, 2014

[96] M. J. Hinton, A. S. Kaddour, P. D. Soden, A comparison of the predictive capabilities of current failure theories for composite laminates, judged against experimental evidence, *Composites Science and Technology*, 62:1725-1797, 2002

[97] M. J. Hinton, A. S. Kaddour, The background to the Second World-Wide Failure Exercise, *Journal of Composite Materials*, 46:2283-2294, 2012

[98] R. Hill, The Mathematical Theory of Plasticity, Clarendon Press, 1998

[99] R. Hill, A Theory of the yielding and plastic flow of anisotropic materials, *Proceedings of the Royal Society A*, 193:281-297, 1948

[100] S. W. Tsai, Strength characteristics of composite materials, NASA CR-224, 1965

[101] V. D. Azzi, S. W. Tsai, Anisotropic Strength of Composites, *Experimental Mechanics*, 5 (9): 283-288, 1965

[102] S. W. Tsai, E. M. Wu, A general theory of strength for anisotropic materials, *Journal of Composite materials,* 5:58–80, 1971

[103] O. Hoffman, The brittle strength of orthotropic materials, *Journal of Composite Materials,* 1:200-206, 1967

[104] J. Schellekens, R. D. Borst, The use of the Hoffman yield criterion in finite element analysis of anisotropic composite, *Computers & Structures*, 37:1087-1096, 1990

[105] R. M. Christensen, Stress based yield/failure criteria for fibre composites, *International Journal of Solids and Structures,* 34:529-543, 1997

[106] A. Rotem, Prediction of laminate failure with the Rotem failure criterion, *Composites Science and Technology,* 58:1083-1094, 1998

[107] A. Rotem, The Rotem failure criterion: theory and practice, *Composites Science and Technology,* 62:1663–1671, 2002

[108] Z. Hashin, Failure criteria for unidirectional fibre composites, *Journal of Applied Mechanics*, 47(2): 329-334, 1980

[109] R. C. Batra, G. Gopinath, J. Q. Zheng, Damage and failure in low energy impact of fibre reinforced polymeric composite laminates, *Composite Structures*, 94: 540–547, 2012

[110] A. Puck, H. Schürmann, Failure analysis of FRP laminates by means of physically based phenomenological models, *Composites Science and Technology*, 58:1045–1067, 1998

[111] A. Puck, H. Schürmann, Failure analysis of FRP laminates by means of physically based phenomenological models, *Composites Science and Technology*, 62:1633–1662, 2002

[112] J. Li, X. B. Zhang, A criterion study for non-singular stress concentrations in brittle or quasi-brittle materials, *Engineering Fracture Mechanics*, 73:505–523, 2006

[113] G. Pijaudier-Cabot, Z. P. Bazant, Non-local Damage Theory, *Journal of Engineering Mechanics*, 113:1512–1533, 1987

[114] J. Li, S. Meng, X. Tian, F. Song, C. Jiang, A non-local fracture model for composite laminates and numerical simulations by using the FFT, *Composites Part B*, 43: 961–971, 2012

[115] C. Hochard, N. Lahellec, C. Bordreuil, A ply scale non-local fibre rupture criterion for CFRP woven plies laminated structures, *Composite Structures*, 80:321–326, 2007

[116] S. Miot, C. Hochard, N. Lahellec, A non-local criterion for modelling unbalanced woven ply laminates with stress concentrations, *Composite Structures*, 92:1574–1580, 2010

[117] P. Chen, Z. Shen, J. Wang, Prediction of the strength of notched fibre-dominated composite laminates, *Composites Science and Technology*, 61:1311–1321, 2001

[118] T. Pyttel, H. Liebertz, J. Cai. Failure criterion for laminated glass under impact loading and its application in finite element simulation, *International Journal of Impact Engineering*, 38:252-263, 2011

[119] Q. Zhu, J. Shao, D. Kondo, A micromechanics-based non-local anisotropic model for unilateral damage in brittle materials, *Comptes Rendus Mecanique*, 336:320–328, 2008

[120] W. Zuo, L. Xiao, D. Liao, Statistical strength analyses of the 3-D braided composites, *Composites Science and Technology*, 67:2095-2102, 2007

[121] J. Dong, M. Feng, Damage Simulation for 3D Braided Composites by Homogenization Method, *Chinese Journal of Aeronautics*, 23:677-685, 2010

[122] A. Matzenmiller, J. Lubliner, R. Taylor, A constitutive Model for Anisotropic Damage in fibre composite, *Mechanics of materials*, 20(2):125-152, 1995

[123] M. Lingett, Multi-scale modelling of polymer composite materials at high rate of strain, PhD thesis, University Of Nottingham, 2012

[124] M. Yazici, Loading rate sensitivity of high strength fibres and fibre/maxtrix interfaces, *Journal of Reinforced Plastics and Composites*, 28 (15):1869-1880, 2009

[125] http://www.gurit.com/default.aspx

[126] W. W. Chen, B. Song, Split Hopkinson (Kolsky) Bar: Design, testing and applications, Mechanical Engineering Series, DOI 10.1007/978-1-4419-7982-7, © Springer science+ Business Media, LLC, 2011

[127] W. Kong, Experimental characterisation of 3D woven polymeric matrix composites and macro scale modelling of their impact response for aero engine fan containment applications, PhD thesis, University of Nottingham, 2016

[128] M. Hinton, Failure Criteria in Fibre Reinforced polymer composites: Can any of the predictive theories be trusted? NAFEMS World Congress, Boston, 23rd-26th May 2011

[129] D. Veit, Simulation in Textile Technology, Elsevier Science, Woodhead Publishing, 2012

[130] Z. Zhang, K. Friedrich, Artificial neural networks applied to polymer composites: a review, *Composites Science and Technology*, 63: 2029-2044, 2003

[131] S. Dreiseitl, L. Ohno-Machado, Logistic regression and artificial neural network classification models: a methodology review, *Journal of Biomedical Informatics*, 35: 352-359, 2002

[132] M. W. Gardner, S. R. Dorling, Artificial neural networks (the multilayer perceptron)-a review of applications in the atmospheric sciences, *Atmospheric Environment*, 32: 2627-2636, 1998

[133] E. Eğrioğlu, G. Aladağ, S. Günay, A new model selection strategy in artificial neural networks, *Applied Mathematics and Computation*, 195: 591-597, 2008

[134] I. A. Basheer, M. Hajmeer, Artificial neural networks: fundamentals, computing, design, and application, *Journal of Microbiological Methods*, 43:3-31, 2000

[135] M. Ardestani, Z. Chen, L. Wang, Q. Lian, Y. Liu, J. He, D. Li, Z. Jin, Feed forward artificial neural network to predict contact force at medial knee joint: Application to gait modification, *Neuro computing*, 139: 114-129, 2014

[136] G Bebis, M. Georgiopoulos, Feed-forward neural networks, IEEE Potentials, 1994

[137] S. Dominic, R. Das, D. Whitley, C. Anderson, Genetic reinforcement learning for neural networks, *IJCNN-91-Seattle International Joint Conference on Neural Networks*, 2012

[138] M. Frean, The Upstart Algorithm: A Method for Constructing and Training Feedforward Neural Networks, *Neural Computation*, 2:198-209, 1990

[139] J. T. Lalis, B. D. Gerardo, Y. Byun, An Adaptive Stopping Criterion for Backpropagation Learning in Feedforward Neural Network, *International Journal of Multimedia and Ubiquitous Engineering*, 9 (8):149–156, 2014

[140] H. Demuth, M. Beale, Neural network toolbox for use with Matlab®, User guide for MathWorks, 1997

[141] M. H. Beale, M. T. Hagan, H. B. Demuth, Neural network toolbox$^{\text{TM}}$ user's guide, The MathWorks, 2015

[142] H. K. D. H. Bhadeshia, Neural Networks in Materials Science, *ISIJ International*, 39: 966–979, 1999

[143] T. Hill, L. Marquez, M. O'Connor, W. Remus, Artificial neural network models for forecasting and decision making, *International Journal of Forecasting*, 10: 5-15, 1994

[144] Á. García, O. Anjos, C. Iglesias, H. Pereira, J. Martínez, J. Taboada, Prediction of mechanical strength of cork under compression using machine learning techniques, *Materials & Design*, 82:304-311, 2015

[145] M. W. Dewan, D. J. Huggett, T. W. Liao, M. A. Wahab, A. M. Okeil, Prediction of tensile strength of friction stir weld joints with adaptive neuro-fuzzy inference system (ANFIS) and neural network, *International Journal of Forecasting*, 92:288-299, 2016

[146] H. E. Kadi, Modeling the mechanical behavior of fiber-reinforced polymeric composite materials using artificial neural networks—A review, *Composite Structures*, 73(1): 1-23, 2006

[147] Y. Al-Assaf, H. E. Kadi, Fatigue life prediction of unidirectional glass fiber/epoxy composite laminate using neural networks, *Composite Structures,* 53(1): 65-71, 2001

[148] J. A. Lee, D. P. Almond, B. Harris, The use of neural networks for the prediction of fatigue lives of composite materials, *Composites Part A: Applied Science and Manufacturing*, 30(10): 1159-1169, 1999

[149] K. Velten, R. Reinicke, K. Friedrich, Wear volume prediction with artificial neural networks, *Tribology International*, 33: 731-736, 2000

[150] Z. Zhang, K. Friedrich, K. Velten, Prediction of tribological properties of short fiber composites using artificial neural networks, *wear,* 252: 668-675, 2002

[151] Z. Jiang, Z. Zhang, K. Friedrich, Prediction on wear properties of polymer composites with artificial neural networks, *Composites Science and Technology*, 67(2):168-176, 2007

[152] H. Zhang, Z. Zhang, K. Friedrich, Effect of fiber length on the wear resistance of short carbon fiber reinforced epoxy composites, *Composites Science and Technology*, 67(2):222-230, 2007

[153] Z. Zhang, P. Klein, K. Friedrich, Dynamic mechanical properties of PTFE based short carbon fiber reinforced composites: experiment and artificial neural network prediction, *Composites Science and Technology*, 62:1001-1009, 2002

[154] M. S. Al-Haik, H. Garmestani, A. Savran, Explicit and implicit viscoplastic models for polymeric composite, *International Journal of Plasticity*, 20:1875-1907, 2004

[155] G. Allan, R. Yang, A. Fotheringham, R. Mather, Neural modelling of polypropylene fiber processing: predicting the structure and properties and identifying the control parameters for specified fibers, *Journal of Materials Science*, 36:3113-3118, 2001

[156] C. A. O. Nascimento, R. Giudici, Neural network based approach for optimisation applied to an industrial nylon-6,6 polymerisation process, *Computers Chemical Engineering*, 22:S595-S600, 1998

[157] D. Heider, M. J. Piovoso, J. W. Gillespie Jr., Application of a neural network to improve an automated thermoplastic tow-placement process, *Journal of Process Control*, 12:101-111, 2002

[158] I. I. C. W. Ulmer, D. A. Smith, B. G. Sumpter, D. I. Noid, Computational neural networks and the rational design of polymeric materials: the next generation polycarbonates, *Computational and Theoretical Polymer Science*, 8:311-321, 1998

[159] R. M. V. Pidaparti, M. J. Palakal, Material model for composites using neural networks, *American Institute of Aeronautics and Astronautics*, 31(8):1533-1535, 1993

[160] P. Labossière, N. Turkkan, Failure Prediction of Fibre-Reinforced Materials with Neural Networks, *Journal of Reinforced Plastics and Composites*, 12:1270-1280, 1993

[161] C. S. Lee, W. Hwang, H. C. Park, K. S. Han, Failure of carbon/epoxy composite tubes under combined axial and torsional loading 1. Experimental results and prediction of biaxial strength by the use of neural networks, *Composites Science and Technology*, 59: 1779–1788, 1999

[162] LS-Dyna® Keyword user's manual, Volume II Material Models, LSTC, 2012

[163] S. Li, M. Wang, L. Jeanmeur, F. Yu, Q. Pan, C. Zhou, Characterization of Matrix Cracking Damaged UD Composites in the CDM Framework, to be published

[164] S. Li, Q. Pan, T. Yu, Damage evolution law in the framework of continuum damage mechanics for UD composites, *The 19th international conference of composites*, 2013

[165] R. M. Jones, Mechanics Of Composite Materials, CRC Press, 1998

[166] F. Chang, K. Chang, A progressive damage model for laminated composites containing stress concentrations, *Journal of Composites*, 21:834-855, 1987

[167] S. R. Kalidindi, A. Abusafieh, Longitudinal and transverse module and strengths of low angle 3-D braided composites, *Journal of Composite Materials*, 30:885–905, 1996.

[168] H. Sun, S. Di, N. Zhang, N. Pan, C. Wu, Micromechanics of braided composites via multivariable FEM, *Computers & Structures*, 81:2021–2027, 2003

[169] A. E. Bogdanovich, M. Karahan, S. V. Lomov, I. Verpoest, Quasi-static tensile behaviour and damage of carbon/epoxy composite reinforced with 3D non-crimp orthogonal woven fabric, *Mechanics of Materials*, 62:14–31, 2013

[170] Z. M. Huang, A bridging model prediction of the ultimate strength of composite laminates subjected to biaxial loads, *Composites science and technology*, 64:395-448, 2004

[171] http://www.tohotenax-eu.com/

[172] http://www.westsystem.com/

[173] http://imagej.net/Welcome

[174] T. Yu, Continuum Damage Models and Their Applications to Composite Components of Aero-Engines, PhD thesis, University of Nottingham, 2016, in preparation

[175] J. P. Lambert, G. H. Jonas, Towards standardization in terminal ballistics testing: velocity representation, DTIC Document, 1976

[176] M. E. Messiry, Theoretical analysis of natural fibre volume fraction of reinforced composites, *Alexandria Engineering Journal*, 52: 301-306, 2013

[177] M. Karahan, The effect of fibre volume fraction on damage initiation and propagation of woven carbon-epoxy multi-layer composites, *Textile Research Journal*, 82:45-61, 2011

[178] H. Abdi, L. J. Williams, Principal component analysis, *Wiley Interdisciplinary Reviews: Computational Statistics*, 2: 433–459, 2010

Appendix 1 Procedure of SHPB testing and the data processing procedures [127]

A photograph of SHPB system used in the tests is shown in Figure 1. The incident and the transmission bars are made of maraging 300 ultra-high strength steel. Its yield strength is higher than 2000 MPa, the density is 8080 kg/m^3 and elastic modulus is 198 GPa. Both of the bars are 1000 mm in length and 25.4 mm in diameter. The steel striker bar is 150 mm in length and 25.4 mm in diameter.

The strain signals were measured by linear strain gauges on the incident bar and the transmission bar. The signals from the strain gauges were magnified by Wheatstone quarter bridges and then recorded by a data acquisition board with 2 MHz of sampling frequency. The magnified strain signals were also displayed and checked on an oscilloscope.

The cured pure resin samples were cut into 8 mm thick disks as the test specimens. A total of sixteen 8 mm thickness samples were tested at strain rates in the range from 763 s^{-1} to 2543 s^{-1}. Specimens were loaded on the end of the disks and the loading direction was perpendicular to the end surface. To ensure that the loading surfaces of the specimen were flat and parallel, cylindrical samples were initially cut by a diamond cutting wheel, and then gradually polished to the final dimensions by using a sample polishing machine and 240 grit sand paper. Prior to testing, RS® High Temperature Grease was applied as lubrication on the specimen/bar interfaces to avoid bulging. The specimens were carefully placed so that their geometric centres were aligned with those of the bars.

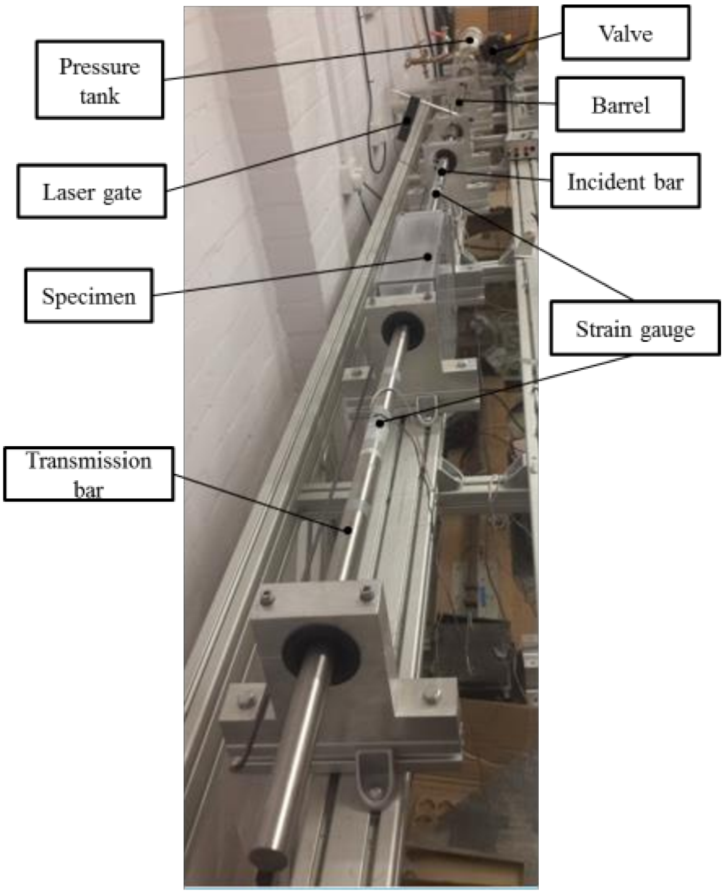

Figure 1 Photograph of SHPB

According to the one dimensional stress wave theory, upon the impact between the striker and the incident bar, a compressive stress pulse of a rectangular shape is generated. Then the stress wave propagates along the incident bar at a velocity of sound, C_{bar}, defined as follows.

$$C_{\mathrm{bar}} = \sqrt{E_{\mathrm{bar}}/\rho_{\mathrm{bar}}} \tag{1}$$

where E_{bar} and ρ_{bar} are the Young's modulus and density of the bar, respectively. The incident strain wave, $\varepsilon_i(t)$, caused by this stress wave is measured and recorded by strain gauges on the bar. The duration of the pulse, t, is determined by the length of the striker, L_{striker}, as follows.

$$t = 2 \times L_{\mathrm{striker}}/C \tag{2}$$

The general principle of SHPB testing is that the time histories of the strain rate, strain, and stress are determined based on the measured reflected and transmission strain signals. The strain rate $\dot{\varepsilon}(t)$ and strain $\varepsilon(t)$of the specimen are calculated as follows.

$$\dot{\varepsilon}(t) = 2\frac{C_{\mathrm{bar}}}{L}\varepsilon_r(t) \tag{3}$$

$$\varepsilon(t) = 2\frac{C_{\mathrm{bar}}}{L}\int_0^t \varepsilon_r\,(t)dt \tag{4}$$

where L is the length of the specimen, $\varepsilon_r(t)$ is the strain caused by the reflected stress wave in the incident bar.

The stress history of the specimen is calculated based on the transmission wave strain signal as follows.

$$\sigma(\mathrm{t}) = \frac{A_{\mathrm{bar}}}{A}E_{\mathrm{bar}} \cdot \varepsilon_t(t) \tag{5}$$

where, $\varepsilon_t(t)$ is the strain caused by the stress wave in the transmission bar. A_{bar} and A are the cross section area of the bars and the specimen, respectively.

The strain signals of the incident and transmission bars were calculated from the voltage of the strain gauges as follows.

$$\varepsilon = \frac{4U_O}{G_F U_I} \tag{6}$$

In which, ε is the strain signal, U_O is voltage signal of the strain gauge, U_I is the excitation voltage of the Wheatstone bridge, G_F is gauge factor of the strain gauge.

For different materials and testing rates, the shapes of the resultant signals show similarities. Typical signals obtained during the compressive SHPB testing pure resin specimens are shown in Figure 2. The signal was processed as follows. Given the length and the density of the striker, the time period of the stress wave was approximately 70 μs. As can be seen in Figure 2, the incident, reflected and transmission pulses occurred within a 350 μs time period. To capture an event of such short duration, the data acquisition was set to be triggered by the signal of the strain gauge on the incident bar. Because of that, the very beginning of the incident pulse was not recorded. Following the incident pulse, there were signal fluctuations of ±0.2 V. This causes an uncertainty in defining the beginning of the reflected pulse signal. In this study, its zero point on the rising slope is regarded as the beginning. On the other hand, the noise level on the transmission bar was very low before the transmission pulse, hence determining its beginning was relatively straightforward. With the reflected and the transmission pulse measured, the strain rate, strain and stress histories were calculated, furthermore, the stress-strain curve was plotted. These are shown in Figure 3.

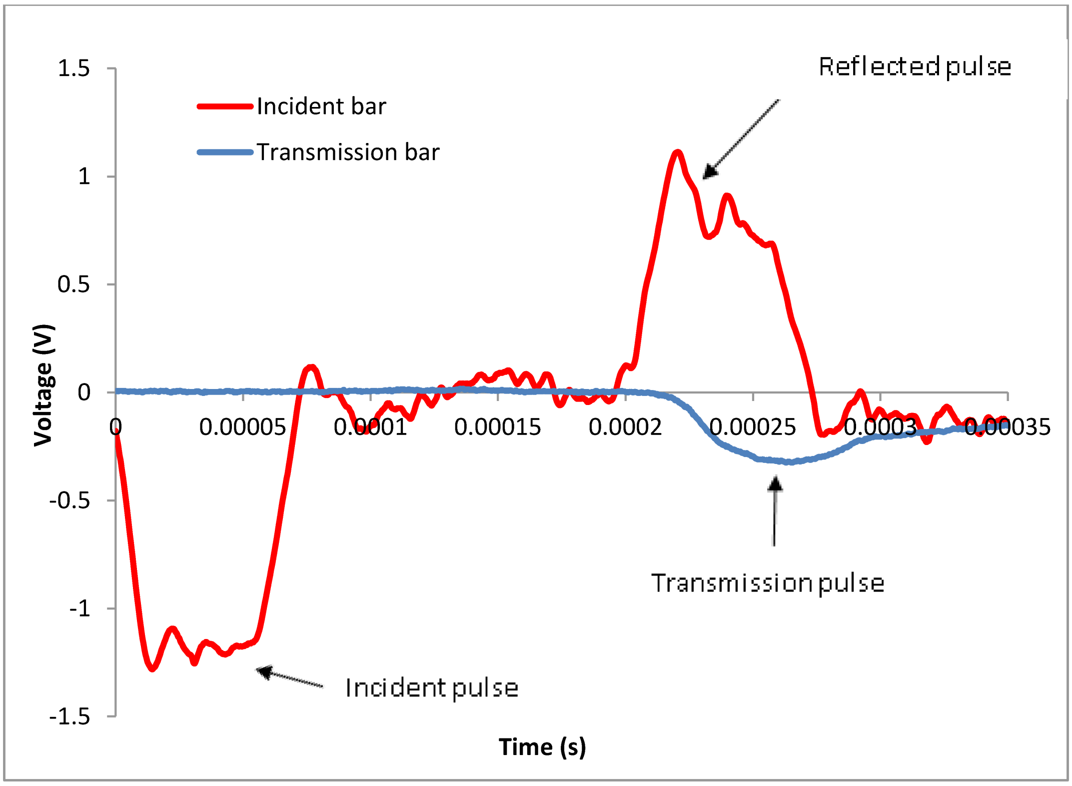

Figure 2 Typical magnified strain gauge output signals in the SHPB test

As can be seen in Figure 3 (a), there are small vibrations in the stain rate history following the initial period of increase. This corresponds to the period from 200 to

630 μs in Figure 3 (b), over which the strain increased almost linearly. The average strain rate of 2451 s^{-1} over this period is regarded as a nominal constant strain rate in the test considered. Over this time period, the stress also reached its maximum, as can be seen in Figure 3 (c), and this is regarded as the compressive strength of the composite at the strain rate of 2451 s^{-1}. The stress-strain curve was plotted by combining the strain history and stress history, which is shown in Figure 3 (d). The gradient of the stress-strain curve over the range of strain from 2% to 12% was treated as the stiffness of the specimen at the strain rate of 2451 s^{-1}, because in this range the strain rate remains approximately constant.

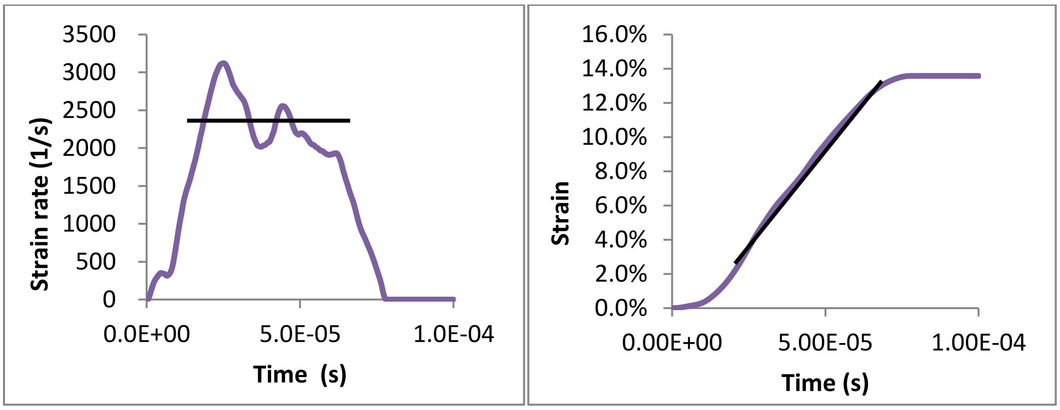

(a) Strain rate history

(b) Strain history

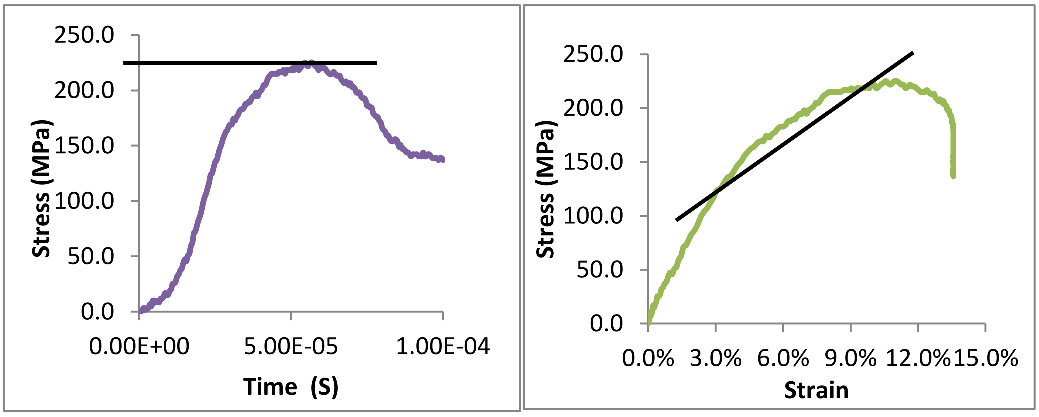

(c) Stress history

(d) Stress-strain curve

Figure 3 Typical processed data of SHPB test